# Yield Surface Identification of Functional Materials and Its Evolution Reflecting Deformation History under Complex Loadings

Thesis submitted in partial fulfilment of the requirement for the degree of

**Doctor of Philosophy**

**In**

**Mechanical Engineering**

by

**Ved Prakash Dubey**

Under the supervision of

**Prof. dr hab. inż. Zbigniew L. Kowalewski (Supervisor)**

**Dr hab. inż. Mateusz Kopeć (Auxiliary supervisor)**



**Department of Experimental Mechanics**

**Institute of Fundamental Technological Research**

**Polish Academy of Sciences**

**Adolfa Pawińskiego 5B, 02-106, Warsaw, Poland**

**May, 2025**

# Declaration

I hereby declare that the work presented in this Thesis is the result of my own original research conducted at the Department of Experimental Mechanics, Institute of Fundamental Technological Research, Polish Academy of Sciences (IPPT PAN), Warsaw, Poland. This Thesis has not been submitted, either in whole or in part, for any other degree or qualification at any other institution.

I affirm that I have complied with all standards of academic integrity and ethical conduct. No part of this work has been fabricated, falsified, or plagiarized. All sources and contributions of other researchers have been appropriately acknowledged and cited.

Ved Prakash Dubey

May, 2025

Dedicated to my parents Vijaya and Suresh Chandra Dubey,

in honour of their continuous love, support, and guidance.

धन्यवाद माँ और पापा।

# Acknowledgements

Ved Prakash Dubey

Warsaw, Poland

May, 2025

# Abstract

The present doctoral Thesis investigates the yield surface identification and its evolution in functional metallic materials under complex loading paths, reflecting pre-deformation histories. The experimental study focuses on CP-Ti (Commercially Pure Titanium), CP-Cu (Commercially Pure Copper), Ti-Cu bimetal, and SS316L stainless steel, offering significant insights into their anisotropic mechanical behaviour and strain-hardening mechanisms. The research addresses the lack of comprehensive data on the impact of pre-deformation on yield surface evolution, a crucial aspect in design engineering and manufacturing processes.

The experimental methodology employs the single specimen approach combined with the sequential probing technique, where the yield surface was identified at various plastic offset strains. The Szczepiński yield criterion was utilized for yield surface approximation. The initial yield surface and its subsequent evolution were determined after pre-deformation induced by uniaxial tension and combined tension-cyclic torsion loading. The results reveal that pre-deformation substantially influences the size, shape, and position of the yield surface, with distinct effects depending on the loading path and material type.

The findings of combined tension-cyclic torsion loading on the mechanical properties of CP-Ti, CP-Cu, and Ti-Cu bimetal indicate a significant reduction in axial stress, with the magnitude of softening increasing with torsional strain amplitude and frequency. Moreover, the anisotropic nature of the initial yield surface of CP-Ti, likely resulting from manufacturing processes, was confirmed through EBSD texture analysis. Whereas, the size of subsequent yield surfaces after pre-deformation of the CP-Ti were reduced in all directions, except of that representing the pure tension. In the case of CP-Cu, pre-deformation through monotonic tension resulted in kinematic hardening, shifting the yield surface in the pre-strain direction. Conversely, combined tension-cyclic torsion pre-deformation induced anisotropic hardening at lower torsional amplitudes and anisotropic softening at higher amplitudes. The dominant influence of torsional strain amplitude over frequency highlights the complex interplay between loading direction and strain path. For the Ti-Cu bimetal, the yield surface evolution reflects the combined mechanical properties of its constituents. The observed kinematic hardening following monotonic tension and kinematic softening after combined loading indicate the critical role of microstructural changes in the bimetal's mechanical response. EBSD analysis confirmed that shear strain magnitude during combined loading triggers recrystallization and the activation of additional slip systems, leading to yield surface anisotropy. The investigation of SS316L explored the yield surface evolution in both wrought and LPBF-printed (Laser Powder Bed Fusion) specimens across different printing orientations. The layer-by-layer additive manufacturing process introduced directional dependencies in yield strength, with Z-oriented specimens exhibiting the lowest mechanical performance. Pre-deformation through monotonic tension resulted in varying degrees of softening, influenced by both material morphology and pre-strain level.

The findings of this Thesis contribute to the broader understanding of anisotropic plasticity and yield surface evolution in metallic materials, offering valuable data for the development of advanced constitutive models in computational mechanics. The experimental validation of the Szczepiński yield criterion highlights its potential as a powerful tool for predicting the mechanical response of materials under complex multiaxial stress states. The outcomes of this study hold significant implications for the design, manufacturing, and structural optimization of functional materials in aerospace, automotive, and biomedical applications.

# Streszczenie

Tytuł rozprawy:

**Identyfikacja powierzchni plastyczności materiałów funkcjonalnych i jej ewolucji uwzględniającej wprowadzoną historię deformacji w warunkach obciążeń złożonych**

Niniejsza rozprawa doktorska dotyczy identyfikacji powierzchni plastyczności i jej ewolucji w funkcjonalnych materiałach metalicznych pod wpływem historii deformacji wywołanej różnymi rodzajami obciążenia. Badania przeprowadzono na komercyjnie czystym tytanie (CP-Ti), komercyjnie czystej miedzi (CP-Cu), bimetalu Ti-Cu oraz stali nierdzewnej SS316L, uzyskując istotne dane opisujące zarówno ich anizotropowy charakter przy zastosowanych obciążeniach, jak i mechanizmy umocnienia odkształceniowego. Badania miały na celu wzbogacenia wiedzy na temat wpływu wstępnego odkształcenia na ewolucję powierzchni plastyczności, co stanowi kluczowe znaczenie w projektowaniu inżynierskim i opracowywaniu nowych procesów produkcyjnych.

W badaniach powierzchni plastyczności zastosowano technikę testowania pojedynczej próbki obciążanej sekwencyjnie, w wyniku różnych kombinacji składowych naprężenia i wartości offsetu plastycznego. Kształt i wymiary powierzchni plastyczności aproksymowano wykorzystując kryterium plastyczności zaproponowane przez Szczepińskiego. Dla każdego badanego materiału wyznaczano początkową powierzchnię plastyczności, a następnie po wprowadzeniu w materiale wstępnej deformacji plastycznej wskutek jednoosiowego rozciągania lub kombinacji jednoosiowego rozciągania i cyklicznego skręcania określano jej ewolucję. Wyniki pokazały, że wstępne odkształcenie plastyczne ma istotny wpływ na rozmiar, kształt i położenie powierzchni plastyczności, z wyraźnymi efektami zależnymi od ścieżki obciążenia i rodzaju materiału.

Wyniki kombinacji jednoczesnego obciążenia o charakterze rozciągająco-skręcającym prowadziło do istotnej redukcji wartości naprężenia osiowego badanego tytanu, miedzi oraz bimetalu Ti-Cu, przy czym wielkość osłabienia wzrastała wraz z amplitudą i częstotliwością odkształcenia skrętnego. Ponadto, anizotropowy charakter początkowej powierzchni plastyczności tytanu, prawdopodobnie wynikający z zastosowanych procesów produkcyjnych, został potwierdzony przez analizę tekstury w badaniach z użyciem EBSD. Natomiast rozmiar kolejnych powierzchni plastyczności po wstępnym odkształceniu tytanu uległ zmniejszeniu we wszystkich rozpatrywanych kierunkach, z wyjątkiem jednego, reprezentującego proste rozciąganie. W przypadku czystej miedzi wstępna deformacja wskutek monotonicznego rozciągania spowodowała powstanie efektu kinematycznego umocnienia, wyrażonego przez przesunięcie początkowej powierzchni plastyczności w kierunku wstępnego odkształcenia. Z kolei, kombinacja monotonicznego rozciągania z cyklicznym skręcaniem prowadziła do wywołania efektu anizotropowego umocnienia przy niższej amplitudzie skręcania i anizotropowe osłabienie przy wyższej jej wartości. Dominujący wpływ amplitudy odkształcenia skrętnego w porównaniu do wpływu wartości częstotliwości pozwolił zidentyfikować złożoną interakcję między kierunkiem obciążenia a ścieżką odkształcenia. W przypadku bimetalu Ti-Cu ewolucja powierzchni plastyczności odzwierciedla łączne właściwości mechaniczne jego składników. Obserwowane kinematyczne umocnienie po monotonicznym rozciąganiu i kinematyczne osłabienie po zastosowaniu kombinacji obciążenia wskazują na istotną rolę zmian mikrostrukturalnych w odpowiedzi mechanicznej bimetalu.

Analiza EBSD potwierdziła, że wielkość odkształcenia ścinającego podczas kombinacji obciążenia wywołuje rekrystalizację i aktywację dodatkowych systemów poślizgu, co prowadzi do ewolucji powierzchni plastyczności wskazującej na powstawanie cech anizotropowych w materiale. Badania stali nierdzewnej SS316L pozwoliły określić ewolucję powierzchni plastyczności zarówno w próbkach materiału wyprodukowanego z zastosowaniem operacji kucia, jak drukowania metodą laserowego spiekania LPBF (Laser Powder Bed Fusion) przy różnych orientacjach procesu. Zastosowany rodzaj drukowania warstwa po warstwie wprowadził zależności kierunkowe w wartościach granicy plastyczności, przy czym próbki zorientowane w kierunku Z wykazywały najniższe parametry mechaniczne. Wstępna deformacja przez monotoniczne rozciąganie skutkowała różnymi stopniami osłabienia, na które wpływ miała zarówno morfologia materiału, jak i poziom wstępnego odkształcenia.

Wyniki prezentowane w rozprawie stanowią przyczynek do szerszego zrozumienia problemu anizotropii plastycznej oraz ewolucji powierzchni plastyczności w wybranych materiałach metalowych, oferując cenne dane mogące znaleźć zastosowanie przy opracowywaniu zaawansowanych modeli konstytutywnych w mechanice komputerowej. Eksperymentalna walidacja kryterium plastyczności Szczepińskiego podkreśla jego potencjał jako efektywnego narzędzia do przewidywania odpowiedzi mechanicznej materiałów w złożonych stanach naprężenia. Przedstawione wyniki badań mogą znaleźć wykorzystanie przy projektowaniu, wytwarzaniu i optymalizacji strukturalnej materiałów funkcjonalnych zarówno w lotnictwie, motoryzacji, jak i w zastosowaniach biomedycznych.

# Contents

# List of Figures

# List of Tables

# Nomenclature

| Symbol | Description |
|---|---|
| $\boldsymbol{\sigma}$ or $\sigma_{ij}$ | A second-order Cauchy stress tensor |
| $\sigma_1, \sigma_2, \sigma_3$ | Principal stresses |
| $\sigma_{xx}, \sigma_{yy}, \sigma_{zz}$ | Normal stress components |
| $\tau_{xy}, \tau_{yz}, \tau_{zx}$ | Shear stress components |
| $I_1, I_2, I_3$ | First, second, and third invariants of the stress tensor |
| $\sigma_m$ | Mean (hydrostatic) stress |
| $S_{ij}$ | Deviatoric stress tensor |
| $\delta_{ij}$ | Kronecker delta |
| $J_1, J_2, J_3$ | First, second, and third invariants of the deviatoric stress tensor |
| $\boldsymbol{\varepsilon}$ or $\varepsilon_{ij}$ | Strain tensor |
| $\varepsilon_{xx}, \varepsilon_{yy}, \varepsilon_{zz}$ | Normal strain components |
| $\varepsilon_{xy}, \varepsilon_{yz}, \varepsilon_{zx}$ | Shear strain components |
| $\sigma_{eq}$ | Equivalent (von Mises) stress |
| $\varepsilon_{eq}$ | Equivalent strain |
| $\nu$ | Poisson's ratio |
| $E$ | Young's modulus |
| $\varepsilon_{eq}^{p}$ | Plastic equivalent strain |
| $F$ | Axial force |
| $T$ | Twisting moment |
| $D$ | Initial outer gauge diameter of the thin-walled tubular specimen |
| $d$ | Initial inner gauge diameter of the thin-walled tubular specimen |
| $\varepsilon_{offset}$ | Offset strain value |
| $\sigma_{engg}$ | Engineering stress |
| $\varepsilon_{engg}$ | Engineering strain |

| | |
|---|---|
| $\sigma^{true}$ | True stress |
| $\varepsilon^{true}$ | True strain |
| $D_0$ | Initial gauge diameter of the solid tubular specimen |
| $A_0$ | Initial gauge cross-sectional area |
| $A_f$ | Final gauge cross-sectional area at failure |
| $l_0$ | Initial length of the specimen |
| $l$ | Length of the specimen during elongation |
| $\delta$ | Axial elongation |
| $\Delta_f$ | Total displacement |
| $\Delta_{load}$ | Axial displacement during loading |
| $\Delta_c$ | Creep displacement |
| $\varepsilon_f^{engg}$ | Uniaxial creep strain at failure (creep ductility) |
| $\varepsilon_{p,load}^{engg}$ | Axial plastic strain at the end of loading |
| $S$ | Metric entropy |
| $N$ | Number of sub-intervals into which the data set of measurement results was divided |
| $p_i$ | Probability of the results in i interval |
| $\sigma_Y$ | Equivalent yield stress |
| $\sigma_{max}$ | Maximum normal stress |
| $\tau_Y$ | Yield limit in shear |
| $\tau_{max}$ | Maximum shear stress |
| $c$ | Cohesion (inherent shear strength) |
| $\varphi$ | Angle of internal friction |
| $f(\sigma_{ij})$ | Yield function |
| $f(I_1, J_2, J_3)$ | Yield function expressed in terms of stress invariants |
| $\mathbb{K}\ or\ K_{ijkl}$ | A fourth-order tensor containing yield parameters of the material |
| $\alpha\ and\ k$ | Drucker-Prager material constants |

| | |
|---|---|
| $F, G, H, L, M$ and $N$ | Hill's anisotropic material constants |
| $m$ | Hill's material parameter with $m > 1$ |
| $k_{ij}$ and $b_{ij}$ | Anisotropic material constants in Szczepiński's yield criterion |
| $Y_{ii}$ | Yield limits under uniaxial tension |
| $Z_{ii}$ | Absolute values of yield limit under uniaxial compression |
| $R_{xy}$ | Yield limit under positive shear stress ($\tau_{xy}$) |
| $S_{xy}$ | Absolute values of yield limit under negative shear stress ($\tau_{xy}$) |
| $A, B, C, D$ and $F$ | Anisotropic material constants used in this work |
| $x_0, y_0$ | Co-ordinates of the ellipse centre of yield surface |
| $\emptyset$ | Rotation angle of the ellipse axes with respect of coordinate system |
| $a$ and $b$ | Major and minor ellipse semi-axes |
| $\beta$ | Biaxial loading angle |

# Chapter 1

# Framework of the Thesis

*This chapter presents the motivation and objectives of the Thesis, describing the scientific background and methodological approach used to achieve the research aims. It provides an overview of the Thesis structure, highlights original contributions, and outlines the potential applications of the findings in advancing anisotropic yield criteria in engineering fields.*

## 1.1 Introduction

The experimental investigation of metallic materials plays a pivotal role in understanding their mechanical properties and behaviour under various loading conditions. Metallic materials exhibit a wide range of properties, including strength, ductility, toughness, and thermal conductivity, making them indispensable across numerous engineering applications. The variety of metallic materials, such as ferrous alloys (steel, cast iron) and non-ferrous alloys (aluminium, copper, titanium), offers personalised solutions for different industrial requirements. These materials are extensively used in automotive, aerospace, construction, energy, and medical industries due to their superior performance and reliability. Experimental investigations, including uniaxial tensile tests, biaxial tests, and shear tests, are essential for characterising the yield behaviour, strain hardening, and failure mechanisms of metallic materials. Understanding these properties enables the development of accurate constitutive models and enhances the prediction of material performance under complex loading scenarios.

## 1.2 Motivation

The accurate identification of yield surfaces of materials under complex loading conditions is a crucial aspect of modern mechanics of materials. Despite significant advancements in yield criteria and plastic deformation theories, experimental studies examining the influence of pre-deformation history on subsequent yield surfaces remain relatively underexplored, especially in the context of complex stress state pre-deformation. In many engineering applications, materials experience pre-deformation due to prior loading histories, such as uniaxial tension or cyclic torsion or complex multiaxial loading, which can significantly alter their yield behaviour. Figure 1.1 presents some of the examples of evolution of the yield surface reflecting the pre-deformation in materials.

In the realm of manufacturing, understanding the effects of pre-deformation under complex loading on yield surfaces can improve processes such as metal forming, and additive manufacturing. For instance, in sheet metal forming, the material undergoes significant plastic deformation, and the resulting anisotropic hardening can affect the final product's dimensional accuracy and mechanical properties.

From an engineering design perspective, the ability to predict the onset of plastic deformation and its evolution under complex loading conditions is crucial for ensuring the safety, reliability, and durability of engineering components. Traditional design approaches often rely on

conservative estimates of material behaviour based on the uniaxial tests, which can lead to over-engineering and increased costs. Understanding of the material behaviour under complex stress loading and the impact of pre-deformation on yield surfaces allows for the optimization of material performance, extending the lifespan of components and minimizing the risk of failure. This knowledge is critical for designing lightweight yet durable components, particularly in industries where weight reduction and safety are paramount such as automotive, aerospace, military, and others.
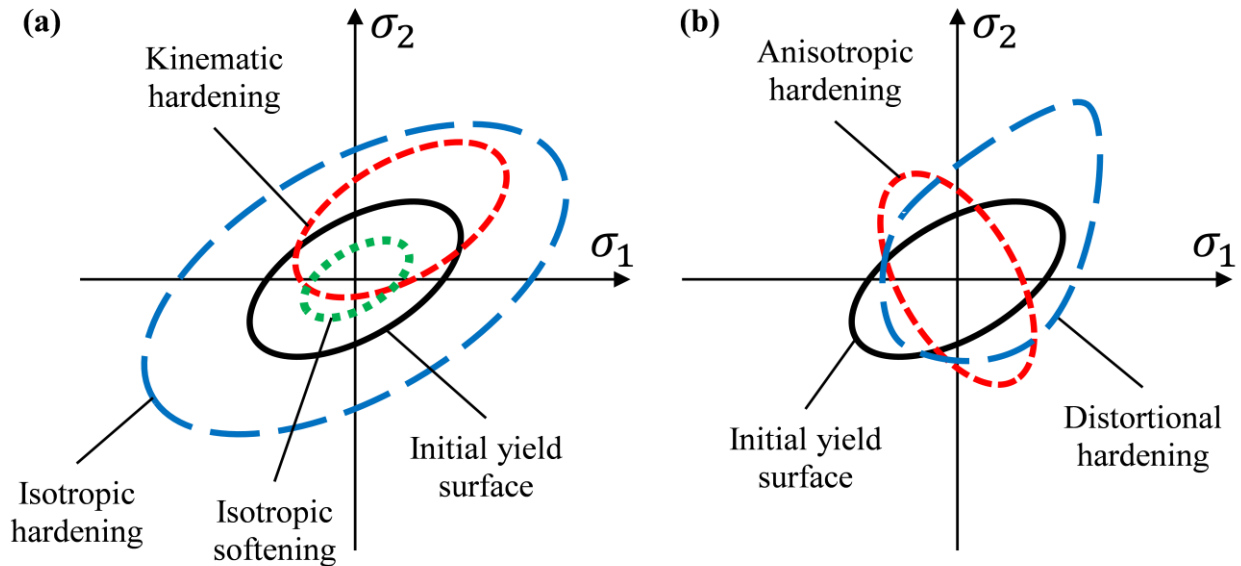


***Figure 1.1.*** *Evolution of the yield locus.*

One of the major challenges in computational mechanics is the development of advanced constitutive models capable of capturing the anisotropic hardening or softening behaviour induced by complex loading histories. Modern computational tools, such as finite element analysis (FEA), rely heavily on accurate material models to simulate complex loading scenarios. Accurate yield surface identification by a yield criterion serves as the cornerstone for formulating such models. Experimental data is essential for validation of these advanced constitutive models, thereby enhancing the numerical simulations of material behaviour in engineering applications.

The aforementioned observations have inspired as the foundation for the preparation of this doctoral Thesis. This research addresses a critical gap in the understanding of the yield surface identification of metallic materials and its evolution under pre-deformation induced by uniaxial and complex loading conditions, which are commonly encountered in practical engineering applications. The primary motivation lies in understanding how pre-deformation alters the initial yield surface and how these changes can be accurately described by appropriate yield criteria. By employing the Szczepiński yield criterion, which incorporates the anisotropic effect through linear stress terms, this research aims to offer a more refined approach to modelling the plastic behaviour of metallic materials. The outcomes will not only advance the scientific understanding of plasticity in metallic materials but also support the development of next-generation materials and structures in engineering design and manufacturing processes.

## 1.3 Objectives

In this Thesis, the experimental identification of yield surfaces for various functional metallic materials is systematically presented. The Szczepiński yield criterion, proposed in 1993, is employed to determine the onset of plastic deformation. This yield criterion extends traditional isotropic yield models by incorporating the effects of material texture and deformation-induced anisotropy, enabling it to accurately capture the anisotropy present in the material. The initial anisotropy arises predominantly from manufacturing processes, which induce texture evolution and consequently change the mechanical properties of the material, deviating from isotropic behaviour. Materials in their as-received state, often without subsequent heat treatment post-manufacturing, tend to exhibit anisotropy due to processes such as rolling, drawing, or extrusion, commonly used in producing metal sheets, bars, or profiles. Engineering applications involving such materials must account for both the inhomogeneous mechanical properties and the undesirable features of anisotropic behaviour, including premature fracture and shear banding.

It is widely recognized that the characterisation of materials based solely on uniaxial testing methods provides limited data, that are not sufficient to identify all aspects of their behaviour, particularly those related to texture and anisotropy induced by manufacturing processes. Therefore,

> *the aim of this Thesis is to carry out a comprehensive experimental and theoretical analysis of the physical mechanisms responsible for the plastic deformation resulting from the complex mechanical loading in functional materials. The materials will be tested both in their as-received state and after prior deformation induced by monotonic or cyclic loading. The yield surface concept will be used to identify the initial texture of the tested materials and for analysing subsequent modifications in their properties by its evolution due to applied loading history induced.*

Thus, to achieve the objectives of this doctoral Thesis, the following methodology is implemented:

- State-of-the-art assessments concerning material characterisation under complex stress states, focusing on materials with varying manufacturing processes and crystal structures. The selected materials include: titanium (HCP), copper (FCC), Ti-Cu bimetal (HCP-FCC), and wrought SS316L (FCC) produced through conventional methods, while LPBF-printed SS316L (FCC) is manufactured via additive manufacturing.

- Fabrication of SS316L specimens in XY, ZX, and Z orientations using the laser powder bed fusion (LPBF) technique with optimized printing parameters.

- Evaluation of the mechanical properties of the chosen materials.

- Development of the specimen geometries for strength tests in a complex state of stress caused respectively by axial load and torque.

- Determination of the initial yield surface with the use of stress components resulting from acting of axial force and twisting moment. Depending on the loading combination

the yield surfaces will represent cross-sections of stress ellipsoid showing the values of yield point of the material in the as-received or as-printed state.

- Development of a loading program combining monotonic tension with cyclic torsion to introduce pre-deformation.

- Analysis of the condition of the tested materials on the basis of secondary stress-strain curves from determination of the yield surface of materials with loading history.

- Determination of the secondary stress ellipsoid of the tested materials reflecting an influence of the loading history induced.

- Microstructural analysis of the tested materials in both the as-received state and after pre-deformation, providing insight into the underlying mechanisms responsible for anisotropy and texture evolution.

## 1.4 Contents of the Thesis

The Thesis is systematically organized into nine chapters, each addressing distinct aspects of the research:

- **Chapter 1: Introduction** – This chapter outlines the general framework of the Thesis, providing the motivation, objectives, original contribution, and scope of the study.

- **Chapter 2: Literature review** – A comprehensive review of historical development of yield surface analysis and effect of pre-deformation processes on material properties is presented. A comparative analysis of mechanical properties in the as-received and pre-deformed states is provided, along with an overview of the most commonly used functional materials.

- **Chapter 3: Experimental techniques** – The experimental methodologies, including quasi-static tension tests and combined monotonic tension-cyclic torsion tests, are detailed. The chapter discusses the state-of-the-art techniques, yield point definitions, specimen geometries, and strain control methods adopted during the experiments.

- **Chapter 4: Yield criteria** – The fundamental principles of yield criteria are introduced, with a concise discussion of historical and widely used models such as Tresca and von Mises. The Szczepiński yield criterion is formulated and adapted to biaxial (axial-shear) stress space, aligning with the experimental framework of the Thesis.

- **Chapter 5: Experimental investigations on CP-Ti** – The mechanical response of commercially pure titanium (CP-Ti) under biaxial stress states is explored. The initial and subsequent yield surfaces in the as-received and pre-deformed states are identified, accompanied by microstructural analysis to assess texture evolution.

- **Chapter 6: Experimental investigations on CP-Cu** – This chapter presents the initial yield surface of commercially pure copper (CP-Cu) and the subsequent yield surfaces following pre-deformation. The mechanical response under biaxial stress states involving combined tension-cyclic torsion loading is examined, with emphasis on anisotropic hardening and softening phenomena.

- **Chapter 7: Experimental investigations on Ti-Cu bimetal** – The mechanical behaviour of Ti-Cu bimetallic structures is analysed under the proposed loading conditions. A literature review on various bimetallic structures is included, along with the effect of monotonic tensile and complex stress state pre-deformation on the initial yield surface and microstructural changes.

- **Chapter 8: Additive manufacturing and experimental investigations of SS316L** – The additive manufacturing of SS316L stainless steel using the LPBF (Laser Powder Bed Fusion) technique is presented. The initial yield surfaces of both wrought and additively manufactured SS316L in XY, ZX, and Z orientations are identified, and their evolution due to tensile plastic pre-deformation at various strain levels is discussed in detail.

- **Chapter 9: Conclusions and recommendations** – The final chapter summarizes the key findings of the Thesis and provides recommendations for future research, highlighting potential directions for better understanding of yield surface evolution in functional materials.

## 1.5 Original contributions

The original contributions carried out in this Thesis are summarised as follows:

- Design, evaluation, and validation of experimental methodologies for strength testing under complex stress states induced by axial force and torque.

- Design and additive manufacturing of SS316L specimens using LPBF technique with optimized printing parameters, ensuring high-quality fabrication.

- Development and presentation of initial and subsequent yield surfaces and curves for selected materials, capturing the impact of pre-deformation on their mechanical response.

- Validation of the Szczepinski yield criterion through its effective application in capturing yield surfaces in both as-received and pre-deformed states under varying pre-strain conditions, across materials with different manufacturing process and crystal structures.

- Comprehensive microstructural analysis of CP-Ti and Ti-Cu bimetal using the Electron Backscatter Diffraction (EBSD) technique to identify texture evolution and grain size changes resulting from pre-deformation.

## 1.6 Applications

Possible application of conclusions and observations included in the Thesis are as follows:

- This research not only advances fundamental understanding of multiaxial plasticity and anisotropy but also offers practical guidance to industries requiring high-performance materials under complex loading. By integrating these findings into design, manufacturing, and simulation workflows, engineers can achieve safer, longer-lasting, and more efficient structural components.

- The insights into torsional strain amplitude in cyclic loading in combination with monotonic tension for CP-Ti, CP-Cu and Ti-Cu bimetal contribute to more accurate fatigue life predictions and failure analyses in components subjected to vibrational and multiaxial operational conditions, such as turbines, pressure vessels, and piping systems.

- The LPBF-printed SS316L results emphasize the influence of build orientation and pre-straining on mechanical anisotropy. This is particularly valuable in industries utilizing additive manufacturing, such as biomedical implants, nuclear components, and high-performance industrial equipment.

- The correlation between microstructural changes and yield behaviour opens avenues for materials scientists to engineer grain structures and crystallographic orientations that optimize strength, ductility, and fatigue resistance based on anticipated loading conditions.

The findings presented in this Thesis have already been published in two peer-reviewed journal articles [1,2]. The first article (*Dubey VP, Kopec M, Łazińska M, and Kowalewski ZL (2023), Yield surface identification of CP-Ti and its evolution reflecting pre-deformation under complex loading. International Journal of Plasticity, 167, 103677*) reports on how the yield surface of CP-Ti was identified and how it evolves when the material is pre-deformed under complex loading conditions. The second article (*Kopec M, Dubey VP, Pawlik M, Wood P, and Kowalewski ZL (2024), Experimental identification of yield surface for additively manufactured stainless steel 316L under tension–compression-torsion conditions considering its printing orientation, Manufacturing Letters, 41, 28-32*) focuses on experimentally determining the yield surface of additively manufactured stainless steel 316L, with a particular emphasis on how different printing orientations affect its mechanical response. Since the content of these articles coincides with the material presented in this Thesis, some chapters, especially Chapters 5 and 8, include content that directly reflects those publications. Elsewhere in the Thesis, the material originating from the articles has been expanded upon and integrated into a broader discussion to provide additional context and depth.

# Chapter 2

# Literature review

*This chapter provides a comprehensive historical review of experimental techniques developed to characterise the yield surface of engineering materials. Additionally, to illustrate the broad applicability of pre-deformation effects proposed in this Thesis, various pre-deformation processes and their influence on material's mechanical properties are presented. The discussed techniques include pre-tension, pre-compression, pre-torsion, and their combined applications. Additionally, a literature-based overview of the key mechanical properties of most commonly used functional materials is provided, highlighting their performance improvements and underlying microstructural mechanisms.*

## 2.1 Introduction

The increasing demand for metallic materials exhibiting enhanced mechanical properties and stability under diverse operating conditions has driven the field of materials science to develop innovative solutions. Among these, the application of pre-deformation has emerged as a widely adopted technique over the past two decades. Pre-deformation involves the intentional introduction of plastic strain into a material during post-processing to modify its microstructure and, consequently, enhance its mechanical performance. This approach can be executed using various deformation techniques, either individually or in combination, by common exploitation processes such as forging, and rolling or typical laboratory loads due to tension, and torsion for example.

The concept of the yield surface has long played a key role in understanding of material behaviour under complex loading conditions. As a fundamental element in theory of plasticity, the yield surface defines the limit beyond which a material undergoes irreversible deformation. The historical development of yield surface determination reflects the broader evolution of continuum mechanics, materials science, and experimental methods, tracing a path from early phenomenological models to sophisticated anisotropic and multiaxial formulations. Early efforts to characterise yielding began in the 19th and early 20th centuries with the classical yield criteria, such as those proposed by Huber, Tresca, and von Mises, which offered simplified but powerful tools for predicting material failure under combined stresses. These models, rooted in macroscopic observations of ductile metals, laid the groundwork for subsequent refinements that incorporated microstructural influences and anisotropic effects. With advances in experimental techniques, particularly the development of biaxial and multiaxial testing machines, have enhanced the understanding of yield behaviour, enabling the empirical mapping of yield loci for a wider range of materials. Throughout the 20th century, the introduction of numerical methods and computational plasticity significantly accelerated the modelling and interpretation of yield surfaces. Researchers began to explore non-associated flow rules, pressure-sensitive criteria, and the influence of texture and loading path history. Yield surface determination thus evolved from simple graphical constructs into complex, multidimensional representations informed by both theory and experiment. This chapter presents a comprehensive literature review divided into two main sections: the first outlines the key historical milestones

in the experimental identification and characterisation of yield surfaces, while the second examines the effects of pre-deformation on the mechanical properties of materials.

## 2.2 Historical assessment of experimental identification of yield surfaces

The determination of the yield surface of materials under multiaxial stress states is critical to understanding plastic deformation. Traditionally, yield surfaces have been modelled using theoretical constructs (e.g., von Mises, Tresca), often assuming perfect material behaviour and isotropy. In his 1958 study, P. M. Naghdi [3] explored the initial and subsequent yield surfaces in plasticity, with a specific focus on the Bauschinger effect and strain-hardening anisotropy in materials subjected to combined torsion-tension-reversed torsion loading paths. Utilizing 27 tubular specimens of extruded 24S-T4 aluminium alloy, the research aimed to establish a detailed understanding of yield surfaces under multiaxial loading. The testing was conducted with precision equipment, including a combined torsion-tension-reversed torsion machine and advanced data recording tools. The results revealed that the initial yield surface closely resembled the Mises yield condition, while subsequent yield surfaces obtained after two predetermined torsional plastic deformation, exhibited a notable Bauschinger effect, especially near the shear stress axis (Figure 2.1). This behaviour supports the need for anisotropic strain-hardening theories to explain material responses, yet the findings also emphasize the role of isotropy in the experimental outcomes. The study's insights into yield surface evolution contribute significantly to the development of plasticity models under complex loading conditions.

The paper by H. J. Ivey in 1961 marks a pivotal contribution to the experimental understanding of yield surfaces in aluminium alloys (Al-alloys) subjected to complex multiaxial loading [4]. Using a systematic series of tension-torsion experiments, the research presents a novel methodology for mapping initial and three subsequent yield surfaces for 19S aluminium alloy. The subsequent yield surfaces were obtained after three different torsional pre-strain values. The hardness variation across the specimens in all states remained within 5–10%, indicating high material uniformity. One of the most significant findings is the clear, smooth translation of the yield surface in the direction of strain hardening, with no evidence of sharp corners or singularities, as shown in Figure 2.2. This directly supports incremental plasticity theories, particularly the Mises-Hencky model, which was validated through accurate prediction of plastic strains even under non-proportional loading paths. The study reveals a pronounced Bauschinger effect, characterised by a diminished elastic range upon stress reversal, particularly near the shear stress axis. However, it also confirms the absence of cross-effects, as tensile yield strength remained unaffected by torsional pre-straining. All observed yield surfaces were convex, and subsequent surfaces no longer enclosed the origin, indicating permanent plastic deformation even after complete unloading. Importantly, the initial modulus of secondary loading matched the elastic modulus, confirming the absence of yield surface "corners." This comprehensive experimental methodology and validation of smooth, convex yield surfaces without invoking corner singularities represents a critical evolution from earlier, less conclusive studies.
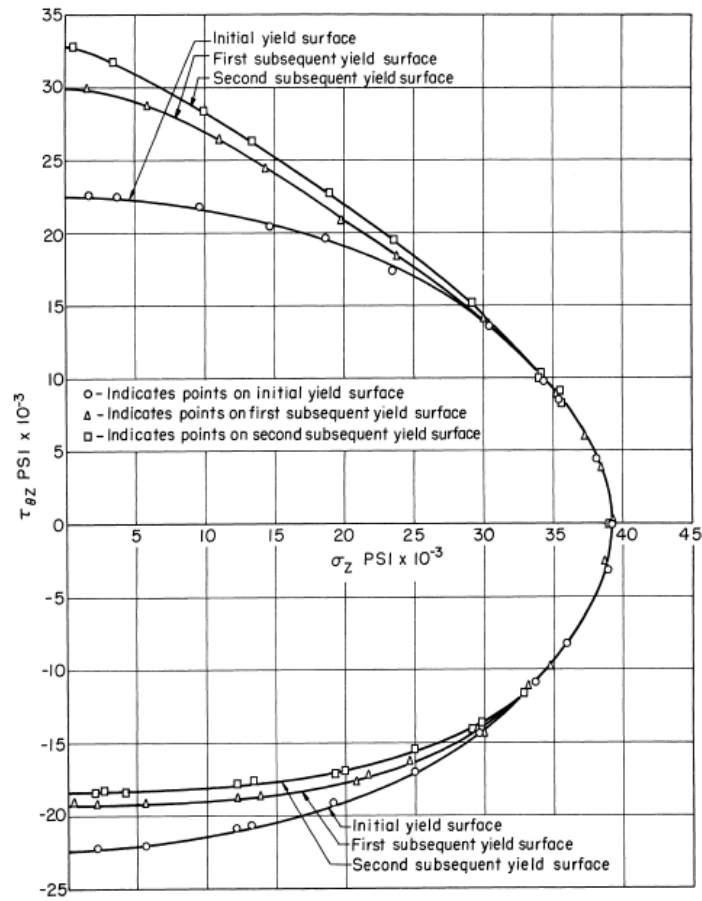
**Figure 2.1.** *The initial and subsequent yield surfaces for 24S-T4 Al-alloy [3].*
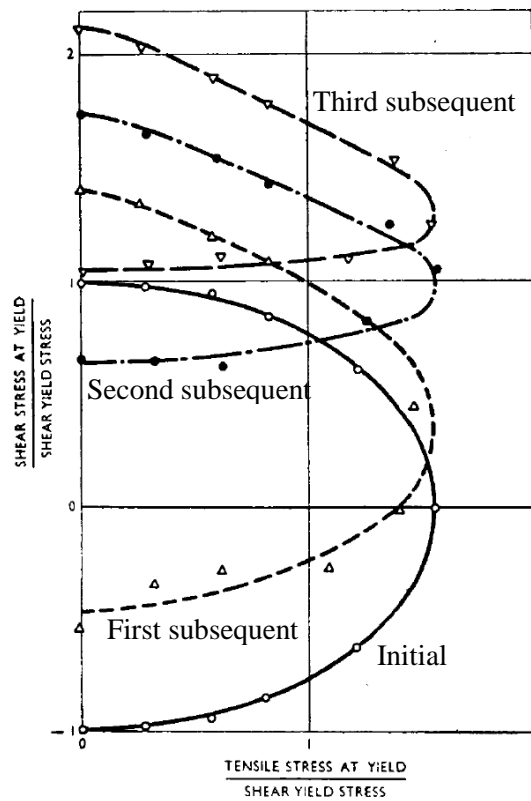


**Figure 2.2.** *Initial and subsequent yield surfaces for 19S Al-alloy [4].*

In 1964, Mair and Pugh presented a detailed experimental investigation into the effect of pre-strain on the yield surfaces of annealed copper, offering novel insights into the hardening behaviour of metals under combined loading [5]. By employing a controlled experimental setup for combined stress and highly isotropic copper, the authors established yield loci after controlled tensile and torsional pre-strains. A key innovation lies in comparing multiple definitions of yield, revealing that the choice of yield criterion significantly affects conclusions, particularly regarding the presence of cross-hardening effects. Unlike prior studies, this work clearly demonstrates a strong cross-effect: torsional pre-strain increases tensile yield stress and vice versa. For instance, tensile yield stress increased from $6.6 \times 10^3$ to $14.0 \times 10^3$ psi as torsional pre-strain rose from 0.25% to 3.0%, confirming non-isotropic hardening. The results also show inflation, distortion, and translation of the yield surface, quantified through deviations from the von Mises circle, supporting Hodge's combined kinematic-isotropic hardening model over simpler theories. Notably, no vertex formation was observed at the pre-strain point, challenging some slip-based theories. This work significantly advances the understanding of yield surface evolution in work-hardening metals, with implications for forming processes.

The series of studies by Szczepinski, Miastkowski, and Marjanowic between 1965 and 1975 significantly advanced the experimental understanding of yield surface evolution in metals under complex loading paths [6–8]. Their research, grounded in meticulous biaxial and multiaxial testing, offers valuable insights that challenge classical hardening models and shape modern plasticity theory. In their 1965 study, Szczepinski and Miastkowski conducted a systematic investigation of the effects of pre-straining on M-63 brass using biaxial loading through internal pressure and axial force [6]. Employing 28 thin-walled tubular specimens, they were able to construct the initial and three subsequent yield surfaces corresponding to equivalent plastic strains ($\varepsilon_p$) ranging from 0.01% to 0.5% (Figure 2.3). The novelty lies in the systematic investigation of how both the shape and orientation of yield surfaces evolve due to different pre-strain paths, a feature rarely quantified in prior studies. A major breakthrough of the study was the observation that yield surfaces evolved differently depending on the direction of pre-strain, particularly at low strain levels. The results show that while high-strain yield surfaces ($\varepsilon_p = 0.5\%$) were largely unaffected by the loading path, early-yield surfaces like the proportional limit and $\varepsilon_p = 0.02\%$ exhibited significant rotation, highlighting sensitivity to pre-strain direction. This rotation contradicts predictions from classical isotropic or kinematic hardening models. Furthermore, the study includes an analysis of strain increment vectors, showing that while plastic strain directions generally conformed to the normality rule, deviations occurred, possibly due to material heterogeneity. These insights enhance the understanding of path-dependent plasticity and challenge existing hardening theories.

Expanding on this path-dependence theme, their 1968 paper examined how varying pre-strain histories influence the yield surface in an aluminium alloy using 56 flat specimens subjected to various complex loading paths (Figure 2.4). This time, they introduced an innovative method: large sheets were pre-strained along different trajectories, then small samples were cut in various directions and tested to map post pre-strain yield loci. A key advance lies in quantifying how different loading histories with identical final stress state affect the yield locus. The results showed that when the final segment of the loading path was significantly longer than the initial one, the material effectively "forgot" the initial deformation history [7]. Yield surfaces in such cases became nearly identical, regardless of the initial paths taken. For example, when the final loading (18 kP/mm²) exceeded the prior pre-strain (14 kP/mm²) by 28.6%, differences in yield

loci disappeared. This "memory fading" effect could not be explained by standard kinematic hardening models, which predict persistent yield surface translation. Although the kinematic model correctly estimated the threshold at which the memory fades i.e., when the final loading exceeded the prior one by about 28.6%, it failed to capture the actual shape of the experimentally derived yield loci (Figure 2.4b). Thus, while some aspects of the classical models held, this work revealed their critical limitations and provided essential experimental data to guide the refinement of path-sensitive plasticity theories.
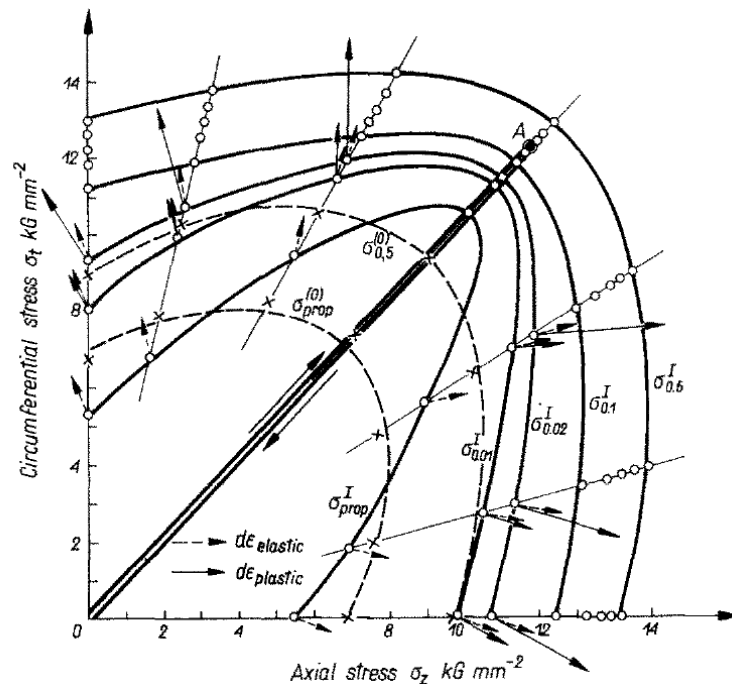


**Figure 2.3.** *Limit curves for the initial material (dashed lines) and pre-strained material until point A (continuous lines) [6].*

The 1975 study by Marjanowic and Szczepinski marked a further step by investigating the post-cyclic yield behaviour of M-63 brass under non-proportional, cyclic loading [8]. Unlike previous experiments that focused on monotonic or unidirectional paths, this study reconstructed yield surfaces based on radial stress paths after cyclic preloading (Figure 2.5). One of the most important findings was observed the evolution of the yield locus after a few cycles of moderate amplitude, the material exhibited fully elastic response within a stabilized yield surface. This phenomenon, resembling structural shakedown, indicates that even though the material was exposed to macroscopically homogeneous cyclic stress fields, but it responded with internal stress redistribution leading to a new stable yield domain. This observation confirmed that cyclic plasticity is governed not only by macroscopic conditions but also by microstructural heterogeneity. Furthermore, the research offered a pathway to quantify shakedown behaviour in terms of cycle amplitude and number of cycles, which has direct implications for fatigue prediction in structural components.

These three studies form a comprehensive experimental foundation for understanding how yield surfaces evolve under various complex loading scenarios. By exposing the inadequacies of classical hardening theories and introducing new empirical methods, the work of Szczepinski and collaborators provide a valuable experimental framework for future yield surface modelling under non-proportional, multiaxial loading conditions.

**(a)**

**(b)**
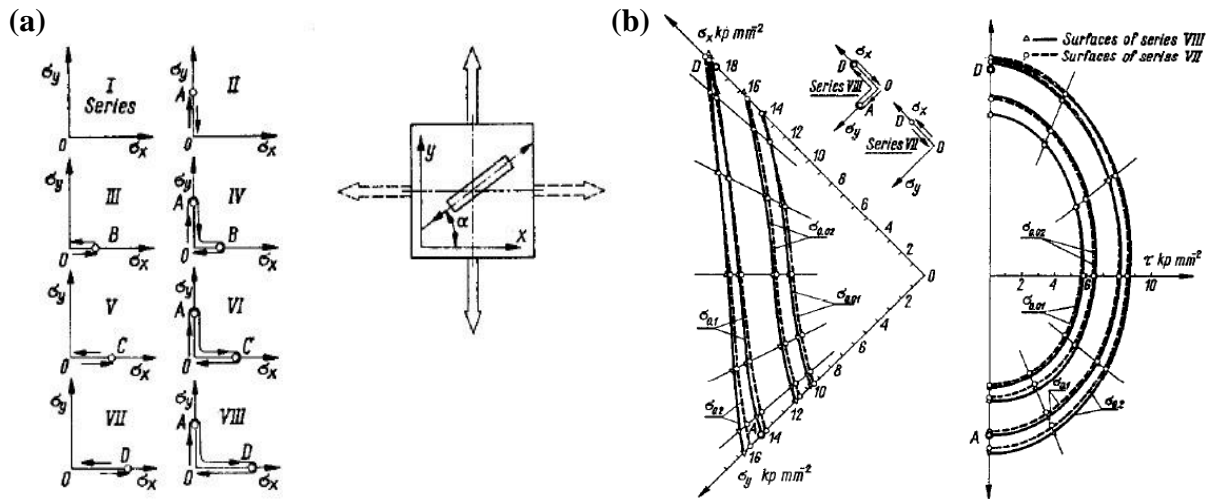


***Figure 2.4.*** *Illustration of pre-stressing programmes (a); and experimental results for the VII-VIII pairs of pre-straining programmes (b) [7].*
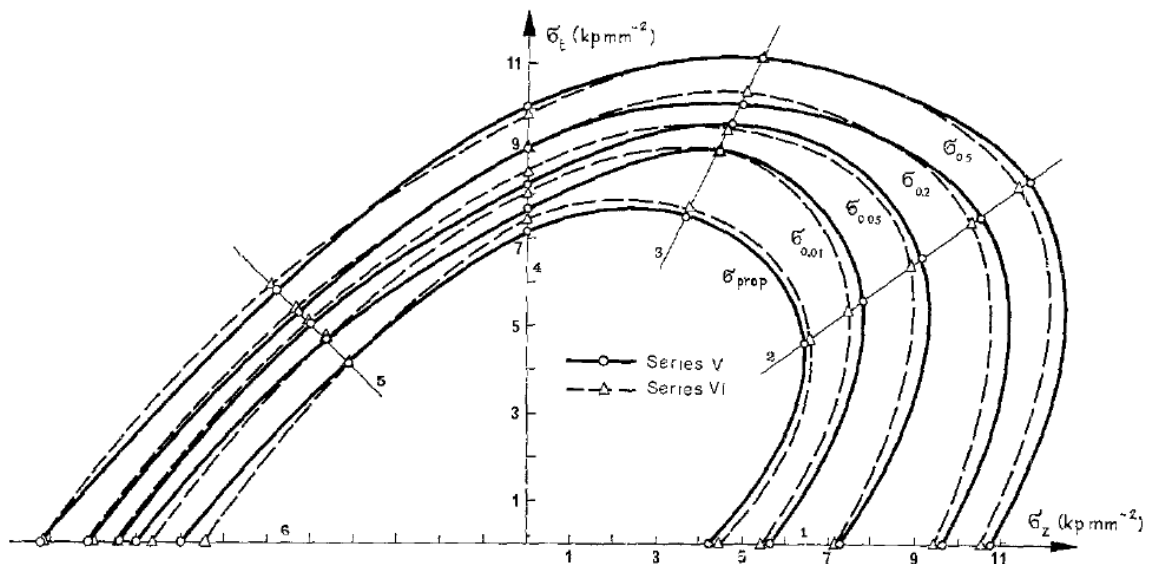


***Figure 2.5.*** *Yield surfaces obtained at various equivalent plastic strains [8].*

The research by Williams and Svensson in 1970 and 1971 provides a foundational contribution to the understanding of yield surface evolution in 1100-F commercially pure aluminium under tensile and torsional pre-strain [9,10]. These studies collectively highlight the complex nature of yield surface distortion, anisotropy development, and the role of underlying microstructural mechanisms in defining yield behaviour.

In their 1970 study, Williams and Svensson conducted an in-depth investigation into the effects of tensile pre-strain on the yield locus [9]. One of the important findings is the significant geometric distortion of the yield surface following plastic deformation. After tensile pre-strain, the yield locus exhibited pronounced flattening in regions opposite to the loading direction and the development of sharply rounded corners at and beyond the loading point (Figure 2.6a). This distortion became more evident as the amount of pre-strain increased, as demonstrated by comparisons between theoretical and experimental loci at 1%, 3%, 7%, and 14% pre-strain. A novel observation was the appearance of additional corners away from the primary loading

direction, indicating that the yield surface distortion is a global phenomenon rather than a localized one. Interestingly, the researchers found no substantial rotation of the yield surface, contradicting some earlier theoretical expectations and minimal cross-effect, which was in contrast to the behaviour under torsional pre-strain. A phenomenological model proposed in this study successfully linked the yield surface changes to internal parameters responsible for the observed distortion. These parameters were found to decay rapidly beyond approximately 100 μin/in proof strain, supporting the conclusion that distortion is predominantly a feature of early-stage plastic flow. Additionally, the study revealed that the Bauschinger effect, considered using a parameter, steadily increased with tensile pre-strain, while the anisotropy effect peaked at 7% before decreasing sharply, a trend not previously reported.

Building upon this, the 1971 follow-up study of Williams and Svensson focused on torsional pre-strain and its influence on the yield surface [10]. This research extended the prior findings by applying 1%, 3%, 6%, and 10% torsional plastic strains to aluminium specimens and analysing the resulting yield loci. A major contribution of this work was the use of a statistically derived yield criterion that closely matched the experimental outcomes. Torsional pre-strain did not lead to noticeable rotation of the yield surface or clear corner formation at the loading point. Nevertheless, the yield surfaces still exhibited severe flattening, especially in regions opposite the pre-strain direction, mirroring trends observed under tensile pre-strain (Figure 2.6b). A particularly noteworthy result was the presence of a stronger cross-effect, indicative of latent hardening, under torsional pre-strain. The authors attributed this to differences in the activation of slip systems between the two loading modes. Torsional loading, characterised by fewer but more intensely activated slip systems, led to higher jog and dislocation densities. In contrast, tensile pre-strain produced a broader, more evenly distributed slip activity with less pronounced individual slip. This insight into microstructural behaviour adds depth to the interpretation of macroscopic yield surface changes.

In 1971, Hecker conducted a comprehensive experimental analysis of yield surface evolution in strain-hardening materials, specifically 1100-0 aluminium and annealed OFHC copper, subjected to uniaxial and multiaxial stress states via simultaneous axial tension and internal pressure [11]. The study systematically examined how the magnitude, direction, and sequence of pre-strain influence subsequent yield surfaces. The research highlights that the definition of yielding significantly affects yield surface shape: small proof strain definitions produce anisotropic surfaces that reflect the material's deformation history, while large proof strains (e.g., 0.2%) result in nearly isotropic surfaces, effectively erasing prior influences. Yield surfaces following tensile pre-strain were defined by small proof strains, demonstrated consistently expansion and translation in the direction of pre-strain and were visibly distorted near the loading point. Additionally, multi-directional pre-strain sequences induced a pronounced negative cross-effect, analogous to the Bauschinger effect, emphasizing path-dependence of plasticity. These findings expose the limitations of traditional continuum plasticity theories. Both isotropic and kinematic hardening models fail to capture the observed anisotropic small strain behaviour, though isotropic hardening performs adequately for large strain responses.

**(a)**



**(b)**
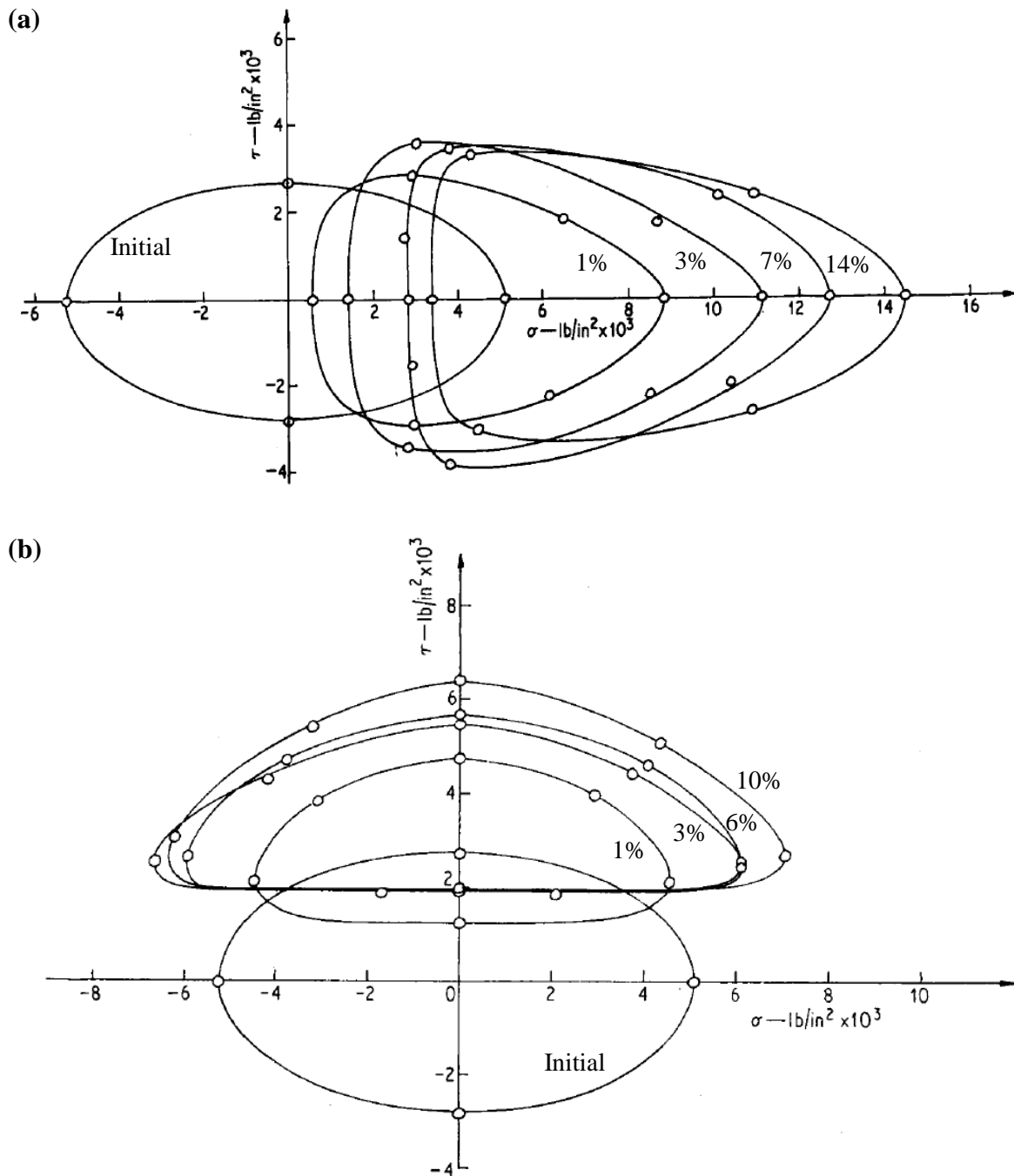


**Figure 2.6.** *Comparison of initial and subsequent yield loci obtained post tensile pre-strains (a); and torsional pre-strains (b) [9,10].*

The pioneering studies conducted by Phillips and his collaborators in the 1970s and 1980s laid a transformative foundation in the experimental exploration of yield surface behaviour, especially under non-isothermal conditions, cyclic loading, and path-dependent pre-stressing [12–20]. These studies focused on commercially pure aluminium (1100-O), using thin-walled tubular specimens loaded in combined tension and torsion, and applied a high-precision, single-specimen method to derive consistent, path-sensitive yield surfaces at both room and elevated temperatures ranging from 70°F to 325°F. One of the key scientific contributions of these studies is the introduction of a new operational definition of the yield point, based on the proportional limit. In contrast to the more commonly used offset or backward-extrapolation

methods, which often lack physical grounding or depend heavily on arbitrary strain thresholds, the proportional limit definition adopted here is rooted in the intersection between a linear elastic line and an incipient strain-hardening line formed by the first three deviating points in the stress-strain curve. This procedure minimizes subjective judgment and allows for early detection of plastic behaviour. With instrumentation sensitivity on the order of 0.25 to 0.5 μin/in and plastic incursions limited to approximately 3 μin/in, this method offers a level of accuracy that ensures the minimal distortion of the evolving yield surface.

A distinguishing methodological decision in these experiments was the use of a single specimen for mapping the entire virgin and subsequent yield surfaces. By avoiding inter-sample variability, the researchers eliminated scatter, which had plagued previous investigations. This approach proved crucial in capturing subtle but important phenomena, such as the Bauschinger effect and asymmetries in hardening behaviour. The consistent and repeatable results obtained across different loading paths and temperatures validate the utility of this method in exploring the true physical characteristics of yield surface evolution.

In their 1972 study, Phillips and Tang investigated the evolution of yield surfaces in pure aluminium subjected to tensile pre-stressing at elevated temperatures ranging from 70°F to 305°F (Figure 2.7) [12]. They introduced a hardening law combining rigid-body motion and directional deformation of the yield surface, effectively capturing the material's response to progressive pre-stressing. Using five specimens, they demonstrated that initial yield surfaces form ellipses lying on isothermal sections of a truncated elliptical cone in $(\sigma, \tau, T)$ space, with an apex extrapolated near the annealing temperature (650°F). A major finding was that subsequent yield surfaces did not pass through the pre-stress points and did not enclose the origin, even at minimal plastic strains as low as 45 με, indicating path dependence in hardening [12]. Additionally, they observed the absence of cross-effects i.e. post pre-strain yield limits in shear remained unchanged from their initial values. At 305°F, the yield surface became undefined, suggesting that under certain conditions, aluminium undergoes continuous creep without an elastic range, defining a temperature-dependent upper limit for the existence of yield surfaces. Additionally, the study confirmed the time-stability of yield surfaces, ruling out time-dependent effects.

In a concurrent 1972 publication, Phillips et al. extended their investigation to combined tension and torsion loading at both room and elevated temperatures up to 325°F [13]. Utilizing thin-walled tubes to ensure a uniform biaxial stress state, they precisely mapped yield surfaces for both virgin and torsional pre-strained material. Key findings included the absence of cross-effects at all temperatures and pre-strain levels, the non-convex nature of yield surfaces that did not enclose the origin, and the observation that yield surfaces did not pass through the pre-stress point [13]. These results challenged traditional plasticity theories and highlighted the critical influence of temperature on yield behaviour. The proposed stress-temperature yield surface methodology, verified against isothermal data, offered a consistent framework for modelling yield phenomena in thermally loaded metals.

In 1974, Phillips et al. examined the evolution of yield surfaces in commercially pure aluminium in the annealed state subjected to complex loading paths at elevated temperatures, using thin-walled tube specimens [14]. A key novelty was the examination of non-monotonic pre-stressing histories, specifically, cyclic torsion and tension with path reversal. They observed that pre-stressing toward the origin of the stress space led to a widening of the yield surface in

the direction of the prior load, a phenomenon not captured by traditional isotropic or simple kinematic hardening models. This supported a previously proposed hardening law, demonstrating its predictive capability under reversed paths. Importantly, they identified the existence of negative plastic strains, where plastic strain opposes the direction of applied stress, signifying a highly path-dependent material response. The study also introduced the concept of a "zero deformation locus," a theoretical boundary in stress space where the yield surface remains unchanged despite loading. Offset yield surfaces, defined through a fixed strain offset, were found to align closely with the envelopes formed by proportional limit yield surfaces, reinforcing their utility in practical material modelling.
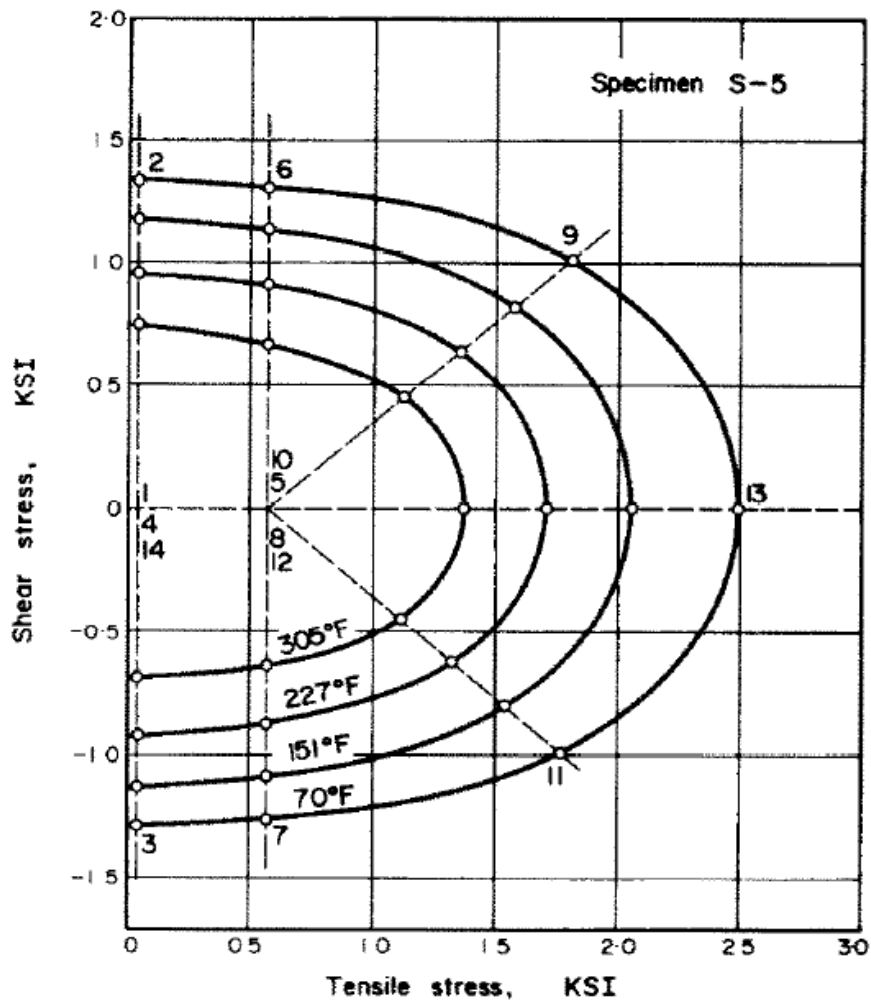


*Figure 2.7. Initial yield surfaces for pure aluminium at various temperature [12].*

In 1976, Phillips and Ricciuti validated their earlier hardening law against three nontrivial pre-stress paths, confirming its accuracy except in cases where the pre-stress path intersected the yield surface at very small angles [15]. Importantly, they confirmed the normality rule for plastic strain rate vectors i.e. the plastic strain rate vector remained normal to the yield surface, reinforcing its applicability even under complex multiaxial states. The study also addressed post pre-strain creep behaviour, showing that while initial creep strain vectors aligned with the plastic strain rate direction, they could deviate over time, indicating evolving deformation

mechanisms. For permanent strains below 1%, plastic deformation adhered to the constant volume hypothesis, whereas creep strains conformed to this only at early stages.

In 1977, Phillips and Moon shifted the focus to the tangency condition between yield and loading surfaces [16]. They identified that yield surfaces become tangential to the loading surface over time. This observation challenged the adequacy of then-dominant hardening models specifically introduced by Prager, Mroz, and Ziegler, which failed to accurately describe experimental data. In contrast, the findings suggested that the previously introduced hardening law by Phillips required modifications, especially when the pre-stressing path was nearly tangential to the yield surface. They asserted that, in situations of conflict between the tangency condition of the yield surface and the hardening law, the tangency condition takes precedence, underscoring the dominant role of geometrical consistency in plasticity theory [16]. The study confirmed that the plastic strain rate vector remains normal to the yield surface and adjusts to become normal to the loading surface as the yield surface aligns tangentially. In 1979, Phillips and Lee expanded this concept, proposing that the loading surface acts as a boundary layer rather than a distinct, sharp delineating boundary [17]. Their observation that yield and loading surfaces may not intersect immediately, even with extended stress exposure, refined the understanding of how plastic strain accumulates, especially under strains of approximately 1%. They also noted the absence of corners on yield surfaces, streamlining modelling efforts and indicating a smoother evolution than previously expected.

In 1984, Phillips and Kawahara further explored the effects of thermal and mechanical loading by analysing isothermal and non-isothermal loading paths at room temperature [18]. They extended equilibrium stress-strain curves to account for both increasing or decreasing stress and thermal effects. Experimental results demonstrated that plastic strain always follows the pre-stress direction, regardless of whether the pre-stressing is directed towards or away from the origin. Their experiments showed time-dependent plastic strains up to $20 \times 10^{-6}$ after 12 hours under isothermal conditions and up to $28 \times 10^{-6}$ under thermal cycling, attributing these to a combination of creep and plasticity [18]. This affirmed the role of temperature in yield surface penetration and deformation evolution. In a parallel effort in 1984, Phillips and Lu conducted tension-torsion experiments under load- and strain-controlled conditions on pure aluminium specimens [19]. They successfully mapped initial and evolving yield surfaces during loadings. The load-controlled experiment allowed for a precise understanding of how the yield surface moves as the stress path progresses. By monitoring the simultaneous increase in strain, they demonstrated that the yield surface becomes tangent to the loading surface, providing deeper insight into how the loading surface itself may be influenced by the amount of plastic strain accumulated during loading. In the strain-controlled experiment, continued stress relaxation was observed at the end of each segment of the strain path. The stress path remained within the loading surface, and plastic strains predominantly accumulated near the loading surface, providing further evidence of the material's response under controlled strain. This study enriched the conceptual framework of yield and loading surfaces and provided empirical data quantifying the evolution of these surfaces under various loading regimes.

In perhaps one of the most expansive studies, in 1985, Phillips and Das systematically compared yield and loading surfaces in commercially pure aluminium and free-cutting brass under varied pre-stressing conditions [20]. The study introduces several novel aspects that mark an important contribution to understanding the evolution of yield surfaces under different pre-stress conditions. One of the primary innovations is the systematic comparison between yield surfaces

and associated loading surfaces under multi-dimensional stress states, with a clear operational definition of yielding based on a limited plastic strains ($2\times10^{-6}$ to $5\times10^{-6}$). This procedure ensured that the yield surface strictly encloses the purely elastic region, providing more precise and physically meaningful yield criteria than traditional definitions. A major novelty lies in the three-dimensional pre-stressing path applied, combining tension, torsion, and internal pressure. Previous investigations largely relied on two-dimensional stress states; thus, this work significantly extends the experimental database to more complex stress conditions, closer to real-world applications. The study carefully traces how initial yield surfaces and subsequent yield surfaces evolve under three-dimensional loading, something rarely achieved before. A major contribution was demonstrating that the yield surface evolves anisotropically based on pre-stress direction. It confirms that when pre-stressing is directed away from the origin, the yield surface contracts along the pre-stressing direction, whereas if pre-stressing moves towards the origin, the yield surface expands [20]. This dynamic behaviour validates theoretical predictions made in Phillips' earlier works and is systematically supported by experimental evidence across different loading paths and temperatures. The study on free-cutting brass offered valuable comparative insights, with brass displaying Tresca-like yield surfaces while aluminium followed Mises-like behaviour. This material-dependent divergence strengthened the general applicability of the proposed framework importantly. The experimental findings also reinforce the lack of cross-effects, meaning that stress components not directly involved in the pre-stress path do not significantly influence the motion of the yield surface — a key assumption in plasticity theories. The observed near-tangential relationship between displaced yield surfaces and corresponding loading surfaces strengthens the two-surface plasticity models.

In 1985, Stout et al. presented valuable insights into the yield and flow behaviour of 1100 aluminium, emphasizing the interplay between microstructure, texture, and plastic flow under various deformation regimes [21]. One of the key advances presented is the identification of distinct yield regimes at different strain levels, highlighting the transition from microstructural to texture-dominated behaviour. At strains below those that induce shear bands, the yield behaviour is characterised by a $5\times10^{-6}$ offset yield criterion, governed by the formation of dislocation cell substructures. The yield locus is observed to distort and translate in the direction of the applied stress, indicating that the developing cell structure carries a memory of the directional history of deformation. This novel finding underscores the importance of microstructural evolution in the early stages of deformation. In contrast, at larger offset yield criteria (back extrapolation technique), the yield locus is less distorted and does not exhibit significant translation, aligning with predictions from texture-based polycrystal plasticity theory (Figure 2.8). This suggests that for large-scale yielding, the texture of the material becomes the dominant factor, overshadowing the influence of microstructural changes. The paper further explores the onset of shear band formation, which occurs at a von Mises effective strain of approximately 0.5 for aluminium in rolling. Once shear bands form, texture alone no longer governs the large offset strain yielding. Instead, shear bands introduce anisotropy in plastic flow, independent of texture, likely due to relaxed constraints on deformation and the specific orientation of the shear bands. This transition signifies a crucial shift in the material's deformation mechanism, where microstructural and textural factors no longer act in isolation, but instead, interact in complex ways to influence the flow behaviour.
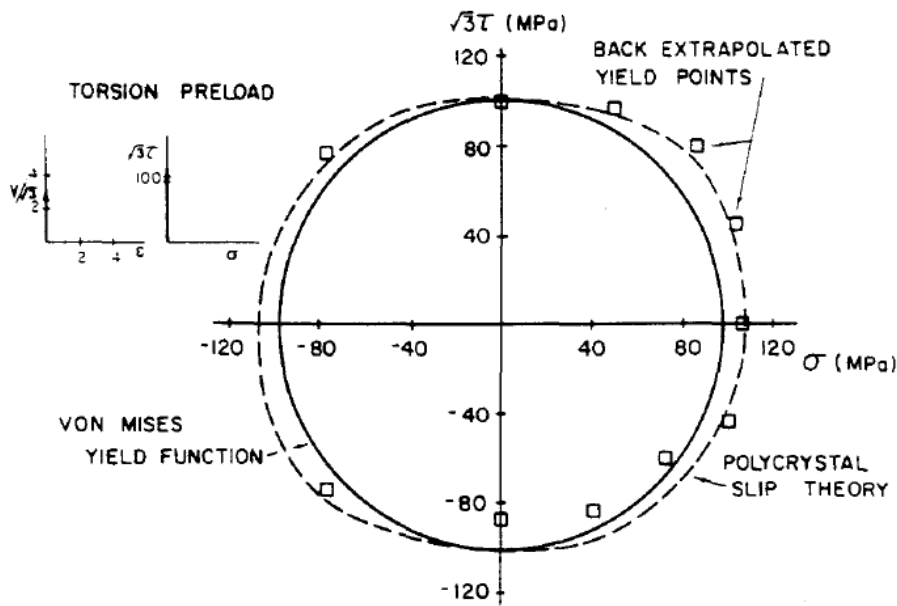
***Figure 2.8.*** *A comparison of the yield locus after a torsional pre-strain of 50% [21].*

In 1986, Helling et al. investigated the small-strain offset yield behaviour ($\varepsilon = 5\times10^{-6}$) of 1100-0 aluminium, 70:30 brass, and 2024-T7 aluminium alloy under various multiaxial pre-stress and pre-strain paths involving combinations of normal and shear stresses, with von Mises effective pre-strains ranging from 1.2% to 32% [22]. The study revealed that the final direction of the pre-strain path, dominantly influences the distortion of the yield locus, rather than the pre-stress direction alone (Figure 2.9). A notable observation was that yield loci could distort without translating, particularly in brass and 2024-T7, challenging traditional assumptions in plasticity models. Moreover, these two materials exhibited a strong memory of their complete pre-strain history and showed primarily kinematic hardening behaviour, with the yield locus translating in stress space. In contrast, 1100-0 aluminium showed less memory effect and mainly isotropic hardening, with the yield locus expanding rather than shifting. The 2024-T7 alloy also uniquely demonstrated shrinkage of the yield surface following plastic deformation. These findings underscore the material-specific nature of yield surface evolution and highlight the limitations of conventional models that overlook the influence of pre-strain direction. The results emphasize the need for constitutive models to incorporate both distortion and memory effects, and to account for differences in hardening mechanisms across materials. Additionally, they suggest that microstructural factors beyond dislocation activity may be responsible for the observed behaviours, underscoring the complexity of accurately modelling yield surfaces in engineering metals under complex loading histories.

In 1991, Wu and Yeh conducted a detailed investigation into the yield surface evolution of annealed AISI 304 stainless steel using a servo-controlled hydraulic testing system and a 5 με ($5\times10^{-6}$) proof strain definition [23]. Their strain-controlled experiments successfully captured the dynamic behaviour of yield surfaces under various loading conditions, despite the challenges posed by the sensitivity of such small strain measurements to factors like probe orientation, data resolution, and loading path. The experiments explored three primary loading paths - pure axial, pure torsional, and proportional axial-torsional - each involving loading, unloading, reloading, and cyclic steady-state phases. The study revealed that the yield surface

undergoes both translation and distortion during plastic deformation (Figure 2.10). Translation occurs in the direction of pre-strain or pre-stress, while distortion patterns are also influenced by these directions. A significant finding is that the pre-stress point becomes part of the evolving yield surface, acknowledging its role in continuous loading histories. As loading proceeds, the yield surface inflates at the forward end and deflates at the rear, forming a sharp front and blunt rear. Upon load reversal, these regions swap, illustrating the reversible and directional nature of yield surface evolution. Notably, the deflation rate at the rear is greater than the inflation rate at the front, leading to an apparent yield surface size reduction during monotonic loading, although the size remains relatively constant in unloading and reloading cycles. The Bauschinger effect is clearly observed, while the cross effect remains weak. Their work emphasized that probe orientation, particularly its perpendicular alignment to the prior loading path, is crucial to minimize Bauschinger related bias in yield point determination.
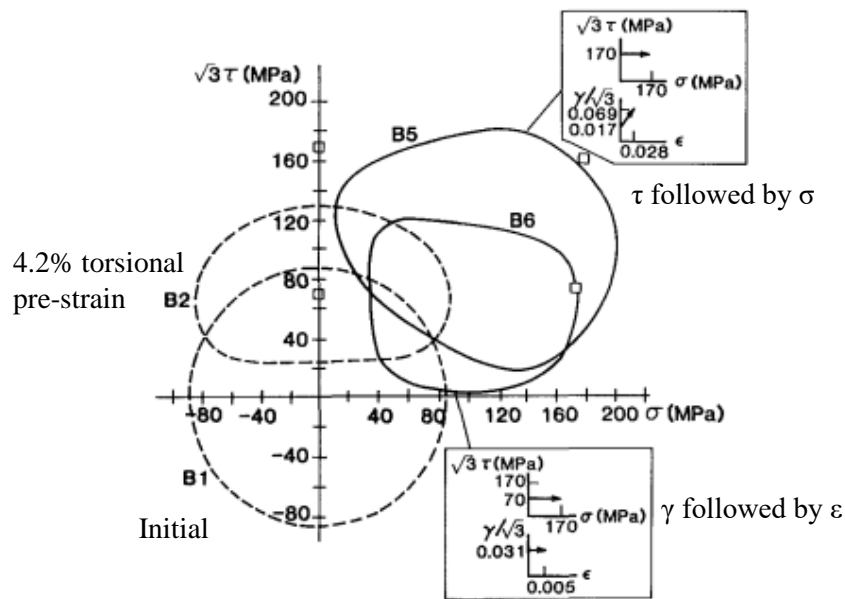


**Figure 2.9.** *A comparison of the yield loci of 70:30 brass after different stress/strain paths [22].*
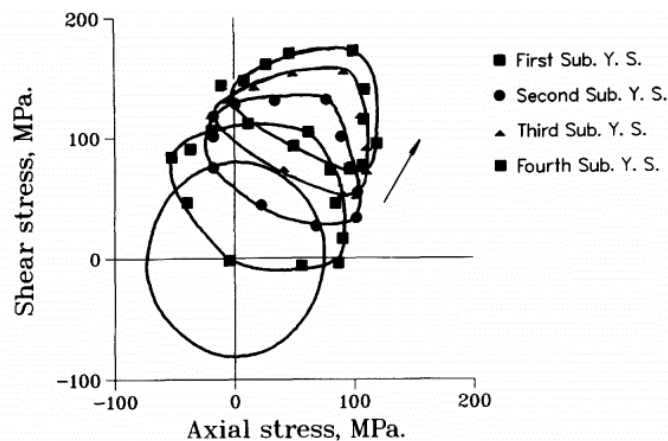


**Figure 2.10.** *Subsequent yield surfaces during proportional axial-torsional loading for 304 stainless steel [23].*

In 1992, Kim presented significant advances in the investigation of yield surface evolution for cold-drawn SAE 1020 steel tubes subjected to different shear strains [24]. The study provides valuable insights into the material's orthotropic behaviour during twisting and its yield locus evolution. Key findings highlight that the orthotropy of the material is maintained during twisting, with the orthotropic axes (x and y) continuously rotating into new orientations. Notably, within a shear strain of up to 30%, the x-axis remains aligned with the orientation of the mechanical fibers, indicating the stability of the material's anisotropic characteristics during deformation. The study also reveals that the plane stress yield locus in the biaxial plane evolves towards an ellipsoidal shape, with the major axis positioned at a 45° angle to the $\sigma_x$-axis, showing a significant change in the yield surface geometry as shear strains increase. Hill's quadratic yield function is confirmed as an effective representation of the material's orthotropic anisotropy at each stage of twisting, offering a more precise characterisation of the yield behaviour under non-proportional loading. While the paper emphasizes that work hardening is path-dependent and cannot be solely attributed to plastic work, the observations serve as a valuable foundation for future experimental studies. A particularly promising area for further investigation is the measurement of the yield locus for tubular specimens subjected to a combination of elongation, expansion, and twist, which could provide deeper understanding of the material's overall work hardening behaviour.

In 1993, Khan and Wang introduced the concept of the equimodulus surface to enhance the experimental investigation of yield surfaces, particularly after large pre-straining [25]. Using fully annealed, copper thin-walled tubular specimens subjected to large torsional loading followed by combined tension-torsion loadings, they experimentally determined the equimodulus surface and subsequent yield surfaces under various offset strain conditions. The equimodulus surface, defined based on the hardening modulus at the point of maximum preloading, was found to lie significantly outside the von Mises loading surface, especially for large von Mises offset strains (Figure 2.11). This suggests the necessity of adjusting hardening modulus values when using two-surface plasticity theories, particularly after load reversals. Their study also demonstrated that subsequent yield surfaces evolve with translation, distortion, and expansion after preloading. When smaller offset strains were applied, more severe distortions appeared; a rounded corner developed at the torsional preloading point, while the region opposite flattened. In contrast, larger offset strains produced yield surfaces that better aligned with the equimodulus surface, expanding beyond the von Mises surface and reflecting more stable plastic behaviour. Interestingly, while von Mises offset strains caused the yield surfaces to pass through the original von Mises loading surface, Tresca offset strains did not, highlighting the importance of the offset strain definition in yield surface determination. Furthermore, the back-extrapolation method yielded subsequent yield surfaces nearly completely outside the von Mises surface, yet closer to the Tresca surface, indicating divergence in prediction models. The study also examined plastic strain increment vectors following sudden changes in loading path and found that these vectors tended to align with the deviatoric stress direction more closely as the offset strain increased, ultimately coinciding at high strain levels. These findings highlight the complex interactions between pre-strain history, offset strain magnitude, and material response in defining accurate yield surfaces.

In 1997, Dietrich and Kowalewski conducted an in-depth experimental investigation on the effects of pre-deformation on the yield surface evolution of aged pure copper under two distinct loading conditions: (a) tension creep at elevated temperatures and (b) monotonic tension at

ambient temperature [26]. The yield surfaces were determined using a probing technique applied to a single specimen, ensuring consistency across comparisons. A least-squares fit using an anisotropic yield condition further quantified the evolution of the surfaces.
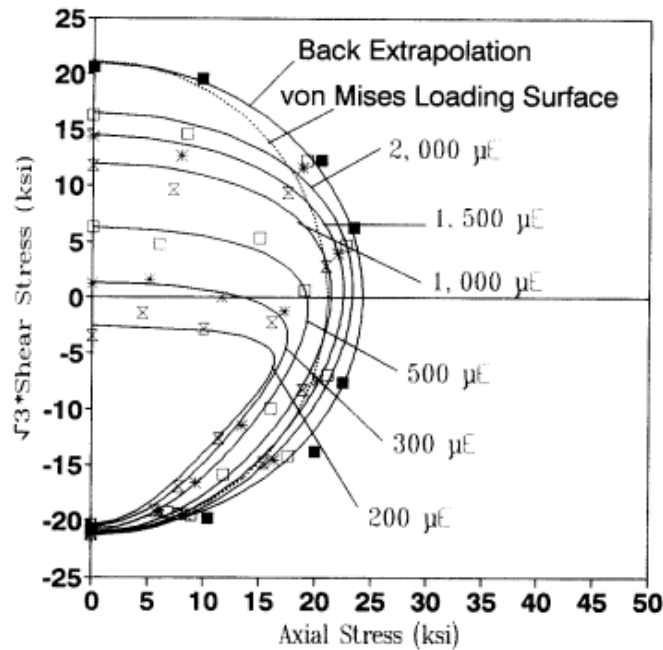


**Figure 2.11.** *Subsequent yield surface of copper after large torsional preloading and its variation with the offset strains [25].*
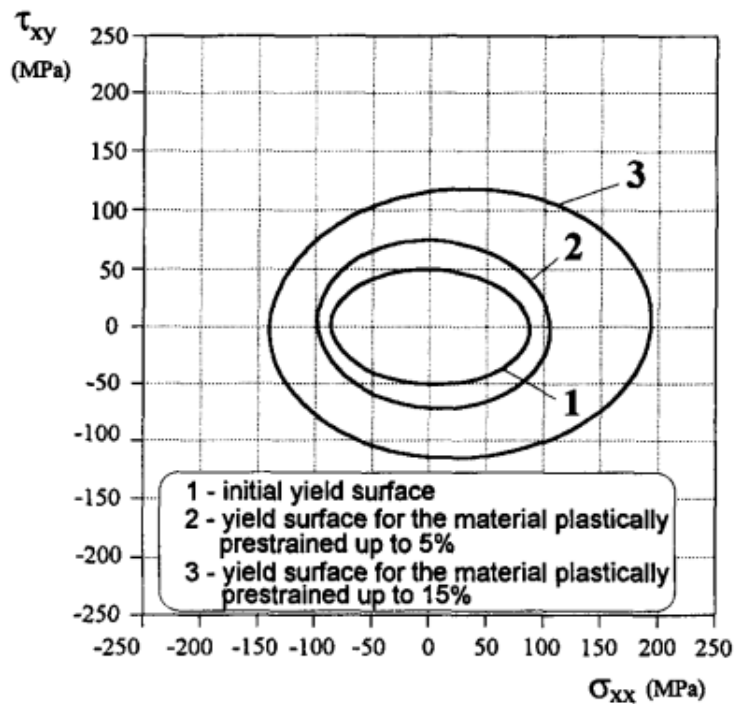


**Figure 2.12.** *Comparison of the initial and subsequent yield surfaces of tensile pre-strained copper [26].*

Initial yield surface of material was well represented by the isotropic Huber-Mises yield criterion and virtually no shift from the origin, providing a reliable baseline for comparison.

Upon subjecting the material to monotonic preloading at ambient temperature, even a small plastic pre-strain of 5% led to significant distortion of the yield surface. The major and minor axes expanded disproportionately, and the axis ratio decreased substantially, eventually stabilizing at a constant value with further increases in pre-strain up to 15% (Figure 2.12). In addition to dimensional changes, a clear translation of the yield surface centre was observed in the direction of preloading, indicating the development of directional anisotropy. When the same level of pre-strain was induced via tension creep at elevated temperature, changes in the yield surface were still evident but noticeably less pronounced. This discrepancy is attributed to the high-temperature exposure, which changes microstructural evolution and affects hardening behaviour differently than room temperature deformation [26]. The findings reveal that while plastic pre-strain, regardless of its origin, can significantly distort the yield surface, the dimensional ratio tends to stabilize with increasing strain, suggesting a form of behavioural convergence.

In 1997, Ishikawa presented significant insights into the behaviour of yield surfaces of 304 stainless steel after tension and/or torsion preloading [27]. The study investigated the subsequent yield surfaces under different loading conditions by using a 50 μm/m offset strain definition of yield. A key advancement is the exploration of three distinct starting points for probing the yield surface, leading to the identification of three types of subsequent yield surfaces. The surface probed from its current centre is confirmed as valid based on the proposed formula, providing a reliable framework for yield surface analysis. The paper demonstrated that during proportional loading, the subsequent yield surface undergoes compression in the direction of pre-stress, accompanied by a translation of its centre. This transformation is captured by an elliptical shape, with the plastic strain experienced being a defining factor in the evolution of yield surface. In the case of non-proportional loading, the study observed more complex transformations, including distortion, translation, and rotation of the yield surface. This highlights the non-linear nature of material response under mixed loading conditions. The paper's proposed formula successfully captures the shape of all subsequent yield surfaces, except after unloading, where a slight expansion of the surface is noted. This behaviour under unloading conditions provides valuable insights into material recovery and potential irreversible changes in the material's structure.

In 1997, Kowalewski and Śliwowski conducted a detailed experimental study on 18G2A low-alloy steel to examine how plastic pre-deformation induced by cyclic loading and monotonic tension affects yield surface shape and dimensions [28]. Initially, in its as-received state, the material showed nearly uniform lower yield limits in all directions within the axial-shear plane, though the shape and position of the yield surface indicated inherent anisotropy. Cyclic loading introduced a significant softening effect, visibly reducing the yield locus size. This softening was direction-dependent, with the maximum reduction always aligned with the pre-strain direction. The study notably quantified the softening caused by monotonic tension, revealing that it exceeds the softening from cyclic loading by over 11% when applied in the same direction and with similar plastic strain (Figure 2.13). Yield surfaces were constructed using sequential probing of a single specimen and modelled effectively using Szczepiński's anisotropic yield criterion [29]. These findings highlight the strong influence of loading history on anisotropic behaviour and yield surface evolution.
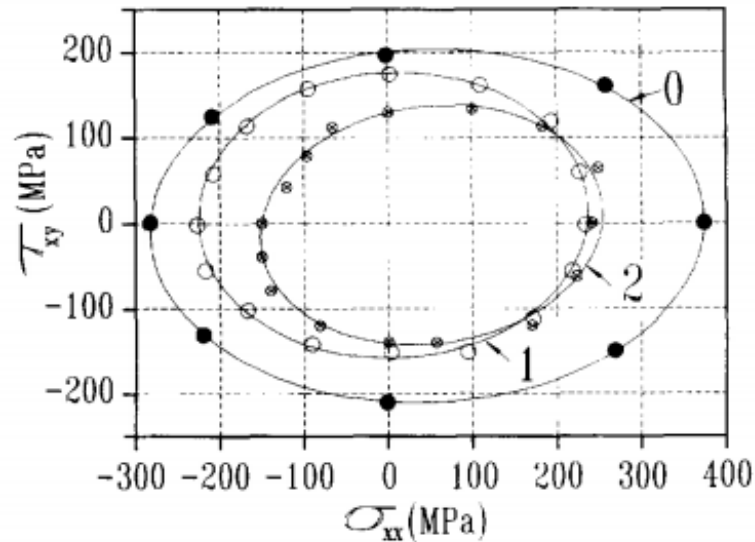
***Figure 2.13.*** *Comparison of the initial yield surface (0) with yield surfaces for the material pre-strained in the same direction due to cyclic loading (1), and monotonic loading (2) [28].*

Akhtar S. Khan's work on yield surface evolution, particularly in the context of materials such as aluminium alloys, has contributed significantly to our understanding of how materials respond under various loading conditions [30–32]. One of Khan's most notable studies, conducted in 2009, examined the evolution of the yield surface in Al 6061-T6511 (a low work hardening alloy), by using a 10 µε deviation from linearity to define yield surfaces, which were experimentally determined under proportional loading paths: tension, torsion, and combined tension–torsion [30]. The initial yield surface closely followed the von Mises prediction, while subsequent yield surfaces showed translation, distortion, and contraction in size with negative cross-effects. A "nose" feature became prominent in the loading direction, especially under tension and combined loading, and surfaces became flattened in the reverse direction. Importantly, yield surfaces obtained after linear, bilinear, and nonlinear unloading paths were smaller than the initial surface but larger than those obtained during prior loading, indicating path dependency [30]. The elastic moduli (Young's and shear) were measured for each yield surface and found to decrease slightly with plastic deformation, much lower than previously reported, due to improved experimental procedures including 1-hour relaxation periods and remounted strain rosettes.

In 2010, Khan extended this work to annealed 1100 Al, a high work hardening alloy [31]. Unlike Al 6061-T6511, the 1100 Al showed yield surface expansion, positive cross-effects, and pronounced noses in the loading direction. Yield surfaces were determined under both proportional and non-proportional loading paths, revealing significant differences such as non-proportional loading caused shrinkage, compounded distortion, and smaller cross-effects compared to proportional paths. After unloading, surfaces translated in the loading direction and retained positive cross-effects. The Young's and shear moduli also declined with increasing strain, more so in combined tension–torsion and this trend was consistent across both proportional and non-proportional loadings. Kinematic hardening was initially dominant but diminished with strain, while isotropic hardening increased.

A further 2010 study investigated yield surfaces under tension–tension stress space in axial, hoop, and combined loadings for both alloys [32]. The same 10 µε offset definition was used.

Yield surface behaviour in this space followed prior observations such as Al 6061-T6511 showed contraction, negative cross-effects, and strong kinematic hardening, while annealed 1100 Al showed expansion, positive cross-effects, and isotropic hardening. The yield surfaces for 1100 Al had sharper noses in axial and hoop directions, and more blunted shapes under combined loading. The elastic modulus decreased by less than 5% after 6% strain in Al 6061-T6511 and after 12% strain in 1100 Al. These comprehensive studies filled a gap in experimental data on yield surface evolution under finite plastic deformation and complex loading paths, offering valuable benchmarks for constitutive model development in plasticity.

In 2012, Dietrich and Socha investigated the degradation of A336 GR5 structural steel under cyclic loading, focusing on yield surface evolution and mechanical property changes [33]. Their study revealed that cyclic loading along both proportional and non-proportional paths in strain space leads to isotropic softening, manifested as a shrinkage of the yield surface in stress space, due to increased inelastic response. This softening indicates a reduced yield limit as fatigue damage accumulates. Notably, the direction of cyclic loading had little impact on the damage rate, which was instead governed by load magnitude. However, proportional loading introduced plastic anisotropy, with the most significant softening occurring in the direction of applied load. In contrast, non-proportional loading paths, such as circular paths, resulted in a higher rate of damage accumulation than proportional paths with the same strain amplitude. These findings enrich the understanding of how complex cyclic loading affects yield behaviour and fatigue-induced softening.

In 2014, Kowalewski et al. conducted a detailed investigation into the multiaxial cyclic behaviour of metallic materials, particularly focusing on the evolution of the yield surface under non-proportional loading [34]. A key observation was the additional hardening effect in 2024 aluminium alloy during non-proportional loading along a circular strain path, an effect absents during proportional loading, indicating a strong dependence of material behaviour on the loading path. The study also revealed a significant phase shift between peak strain and stress signals, which varied with material type, strain amplitude, and frequency, highlighting the complex nature of cyclic deformation. Through experiments involving torsion-reverse-torsion superimposed on monotonic tension in X10CrMoVNb9-1 steel and Cu 99.9 E copper, the authors identified a notable reduction in axial stress associated with increasing shear strain amplitude. However, yield surface analyses using a 0.005% offset strain revealed that this axial stress reduction was not permanent but transient, disappearing once the cyclic torsion ceased. This behaviour demonstrated that stress drops resulted from loading history rather than irreversible material degradation. Additionally, experiments under square strain path non-proportional loading showed stress reductions regardless of deformation direction. The Mróz and Maciejewski three-surface model was successfully applied to predict hysteresis loops and stress-strain behaviour under square, circular, and combined loading paths, further confirming the importance of cyclic loading history in shaping yield surface evolution. This work provided critical insight into the transient, history-dependent nature of yield surface changes in metallic materials under complex multiaxial loading.

These above reported investigations establish a comprehensive experimental and theoretical basis for analysing the evolution of yield surfaces under various pre-strain conditions. The findings emphasize the significant influence of loading path, microstructural evolution, and early-stage plastic deformation on the geometry and progression of the yield surface. Such insights have direct implications for the accurate characterisation and predictive modelling of

materials subjected to multiaxial and non-proportional loading conditions. Furthermore, by highlighting the sensitivity of yield surface determination to the choice of yield definition and loading sequence, these studies reinforce the necessity for advanced constitutive models. These models should incorporate the underlying physical mechanisms of plasticity to enable more accurate predictions of material response, particularly in the low strain regime where conventional formulations often fall short. Table 2.1 summarize the historical development of the yield surface determination.

*Table 2.1. Summary timeline of yield surface analysis*

| Period | Key developments | Materials Focus |
|---|---|---|
| 18th–19th century | Simple friction and tension tests, basic yield criteria (Coulomb, Tresca) | Metals, soils |
| Early 20th century | Multiaxial stress experiments (Bridgman), pressure dependence studies | Ductile metals |
| Mid-20th century | Anisotropic yielding (Hill), pressure-sensitive models (Drucker–Prager) | Metals, soils, concrete |
| Late 20th century | Cyclic loading, evolving yield surfaces, large deformation | Metals, soils |
| 21st century | DIC, micro/nano testing, true triaxial tests, high-rate effects | Metals, composites, soils, rocks |

## 2.3 Effects of pre-deformation on the mechanical properties

Pre-deformation has been shown to induce notable changes in the microstructural characteristics of materials. For instance, it refines the grain structure, introduces dislocation networks, and can facilitate the formation of deformation bands or sub-grains. These microstructural alterations enhance the yield strength due to increased resistance to dislocation motion while potentially reducing ductility. The influence of pre-deformation on mechanical behaviour has been extensively investigated in the literature [35–42]. Researchers have examined the effects of various pre-strain levels on overall mechanical properties including yield strength, ultimate strength, ductility, fatigue life, and creep resistance. Such studies are critical for optimizing the mechanical performance of materials in demanding engineering applications.

During the manufacturing of structural components, engineering materials often experience pre-deformations as a result of their processing history. This mechanical prehistory, commonly referred to as pre-straining, significantly alters the subsequent mechanical behaviour of the material. Pre-straining induces dislocation multiplication, work hardening, and residual stresses, which collectively influence the yield strength, ductility, fatigue resistance, creep behaviour, and plastic deformation capacity of the material. The magnitude of these property modifications is closely associated with the degree of induced pre-deformation and the nature of the loading conditions that induce pre-strain.

An illustrative example of pre-deformation application is the work conducted by Piao et al. [43,44], who developed a method to control the transformation temperature in shape memory alloys through pre-deformation. This advancement has practical implications in the manufacturing of pipe couplings and sealing components, where precise control over phase transformation behaviour is crucial. The initial observation of this phenomenon was made by Melton et al. [45,46], while subsequent detailed investigations were carried out by Zhao et al. [47,48]. Their research demonstrated that pre-deformation could effectively tailor the functional properties of alloys, making them more suitable for specialized industrial applications.
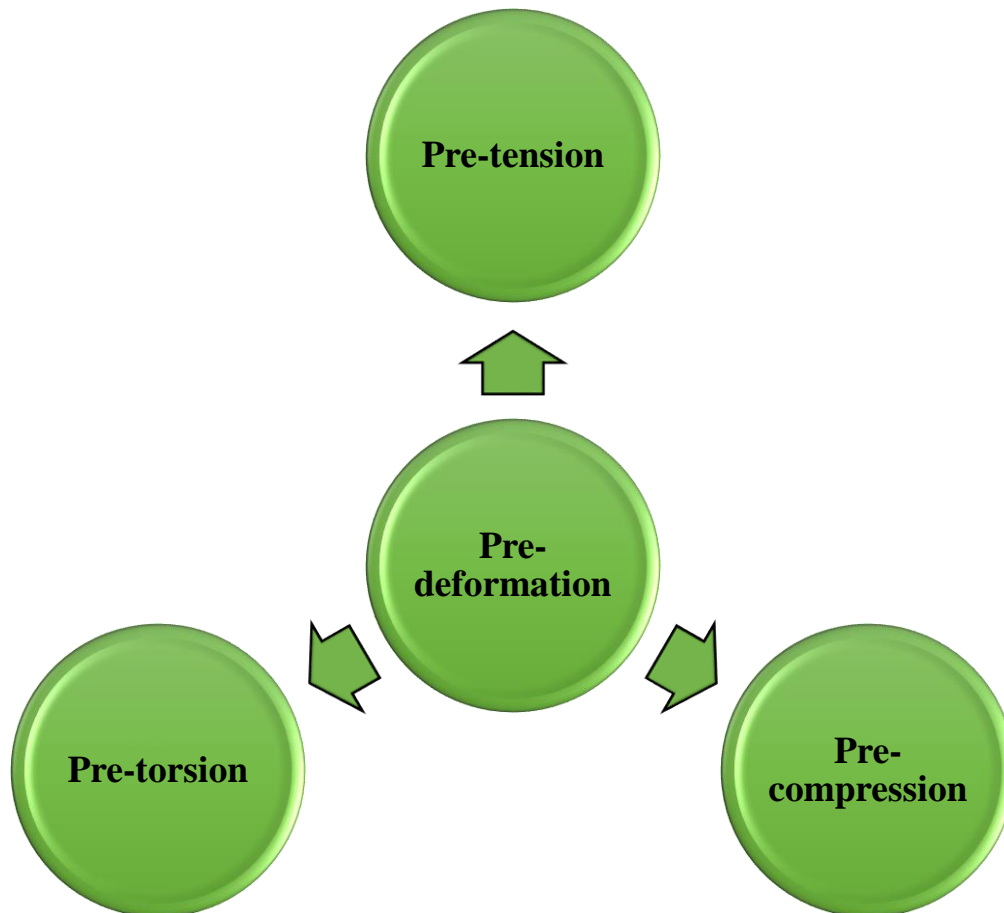


*Figure 2.14. Ways of causing pre-deformation in a material.*

In summary, pre-deformation is a critical processing technique that has proven instrumental in enhancing the mechanical performance and functionality of engineering materials. By comprehensively understanding the relationship between pre-deformation, microstructural evolution, and mechanical properties, researchers and engineers can optimize material processing strategies to meet the stringent requirements of modern industrial applications. Pre-deformation processes can broadly be classified into two categories: (a) laboratory-scale mechanical testing methods, including uniaxial tension, compression, torsion, and bending; and (b) industrial-scale or processing-related techniques, such as rolling, extrusion, forging, and drawing. The former group is primarily employed in research settings to investigate the fundamental deformation mechanisms and microstructural evolution under controlled conditions, while the latter represents real-world applications where materials are subjected to complex strain histories during manufacturing.

In the context of this Thesis, experiments have been systematically performed through three laboratory-based loading modes—tension, compression, and torsion. These modes were selected due to their relevance in evaluating anisotropic plasticity and yield surface evolution in metals in a biaxial (normal-shear) stress space. Accordingly, the literature review presented in the subsequent sections focuses specifically on the effects of tensile, compressive, and torsional pre-deformation, as illustrated in Figure 2.14. This targeted review aims to provide a scientific foundation for understanding the influence of these deformation modes on the mechanical response and microstructural behaviour of metallic materials.

### 2.3.1 Effects of pre-deformation caused by tension

This section of the chapter examines the influence of tensile pre-deformation on the mechanical behaviour of various materials. Yang et al. [49] conducted a detailed investigation into the effect of tensile pre-deformation on the mechanical properties of the aluminium alloy AA2219. In their study, specimens were subjected to different pre-strain levels of 0%, 3%, 6%, 9%, and 15%, with a deformation speed of 2 mm/min. Following this pre-deformation process, the samples underwent stress relaxation aging for 720 minutes. Table 2.2 presents the strength data of AA2219 alloy subjected to various levels of pre-deformation. The results indicate that increasing the pre-deformation level from 0% to 3% leads to a notable enhancement in mechanical properties, with ultimate tensile strength (UTS) and tensile yield strength (TYS) increasing by 12.9% and 38.9%, respectively. However, further increments in pre-deformation from 3% to 9% result in only marginal improvements, with UTS and TYS increasing by an additional 3.0% and 5.0%, respectively. Beyond this range, at a pre-deformation level of 15%, the strength exhibits a slight decline. The strengthening effect of tensile pre-deformation can be attributed to its role in promoting the nucleation and growth of the primary strengthening phases, such as θ' precipitates, during the subsequent aging process. This microstructural refinement enhances the dislocation interaction with precipitates, thereby improving strength. However, excessive pre-deformation, such as the 15% level, can lead to the formation of precipitate-free zones (PFZs) and coarsening of precipitates. These microstructural defects reduce the dislocation-pinning effect, resulting in a decline in mechanical strength [49]. These findings suggest that tensile pre-deformation can either enhance or diminish the strength of materials, depending on the magnitude of the applied pre-strain. There exists an optimal pre-deformation level that maximizes the strengthening effect, beyond which the material's mechanical performance deteriorates due to adverse microstructural changes.

***Table 2.2.*** *Mechanical strength of the AA2219 alloy under various pre-deformations.*

| Pre-deformation level | Tensile yield strength (MPa) | Ultimate tensile strength (MPa) |
| :---: | :---: | :---: |
| 0% | 259.55 | 401.00 |
| 3% | 360.10 | 453.00 |
| 6% | 366.20 | 458.33 |
| 9% | 378.05 | 466.75 |
| 15% | 375.38 | 456.42 |

Wang et al. [50] examined the effect of 4% tensile pre-deformation on the mechanical properties aluminium alloy AA7093 subjected to a 20-minute pre-aging treatment. AA7093 is a novel zinc-containing 7XXX series aluminium alloy that has been specifically developed to meet the high-performance requirements of structural components in the aerospace and automotive industries [51]. The study revealed that the hardness of the alloy increased by approximately 30%, the tensile yield strength improved by nearly 12%, and the ultimate tensile strength exhibited an increase of 4.3% after the pre-tension and pre-aging treatments. These improvements in mechanical properties can be primarily attributed to two synergistic mechanisms: (1) the formation of fine, uniformly dispersed strengthening precipitates during the pre-aging process, which act as effective obstacles to dislocation motion; and (2) the introduction of dislocations during the pre-stretching step, which increases dislocation density and promotes dislocation-particle interactions, thereby enhancing resistance to plastic deformation. The combined effect of these microstructural changes leads to enhancement in the material's mechanical performance.

Hu et al. [52] conducted a comprehensive study on the influence of pre-tension strain on the mechanical properties and microstructural evolution of hot-rolled magnesium alloy (Mg-Sn-Zn). Specimens were subjected to pre-strains of 0%, 3%, and 10% at room temperature, followed by isothermal aging for 48 hours at 150°C in a silicone oil bath. Tensile samples with dimensions of 18 mm × 6 mm × 2 mm were prepared along both the rolling direction (RD) and the transverse direction (TD). Uniaxial tensile tests were subsequently carried out on these specimens at a crosshead speed of 0.5 mm/min. The corresponding mechanical properties are summarized in Table 2.3. The experimental results revealed that with increasing pre-tension strain, the strength of the magnesium alloy increased, but at the expense of ductility. This strengthening trend was consistently observed in both RD and TD samples. The enhancement in strength was attributed to multiple microstructural factors induced by pre-tension deformation.

***Table 2.3.*** *Mechanical properties of hot rolled Mg-alloy at various pre-tension deformation level.*

| Direction | Pre-tension | TYS (MPa) | UTS (MPa) | Elongation (%) |
|---|---|---|---|---|
| | 0% | 196 | 278 | 17.7 |
| Rolling Direction | 3% | 233 | 294 | 14.1 |
| | 10% | 260 | 296 | 10.6 |
| | 0% | 189 | 279 | 17.3 |
| Transverse Direction | 3% | 228 | 284 | 16.0 |
| | 10% | 263 | 299 | 12.2 |

Pre-straining was found to weaken the basal texture of the alloy [53], introducing a high density of dislocations and a limited number of tensile twins. These deformation-induced defects facilitated the heterogeneous nucleation of $Mg_2Sn$ precipitates during aging, which acted as

effective barriers to dislocation motion. The existence of tension twins in adverse orientation has also been reported in the literature [54–57], suggesting that twin formation may contribute to anisotropic mechanical responses in magnesium alloys. The overall strengthening effect can be attributed to three primary mechanisms: (1) precipitation strengthening due to the formation of $Mg_2Sn$ precipitates, contributing approximately +22 MPa with 10% pre-tension; (2) dislocation strengthening resulting from an increased dislocation density; and (3) texture weakening, which slightly reduces the strength by approximately -14 MPa with 10% pre-tension [52].

Park et al. [55] investigated the effects of pre-tension on the mechanical behaviour of hot-rolled magnesium alloy AZ31 (Mg-3Al-1Zn) with pre-strain levels of 0%, 2%, 5%, and 10% applied along the rolling direction. The room-temperature compressive behaviour of pre-strained cylindrical samples ($\phi$6mm x 9mm) was evaluated under a strain rate of $10^{-3}s^{-1}$, as shown in Figure 2.15. The initial stage of compression testing revealed that all samples exhibited a characteristic concave-upward stress-strain curve. This behaviour was primarily attributed to twinning-dominated deformation. The pre-tension process produced an insignificant volume fraction of twins; however, the pre-strained grains were favorably oriented to support {10-12} tensile twinning during subsequent compression along the rolling direction. With the increase of pre-tension, the compressive yield strength exhibited a progressive increase, with values of 66 MPa, 79 MPa, 95 MPa, and 116 MPa corresponding to pre-strain levels of 0%, 2%, 5%, and 10%, respectively. This enhancement in compressive yield strength is associated with the increased dislocation density generated during pre-tension. The accumulation of dislocations raises the critical shear stress required for the activation of {10-12} tensile twinning, thereby delaying twin initiation and enhancing the material's resistance to plastic deformation. Although, twinning acts as main mode of deformation mechanism under compression, but basal slip was also observed to contribute significantly to plastic deformation, accounting for approximately 35% of the overall deformation within twinning-dominated regions. This observation is consistent with the findings of other research study [58], which suggest that basal slip can complement twin propagation, leading to a more complex deformation mechanism in magnesium alloys.
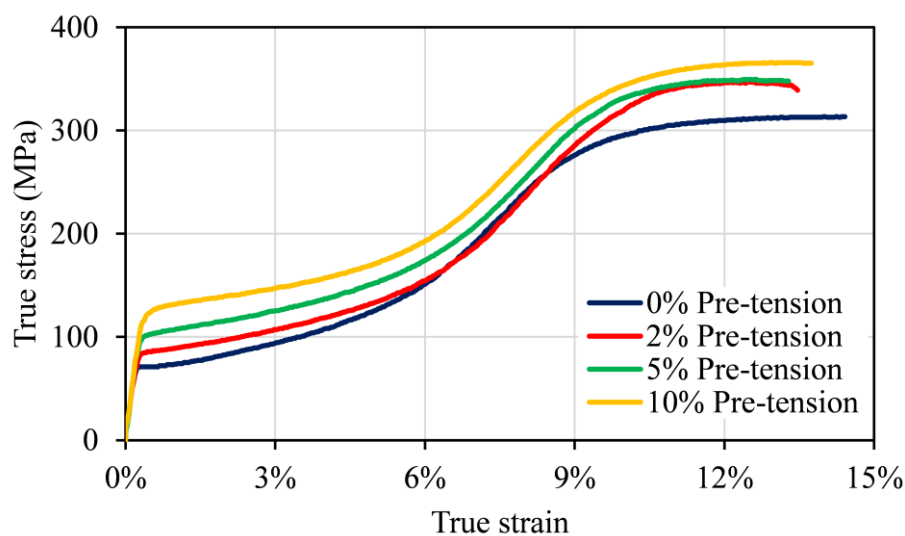


**Figure 2.15.** *Compressive stress-strain curves of Mg alloy AZ31 at various pre-tension levels.*

Park et al. [55] also studied the effects of pre-tension on the fatigue behaviour of hot-rolled AZ31. During cycle deformation, all samples showed asymmetric hysteresis loops, which were attributed to the {10-12} twinning-detwinning activity occurring in the compressive region of the stress cycle. This behaviour is characteristic of hexagonal close-packed (HCP) magnesium alloys due to their limited slip systems and the ease of twinning under compressive stress.

It was observed that, following the first loading cycle, both the tensile and compressive peak stresses increased with increasing pre-tension. This increase in peak stress was primarily driven by the elevated dislocation density introduced during the pre-tension process. Further evaluation of the cyclic deformation behaviour revealed that during the initial 50 cycles, samples pre-strained to 10% exhibited cyclic strain softening, whereas the undeformed (0% pre-tension) samples displayed cyclic strain hardening. The strain softening in the pre-strained samples was likely due to the rearrangement and annihilation of pre-existing dislocations, as well as the activation of twinning-detwinning mechanisms that facilitated plastic deformation.

***Table 2.4.*** *Low cycle fatigue response of AZ31 at various pre-tension levels.*

| No. of cycles | Pre-tension level | Tensile peak stress (MPa) | Compressive peak stress (MPa) | Mean stress (MPa) |
|---|---|---|---|---|
| 1 | 0% | 174.73 | -55.73 | 46.80 |
| | 2% | 208.25 | -67.20 | 59.35 |
| | 5% | 234.57 | -83.44 | 65.62 |
| | 10% | 272.07 | -105.41 | 75.03 |
| 10 | 0% | 194.68 | -85.35 | 44.44 |
| | 2% | 211.44 | -89.17 | 52.03 |
| | 5% | 222.60 | -101.60 | 51.76 |
| | 10% | 247.34 | -114.97 | 58.30 |
| 100 | 0% | 228.19 | -108.28 | 52.29 |
| | 2% | 234.57 | -109.24 | 53.07 |
| | 5% | 232.98 | -115.92 | 52.55 |
| | 10% | 249.73 | -125.48 | 55.69 |

Conversely, the strain hardening in the undeformed samples can be attributed to the progressive accumulation of dislocations during cyclic loading. Interestingly, after 100 cycles, the differences in fatigue response among the samples with varying pre-tension levels diminished, as shown in Table 2.4. This convergence in fatigue behaviour suggests that the microstructural evolution during cyclic loading mitigates the initial variations induced by pre-strain. The

findings of this study [55] suggest that pre-tension can be employed as a processing technique to enhance the compressive yield strength of hot-rolled magnesium alloys without significantly compromising their low-cycle fatigue strength. This is particularly important for structural applications where improved yield strength is desired alongside satisfactory fatigue resistance, such as in automotive and aerospace components made from magnesium alloys.

Zheng et al. [59] conducted a detailed investigation into the effect of pre-stretching prior to artificial aging (200ºC for 24 hours) on the mechanical properties of a Mg alloy with the composition Mg-11Gd-2Nd-0.5Zr. Pre-strains of 0%, 5%, and 10% were applied to the samples before aging. The age-hardness measurements were performed using a load of 49 N and a dwell time of 30 s, as summarized in Table 2.5. The results indicated that pre-deformation enhanced the hardness of the alloy, increasing from 74.55 HV for the 0% pre-stretch condition to 76.1 HV and 80.0 HV for the 5% and 10% pre-stretch conditions, respectively.

The aging kinetics were also significantly influenced by pre-stretching. In the 0% pre-stretch samples, the peak hardness of 117 HV was achieved after 64 hours of aging. In contrast, the peak hardness was attained within a reduced aging time of 24-32 hours for the 5% pre-stretch samples (117 HV) and the 10% pre-stretch samples (118 HV). This acceleration in aging response can be attributed to the introduction of dislocations and deformation twins due to pre-stretching, which serve as heterogeneous nucleation sites for the precipitation of $\beta''$ and $\beta'$ phases. These phases predominantly govern the age-hardening behaviour, while the $\beta_1$ phase has a relatively minor influence before peak aging [59]. However, during prolonged aging, the heterogeneous precipitation of the $\beta_1$ phase at dislocations and twin boundaries becomes more pronounced, advancing the peak aging time.

***Table 2.5.*** *Age hardness of Mg alloy at 0%, 5% and 10% pre-deformed specimens.*

| Aging time (h) | Vickers hardness value (HV) | | |
|:---:|:---:|:---:|:---:|
| | 0% pre-deformed | 5% pre-deformed | 10% pre-deformed |
| 0 | 74.55 | 76.17 | 80.00 |
| 1 | 92.52 | 93.46 | 99.89 |
| 10 | 108.47 | 110.89 | 113.43 |
| 100 | 115.31 | 114.77 | 113.84 |
| 300 | 111.96 | 109.68 | 106.86 |

Table 2.6 presents the tensile properties of the pre-deformed and aged specimens tested at various temperatures. The tensile tests were conducted on rectangular specimens (2 mm x 3.5 mm x 15 mm) at a strain rate of 1 mm/min [59]. At temperatures up to 250°C, the alloy exhibited a progressive increase in strength with increasing pre-deformation. Under peak-aged conditions, the yield strength increased by 24% and 34% in the 5% and 10% pre-deformed samples, respectively, compared to the 0% pre-deformed samples. However, this strength enhancement was achieved on the expense of 20% and 44% loss in ductility for the 5% and 10% pre-stretch conditions, respectively. This trade-off between strength and ductility is

primarily attributed to the presence of deformation twins, increased dislocation density, and heterogeneous precipitation of the $\beta_1$ phase along twin boundaries. Serra et al. [60,61] also demonstrated that in hexagonal close-packed (HCP) metals, twins can act as effective barriers to basal slip, thereby enhancing strength. However, when the testing temperature exceeds 250°C, a decline in the strength of pre-deformed samples is observed, falling below that of undeformed samples. This degradation in strength is primarily due to rapid over-aging, which coarsens the strengthening precipitates, and the activation of non-basal slip systems at elevated temperatures, facilitating plastic deformation. These observations align with the findings of Ahmad et al. [62], further emphasizing the temperature-dependent nature of magnesium alloys.

***Table 2.6.** Tensile properties of Mg alloy specimens at various temperatures.*

| Condition | Temperature (ºC) | TYS (MPa) | UTS (MPa) | Elongation (%) |
|---|---|---|---|---|
| 0% pre-deformed | Room Temperature | 222 | 336 | 2.5 |
| | 200 | - | 339 | 9.9 |
| | 250 | - | 300 | 11.2 |
| | 300 | - | 251 | 12.9 |
| 5% pre-deformed | Room Temperature | 276 | 351 | 2.0 |
| | 200 | - | 348 | 6.3 |
| | 250 | - | 328 | 8.2 |
| | 300 | - | 250 | 14.6 |
| 10% pre-deformed | Room Temperature | 298 | 381 | 1.4 |
| | 200 | - | 365 | 5.0 |
| | 250 | - | 336 | 7.1 |
| | 300 | - | 247 | 15.2 |

### 2.3.2 Effects of pre-deformation caused by compression

This section of the chapter presents the influence of compressive pre-deformation on the mechanical behaviour of various materials. Mehmanparast et al. [63] conducted a comprehensive investigation into the influence of pre-compression on the mechanical properties of Type 316H stainless steel. Specimens were subjected to 8% pre-compression strain at room temperature, and their properties were subsequently compared with as-received (AR) material. Table 2.7 presents the tensile behaviour of AR and pre-compressed (PC) specimens at 550°C. The results indicate a substantial increase in tensile yield stress (approximately 50%) in PC material compared to AR material. This increase is attributed to work hardening induced by room temperature pre-compression, which results in strain accumulation and microstructural modifications. Microstructural analysis revealed that the

cracking mode in PC specimens exhibited brittle intergranular characteristics [63]. Despite the enhanced yield stress, the elastic Young's modulus and ultimate tensile strength remained nearly identical between AR and PC materials, although PC specimens exhibited reduced failure strain. A similar trend was reported by Davies et al. [64], who observed comparable behaviour at 4% pre-compression in 316H stainless steel tested at 550°C.

**Table 2.7.** *Tensile properties of as-received and 8% pre-compressed materials at 550°C.*

| Material state | Young's modulus (GPa) | TYS (MPa) | UTS (MPa) | Elongation (%) |
|:---:|:---:|:---:|:---:|:---:|
| AR | 140 | 177 | 432 | 46.70 |
| 8% PC | 140 | 259 | 441 | 40.24 |

The study further examined the effects of pre-compression on uniaxial creep deformation and creep ductility at 550°C [63]. Table 2.8 shows the loading conditions and creep behaviour of AR and PC materials. AR specimens experienced significant plastic strains (2.5–6%) under nominal stress levels of 257–300 MPa, whereas PC specimens exhibited predominantly linear behaviour under identical conditions. This discrepancy is due to the lower yield stress of AR material, which facilitates plastic strain development during loading at elevated temperatures. In contrast, the hardened PC specimens demonstrated limited plasticity owing to prior strain hardening.

Creep ductility was evaluated using axial failure strain and reduction of area (ROA) measurements, as described by equations 2.1 and 2.2. The ROA method provides localized measurements in the failure region, typically resulting in higher ductility values compared to the average strain values obtained from the axial failure strain approach, as summarized in Table 2.8.

Uniaxial creep strain at failure (known as creep ductility) using axial elongation and reduction of area can be defined as [65];

$$\varepsilon_f^{engg}\big|_{axial} = \frac{\Delta_f - \Delta_{load}}{l_0} = \frac{\Delta_c}{l_0} \tag{2.1}$$

$$\varepsilon_f^{engg}\big|_{ROA} = \frac{A_0 - A_f}{A_0} - \varepsilon_{p,load}^{engg} \tag{2.2}$$

where, $\Delta_f$ = total displacement, $\Delta_{load}$ = axial displacement during loading, $\Delta_c$ = creep displacement, $l_0$ = initial gauge length, $A_0$ = initial cross-sectional area, $A_f$ = final cross-sectional area at failure, and $\varepsilon_{p,load}^{engg}$ = axial plastic strain at the end of loading.

The true failure strain and stress can be written as;

$$\varepsilon^{true} = \ln(1 + \varepsilon^{engg}) \tag{2.3}$$

$$\sigma^{true} = \sigma_{engg}(1 + \varepsilon^{engg}) \tag{2.4}$$

where, $\sigma_{engg}$ is the engineering (i.e. nominal) stress and $\varepsilon^{engg}$ is the engineering strain.

***Table 2.8.*** *Comparison of load up strain and creep ductility for AR and PC specimens.*

| Material | $\sigma_{engg}$ (MPa) | $\sigma^{true}$ (MPA) | $\varepsilon_{load}^{engg}$ (%) | $\varepsilon_{p,load}^{engg}$ (%) | $\varepsilon_f^{engg}$ Axial (%) | $\varepsilon_f^{true}$ Axial (%) | $\varepsilon_f^{engg}$ ROA (%) | $\varepsilon_f^{true}$ ROA (%) |
|---|---|---|---|---|---|---|---|---|
| | 335 | 356 | 6.20 | 5.96 | 12.14 | 11.46 | 17.56 | 20.79 |
| | 300 | 313 | 4.35 | 4.07 | 13.39 | 12.56 | 21.35 | 25.34 |
| AR | 290 | 304 | 4.75 | 4.60 | 10.97 | 10.41 | 22.73 | 27.27 |
| | 280[a] | 293[a] | 4.42[a] | 4.18[a] | - | - | - | - |
| | 257 | 264 | 2.90 | 2.69 | 14.99 | 13.97 | 29.24 | 35.82 |
| | 300 | 301 | 0.24 | 0.03 | 3.41 | 3.35 | 23.04 | 26.20 |
| 8% PC | 280 | 281 | 0.28 | 0.07 | 2.93 | 2.89 | 11.33 | 12.04 |
| | 270 | 271 | 0.25 | 0.05 | 3.07 | 3.02 | 8.62 | 9.02 |
| | 257 | 258 | 0.19 | 0.01 | 1.20 | 1.19 | 4.25 | 4.34 |

[a] Prematurely stoppage of test prior to final failure.

He et al. [66] explored the effects of compressive pre-deformation on the mechanical properties of hot-extruded AZ31 (Mg-3Al-1Zn) alloy. Pre-compression was applied at a constant rate of $10^{-4}$ s$^{-1}$, with strain levels of 0.5%, 1.5%, 1.7%, and 3.0% along the extrusion direction (ED). The mechanical responses under tensile and compressive loading are summarized in Table 2.9. Tensile yield stress initially decreased sharply with increase of pre-compression strain from 0% to 1.5%. However, beyond this level of pre-strain, tensile yield strength followed a gradual decline. This behaviour is attributed to detwinning within twinned regions generated by compressive pre-deformation. Conversely, compressive yield stress increased consistently with pre-compression strain. This increase results from crystal reorientation from soft to hard orientations and the requirement of higher stress levels for continued twin growth. The evolving texture impedes deformation, necessitating greater stress for further twin activation [67,68]. Yield asymmetry between tension and compression decreased before 1.5% pre-compression but increased thereafter. This finding highlights the potential for controlling compressive pre-strain levels to minimize yield asymmetry in AZ31 alloy [66].

Sarker and Chen [69] investigated the effects of pre-compression along the extrusion direction (ED) in extruded magnesium alloy (AM30). Specimens were pre-strained to 1.5%, 2.3%, 4.0%, 5.8%, 7.5%, and 8.2% at a strain rate of 1.25 x $10^{-4}$s$^{-1}$ and room temperature. Figure 2.16 displays the compressive properties of pre-strained samples subjected to re-compression until failure along ED (denoted x%ED-ED) or transverse direction (TD) (denoted x%ED-TD), where x represents the pre-strain level. The compressive yield strength (CYS) increased linearly with pre-strain in x%ED-ED samples (e.g., from 91 MPa at 0% to 232 MPa at 8.2% pre-strain). In contrast, CYS in x%ED-TD samples increased nonlinearly, showing saturation beyond 5.2% pre-strain.

***Table 2.9.*** *Strength of samples in tensile and compressive state at various pre-compression levels.*

| Loading Mode | Pre-compression (%) | Yield strength (MPa) | Ultimate strength (MPa) |
|---|---|---|---|
| Compression | 0 | 125 | 418 |
| Compression then compression | 0.5 | 129 | 407 |
| | 1.5 | 140 | 419 |
| | 1.7 | 149 | 423 |
| | 3.0 | 163 | 415 |
| Tension | 0 | 202 | 326 |
| Compression then tension | 0.5 | 194 | 312 |
| | 1 | 150 | 320 |
| | 1.5 | 125 | 322 |
| | 1.7 | 120 | 325 |
| | 3.0 | 118 | 332 |
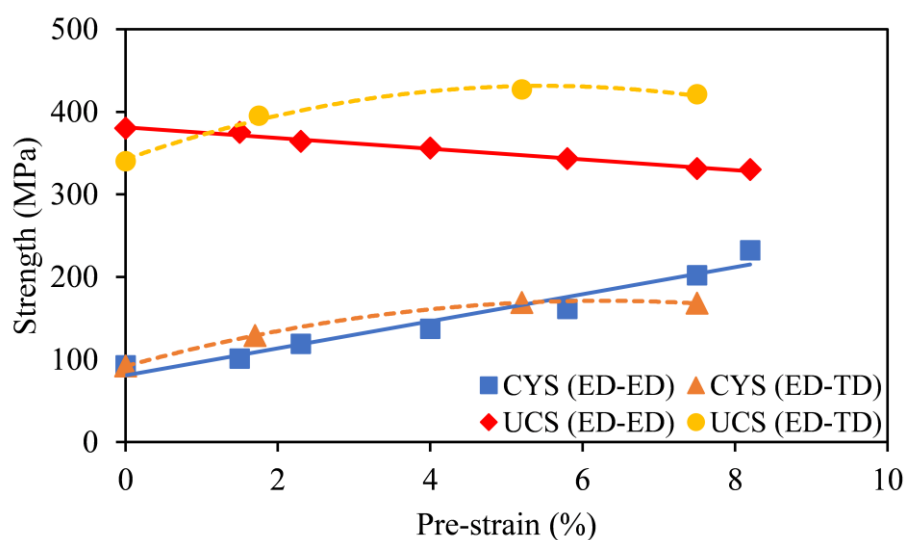


***Figure 2.16.*** *Compressive properties of pre-strained extruded AM30 alloy.*

Figure 2.16 also demonstrates that the effect of pre-compression on ultimate compressive strength (UCS) of AM30 alloy depends greatly on the re-compression loading direction. UCS of x%ED-ED samples decreased linearly with the increase of pre-strain level, whereas, UCS of x%ED-TD samples initially increased and then reached to saturation. The increase in CYS and UTS in x%ED-TD samples is attributed to the formation of new twins during re-compression along TD, which resulted in grain subdivision and a refinement effect. In contrast, re-compression along the same direction (x%ED-ED) led to linear change in CYS and UCS due to twin boundary coalescence, twin growth, or twin disappearance (also reported by Hong et al.

[70]). Twin growth is facilitated by interactions between dislocations and twin boundaries, which depends on the driving stress and characteristics of dislocations [71–73]. Furthermore, it has been found that extension twins formed during pre-compression along ED can recover (known as detwinning) upon reverse loading along TD. This detwinning behaviour has been reported by Park et al. [74–76] and other researchers [77–81]. The evolution of twinning-detwinning and twin boundary dynamics significantly impacts the anisotropic mechanical behaviour of magnesium alloys under different pre-strain and loading conditions.

## 2.3.3 Effects of pre-deformation caused by torsion

Torsional deformation is an effective method for introducing large plastic strains dominated primarily by shear deformation [82]. Compared to conventional tensile and compressive deformation, torsional pre-straining can accumulate higher plastic strain while avoiding strain localization and premature fracture [83,84]. This is particularly advantageous for achieving uniform deformation across the specimen.

Jie et al. [85] investigated the effect of torsional pre-deformation on the mechanical properties of commercially pure titanium at room temperature. The torsional pre-straining was conducted at a rotational speed of 30 rpm, with samples subjected to 1, 2, and 3 full rotations, designated as Torsion-1, Torsion-2, and Torsion-3, respectively. The micro-hardness of the pre-strained and unstrained samples was measured along both transverse and longitudinal sections using a Vickers indenter under a 4.903 N load with a 15 s dwell time, as depicted in Figure 2.17. The results indicated a significant increase in hardness with an increasing number of torsional turns, which is attributed to the progressive grain refinement. The average grain size reduced from 70 μm in the un-deformed sample to approximately 60 μm, 50 μm, and 40 μm in the Torsion-1, Torsion-2, and Torsion-3 samples, respectively.
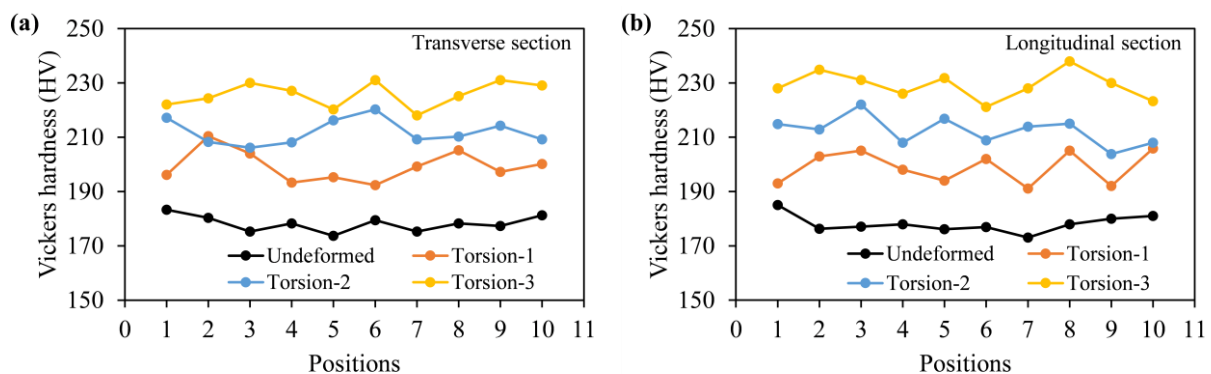


***Figure 2.17.*** *Variation of Vickers hardness of torsional pre-deformed titanium.*

Furthermore, Jie et al. [85] examined the combined effects of torsional and tensile pre-deformation on hardness. Tension pre-deformation was conducted at a strain rate of $10^{-3}$ s$^{-1}$, with the tensile pre-strained samples referred to as Torsion-0-Tension, Torsion-1-Tension, Torsion-2-Tension, and Torsion-3-Tension. The hardness results, shown in Figure 2.18, revealed that the combined torsion-tension pre-deformation samples exhibited a more pronounced increase in hardness, with increments of approximately 48 HV, 56 HV, and 65 HV compared to un-deformed samples. Whereas, the increment in hardness of deformed samples by single-mode deformation was about 50 HV by torsion deformation, which is higher than that by tension deformation (about 40 HV). Microstructure analysis [85] confirmed that torsion pre-

deformation effectively enhanced grain refinement, which was further intensified when combined with subsequent tensile deformation. The Torsion-2-Tension sample exhibited the finest grain size of 25 μm, surpassing the refinement achieved through single-mode tension (40 μm) and torsion (40 μm) processes.
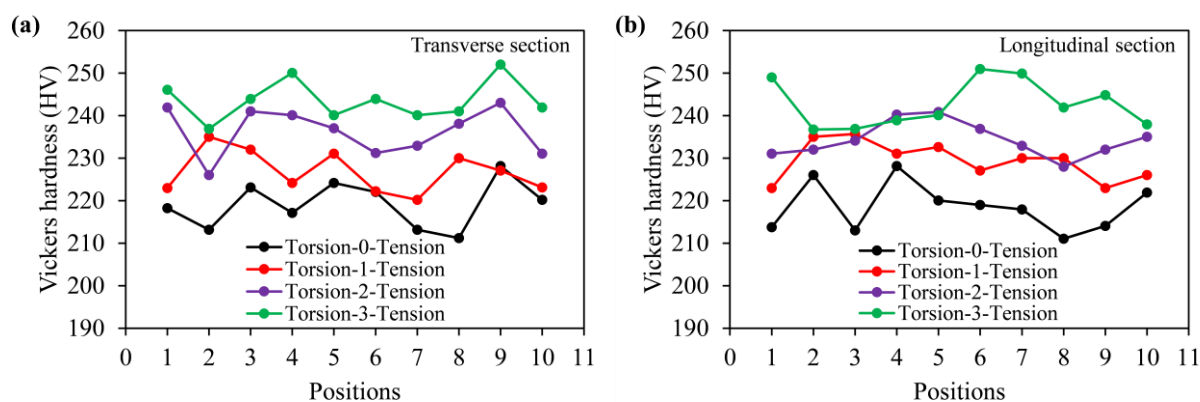


***Figure 2.18.*** *Variation of Vickers hardness of combined torsion-tension pre-deformed titanium.*

The tensile properties of the torsion-pre-deformed titanium samples are summarized in Table 2.10. The results demonstrated a significant increase in yield strength and ultimate tensile strength with an increasing number of torsional turns, while the ductility exhibited a declining trend. Fractographic analysis [85] revealed that samples subjected to combined torsion-tension pre-deformation displayed larger and deeper dimples compared to those pre-deformed by tension alone. With increased pre-deformation, non-uniform plastic deformation zones became more prominent, suggesting an enhancement in local toughness.

***Table 2.10.*** *Mechanical properties of pre-deformed titanium samples after twisting different turns.*

| Pre-deformation | TYS (MPa) | UTS (MPa) | Elongation (%) |
|---|---|---|---|
| Torsions-0 | 365.06 | 503.81 | 21.1 |
| Torsion-1 | 457.45 | 564.19 | 19.6 |
| Torsion-2 | 517.77 | 614.29 | 13.5 |
| Torsion-3 | 545.90 | 660.74 | 9.84 |

Many researchers have investigated the effects of pre-strain at room temperature on the mechanical properties of magnesium alloys [59,66,76,86–89] and steel alloys [90,91]. Guo et al. [92] investigated the effect of pre-torsion on the tensile and compressive properties of extruded magnesium alloy AZ31 and its microstructural evolution. Cylindrical extruded AZ31 rods were twisted to nominal angles of 0°, 36°, 72°, and 144° at a constant rotational speed of 2 rpm. Due to elastic spring-back, the actual twisted angles were measured as 0°, 23°, 55°, and 130°, respectively, and were denoted as PT-0, PT-36, PT-72, and PT-144 respectively. Tensile

and compressive tests were performed along the extrusion direction (ED) at a strain rate of $1\times10^{-3}$ s$^{-1}$, with the mechanical properties summarized in Table 2.11.

The results highlighted the notable yield asymmetry characteristic of extruded AZ31, defined as the ratio of compressive yield strength (CYS) to tensile yield strength (TYS). With increasing torsional angle from 0° to 72°, the tensile yield strength initially increased, peaking at PT-72, before decreasing at PT-144. The TYS values increased by 6 MPa, 23 MPa, and 16 MPa for PT-36, PT-72, and PT-144 samples, respectively, compared to PT-0. Conversely, the CYS demonstrated a continuous increase with the pre-torsion angle, with increments of 12 MPa, 21 MPa, and 35 MPa, respectively. The enhancement in yield strength under both tensile and compressive loading was attributed to the increased dislocation density and the activation of twinning deformation during pre-torsion. Additionally, pre-torsion weakened the pre-existing extruded fiber texture in AZ31 alloy, which contributed to the observed non-monotonic variation in TYS. Texture weakening reduced the basal plane alignment parallel to the loading direction, thereby increasing the stress required for basal slip and enhancing CYS. The decrease in yield asymmetry with increasing pre-torsion was primarily attributed to the weakened fiber texture, which reduced the dominance of basal slip and facilitated the activation of non-basal slip systems [92]. However, pre-torsion increases the ultimate compressive strength but decreases ultimate tensile strength. Additionally, it should be point out that pre-torsion reduced the strain values at failure.

*Table 2.11. Tensile and compressive properties of AZ31 at various pre-torsion levels.*

| Pre-deformation | Conditions | Yield strength (MPa) | Ultimate strength (MPa) | Ductility (%) | Yield asymmetry = (CYS/TYS) |
|---|---|---|---|---|---|
| PT-0 | Tension | 196 | 321 | 10.0 | 0.61 |
| | Compression | 119 | 337 | 14.0 | |
| PT-36 | Tension | 202 | 309 | 8.9 | 0.65 |
| | Compression | 131 | 375 | 13.8 | |
| PT-72 | Tension | 219 | 317 | 6.4 | 0.64 |
| | Compression | 140 | 359 | 12.3 | |
| PT-144 | Tension | 212 | 316 | 8.0 | 0.73 |
| | Compression | 154 | 370 | 14.9 | |

Overall, pre-torsion processing is a promising technique for enhancing the mechanical properties of magnesium alloys and titanium by promoting grain refinement, increasing dislocation density, and altering crystallographic texture, ultimately reducing yield asymmetry in hexagonal close-packed (HCP) metals.

## 2.4 Concluding remarks

Over the decades, yield surface determination has undergone significant evolution, driven by the need to accurately describe plastic deformation behaviour under complex loading conditions. The literature reveals a transition from simplified models, such as von Mises and Tresca, to more sophisticated and physically grounded approaches that incorporate microstructural characteristics, anisotropy, and path-dependence. Notably, advanced characterisation techniques and computational methods have enabled a development of more accurate constitutive models that better reflect real material behaviour. In parallel, pre-deformation has emerged as a highly effective technique for enhancing the mechanical properties and stability of metallic materials. Research findings suggest that a balance between pre-deformation intensity and post-processing treatments is essential to maximize mechanical performance while minimizing potential drawbacks. The key findings can be summarized in below points:

- **Microstructural refinement and strengthening**

  By introducing controlled plastic strain before subsequent processing or aging treatments, pre-deformation increases dislocation density, refines grain structure, and facilitates the precipitation of strengthening phases, leading to improved yield strength and hardness.

- **Need of optimal strain levels for maximum performance**

  While moderate pre-deformation enhances mechanical properties, excessive pre-strain can lead to microstructural defects, such as precipitate-free zones (PFZs) and coarsened precipitates, which adversely affect ductility and fatigue resistance. Balancing pre-strain is thus critical.

- **Material-specific effects**

  The effects of pre-deformation and subsequent yield behaviour vary across different alloys. For instance, in aluminium and magnesium alloys exhibit enhanced aging responses with pre-strain, while stainless steels benefit primarily through work hardening and dislocation accumulation

- **Advancements in yield surface characterisation**

  The evolution of experimental techniques, such as Bauschinger effect tests, digital image correlation, and biaxial testing alongside computational modeling has enabled deeper insights into yield locus evolution, anisotropy, and kinematic hardening phenomena.

- **Industrial relevance and future research**

  Pre-deformation is widely applied in aerospace, automotive, and structural applications. Future investigations should focus on optimizing deformation-processing sequences, quantifying the influence of loading paths on evolving yield surfaces, and understanding long-term implications for fatigue, corrosion, and service life.

# Chapter 3

# Experimental techniques and their methodology

*A general summary of the experimental techniques for material characterisation under quasi-static conditions is reported. The experimental methods include uniaxial tension and bi-axial stress space loading conditions, where pre-deformation methods are applied. These methods simulate realistic stress conditions, with a focus on yield surface determination to define material limits. The relations required to obtain material characteristics under different loading conditions are given. Additionally, microstructural testing, which complements mechanical tests by analysing structural changes at the microscopic level is discussed. The study of the literature concerning the tests discussed is also included.*

## 3.1 Introduction

Understanding of material behaviour under various loading conditions is fundamental for developing and designing materials that meet the demands of engineering applications. In this chapter the experimental framework used in the Thesis are described. The discussed experiments are applied to characterise the Thesis materials. Study on the metal's deformation in uniaxial and bi-axial stress space offers valuable insights into how materials respond to different stress combinations, yielding critical data that directly influences the optimization of materials for strength, durability, and other essential performance parameters. Although the basic principles of the testing techniques are rather straightforward, interpretation of the experimental results is less obvious. By defining and analysing yield surfaces, determining yield strength, and conducting microstructural evaluations, the framework provides a comprehensive view of both mechanical and structural material characteristics. This introduction outlines the significance of these techniques, their implementation, and their role in advancing material science.

The strength tests are performed to determine the mechanical characteristics of the materials. However, the mechanical testing of these materials is still primarily performed under simple stress conditions in research and commercial facilities. The most common form of testing is tension and compression of solid cylindrical specimens. Such types of testing can only generate limited results concerning the mechanical strength and damage of materials in a single direction which does not simulate the real-world stress conditions encountered by materials in most engineering applications. Therefore, this Thesis also aims to report complex stress loading experiments to understand the physical mechanism accountable for plastic deformation caused by monotonic tension and tension assisted by cyclic torsion of the materials considered.

The experimental programme comprised of following steps:

- Uniaxial tensile tests for determining the mechanical properties of the materials;
- Determination of the initial yield surface of the as-received material;
- Introduction of the plastic pre-deformation in the specimens;
- Determination of the subsequent yield surfaces of the pre-deformed specimens;
- The microstructural analysis of the as-received and pre-deformed specimens.

The uniaxial tension test is conventional test used to obtain basic characteristics of the material – details in Section 3.2. Under quasi-static tension loading the testing procedure is normalized and well established for several materials. Material characterisation under complex stress states requires a detailed approach to accurately capture the stress-strain relationships, yield criteria, and deformation mechanisms that materials undergo under load. Such experimental data is indispensable, especially for applications in aerospace, automotive, civil engineering, and other fields where materials must withstand high-stress conditions without compromising functionality. In these industries, materials are often exposed to multiaxial loading environments, where stresses do not act purely in one direction but instead combine to create complex load paths. Traditional uniaxial testing methods, while useful, provide only a partial understanding of material behaviour, highlighting the importance of biaxial stress testing in a complete characterisation. This combined approach supports the development of materials with predictable and reliable properties, leading to safer and more efficient applications.

One of the experimental techniques included in this framework is the introduction of pre-deformation in materials, a critical step for simulating the effects of initial stresses or loads that materials may experience during processing or in-service application. Pre-deformation influences material properties by introducing residual stresses or dislocation structures that alter the way materials respond to subsequent loading. Pre-loading of materials in uniaxial or biaxial directions enables researchers to assess an influence of prior deformation on yield behaviour, fracture toughness, and fatigue life, all of which are crucial for understanding long-term performance and durability. This approach is especially relevant for high-strength and ductile materials that are used in structures subjected to cyclic or combined stress states, such as in pressure vessels, pipelines, and load-bearing components.

A primary goal of the experimental framework is to determine yield strength under different stress states and map the yield surface for materials subjected to biaxial stress loading. Yield strength, the point at which a material begins to deform plastically, is a critical property that influences the overall structural integrity and performance of the material in practical applications. Different loading conditions can alter the yield strength, affecting how the material performs under real-world stress scenarios. Uniaxial testing provides basic information on yield properties in a single direction, while biaxial testing captures more complex yield behaviour, allowing for a complete understanding of material responses in multidimensional stress spaces. By exploring the yield surface, or the boundary in stress space where yielding occurs, this framework aims to predict material performance in more intricate and realistic stress environments.

To accurately identify how materials behave under testing, we need to carefully consider factors like external conditions, friction, and boundary constraints, as these elements significantly affect the results. The material's response does not only depend on its inherent qualities but is also influenced by the test setup and the structural aspects of the sample being tested. Advanced measurement techniques are essential for capturing the intricate interactions between external conditions and material behaviour. Additionally, new methods for both conducting and interpreting these tests are key to providing a more complete and accurate picture of how materials perform under different stresses. Working with experimental data requires a lot of attention to detail, especially in setting up tests, calibrating equipment, and choosing the right measurement methods. The shape of the test samples also plays an important role; choosing the optimal geometry can minimize potential inaccuracies. Without careful attention to these

factors, experimental data could introduce errors that compromise the reliability of theoretical models and conclusions.

Equally important to the mechanical tests is the microstructural analysis, which complements and enhances the understanding gained from stress tests. Microstructural testing investigates the internal changes that materials undergo during deformation, such as dislocation movement, grain boundary behaviour, and phase transformations. These microstructural features provide a link between the macroscopic properties measured in mechanical tests and the fundamental atomic and molecular interactions that define material behaviour. Techniques such as scanning electron microscopy (SEM), transmission electron microscopy (TEM), and X-ray diffraction (XRD) reveal critical insights into how structural changes at the micro and nano-levels influence the overall mechanical properties of the material. In the Thesis, fractured surface of materials was analysed using SEM, whereas, grain orientation and texture evolution was observed using Electron Backscatter Diffraction (EBSD) technique.

The implications of this experimental framework are far-reaching, as the data obtained from these tests directly impacts the design, selection, and application of materials in engineering fields. The ability to predict material behaviour under complex loading is invaluable for industries where structural failure could lead to catastrophic outcomes, such as in aerospace and civil engineering. In these high-stakes applications, understanding the yield behaviour of materials ensures that components are reliable, durable, and meet safety standards. Additionally, as new materials are developed with tailored properties for specific applications, the experimental techniques outlined in this chapter provide a foundation for evaluating their suitability under real-world stress conditions.

### 3.1.1 Determination of the yield strength

Yield strength is a fundamental property that defines the stress threshold at which materials transition from elastic to plastic behaviour. Yield strength is commonly determined through tensile testing, where a sample is subjected to increasing uniaxial stress until it begins to deform plastically. However, real-world applications often involve complex stress states, requiring a more nuanced understanding of yield strength across different loading conditions. When stress is applied in more than one direction, the material's behaviour may differ significantly compared to uniaxial loading. For instance, in biaxial or triaxial stress conditions, yield strength can be influenced by the interaction of many components of the stress tensor, leading to yield criteria that vary depending on the combination of stresses involved. Traditional criteria, such as the Huber, von Mises, and Tresca, are commonly used to predict yield behaviour under complex stress states. They are helpful to construct yield surfaces, providing a visual representation of yield points across different stress combinations, which is crucial for designing components subjected to multidimensional loads. Various examples of yield criteria are given in Chapter 4 of the Thesis.

The yield strength of a material is affected by various factors, including surface characteristics, internal structure, and geometry, all shaped by production and mechanical treatments. These processes can result in residual stresses, voids, and irregularities, which may weaken the material. Heat treatments, such as annealing, can help normalize the material's structure and reduce internal stresses.

It is important in strength testing that samples used have to be free of surface defects, since imperfections like scratches or voids introduce areas of local stress concentration, leading to early deformation. A polished surface generally enhances yield strength by minimizing the stress concentration points, while rough surfaces with micro-cracks reduce it. Surface treatments, such as anodizing or carburizing, can further increase yield strength by hardening the material's surface. Internally, defects like dislocations and inclusions play a critical role, with dislocations potentially causing atomic slip, although strain hardening can counteract this in cold-worked materials. However, clustered dislocations at grain boundaries can create localized stress points.

The geometry of the sample is also equally crucial; for example, "dog-bone" shapes in tensile testing minimizes stress concentration at the grips and leads to an uniform deformation across the gauge length. However, in samples with notches or complex shapes, stress may localize, resulting in premature yielding at these points. Thickness also plays a role; thinner samples may exhibit a phenomenon known as size effect, where yield strength appears higher due to a more limited number of slip systems available for deformation. This is especially true in micro- or nano-scale samples, where surface effects and grain size can significantly influence yield behaviour. Thus, optimizing sample preparation is essential to accurately determine yield strength values.

Yield strength refers to the stress level at which a material begins to undergo irreversible plastic deformation, indicating the limit of its elastic behaviour. It is crucial to clearly define the specific type of yield when using terms such as "yield," "yield strength," or "yield point" to avoid misunderstandings and inaccurate measurements. The selection of a suitable technique for determining yield points under different loading conditions is essential for the accurate identification of the yield surface. There are several distinct methods available to define the yield point, each designed for specific material behaviours and testing conditions. Here are some of the most common approaches:

- **Upper and Lower Yield Points:** In some materials, like low-carbon steel, a clear yield point phenomenon clearly occurs on the stress-strain curve, where an initial peak (upper yield point) is followed by a lower, steady stress (lower yield point) – Figure 3.1. Here, the yield point can be taken as either the upper or lower yield stress, depending on the intended application.
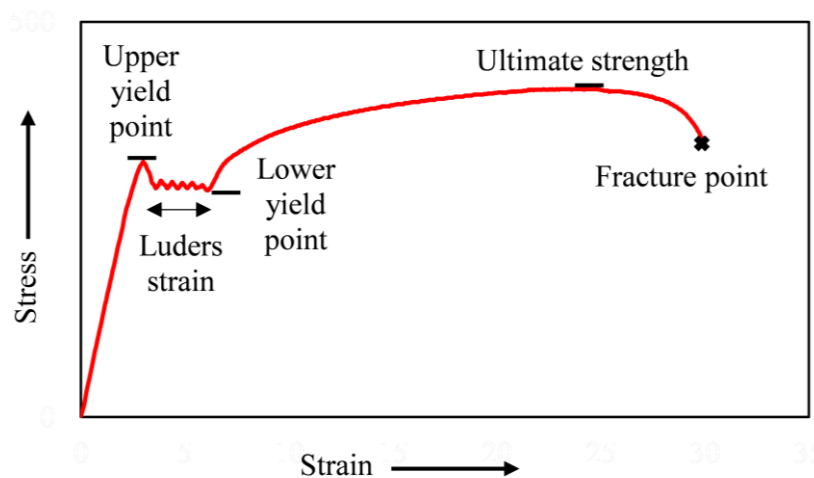


***Figure 3.1.*** *Stress-strain curve for low-carbon steel.*

- **Designated Offset Strain:** The most widely used approach, especially for metals, where a line is drawn parallel to the initial linear portion of the stress-strain curve, offset by a predetermined amount of strain (example: 0.2% strain). The point where this line intersects the stress-strain curve defines the yield point – Figure 3.2. The onset of yielding may be identified with the beginning of inelastic strain, as defined in Eq.3.1:

$$\varepsilon_{offset} = \varepsilon_{total} - \left(\frac{\sigma}{E}\right) \tag{3.1}$$

where, $\varepsilon_{offset}$ - offset strain value; $\varepsilon_{total}$ - total strain and $E$ - Young's modulus.
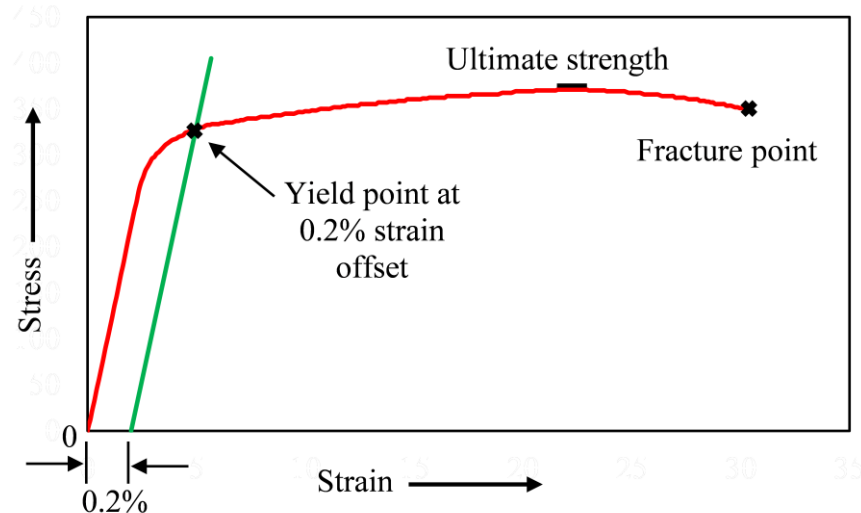


***Figure 3.2.*** *Designated offset strain method to define the yield point.*

- **Backward Extrapolation or Double Secant Line:** In this method two lines are drawn on the stress-strain curve, where one line reflects the elastic deformation behaviour and the other reflects the plastic stage deformation behaviour. The point of intersection of these two secant lines corresponds to the yield point – Figure 3.3.
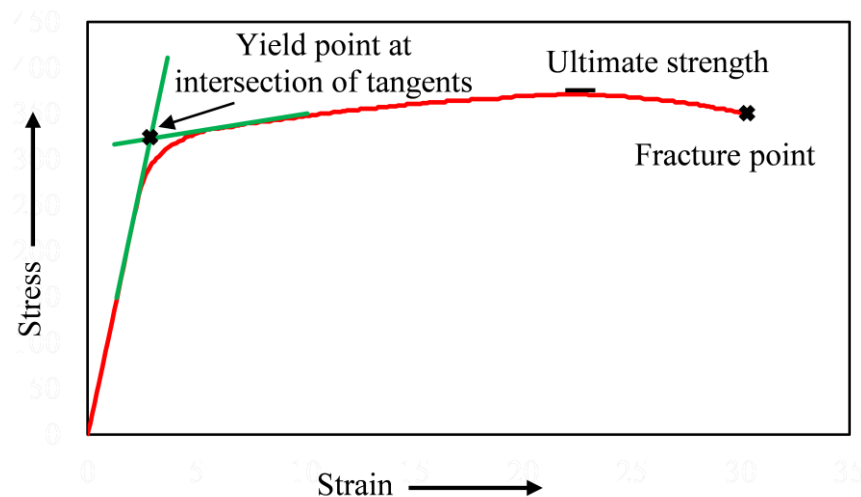


***Figure 3.3.*** *Double secant line method to define the yield point*

- **Thermoelastic Effect:** Specimen temperature is measured during loading condition and the stress corresponding to the minimum change of the specimen temperature defines

the yield point – Figure 3.4. The thermoelastic method is a non-contact, full-field experimental technique conducted under adiabatic conditions, highly sensitive to small plasticity, capable of detecting yield points even without a clear mechanical indication, and effective for accurate yield point detection in metals, composites, and thin sheets. It has to be mentioned, however, that this method can only be used for materials having a positive thermal expansion coefficient.
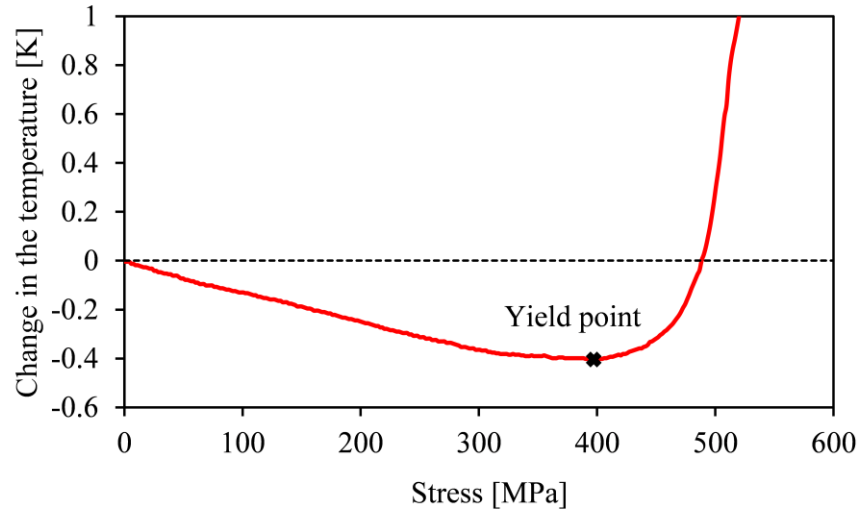


*Figure 3.4. Thermoelastic effect method to define the yield point.*

- **K-S entropy approach:** The K-S entropy approach (Kolmogorov-Sinai entropy method) is a statistical technique used to identify the yield strength of materials during tensile testing. This method relies on detecting the transition from elastic to plastic deformation based on entropy changes in the stress-strain data. The transition between these two states corresponds to the yield point, where significant internal rearrangements occur (e.g., dislocation movement, slip activation). For materials showing the physical yield point, the K-S entropy method enables its clear identification by marked drop of the metric entropy (entropy of measurement data) – Figure 3.5.
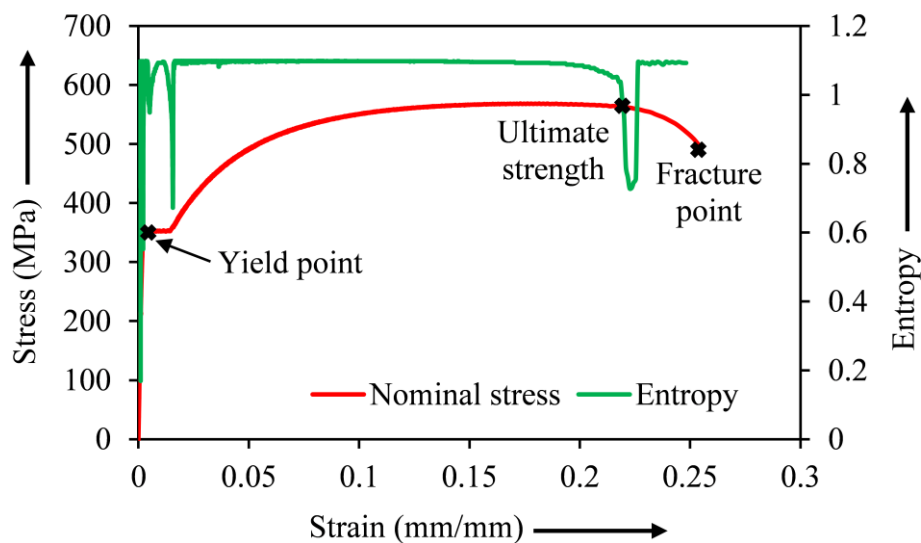


*Figure 3.5. K-S entropy approach to define the yield point of C45 (medium carbon steel).*

The K-S metric entropy for a discrete probability distribution is expressed by the Eq.3.2:

$$S = -\sum_{i=1}^{N} p_i \times \ln p_i \tag{3.2}$$

where, $S$ – the metric entropy; $N$ – the number of sub-intervals into which the data set of measurement results was divided and $p_i$ – the probability of the results in $i$ interval, (where by definition $p \times \ln p \equiv 0$, if $p = 0$).

In the Thesis, the designated offset strain method was used to obtain the yield point since it was found as the most reliable for Thesis materials. The yield point determined for different values of the offset strain equal to:

- 0.2% for uniaxial tension test, this value of the offset strain represents commonly used standard in the available literature to report the yield strength of materials;
- 0.001%, 0.005%, and 0.01% for the complex stress state test. Such a small offset strain for the definition of yield should be used during determination of the yield surface applying a single specimen in order to reduce an effect of plastic strain accumulation from the previous loading paths to negligible small amount (detailed explanation is provided in Section 3.3.2).

*The subsequent sections will explore into each experimental technique in detail, illustrating how these methods collectively contribute to a robust understanding of material behaviour and provide a basis for the design and optimization of materials in engineering applications.*

## 3.2 Uniaxial tension test

The uniaxial tension test is one of the most fundamental and widely used methods for evaluating the mechanical properties of materials. By applying a controlled tensile load along a single axis, this test provides valuable insights into the material's response under uniaxial stress, including elastic and plastic behaviour, and fracture characteristics. The stress-strain curve generated from the test serves as a comprehensive tool for determining properties such as Young's modulus, yield strength, tensile strength, ductility, and elongation at break. These properties are essential for material selection, quality control, and engineering design.

The uniaxial tension test is particularly suitable for isotropic materials, as the uniform stress state allows accurate determination of mechanical properties. However, precise results require careful consideration of specimen geometry, as it directly influences stress and strain uniformity. Thin rods with constant cross-sections or optimized dog-bone geometries fulfil these conditions, ensuring accurate measurement of applied load and surface displacement. The simplicity and reliability of this test method have made it the primary tool for characterising materials, offering a standardized approach to comparing properties across different materials and applications.

One of the significant advantages of the uniaxial tension test is its straightforward interpretation. The simple stress state ensures that results can be directly compared with data from literature and other materials. The experiment involves application of a tensile force to a specimen, typically dog-bone-shaped, with standardized dimensions. This geometry is specifically

designed to ensure uniform stress and strain distribution across the gauge length, minimizing stress concentrations at the gripping ends. The gauge section, with its reduced cross-section, ensures that deformation and failure occur in this region, making it the focal point of the analysis.

The standard specimen with a diameter of 6 mm in the gauge length was used for determination of material tensile characteristics under constant strain rate of 0.005 s$^{-1}$. Engineering drawing of the tubular specimen is shown in Figure 3.6. All the specimens were machined in a Computer Numerical Control (CNC) lathe machine to ensure precise dimensions.
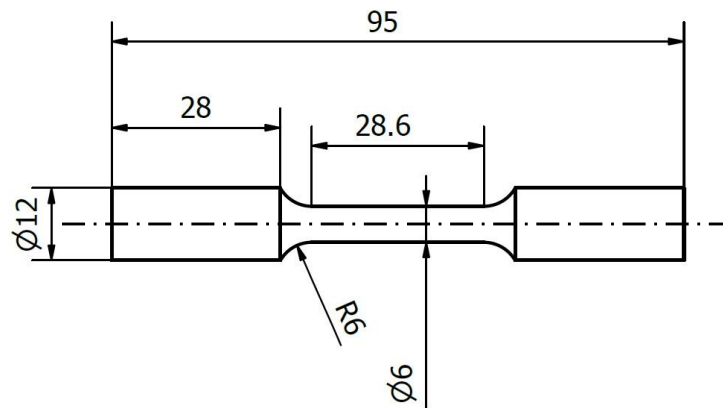


*Figure 3.6. Engineering drawing of the solid tubular specimen for uniaxial tensile tests (dimensions in millimeters).*

All mechanical testing were performed on the MTS 858 servo-electrohydraulic biaxial testing machine with maximum capacity of ± 25 kN axial force and ± 100 Nm torque (Figure 3.10a and Figure 3.10b). The testing machine employs a load unit that features two vertical columns with maximum stroke of ± 50 mm and a generous horizontal test space between the columns, which enables easy specimen mounting. The load unit uses an integral crosshead-mounted linear actuator with an attached manifold. This provides close-coupled servovalves and accumulators for improved performance and reduced pressure fluctuations. The testing machine was properly calibrated to operate at constant rates of crosshead motion. During the test, the axial force $F$ is recorded directly from the testing machine, whereas, the axial elongation δ is measured by an MTS extensometer on the gauge section – Figure 3.7.
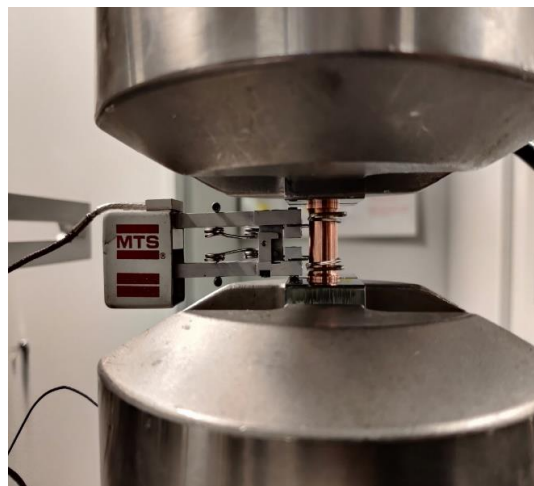


*Figure 3.7. MTS extensometer used to measure axial elongation.*

To eliminate the effect of sample geometry on the response of the material, the stress-strain relation is given in the engineering (nominal) coordinates:

$$A_0 = \frac{\pi \times D_0^2}{4} \tag{3.3}$$

$$\delta = l - l_0 \tag{3.4}$$

$$\sigma_{engg} = \frac{F}{A_0} \tag{3.5}$$

$$\varepsilon_{engg} = \frac{\delta}{l_0} \tag{3.6}$$

where, $A_0$ – initial gauge length cross-sectional area; $D_0$ – initial diameter of the specimen in the gauge length; $\delta$ – axial elongation; $l$ – current gauge length of the specimen during elongation; $l_0$ – initial gauge length of the specimen; $\sigma_{engg}$ – engineering stress; $F$ – axial force and $\varepsilon_{engg}$ – engineering strain.

Each test was repeated three times to guarantee the reliability of the results obtained. The tests were performed at room temperature (23°C).

## 3.3 Complex stress state test

The complex stress state test is an advanced method for characterising material behaviour under multi-axial loading conditions, where stresses are applied simultaneously along different directions. Unlike uniaxial tests, which provide valuable data under simple stress states, complex stress state tests simulate real-world scenarios where materials often experience combined stresses, such as tension, torsion, and compression. These tests are essential for understanding material responses in applications involving structural components, pipelines, and rotating machinery, where multi-axial loads and cyclic stresses are common.

The primary objective of the complex stress state test is to capture the material's yield and failure behaviour under non-uniform stress distributions. In the Thesis to study the material's mechanical properties under the complex path of loading, *tension-cyclic torsion* and *tension-torsion-compression tests* were employed. As a result of these complex stress states, the material's yield surface was obtained, which defines the boundary between elastic and plastic deformation in multi-axial stress space. These data are critical for developing accurate constitutive models, which predict material behaviour under service conditions.

### 3.3.1 Introduction of the pre-deformation

Pre-deformation refers to the application of an initial strain or deformation to a material before subjecting it to subsequent loading. This process plays a critical role in understanding and tailoring the mechanical behaviour of materials, as it alters their initial microstructure, stress distribution, and mechanical properties. In industrial applications, pre-deformation is commonly encountered during forming, machining, or other preparatory processes, making its study essential for predicting the material's performance under service conditions. The detailed analysis of pre-deformation is provided in Chapter 2 of the Thesis.

The processes that causes initial plastic deformations are also one of the reasons of the acquiring of undesired anisotropic properties in the material, which are difficult to remove by heat

treatment. Therefore, it is important to study experimentally the influence of the load history on evolution of mechanical properties. In the Thesis, pre-deformation is explored under *monotonic tension* and *combined tension-cyclic torsion* loading conditions. The monotonic tension pre-deformation provides insights into the material's behaviour under uniform, unidirectional loading, while the combined tension-cyclic torsion introduces complex, multi-axial stress states that simulate more realistic loading paths. These experiments help to identify how the pre-deformation affects the yield surface, and anisotropic behaviour of the material. Understanding of these effects is crucial for developing predictive models and optimizing materials for applications where they are subjected to sequential or cyclic loading after pre-deformation, ensuring enhanced performance and reliability.
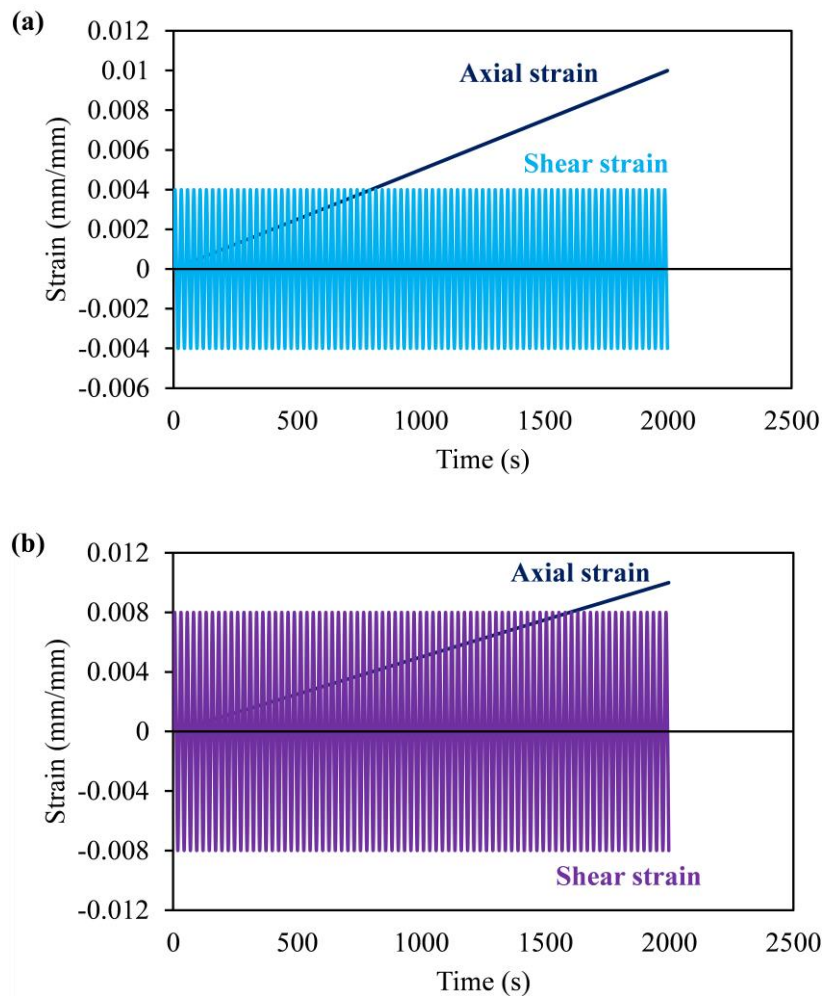


***Figure 3.8.*** *Strain controlled complex loading programme with monotonic tension and cyclic torsion with strain amplitudes of ±0.4% (a); and ±0.8% (b) at a frequency of 0.5 Hz.*

In the Thesis to study the material's mechanical properties following plastic pre-deformation were introduce in the material:

- Monotonic tension up to 1% permanent strain under a constant strain rate of $5\times10^{-6}$ s$^{-1}$.
- Combination of monotonic tension up to 1% permanent strain under a constant strain rate of $5\times10^{-6}$ s$^{-1}$, and torsion-reverse-torsion cyclic loading for different magnitudes of strain amplitude (example of ±0.4% and ±0.8%, Figure 3.8) at different values of frequency.

In a combined monotonic tension – cyclic torsion pre-deformation, a specimen was subjected to axial tension while cyclic torsional loads were applied simultaneously, allowing for the evaluation of the material's response to combined static and dynamic stresses.

Complex loading tests were performed on the thin-walled tubular specimens. Engineering drawing of the thin-walled tubular specimen is shown in Figure 3.9. The wall thickness of the thin-walled tubular specimen was large enough to satisfy the thin-walled tube criterion and to avoid buckling during sequential loading.
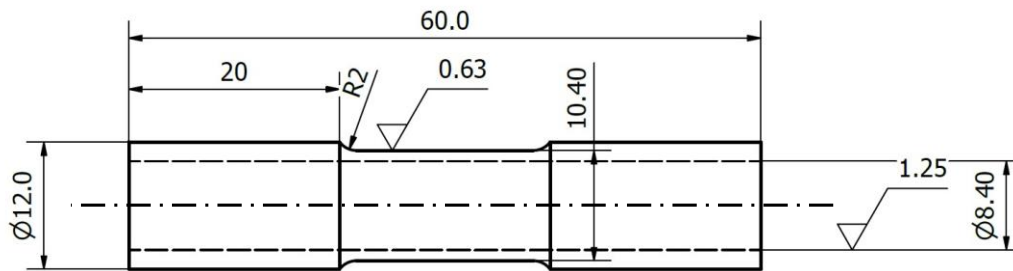


***Figure 3.9.*** *Engineering drawing of the thin-walled tubular specimen for complex loading tests and yield surface determination (dimensions in millimeters).*

Vishay 120Ω temperature compensated strain gauges were bonded on the outer surface of the tubular specimens to measure and control axial, shear and hoop strain, Figure 3.10c and Figure 3.10d. Two sets of strain gauges were used:

- The axial and shear strain components were measured using three-element 45° rectangular rosette EA-05-125RA-120 with a gauge length equal to 3.18 mm.
- The hoop strain was measured using linear pattern rosette EA-13-062AK-120 with a gauge length equal to 1.57 mm.

Both gauges were produced by Vishay. The gauges were bonded using M-Bond 610 adhesive produced by Measurements Group Inc. The three-element rectangular rosette was arranged in a manner, that one strain gauge cemented along the longitudinal axis of the specimen was used as the quarter bridge circuit to measure the axial strain, whereas, the other two strain gauges located at +45° and -45° angle with respect to the longitudinal axis of the specimen were used as the half-bridge circuit to measure the shear strain. The hoop strain was measured using a linear rosette by means of the additional half-bridge circuit perpendicular to the longitudinal axis of the specimen.

This strain gauges measurement systems enabled independent monitoring of strain. Since they were directly connected to the machine controller, the precise strain control of tests was ensured. Before each test, bridge circuits were calibrated to guarantee the high accuracy of the test.
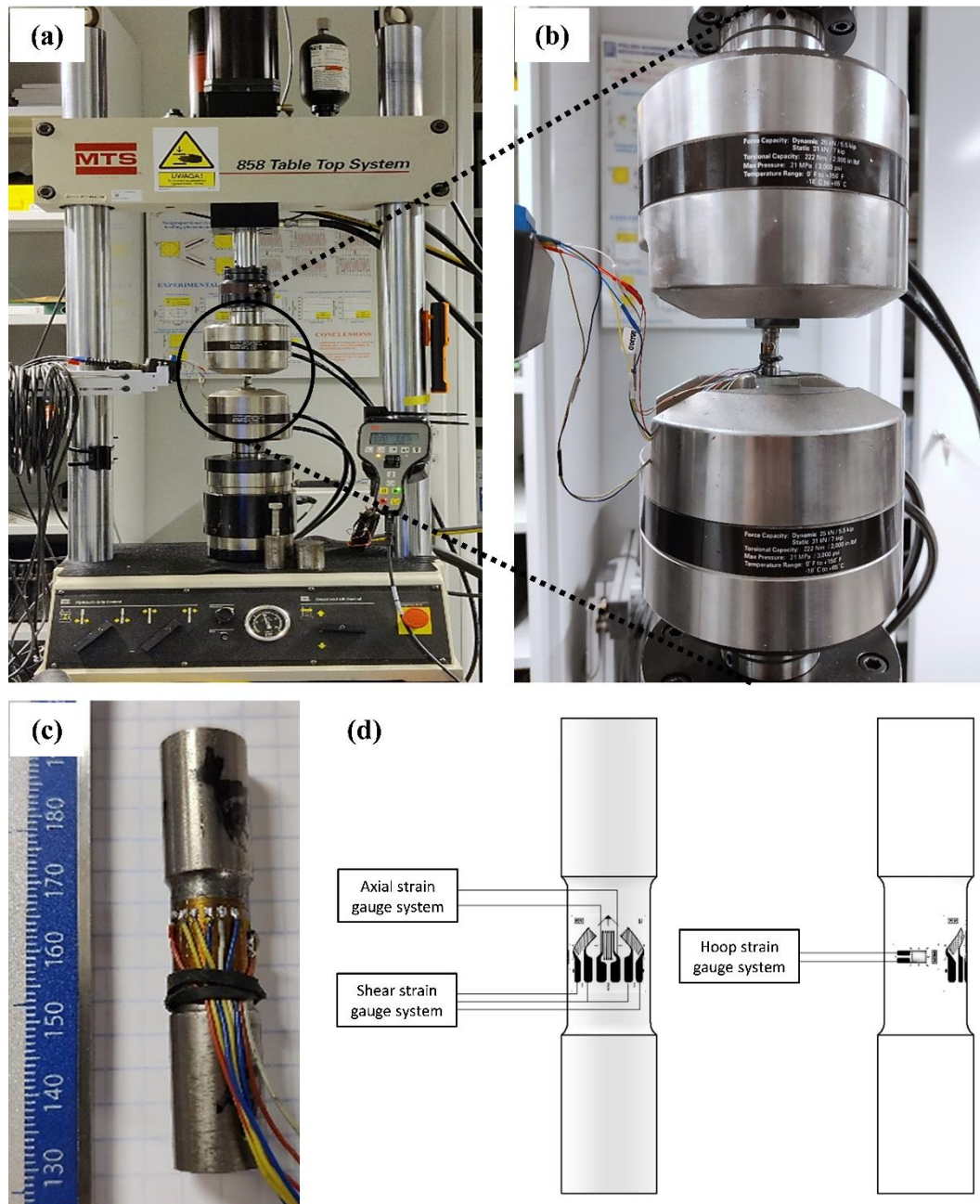
***Figure 3.10.*** *Set-up of the MTS 858 biaxial testing machine with the strain gauges bonded to the thin-walled tubular specimen (a); and its magnified view (b); image of the strain gauges bonded to the thin-walled tubular specimen (c); schemes of the strain gauge circuits on the specimen (d).*

### 3.3.2 Determination of the yield surface

Yielding process and strain hardening effect are the primary issues studied in the framework of the material plasticity. An evolution of the initial yield surface well illustrates the characteristics of plastic deformation [93]. In order to better understand and describe fairly accurately a mechanical behaviour of the material in question, it is important to carry out the comprehensive experimental investigations of subsequent yield surfaces after different loading histories. A challenge in the initial yield surface determination and its evolution due to deformation history have received much attention in the literature. The internal area of yield surface can be

described as a region in the stress space where the material always behaves as elastic. The effects of yielding, along with that of isotropic and kinematic hardening, can all be described by using the yield surface. It was found, that various materials exhibited a wide range of shapes of the yield surface in the stress space [31,34]. The position, dimensions and shape of the yield surface of a material are substantially impacted by the experimental probe technique (single specimen or multiple identical specimens) used, the loading paths, and a definition of the yielding [94].

***Table 3.1.*** *A comparative table summarizing the key differences between single-specimen and multiple-specimen techniques for yield surface determination.*

| Factor | Single-specimen technique | Multiple-specimen technique |
|---|---|---|
| Number of specimens required | One specimen tested under various loading paths. | Multiple specimens, each tested under a specific loading condition. |
| Cost | Lower overall testing cost. | Higher cost, due to preparation and testing of several specimens. |
| Time Requirement | Relatively faster, as a single specimen is used for all tests. | More time-consuming due to the need to test each specimen separately. |
| Accuracy and Resolution | Comparatively lower, as the specimen might accumulate additional plastic strain from previous loading paths during sequential loading. | Higher, as fresh specimens are used for each loading path, ensuring accurate results. |
| Applicability | Suitable for materials with minimal degradation under sequential loading. | Preferred for materials sensitive to prior deformations or for highly anisotropic materials. |
| Reproducibility | Lower reproducibility, as the specimen's condition changes during testing. | Higher reproducibility, as each test uses an undisturbed specimen. |
| Experimental Challenges | Requires application of small offset strain as definition of yielding to limit an influence of loading history. | Requires careful preparation to ensure all specimens are identical. |

Yield surfaces can be determined by testing a single specimen or multiple identical specimens which are loaded in different stress directions [94]. Previous experiments show, that results obtained using multiple identical specimens are qualitatively best in comparison to the single

specimen technique. It should be mentioned, however, that multiple specimens method for a single yield surface make the experiment costly and machining of geometrically identical testing specimens is nearly impossible [95]. The comparison of both probe techniques is summarized in Table 3.1.

The disadvantage of single specimen probe technique is the accumulation of additional plastic strain from the previous loading direction on the same specimen. However, this disadvantage can be successfully overcome if loading in one direction is carried till very limited measurable plastic strain that leads to defining the yield point at small offset plastic strain and also the loading path is following a specific sequence to determine the yield surface.

Researchers have followed different sequences of loading paths to obtain the yield surface among which the most preferable are:

- starting from zero stress level, the specimen is gradually loaded in the tensile direction of a defined stress space and after achieving the desired level of plastic strain, further loading stops and the specimen is unloaded to zero stress level, then this loading-unloading cycle is repeated in the exactly opposite direction of the same offset strain in the stress space defined. The next loading path differs from the previous path by a chosen angular increment – Figure 3.11 [96];
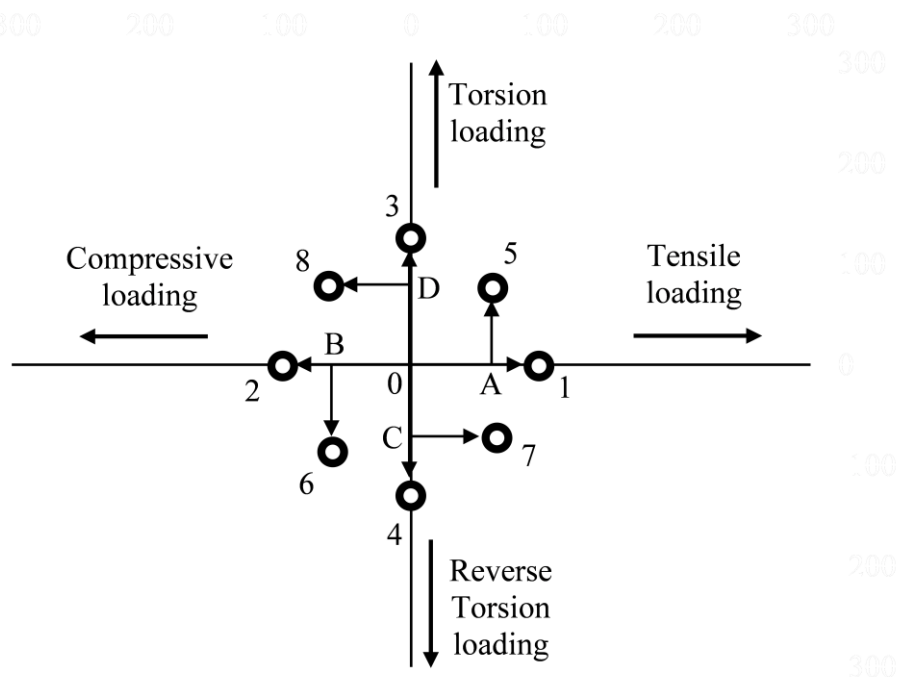


**Figure 3.11.** *Schematics of yield locus determination adopted by Khan et al. [30].*

- the loading sequence follows a predetermined proportional (or radial) loading path, starting from zero stress, the specimen is first loaded in tension direction only till yielding occurs and then the specimen is completely unloaded and again loaded with some angular increment in the tension-torsion direction of a fixed defined stress space. This loading sequence is carried out till it reaches again the path representing the tension direction only – Figure 3.12 [33].
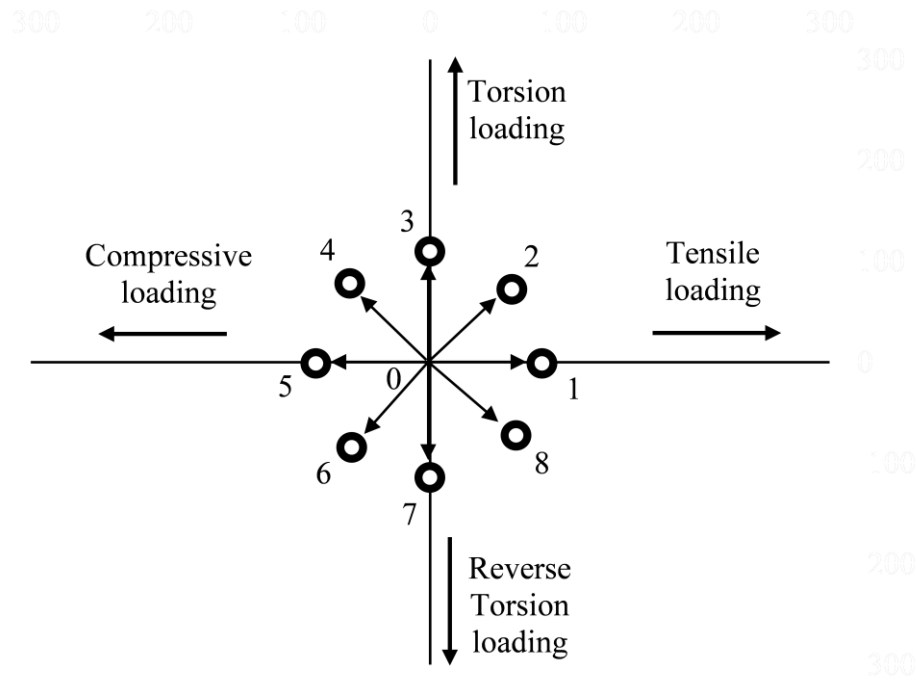
***Figure 3.12.*** *Schematics of yield locus determination adopted by Dietrich and Socha [33].*

The second sequence is the most suitable for the single specimen technique as previous results obtained using the first one introduces the Bauschinger effect [97].

The yield surface concept in the two-dimensional stress space ($\sigma$, $\tau$) was applied to identify the impact of plastic pre-deformation on the material by evaluation of the yield points. Yield points were determined by the technique of sequential probes of the single-specimen along different paths in the plane stress state. Starting from the origin, loading in each direction took place until a limited plastic strain was observed (in our case it was $2 \times 10^{-4}$). The limited plastic strain of $2 \times 10^{-4}$ (0.02%) was employed for probing in individual loading paths to ensure, that the plastic offset strain falls within the appropriate range of yield definition assumed. The loading components were strain controlled maintaining a constant ratio of the strain components. Subsequently, the unloading was carried out under stress control until zero force and torque were reached. The experimental procedure was performed along 17 stress paths (Figure 3.13), starting with simple tension and finishing with tension in the same direction. The loading and unloading were carried out for the following strain paths $0^0$, $30^0$, $45^0$, $60^0$, $90^0$, $120^0$, $135^0$, $150^0$, $180^0$, $210^0$, $225^0$, $240^0$, $270^0$, $300^0$, $315^0$, $330^0$, $360^0$ in the ($\varepsilon_{xx}$, $\sqrt{(3/(1+\nu)^2)}\varepsilon_{xy}$) strain plane, Figure 3.13. Separate specimens were utilized for each yield surface (initial and pre-deformed) following the aforementioned sequential loading paths. It should be noted, that all specimens after pre-strain in tension or combined tension-torsion were relaxed for 1 hour, and then, subjected to the yield surface determination procedure. By incorporating the relaxation step, it was aimed to limit the effect of different strain rates during pre-deformation and probing since metals have relatively high strain rate sensitivity.
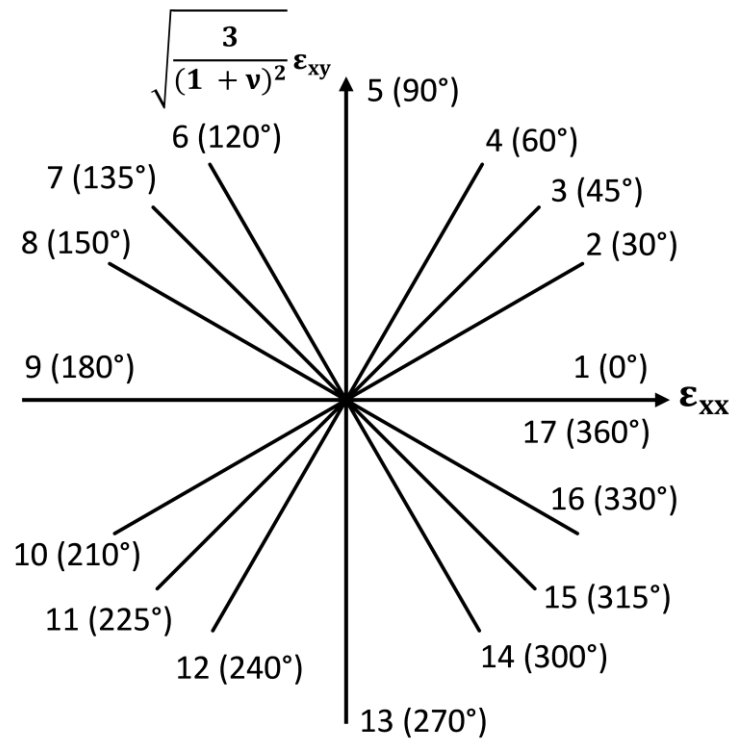
***Figure 3.13.*** *Loading sequence of strain paths for yield points determination in the biaxial strain space.*

One should highlight the importance of careful selection of the plastic offset strain value as a definition of yield point in the yield surface characterisation. In several investigations presented in the literature, the plastic offset definition of yield ranging from 0.0005% to 0.2% was often used for determination of the yield surface [20,23,27,30,98–100]. A small plastic offset strain is recommended for the yield definition when only single specimen is used to determine the yield surface. This is due to the fact that the accumulation of additional plastic strain from the previous loading path should be as small as possible to be treated as negligible [30]. Therefore, to provide a more realistic elastic-to-plastic transition, the yield stress was defined as the equivalent plastic offset strain equal to 0.005% and 0.01% for each of the loading directions considered. The chosen plastic offset strain definition of yield in this investigation exceeded the 0.001% used in Khan et al. [30] due to the selection of a different sequential probing path for yield surface determination. However, yield stress definition of 0.001% plastic offset strain was used in the investigation of SS316L due to application of three pre-strain levels on a single specimen. The yield surfaces investigated using these probing parameters showed negligible effect from the history of previous loading paths of the same specimen. The yield surface is formed using yield point values determined for 16 different loading directions in the strain space under consideration (Figure 3.13). The last loading path, designated as 17, corresponds to pure tension, and it coincides with the initial loading path, denoted as 1. It was assumed, that 16 different directions of loading in the stress space would be sufficient for determination of a yield surface shape represented by the ellipse.

Szczepinski anisotropic yield condition was applied for the numerical calculation of yield surface [29]. To fit the experimental yield points by the Szczepinski anisotropic yield equation, the least squares method was used. The aforementioned methodology was applied to determine

the initial and subsequent yield surfaces. Szczepinski anisotropic yield condition and applied methodology have been comprehensively outlined in Chapter 4 of the Thesis.

When an arbitrary solid body oriented in a Cartesian coordinate system is subjected to a number of forces in different directions such that the net force (i.e., the vector sum of all forces) acting on the body is zero, the body is said to be in static equilibrium. Under these conditions, the stress and strain states can be systematically expressed using tensors in a matrix form as:

$$\boldsymbol{\sigma} = \begin{bmatrix} \sigma_{xx} & \tau_{xy} & \tau_{xz} \\ \tau_{yx} & \sigma_{yy} & \tau_{yz} \\ \tau_{zx} & \tau_{zy} & \sigma_{zz} \end{bmatrix} \ \& \ \boldsymbol{\varepsilon} = \begin{bmatrix} \varepsilon_{xx} & \varepsilon_{xy} & \varepsilon_{xz} \\ \varepsilon_{yx} & \varepsilon_{yy} & \varepsilon_{yz} \\ \varepsilon_{zx} & \varepsilon_{zy} & \varepsilon_{zz} \end{bmatrix} \tag{3.7}$$

During all tests, the stress state components were defined by the following well-known relationship for thin-walled tubes:

$$\sigma_{xx} = \frac{4 \times F}{\pi \times (D^2 - d^2)} \tag{3.8}$$

$$\tau_{xy} = \frac{16 \times T \times D}{\pi \times (D^4 - d^4)} \tag{3.9}$$

The equivalent stress is computed from the following equation based upon the distortion-energy theorem (also known as the shear-energy or von Mises theory):

$$\sigma_{eq} = \sqrt{\frac{1}{2}\left[(\sigma_{xx} - \sigma_{yy})^2 + (\sigma_{yy} - \sigma_{zz})^2 + (\sigma_{zz} - \sigma_{xx})^2 + 6(\tau_{xy}^2 + \tau_{yz}^2 + \tau_{zx}^2)\right]} \tag{3.10}$$

Complex stress state tests were performed in the tension and torsion stress conditions, i.e. except $\sigma_{xx}$ and $\tau_{xy}$ , all other stress components were equal to zero. The equivalent stress becomes:

$$\sigma_{eq} = \sqrt{\sigma_{xx}^2 + 3 \times \tau_{xy}^2} \tag{3.11}$$

The equivalent strain was determined from the general formula involving Poisson's ratio $v$:

$$\varepsilon_{eq} = \frac{\sqrt{2}}{2(1+v)}\sqrt{(\varepsilon_{xx} - \varepsilon_{yy})^2 + (\varepsilon_{yy} - \varepsilon_{zz})^2 + (\varepsilon_{zz} - \varepsilon_{xx})^2 + 6(\varepsilon_{xy}^2 + \varepsilon_{yz}^2 + \varepsilon_{zx}^2)} \tag{3.12}$$

which leads with $\varepsilon_{yy} = \varepsilon_{zz} = -v\varepsilon_{xx}$ and $\varepsilon_{yz} = \varepsilon_{zx} = 0$ to the relationship

$$\varepsilon_{eq} = \sqrt{\varepsilon_{xx}^2 + \frac{3}{(1+v)^2} \times \varepsilon_{xy}^2} \tag{3.13}$$

$$\varepsilon_{eq}^p = Equivalent\ strain - Elastic\ strain \tag{3.14}$$

$$\nu = -\frac{Transverse\ strain}{Axial\ strain} \qquad (3.15)$$

The effective Young's modulus was determined from the initial linear region of the equivalent stress-equivalent strain curves corresponding to each loading path employed in the yield point determination, as illustrated in Figure 3.13. It quantifies the stiffness of a material and is defined as:

$$E_{eff} = \frac{\sigma_{eq}}{\varepsilon_{eq}} \qquad (3.16)$$

where, $\sigma_{xx}$ - axial stress; $F$ - axial force; $D$ - initial outer gauge diameter of the specimen; $d$ - initial inner gauge diameter of the specimen; $\tau_{xy}$ - shear stress; $T$ - twisting moment; $\sigma_{eq}$ - equivalent stress; $\varepsilon_{eq}$ - equivalent strain; $\varepsilon_{xx}$ - total axial strain; $\varepsilon_{xy}$ - total shear strain; $\varepsilon_{eq}^{p}$ – equivalent plastic strain; $E_{eff}$ - effective Young's modulus; $\nu$ - Poisson's ratio and $\varepsilon_{yy}$ - hoop strain.

The Poisson's ratio for the testing materials was experimentally determined as the negative value of ratio of hoop (circumferential) to axial (longitudinal) strain values (Eq. 3.15). These strains components were precisely recorded by the strain gauges attached to the surface of the specimen's gauge length. The average value of the Poisson's ratio was simultaneously used in Eq. 3.13 for a given range of plastic deformation determined for the material in preliminary tests.

The use of Eqns. (3.8) -(3.16) was solely intended for controlling the tests in order to obtain a predetermined pre-strain value. It is important to note, that these equations did not have any influence on the actual mechanical response of the material during the loading program, which was the main focus of the study. However, during the experiments, individual components of stress and strain were recorded as the function of time. On their basis, the components of stress are recalculated as functions of the corresponding strain components.

## 3.4 Microstructural test

Microstructural analysis is an essential component of materials science, providing understanding of a material's internal structure and how it evolves under various mechanical and thermal conditions. The microstructural test connects the macroscopic mechanical properties of a material with its microscopic characteristics, including grain structure, grain orientation, phase distribution, and defects like dislocations and voids. Understanding these characteristics is crucial for predicting material behaviour, enhancing mechanical performance, and customizing materials for specific applications.

In the Thesis, one of the key motivations for conducting microstructural tests is to study the effects of pre-deformation on a material's internal structure. Pre-deformation, whether through monotonic tension or combined tension-cyclic torsion, induces significant changes in the microstructure, particularly in grain size and texture or grain orientation. These changes can influence mechanical properties, such as yield strength, ductility, and fatigue resistance, by modifying the material's ability to accommodate further deformation.

Microstructural tests are performed using advanced techniques such as optical microscopy, scanning electron microscopy (SEM), electron backscatter diffraction (EBSD), and transmission electron microscopy (TEM). These techniques provide detailed visualization and

quantification of grain size, shape, and orientation, as well as the identification of phase boundaries and defects. For example, EBSD is particularly effective in mapping texture and assessing changes in grain orientation, enabling researchers to link the observed microstructural characteristics to the deformation history of the material. Additionally, knowledge of grain orientation and texture evolution is critical in processes such as rolling, forging, and additive manufacturing, where the mechanical properties of the final product are strongly connected to its microstructure.

In the Thesis, the microstructural analysis was performed by using a FEI Quanta 3D field emission gun scanning electron microscope (FEG-SEM) operated at 20 kV. The Quanta 3D SEM was equipped with an energy dispersive spectroscopy (EDS) and an electron backscatter diffraction (EBSD) systems. The specimens were collected from the central part of the gauge length area and were prepared by conventional metallographic procedures for metals, including, grinding, initial polishing and electro-polishing. The specimens were ground in a sequence (low to high granulation size) by using 600, 800, 1200, and 2400 SiC graded papers. In the next step, initial polishing was performed with diamond suspensions of 3, 1, and 0.25 μm grain sizes. Finally, electro-polishing was conducted with following conditions: an electrolyte of 95% acetic acid and 5% perchloric acid, a voltage of 50–60 V, and a temperature of 14–16 °C. The samples for EBSD analysis require a highly polished flat surface to obtain reliable and high-quality results. Any contamination, deformation, or oxidation near the surface can significantly hinder the process, as EBSD signals depend on electrons diffracted from only a few tens of nanometres beneath the specimen surface. Figure 3.14 represents a schematic of the specimen planes [Extrusion direction (ED) – Transverse direction (TD) – Radial direction (RD)] of the thin-walled tubular specimen for EBSD observations. In the Thesis, EBSD scan was acquired for ED – RD plane.
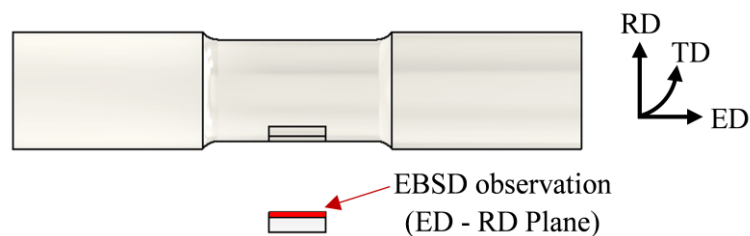


**Figure 3.14.** *Scheme of the thin-walled tubular specimen planes for EBSD.*

In the Thesis, microstructural tests are conducted on materials subjected to monotonic tension and combined tension-cyclic torsion loadings. These tests aim to characterise the differences in microstructure evolution under simple and complex loading conditions. For monotonic tension, the focus is on understanding how uniform strain affects grain elongation and texture. For combined tension-cyclic torsion, the analysis explores how multi-axial stress states and cyclic loading lead to unique texture patterns.

By correlating microstructural changes with mechanical performance, these tests provide a comprehensive understanding of material behaviour. This information is invaluable for developing predictive models that account for microstructural effects and for optimizing processing conditions to achieve desired mechanical properties. Ultimately, microstructural tests are an important component of modern materials research, enabling the design of advanced materials which fulfil the demanding requirements of various engineering applications.

## 3.5 Concluding remarks

This chapter has provided a comprehensive review of the experimental techniques and methodologies employed to characterise the Thesis material's behaviour under different loading conditions, highlighting their significance in understanding mechanical properties and microstructural evolution. From determining yield strength through uniaxial and complex stress state tests to analysing pre-deformation effects and microstructural changes, each experimental approach contributes to building a comprehensive understanding of how materials respond to various mechanical stimuli.

The uniaxial tension test, widely regarded as a fundamental tool of mechanical testing due to its simplicity and ability to derive fundamental properties like Young's modulus, yield strength, and tensile strength. However, the limitations of uniaxial testing under idealized conditions necessitate more advanced methods, such as complex stress state tests, to simulate real-world multi-axial loading scenarios. The complex stress state test allows to obtain more data points in the stress space because it applies combined loadings. By using a biaxial stress state, experimental yield points can be measured in both the positive and negative ranges of the stress axes.

Through microstructural testing, the framework provides a comprehensive understanding of the material's structural characteristics on the role of grain structure, and texture in influencing material performance. By correlating mechanical test results with microstructural changes, such as those induced by pre-deformation, the insights gained are invaluable for optimizing materials for specific applications.

Overall, the experimental methods described in this chapter are crucial for improving material design and performance. They provide the data needed to ensure materials behave reliably under real-world conditions, supporting advancements across industries like aerospace, automotive, and construction, where safety and durability are crucial. These techniques are not only tools for scientific discovery but also for driving innovation in engineering and manufacturing.

# Chapter 4

# Yield criteria

*The study of the yielding and failure behaviour of materials is crucial in solid mechanics and materials science. This chapter presents an overview of yield criteria, forming the theoretical basis of the Thesis. Before introducing the Szczepiński anisotropic yield criterion (1993), techniques for yield surface visualization are outlined. Historical and widely used yield models, including Tresca and von Mises, are briefly discussed, emphasizing their evolution. The Szczepiński criterion, which accounts for the Bauschinger effect and anisotropy, is simplified for biaxial (axial-shear) stress space to align with the Thesis experiments. This approach provides a practical framework for interpreting experimental data and evaluating the anisotropic properties of tested materials.*

## 4.1 Introduction

Research into the strength of materials and structures plays a pivotal role in the design and safety assessment of various engineering applications. The accurate evaluation of material strength under complex stress states is essential for ensuring structural integrity and performance. The strength of materials is influenced by several factors, including temperature, loading rates, and the applied stress state. Understanding how these factors interact poses a significant scientific challenge, particularly under multiaxial loading conditions. Materials, both in nature and engineering applications, are frequently subjected to complex stress systems, which can be represented as a point or a cubic element subjected to combined stresses on its faces. These combined stresses are described by nine stress components, of which only six are independent due to the symmetry of the stress tensor. This complexity makes it difficult to derive a universal solution for material strength under arbitrary loading conditions, even when the problem is simplified to three principal stresses in isotropic materials.

Principal stresses, which represent the normal stresses acting on specific planes with zero shear stresses, form the basis of many yield criteria. The three-dimensional representation of principal stresses, often referred to as triaxial stresses is shown in Figure 4.1. The uniaxial and biaxial stress states are special cases. Understanding the behaviour of materials under these stress conditions is fundamental for predicting the onset of plastic deformation and designing structures that can withstand diverse loading scenarios.
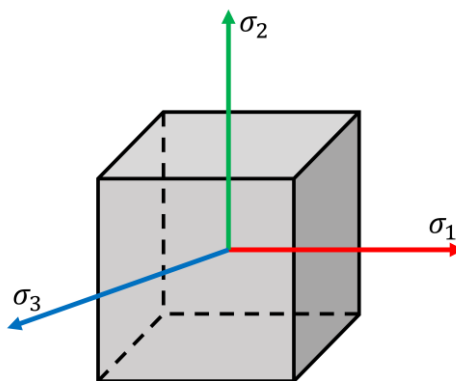


**Figure 4.1.** *Principal stresses acting on an element.*

Different materials exhibit distinct mechanical behaviour, characterised by their uniaxial stress-strain curves, which vary significantly depending on material properties. The yield point in a uniaxial stress-strain curve represents a critical threshold where materials transition from elastic (reversible) to plastic (irreversible) deformation. This yield point marks the limit of linear behaviour, beyond which permanent deformation occurs. When extended to three-dimensional complex stress states, the mathematical representation of the yield point is described by the yield criterion.

The yield criterion is a cornerstone concept in solid mechanics, serving as the theoretical basis for understanding the load-bearing capacity of materials and the development of elastoplastic constitutive relations. It provides a mathematical framework to predict the onset of plastic deformation under applied stresses. In engineering applications, particularly for metals used in structural, automotive, and aerospace industries, accurate yield models are critical for designing components that balance strength, durability, and weight efficiency. Yield criteria are indispensable for describing the complex interplay of stresses that govern material behaviour under multiaxial loading conditions. They allow engineers to anticipate material performance, optimize structural designs, and ensure safety under various service conditions. For example, in structural engineering, yield models guide the design of beams and columns to prevent permanent deformation under load. In the automotive and aerospace sectors, yield criteria enable the development of lightweight yet resilient components, enhancing both energy efficiency and crashworthiness. The continuous advancement of yield models, integrating both experimental and computational methods, is essential for addressing the demands of modern engineering applications.

The scope of this chapter encompasses a range of approaches to describing yielding, starting from classical isotropic criteria, such as the Tresca and von Mises criteria, to contemporary anisotropic models that account for the direction-dependent behaviour of metals. While isotropic criteria assume uniform properties in all directions, anisotropic criteria consider the influence of factors like texture, grain orientation, and prior deformation history, which are particularly significant in processed metals such as rolled sheets and extruded profiles.

The objectives of this chapter are twofold:

- To trace the historical development of yield criteria and highlight key theoretical advancements.

- To compare isotropic and anisotropic yield criteria, discussing their assumptions, applications, and limitations. Discussion of the Szczepinski yield criteria used in this Thesis for yield surface visualization.

## 4.2 General formulation and visualization of yield criteria

In uniaxial stress states, the onset of plastic deformation is defined by the yield strength limit or yield point, where materials transition from elastic to plastic behaviour. However, for complex stress states, yielding occurs only when the components of the stress tensor ($\sigma_{ij}$) satisfy a specific function known as the yield criterion. This yield criterion, expressed through the yield function $f(\sigma_{ij})$, defines a hypersurface in the stress space dependent on the stress tensor components.

The yield function can be formally expressed as:

$$f(\sigma_{ij}) < 0 \qquad \rightarrow \quad elastic\ behaviour \tag{4.1}$$

$$f(\sigma_{ij}) = 0 \qquad \rightarrow \quad elasto-plastic\ behaviour \tag{4.2}$$

The condition $f(\sigma_{ij}) > 0$ holds no physical meaning, as yielding is not possible beyond the yield surface. The equation $f(\sigma_{ij}) = 0$ defines a yield surface in the six-dimensional stress space.

The stress tensor $\sigma_{ij}$ is a second-order Cauchy stress tensor, representing the general state of stress at a point and can be written as:

$$\sigma_{ij} = \begin{bmatrix} \sigma_{xx} & \tau_{xy} & \tau_{xz} \\ \tau_{yx} & \sigma_{yy} & \tau_{yz} \\ \tau_{zx} & \tau_{zy} & \sigma_{zz} \end{bmatrix} \tag{4.3}$$

The three eigenvalues $(\sigma_1, \sigma_2, \sigma_3)$ of the stress tensor represent the principal stresses, which can be described as the normal stresses acting on a particular plane (principal planes) with zero shear stresses. Principal stresses are obtained as the three roots of the characteristic equation:

$$\sigma^3 - I_1\sigma^2 + I_2\sigma - I_3 = 0 \tag{4.4}$$

Principal stresses can be presented as:

$$\sigma_{ij} = \begin{bmatrix} \sigma_1 & 0 & 0 \\ 0 & \sigma_2 & 0 \\ 0 & 0 & \sigma_3 \end{bmatrix} \tag{4.5}$$

The three invariants $(I_1, I_2, I_3)$ of the stress tensor at a given point are scalar quantities that remain invariant under coordinate system transformations, making them independent of the orientation of the chosen axes. These invariants can be expressed in terms of the components of the Cauchy stress tensor or the principal stresses:

$$I_1 = \sigma_{xx} + \sigma_{yy} + \sigma_{zz} = \sigma_1 + \sigma_2 + \sigma_3 = tr(\sigma_{ij}) \tag{4.6}$$

$$I_2 = \sigma_{xx}\sigma_{yy} + \sigma_{yy}\sigma_{zz} + \sigma_{zz}\sigma_{xx} - \tau_{xy}^2 - \tau_{yz}^2 - \tau_{zx}^2 = \sigma_1\sigma_2 + \sigma_2\sigma_3 + \sigma_3\sigma_1 =$$
$$\frac{1}{2}\left[\left(tr(\sigma_{ij})\right)^2 - tr(\sigma_{ij}^2)\right] \tag{4.7}$$

$$I_3 = \det(\sigma_{ij}) = \sigma_1\sigma_2\sigma_3 \tag{4.8}$$

However, for practical applications in plasticity, the stress tensor $(\sigma_{ij})$ is often decomposed into the mean or hydrostatic stress tensor $(\sigma_m\delta_{ij})$ and the deviatoric stress tensor $(S_{ij})$. The relation can be expressed as:

$$\sigma_{ij} = \sigma_m\delta_{ij} + S_{ij} \tag{4.9}$$

where, the mean stress and the Kronecker delta are defined as:

$$\sigma_m = \frac{1}{3}\left(\sigma_{xx} + \sigma_{yy} + \sigma_{zz}\right) = \frac{1}{3}(\sigma_1 + \sigma_2 + \sigma_3) = \frac{I_1}{3} \tag{4.10}$$

$$\delta_{ij} = \begin{bmatrix} 1 & 0 & 0 \\ 0 & 1 & 0 \\ 0 & 0 & 1 \end{bmatrix} \tag{4.11}$$

and the deviatoric stress tensor can be determined as:

$$S_{ij} = \sigma_{ij} - \sigma_m \delta_{ij} = \begin{bmatrix} \sigma_{xx} - \sigma_m & \tau_{xy} & \tau_{xz} \\ \tau_{yx} & \sigma_{yy} - \sigma_m & \tau_{yz} \\ \tau_{zx} & \tau_{zy} & \sigma_{zz} - \sigma_m \end{bmatrix} \tag{4.12}$$

also, the deviatoric stress tensor on the principal plane can be defined as:

$$S_{ij} = \begin{bmatrix} \sigma_1 - \sigma_m & 0 & 0 \\ 0 & \sigma_2 - \sigma_m & 0 \\ 0 & 0 & \sigma_3 - \sigma_m \end{bmatrix} \tag{4.13}$$

The deviatoric stress invariants are given by:

$$J_1 = tr(S_{ij}) = 0 \tag{4.14}$$

$$J_2 = \frac{1}{2} S_{ij} S_{ij} = \frac{1}{6}[(\sigma_1 - \sigma_2)^2 + (\sigma_2 - \sigma_3)^2 + (\sigma_3 - \sigma_1)^2] \tag{4.15}$$

$$J_3 = \det(S_{ij}) = (\sigma_1 - \sigma_m)(\sigma_2 - \sigma_m)(\sigma_3 - \sigma_m) \tag{4.16}$$

The yield function is typically expressed in terms of the invariants of stress tensor and its deviator, as they are independent of the coordinate system. The general form of the yield criterion can be written as:

$$f(I_1, J_2, J_3) = 0 \tag{4.17}$$

This formulation for an isotropic material can be geometrically interpreted within the three-dimensional principal stress space, where the principal stresses serve as the coordinate axes, as illustrated in Figure 4.2. This conceptual representation was first introduced by Haigh and Westergaard in 1920 [101,102] and is often referred to as the Haigh–Westergaard space. The primary advantage of this space lies in its simplicity and the intuitive visualization of the stress state. In this principal stress space, each point corresponds to a unique stress state characterised by its three principal stress components $(\sigma_1, \sigma_2, \sigma_3)$. The yield criterion is represented by a surface, known as the yield surface, which delineates the boundary between elastic and plastic behaviour of the material. If a given stress point lies inside the yield surface, the yield function satisfies f < 0, indicating that the material remains in the elastic regime. When the stress point reaches the yield surface, the yield function becomes zero, f = 0, signifying the onset of yielding. Stress states outside the yield surface are not physically possible for perfectly plastic materials Figure 4.3. This geometric interpretation simplifies the analysis of yielding under multiaxial stress states, offering valuable insights into material behaviour under various loading conditions.
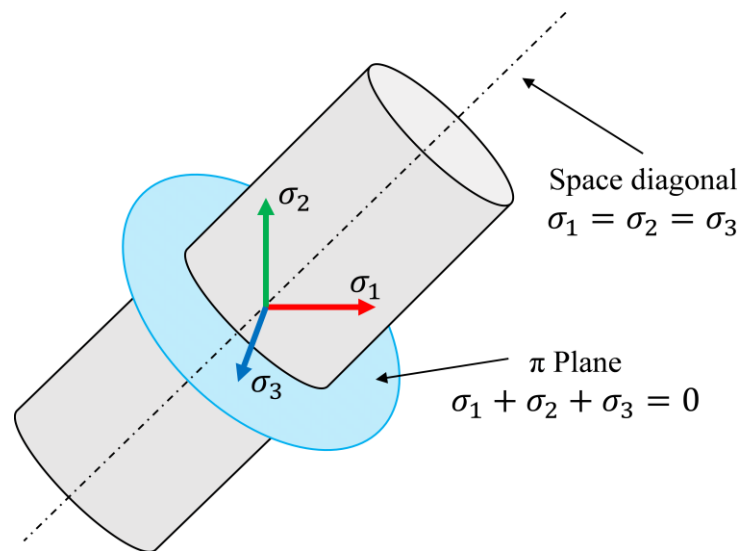
*Figure 4.2. Three-dimensional representation of a yield surface.*
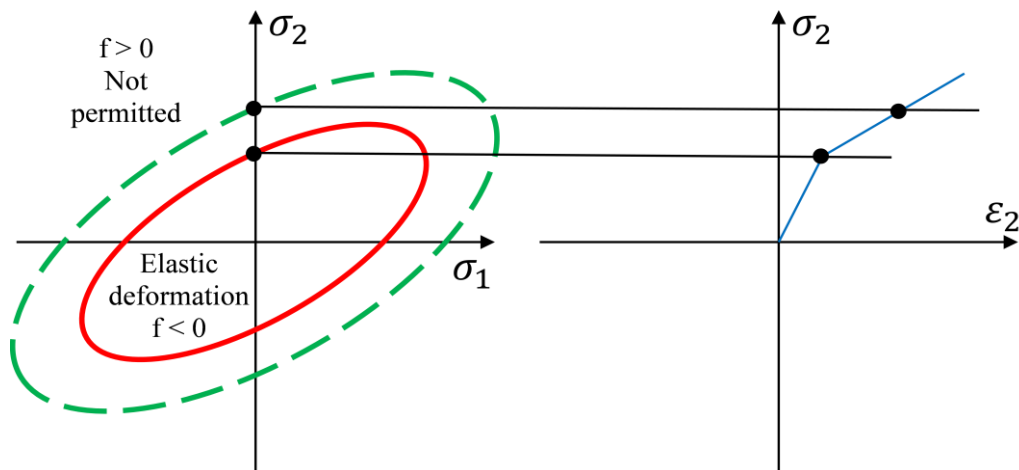


*Figure 4.3. The yield curve in the plane stress state ($\sigma_3=0$).*

## 4.3 Historical development of yield and failure criteria

The development of yield and failure criteria has evolved gradually over several centuries, with significant contributions from pioneering scientists. The earliest documented investigations into material strength can be traced back to Leonardo da Vinci (1452–1519) and Galileo Galilei (1564–1642) [103]. Da Vinci hypothesized that the strength of an iron wire was influenced by its length, while Galileo proposed that fracture occurs when a critical stress threshold is reached [104]. These early observations laid the groundwork for what later became known as the maximum normal stress strength theory, often regarded as the first strength theory. The subsequent advancements in yield criteria were marked by the emergence of various theories addressing different aspects of material behaviour. The maximum strain strength theory proposed in 1686 by Marriott, though published posthumously, introduced strain-based failure conditions [105]. A significant contribution was made by Charles-Augustin de Coulomb (1736–1806), who extended the maximum shear stress theory in 1773 by incorporating the effects of normal stress on shear failure [106], which became the basis for the Mohr-Coulomb yield

criterion. Coulomb's work profoundly influenced the mechanics of elastic bodies and the analysis of materials in geotechnical engineering [103]. Later, the maximum shear stress strength theory was developed by Henri Tresca in 1864, which played a fundamental role in describing ductile material behaviour under multiaxial stress states [107]. Further refinements were introduced with the shear strain energy strength theory, independently proposed by Huber in 1904 and von Mises in 1913 [108,109]. This theory emphasized the role of deviatoric stress in yielding, leading to the development of the widely applied Huber-von Mises-Hencky (HMH) criterion. The single-shear strength theory, introduced by Christian Otto Mohr in 1900, was a critical milestone that provided a geometric interpretation of failure conditions through Mohr's circle [110].

In the latter half of the 20th century, more advanced models emerged to address anisotropic materials and directional dependencies. The anisotropic yield criteria proposed by Hill in 1948 accounted for texture-induced variations in yield behaviour [111]. Additionally, the twin-shear stress yield criterion, developed by Mao-Hong Yu in 1983, extended earlier single-shear models to provide more comprehensive descriptions of yielding [112]. The continuous evolution of yield criteria reflects the increasing complexity of material behaviour observed in experimental studies and the need for more accurate predictive models.

Modern yield criteria are often categorized based on various factors, including:

- Material Effort: Stress-based, strain-based, or energy-based formulations.

- Yield Surface Geometry: Cylindrical (Huber), conical (Drucker-Prager), or paraboloid (Theocaris) shapes.

- Directionality: Isotropic or anisotropic response.

- Material Type: Metals, polymers, rocks, soils, ceramics, or composite materials.

The development of yield criteria has been pivotal in advancing our understanding of material behaviour under complex stress states. The concept of yielding, or the onset of plastic deformation, emerged from early experimental observations and gradually evolved into robust mathematical models. This section traces the historical milestones in yield criterion research, focusing on the key theories and their implications for isotropic and anisotropic materials.

### 4.3.1 Tresca criterion (1864)

Henri Tresca made one of the earliest significant contributions to yield theory by proposing a mathematical formulation of the yield criterion in the mid-19th century [107]. His pioneering work focused on the flow of metals under compression, where he proposed that yielding occurs when the maximum shear stress within a material reaches a critical value. This concept marked a departure from earlier ideas that relied solely on normal stress considerations, offering a more refined perspective on material failure. Subsequent refinements to Tresca's model were introduced by Guest, who simplified the criterion to enhance its applicability to a broader range of ductile materials [113]. The Tresca-Guest criterion, also referred to as the maximum shear stress criterion, is mathematically expressed as:

$$f(\sigma_{ij}) \equiv |\max(\sigma_1, \sigma_2, \sigma_3) - \min(\sigma_1, \sigma_2, \sigma_3)| - \sigma_Y = 0 \tag{4.18}$$

$$\sigma_Y = |\max(\sigma_1, \sigma_2, \sigma_3) - \min(\sigma_1, \sigma_2, \sigma_3)| \tag{4.19}$$

$$\tau_{max} = \frac{\sigma_Y}{2} \tag{4.20}$$

where, $\sigma_Y$ is the equivalent uniaxial yield stress and $\tau_{max}$ is the yield shear stress of the material.

This hypothesis aligns well with the observation that shear stress, rather than normal stress, governs plastic deformation in ductile materials. Consequently, Tresca's criterion provided a more practical and experimentally verifiable method for predicting material yielding under uniaxial and multiaxial loading conditions. The shape of Tresca-Guest criterion is a hexagonal cylinder in the 3-dimensional principal stress space as shown in Figure 4.4. The Tresca-Guest criterion exhibits certain limitations. It tends to overestimate yield strength under multiaxial loading conditions and fails to account for the influence of intermediate principal stresses. However, its straightforward nature makes it highly suitable for analytical calculations in cases involving simple stress states.
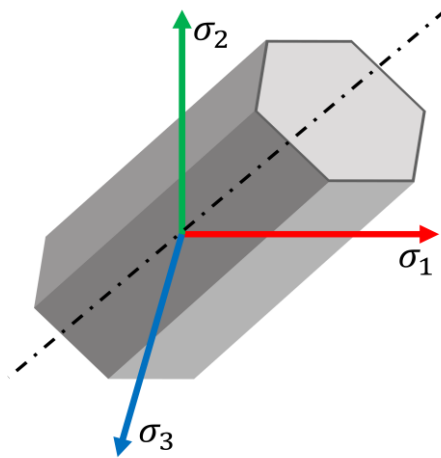


***Figure 4.4.*** *Graphical representation of the Tresca-Guest criterion.*

### 4.3.2 Mohr-Coulomb criterion (1900)

The Mohr-Coulomb criterion extends the Tresca approach by incorporating the effects of normal stress on shear failure. Coulomb hypothesized that failure occurs due to sliding along specific planes within a material. He proposed that failure initiates when the shear stress along a plane exceeds the material's inherent cohesive resistance, combined with the frictional resistance generated by the normal stress acting on that plane [106]. The Mohr hypothesis further refined this understanding by establishing a functional relationship between shear stress and normal stress on the failure plane. According to Mohr, failure occurs when the stress state on a plane reaches a critical combination of shear and normal stresses, which can be represented as a failure envelope in stress space [110,114]. The Mohr-Coulomb criterion mathematically expresses this relationship as a linear failure envelope (Figure 4.5), given by the equation:

$$\tau_{max} = c + \sigma_{max} \tan \varphi \tag{4.21}$$

The Mohr-Coulomb criterion in terms of principal stresses:

$$(\sigma_1 - \sigma_3) = (\sigma_1 + \sigma_3) \sin \varphi + 2c \cos \varphi \tag{4.22}$$

where, $\tau_{max}$ = shear stress on the failure plane, $c$ = cohesion (inherent shear strength), $\sigma_{max}$ = normal stress on the failure plane, $\varphi$ = angle of internal friction, $\sigma_1$ = maximum principal stress, and $\sigma_3$ = minimum principal stress.
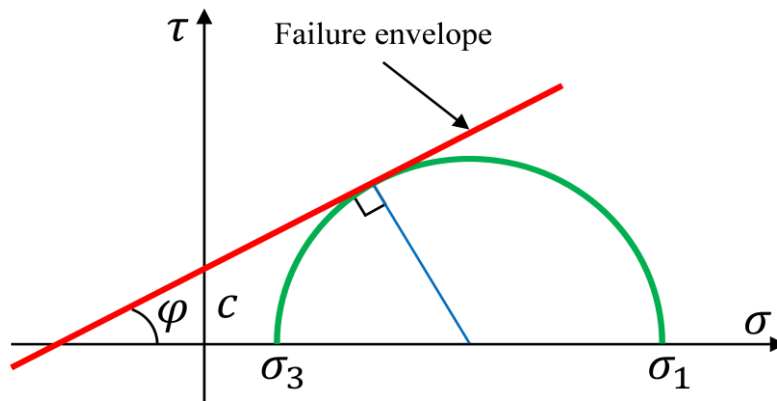


**Figure 4.5.** *Mohr diagram and failure envelope.*

The Mohr-Coulomb criterion introduces two material constants ($c$ and $\varphi$), unlike the Tresca criterion, which relies on a single material constant (the yield shear stress). Notably, when the angle of internal friction $\varphi$ becomes zero, the Mohr-Coulomb criterion reduces into the Tresca criterion, indicating that the critical shear stress is no longer influenced by normal stress. This highlights the versatility of the Mohr-Coulomb criterion in describing a broader range of material behaviours. However, both the Tresca and Mohr-Coulomb criteria share a significant limitation: they do not account for the intermediate principal stress. This omission can lead to inaccuracies in predicting material failure, as the intermediate principal stress can influence the stress state and failure characteristics of materials, even when its value is zero. Despite its limitations, the Mohr-Coulomb criterion remains widely used in geotechnical, structural, and geological engineering due to its simplicity and effectiveness in modelling the failure of frictional materials [115]. In three-dimensional principal stress space, the Mohr-Coulomb criterion takes the form of a hexagonal pyramid (Figure 4.6).
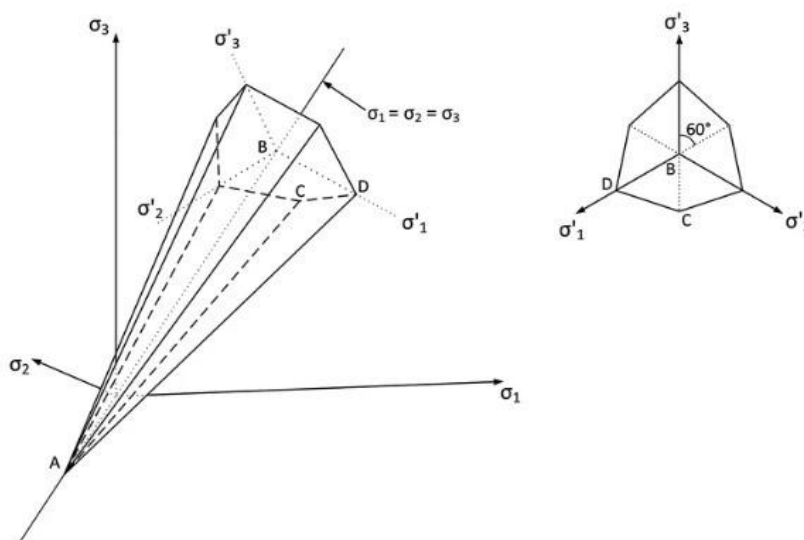


**Figure 4.6.** *Graphical representation of the Mohr-Coulomb criterion* [116].

### 4.3.3 Huber-von Mises-Hencky criterion (1913)

The Huber-Mises-Hencky (HMH) yield criterion, also known as the von Mises isotropic yield criterion, is a fundamental one-parameter model widely used to predict the onset of yielding in metallic materials that exhibit identical yield stresses in tension and compression. This criterion is particularly applicable to isotropic materials, which exhibit uniform mechanical properties in all directions, and assumes that yielding is insensitive to the hydrostatic stress tensor. The HMH criterion is based on the concept of distortion energy, which suggests that yielding begins when the energy associated with the change in shape (distortion) of a material reaches a critical value. The development of the HMH criterion has a rich historical background. It was first proposed by James Clerk Maxwell in 1865 [117], who laid the groundwork for the concept of energy-based yield criteria. Later, it was independently refined by Huber in 1904, Richard von Mises in 1913, and Hencky in 1924 [108,109,118]. These contributions culminated in the formulation of the HMH criterion, which states that yielding of materials begins when the second invariant of the deviatoric stress tensor reaches a critical value. The HMH criterion is also known as the maximum distortion energy criterion, as it focuses on the energy associated with shear deformation rather than volumetric changes. The HMH criterion is expressed mathematically as:

$$f(J_2) \equiv J_2 - \frac{\sigma_Y^2}{3} = 0 \tag{4.23}$$

$$J_2 = \frac{\sigma_Y^2}{3} \quad \rightarrow \quad \sigma_Y^2 = 3J_2 \quad \rightarrow \quad \sigma_Y^2 = 3\left[\frac{1}{6}\{(\sigma_1 - \sigma_2)^2 + (\sigma_2 - \sigma_3)^2 + (\sigma_3 - \sigma_1)^2\}\right] \tag{4.24}$$

$$\sigma_Y = \sqrt{\frac{1}{2}[(\sigma_1 - \sigma_2)^2 + (\sigma_2 - \sigma_3)^2 + (\sigma_3 - \sigma_1)^2]} \tag{4.25}$$

Whereas, in an arbitrary system of reference the HMH isotropic criterion is expressed as follows:

$$\sigma_Y = \sqrt{\frac{1}{2}\left[\left(\sigma_{xx} - \sigma_{yy}\right)^2 + \left(\sigma_{yy} - \sigma_{zz}\right)^2 + (\sigma_{zz} - \sigma_{xx})^2 + 6(\tau_{xy}^2 + \tau_{yz}^2 + \tau_{zx}^2)\right]} \tag{4.26}$$

The yield limit in shear according to the uniaxial yield stress can be expressed as:

$$\tau_Y = \frac{\sigma_Y}{\sqrt{3}} \tag{4.27}$$

In three-dimensional principal stress space, the von Mises criterion is represented as a circular cylindrical yield surface of infinite length, with its axis equally inclined to the three principal stress axes (Figure 4.7).The von Mises criterion is widely used for isotropic materials due to its ability to account for the influence of all stress components, providing a more comprehensive description of yielding compared to the Tresca criterion, which only considers the maximum shear stress. It is useful in engineering design and analysis due to its good correlation with experimental data for many ductile materials. It provides a more accurate prediction of yielding compared to the Tresca criterion under complex loading conditions, including multiaxial stress states. Despite its widespread use, the HMH criterion has limitations. It is not suitable for

materials that exhibit pressure-dependent yielding (e.g., soils, polymers, or composites) or anisotropic behaviour (e.g., rolled metals or fiber-reinforced materials).
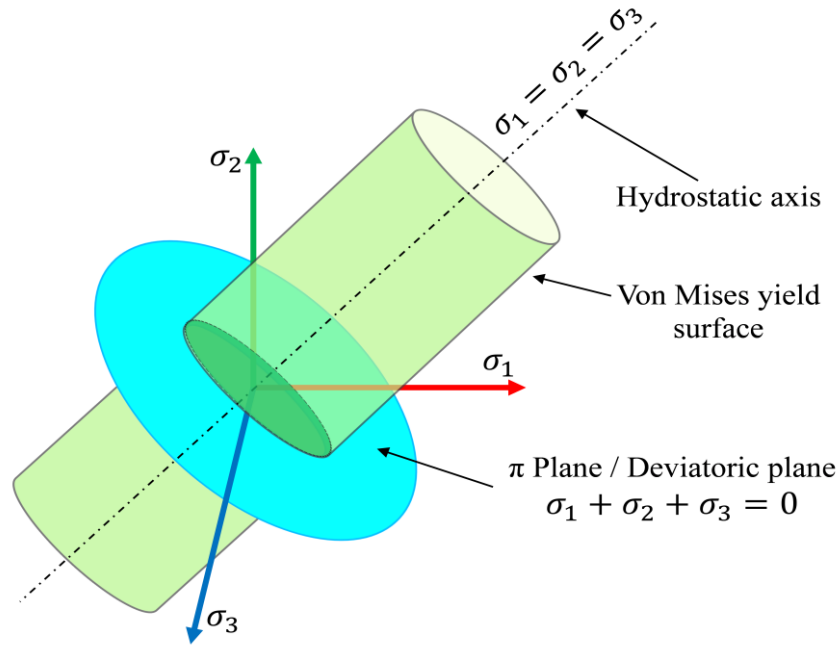


***Figure 4.7.*** *Cylindrical yield surface predicted by the HMH criterion.*

**Anisotropic criterion by von-Mises (1928):**

Later, in 1928, von-Mises generalized his yield function to consider the anisotropy in materials [119]. The criterion can be presented as:

$$2f\left(\sigma_{ij}\right) \equiv \sigma_{ij}K_{ijkl}\sigma_{kl} = 1 \qquad \rightarrow \qquad \boldsymbol{\sigma}^T \mathbb{K} \boldsymbol{\sigma} = 1 \qquad\qquad (4.28)$$

In Eq. (4.28), no prior assumptions are made regarding the isotropy characteristics of the fourth-order tensor, represented by $\mathbb{K}$, contain the yield parameters of the material. Components of $\mathbb{K}$ are indexed by $i$, $j$, $k$, $l$ each ranging from 1 to 3 in 3D space, resulting in $3^4 = 81$ components. By an adequate selection of the components of $\mathbb{K}$ along material axes, this tensor can describe a full anisotropy, orthotropy, transversally isotropy or, even, an isotropy yield condition. Also, Eq. (4.28) is directly written in terms of the stress tensor, denoted by $\boldsymbol{\sigma}$, and not in terms of its deviatoric part, $\boldsymbol{S}$, so the equation is able to predict yield under either hydrostatic or deviatoric stresses.

Eq. (4.28) is presented using classical tensor notation. However, when dealing with actual calculations, the Voigt's matrix format is more convenient. With this format, Eq. (4.28) is re-written as Eq. (4.29), where tensor indices now span in the range $i, j \in \{1, 2, 3, 4, 5, 6\}$. Here, the fourth-order tensor of yield parameters $\mathbb{K}$ is written as a $6 \times 6$ square matrix ($\boldsymbol{K}$), while the second-order tensor of stress $\boldsymbol{\sigma}$ is written as $6 \times 1$ column matrix ($\sigma$), presented in Eq. (4.30).

$$2f\left(\sigma_{ij}\right) \equiv \sigma_i K_{ij}\sigma_j = 1 \qquad \rightarrow \qquad \sigma^T \boldsymbol{K} \sigma = 1 \qquad\qquad (4.29)$$

As Eqs. (4.28) and (4.29) are a quadratic form in $\sigma$, and quadratic forms generally exhibit insensitivity to the skew-symmetric part of **K**, choosing **K** to have a symmetric matrix does not affect the generality of the equation. Thus, for the fully anisotropic case, **K** has 21 independent components, reflecting the anisotropic nature of the material under consideration.

$$\sigma_i = \begin{bmatrix} \sigma_{xx} \\ \sigma_{yy} \\ \sigma_{zz} \\ \tau_{xy} \\ \tau_{yz} \\ \tau_{zx} \end{bmatrix} \quad \& \quad K_{ij} = \begin{bmatrix} k_{11} & k_{12} & k_{13} & k_{14} & k_{15} & k_{16} \\ & k_{22} & k_{23} & k_{24} & k_{25} & k_{26} \\ & & k_{33} & k_{34} & k_{35} & k_{36} \\ & & & k_{44} & k_{45} & k_{46} \\ & & & & k_{55} & k_{56} \\ sym & & & & & k_{66} \end{bmatrix} \tag{4.30}$$

Inserting Eq. (4.30) into Eq. (4.29) and expanding the quadratic form, results in the scalar yield criterion given by Eq. (4.31).

$$2f(\sigma_{ij}) \equiv (k_{11}\sigma_{xx}^2 + k_{22}\sigma_{yy}^2 + k_{33}\sigma_{zz}^2 + k_{44}\tau_{xy}^2 + k_{55}\tau_{yz}^2 + k_{66}\tau_{zx}^2) +$$
$$2(k_{12}\sigma_{xx}\sigma_{yy} + k_{13}\sigma_{xx}\sigma_{zz} + k_{14}\sigma_{xx}\tau_{xy} + k_{15}\sigma_{xx}\tau_{yz} + k_{16}\sigma_{xx}\tau_{zx} +$$
$$k_{23}\sigma_{yy}\sigma_{zz} + k_{24}\sigma_{yy}\tau_{xy} + k_{25}\sigma_{yy}\tau_{yz} + k_{26}\sigma_{yy}\tau_{zx} + k_{34}\sigma_{zz}\tau_{xy} + k_{35}\sigma_{zz}\tau_{yz} +$$
$$k_{36}\sigma_{zz}\tau_{zx} + k_{45}\tau_{xy}\tau_{yz} + k_{46}\tau_{xy}\tau_{zx} + k_{56}\tau_{yz}\tau_{zx}) = 1 \tag{4.31}$$

The anisotropic von Mises criterion is limited in its ability to describe different elastic limits of materials under tension and compression loading conditions. Since the criterion remains invariant when the sign of all stress components is reversed, making it unable to capture the phenomenon of the Bauschinger effect. As such, the anisotropic von Mises criterion may not provide a complete and accurate representation of the behaviour of materials under various loading conditions.

### 4.3.4 Drucker-Prager criterion (1952)

The Drucker-Prager yield criterion is an elastoplastic isotropic model, that serves as a smooth approximation of the Mohr-Coulomb criterion. It is specifically designed to predict the onset of plastic deformation in pressure-sensitive materials, such as soils, concrete, and rocks [120,121]. Unlike the Huber-Mises-Hencky criterion, which is independent of hydrostatic pressure, the Drucker-Prager criterion explicitly incorporates the influence of mean stress (hydrostatic pressure) on the shearing resistance of a material. This makes it particularly suitable for modelling the behaviour of brittle materials, although it has also been applied to metals under specific conditions, such as high-pressure environments or porous materials [122–125]. The Drucker-Prager criterion is based on the assumption that the octahedral shear stress at failure depends linearly on the octahedral normal stress through material constants. Mathematically, the criterion is often expressed as:

$$f(I_1, J_2) \equiv \alpha I_1 + \sqrt{J_2} - k = 0 \quad \rightarrow \quad \sqrt{J_2} = \alpha I_1 + k \tag{4.32}$$

where, $\alpha$ and $k$ are material constants.

Drucker-Prager model can be also expressed by using the principal stresses:

$$\sqrt{\frac{1}{6}[(\sigma_1 - \sigma_2)^2 + (\sigma_2 - \sigma_3)^2 + (\sigma_3 - \sigma_1)^2]} = \alpha(\sigma_1 + \sigma_2 + \sigma_3) + k \qquad (4.33)$$

In three-dimensional principal stress space, the Drucker-Prager criterion is represented as a conical yield surface (Figure 4.8). This conical shape reflects the criterion's dependence on hydrostatic pressure, with the yield strength increasing as the hydrostatic pressure increases. Unlike the Mohr-Coulomb criterion, which has a hexagonal pyramid-shaped yield surface with sharp corners, the Drucker-Prager criterion provides a smooth failure envelope. This smoothness avoids numerical difficulties associated with sharp corners in stress space, making it more computationally efficient for finite element analysis and other numerical simulations. The Drucker-Prager criterion is particularly valuable for modelling the behaviour of geomaterials and other pressure-sensitive materials under complex loading conditions. It provides a more accurate prediction of material behaviour compared to the HMH criterion for materials like soils and rocks, where the influence of hydrostatic pressure on yielding is significant. However, the criterion has notable limitations:

- The Drucker-Prager criterion tends to overestimate material strength for general stress states, particularly in triaxial extension (where the intermediate principal stress is significantly different from the minimum principal stress).

- Due to its conical failure surface, the criterion is only accurate within a limited range of hydrostatic stress. It fails to properly describe material behaviour near the apex of the cone, where the hydrostatic pressure is very high or very low.

- The criterion assumes isotropic material behaviour, which limits its applicability to anisotropic materials or materials with complex microstructures.
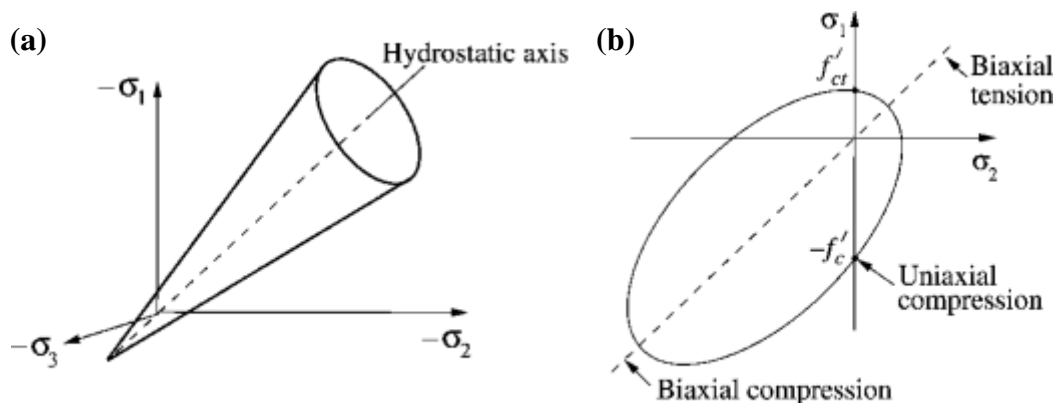


*Figure 4.8. Yield surface of Drucker-Prager criterion in the principal stress space (a), in the plane of $\sigma_3 = 0$ [126].*

**4.3.5 Hill's criterion for anisotropic materials (1948)**

Hill's anisotropic yield criterion, proposed by Rodney Hill in 1948, represents a significant advancement in plasticity theory by extending the von Mises yield criterion to account for material anisotropy. Hill's criterion introduces anisotropic yield functions incorporate the directional dependence of material properties. This makes it particularly suitable for materials

such as rolled metal sheets, extruded components, and fiber-reinforced composites, which exhibit distinct mechanical properties along different axes due to their microstructure or manufacturing processes [111]. Unlike the von Mises anisotropic criterion (Eq. (4.28)) which employs a fourth-order tensor of yield parameters ($K_{ijkl}$), Hill instead directly derives a scalar expression that is quadratic in the differences between the normal stress components and every single shear stress. As a result, the Hill criterion focuses exclusively on the deviatoric part of the stress tensor and does not account for the influence of hydrostatic stress on yielding. This simplification is consistent with the assumption that yielding is primarily driven by shear deformation rather than volumetric changes. Mathematically, the general form of the Hill yield criterion can be expressed as:

$$2f(\sigma_{ij}) \equiv F(\sigma_{yy} - \sigma_{zz})^2 + G(\sigma_{zz} - \sigma_{xx})^2 + H(\sigma_{xx} - \sigma_{yy})^2 + 2L\tau_{yz}^2 + 2M\tau_{zx}^2 + 2N\tau_{xy}^2 = 1 \tag{4.34}$$

where, $F, G, H, L, M$ and $N$ are coefficients representing the anisotropic material constants. If $F = G = H = 1$ and $L = M = N = 3$, the Hill criterion will turn into Huber-Mises-Hencky isotropic yield criterion.

Hill's criterion is particularly well-suited for orthotropic materials, where the material properties are symmetric along three mutually perpendicular axes. It has been widely applied in industries such as aerospace, automotive, and manufacturing, where materials like rolled metal sheets and fiber-reinforced composites are commonly used. Thus, the Hill criterion, as defined by Eq. (4.34), only captures orthotropic behaviour but not full anisotropy. This restricts its applicability to materials with more complex directional properties.

Similarly, to the von Mises anisotropic criterion (Eq. (4.31)), linear term in the stress is not present in the Hill criterion (Eq. (4.34)). The quadratic nature of Hill's criterion means that changes in the signs of stress components do not affect the yield condition. This can lead to inaccuracies in predicting yielding under certain stress states, such as biaxial tension-compression or cyclic loading.

To address some of these limitations, Hill proposed a generalized yield function in 1979 [127,128]. This extended formulation is non-quadratic and expressed in terms of the principal stress components, allowing for a better approximation of material behaviour under complex stress states. The generalized Hill criterion can be written as:

$$F|\sigma_2 - \sigma_3|^m + G|\sigma_3 - \sigma_1|^m + H|\sigma_1 - \sigma_2|^m + L|2\sigma_1 - \sigma_2 - \sigma_3|^m + M|2\sigma_2 - \sigma_3 - \sigma_1|^m + N|2\sigma_3 - \sigma_1 - \sigma_2|^m = \sigma_Y^m \tag{4.35}$$

where, $m$ is the material parameter with $m > 1$.

However, this criterion is limited to stress states where the directions of the principal stresses are aligned with the orthotropic axes of the material. This restriction reduces its applicability for materials subjected to arbitrary loading directions.

### 4.3.6 Contemporary developments and advanced models

Modern research in plasticity theory has led to the development of advanced yield criteria that integrate experimental data, computational methods, and microstructural considerations. These advancements are driven by the need to accurately predict the plastic behaviour of materials

under complex loading conditions, such as uniaxial tension, equi-biaxial tension, near-plane strain, and pure shear, which are commonly encountered during manufacturing and engineering applications. To address these challenges, researchers have developed new yield criteria or modified existing ones to better capture the plastic anisotropy and stress-state dependence of materials [129]. Some of the most notable contributions in this field are presented as follows:

**Hosford yield criterion:** In 1972, William F. Hosford proposed an isotropic yield criterion that generalized the Huber-Mises-Hencky criterion while emphasizing the role of stress triaxiality [130]. The criterion introduced a material-dependent exponent to better fit the yield behaviour of face-centered cubic (FCC) and body-centered cubic (BCC) metals. Later, in 1980, Logan and Hosford proposed an anisotropic yield criterion which is a special case of generalized Hill criterion (Eq. (4.35)), specifically designed for planar anisotropy in sheet metals [131]. It accounts for differences in yield strength between rolling, transverse, and diagonal directions. The model provides more realistic predictions in deep drawing and other forming operations.

**Barlat yield criterion:** Frédéric Barlat and colleagues developed a series of anisotropic criteria, including YLD 89, YLD91, YLD2000-2d, and YLD2004 [132–135]. These criteria improve upon earlier models like the Hill and Hosford criteria for the case where the directions of the orthotropic axes are not coincident with the directions of the principal stresses. These criteria offer more accurate predictions of yield surfaces for materials with pronounced anisotropic properties, such as aluminium alloys, steels, and textured metals. For example, the YLD2000-2d criterion is widely used for sheet metal forming applications. It incorporates linear transformations of the stress tensor to better capture the anisotropic yield surface, making it highly accurate for predicting yield behaviour under complex loading conditions. The Barlat criteria have become a standard in industries such as automotive and aerospace, where precise modelling of anisotropic materials is critical.

**Gurson–Tvergaard–Needleman (GTN) yield criterion:** The GTN yield criterion is a mesomechanical model developed to predict the ductile fracture behaviour of porous materials under plastic deformation. The criterion was initially proposed by Gurson in 1977 [136] to model the plastic flow and fracture of ductile metals considering the effects of hydrostatic stress and later modified by Tvergaard and Needleman in 1984 through introducing three additional fitting parameters [137–139]. This criterion describes the influence of void nucleation, growth, and coalescence on the yielding and failure of ductile materials.

**Crystal plasticity-based yield criteria:** Crystal plasticity has emerged as a powerful framework for understanding the plastic behaviour of polycrystalline materials by considering their microstructural characteristics, such as grain orientation, slip systems, and crystallographic texture. Unlike conventional yield criteria, which treat materials as homogeneous and isotropic, crystal plasticity-based models account for the anisotropy and heterogeneity of individual grains. These models are particularly useful for materials like metals, alloys, and single crystals, where microscopic deformation mechanisms play a critical role in macroscopic behaviour. Crystal plasticity-based yield criteria use crystallographic texture and intrinsic single-crystalline anisotropy as inputs to model phenomena such as: micro-crack initiation and propagation, fatigue and creep in small-scale plasticity, texture evolution during deformation, damage parameter calculation, fracture criteria for crystalline materials [140–142]. These models are often implemented in finite element simulations to predict the deformation and failure of materials at both the microscopic and macroscopic scales. They have

found applications in material design, process optimization, and failure analysis, particularly in industries where precise control over material properties is essential, such as aerospace, automotive, and additive manufacturing.

## 4.4 Anisotropic yield criterion by Szczepiński (1993)

Wojciech Adam Szczepiński (1924–2010) was a prominent Polish scientist who made significant contributions to the fields of mechanics and theory of plasticity. In 1993, Szczepiński proposed an anisotropic yield criterion that extended traditional isotropic yield models by incorporating the effects of material texture and deformation-induced anisotropy [29]. His work was particularly focused on addressing the Bauschinger effect, a phenomenon observed in metals where the yield strength in one direction (e.g., tension) differs from that in the opposite direction (e.g., compression) after plastic deformation. This effect is critical in materials subjected to cyclic loading or reverse loading conditions, such as in metal forming and fatigue analysis.

Szczepiński's criterion builds upon the von Mises anisotropic yield criterion (Eq. (4.31)), which is a quadratic function of the stress components. However, unlike the von Mises criterion, which does not account for the Bauschinger effect or directional dependence of yield strength, Szczepiński introduced linear terms with respect to the stress components into the yield condition. This modification allows the criterion to better capture the asymmetric yielding behaviour observed in anisotropic materials. Mathematically, Szczepiński's yield criterion can be expressed as:

$$
\begin{aligned}
f(\sigma_{ij}) &= k_{12}(\sigma_{xx} - \sigma_{yy})^2 + k_{23}(\sigma_{yy} - \sigma_{zz})^2 + k_{31}(\sigma_{zz} - \sigma_{xx})^2 + \\
&2\tau_{xy}[k_{16}(\sigma_{zz} - \sigma_{xx}) + k_{26}(\sigma_{zz} - \sigma_{yy})] + 2\tau_{yz}[k_{24}(\sigma_{xx} - \sigma_{yy}) + k_{34}(\sigma_{xx} - \\
&\sigma_{zz})] + 2\tau_{zx}[k_{35}(\sigma_{yy} - \sigma_{zz}) + k_{15}(\sigma_{yy} - \sigma_{xx})] + k_{44}\tau_{yz}^2 + k_{55}\tau_{zx}^2 + \\
&k_{66}\tau_{xy}^2 - b_{12}(\sigma_{xx} - \sigma_{yy}) - b_{23}(\sigma_{yy} - \sigma_{zz}) - b_{31}(\sigma_{zz} - \sigma_{xx}) + b_{44}\tau_{yz} + \\
&b_{55}\tau_{zx} + b_{66}\tau_{xy} = 1
\end{aligned}
\tag{4.36}
$$

where, $k_{ij}$ and $b_{ij}$ are coefficients representing the anisotropic material constants.

The Szczepiński's yield criterion presented by Eq. (4.36) is simplified according to the experiments performed for yield surface identification of materials in this Thesis. The experiments were performed in the plane stress conditions for which except $\sigma_{xx}$ and $\tau_{xy}$, all other components of stress were equal to zero. So, yield condition for the plane stress is simplified as follows:

$$
f(\sigma_{ij}) = (k_{12} + k_{31})\sigma_{xx}^2 - 2k_{16}\tau_{xy}\sigma_{xx} + k_{66}\tau_{xy}^2 + (b_{31} - b_{12})\sigma_{xx} + b_{66}\tau_{xy} = 1
\tag{4.37}
$$

Physical interpretation of some of the coefficients $k_{ij}$ and $b_{ij}$ can be expressed as:

$$
k_{12} = \frac{1}{2}\left(\frac{1}{Y_{xx}Z_{xx}} + \frac{1}{Y_{yy}Z_{yy}} - \frac{1}{Y_{zz}Z_{zz}}\right)
$$

$$k_{31} = \frac{1}{2}\left(\frac{1}{Y_{xx}Z_{xx}} - \frac{1}{Y_{yy}Z_{yy}} + \frac{1}{Y_{zz}Z_{zz}}\right)$$

$$k_{66} = \frac{1}{R_{xy}S_{xy}} \tag{4.38}$$

$$b_{31} - b_{12} = \frac{1}{Y_{xx}} - \frac{1}{Z_{xx}}$$

$$b_{66} = \frac{1}{R_{xy}} - \frac{1}{S_{xy}}$$

where, $Y_{xx}, Y_{yy}, Y_{zz}$ are the yield limits under uniaxial tension and $Z_{xx}, Z_{yy}, Z_{zz}$ are the absolute values of yield limit under uniaxial compression in x, y, z directions, respectively; $R_{xy}$ is the yield limit under simple shear by positive shear stress $\tau_{xy}$; and $S_{xy}$ is the absolute value of yield limit under simple shear by negative shear stress $\tau_{xy}$.

Taking into account the physical interpretation of anisotropic coefficients, $k_{ij}$ and $b_{ij}$ can be written in following coefficients:

$$A = k_{12} + k_{31} = \frac{1}{Y_{xx}Z_{xx}}$$

$$B = -k_{16}$$

$$C = k_{66} = \frac{1}{R_{xy}S_{xy}} \tag{4.39}$$

$$2D = b_{31} - b_{12} = \frac{1}{Y_{xx}} - \frac{1}{Z_{xx}}$$

$$2F = b_{66} = \frac{1}{R_{xy}} - \frac{1}{S_{xy}}$$

After replacing the coefficients $k_{ij}$ and $b_{ij}$ in Eq. (4.37) by the coefficients A, B, C, D and F from Eq. (4.39), the second order equation representing the yield surface in biaxial stress plane can be written as follows:

$$A\sigma_{xx}^2 + 2B\sigma_{xx}\tau_{xy} + C\tau_{xy}^2 + 2D\sigma_{xx} + 2F\tau_{xy} = 1 \tag{4.40}$$

It can be observed that coefficients $A$ and $D$ are related to axial yield limits for tension and compression, whereas, coefficients $C$ and $F$ represents functions of yield limits under torsion and reverse torsion. However, the coefficient $B$ has no simple physical interpretation and it cannot be determined by a simple uniaxial test. It is proportional to the rotation of the yield surface with respect to the biaxial $(\sigma_{xx}, \tau_{xy})$ co-ordinate axes. Its value can only be obtained by performing at least one test in combined axial-shear loading condition.

The yield surface for the anisotropic materials can be determined by the five main ellipse parameters, that can be expressed by coefficients of the above mentioned second-order equation in the following way:

(1) Co-ordinates of the ellipse centre:

$$x_0 = \frac{B \times F - C \times D}{\delta} \tag{4.41}$$

$$y_0 = \frac{B \times D - A \times F}{\delta} \tag{4.42}$$

(2) Rotation angle of the ellipse axes with respect of ($\sigma_{xx}$ , $\tau_{xy}$) co-ordinate system:

$$\emptyset = \frac{1}{2} \times atan \left( \frac{2 \times B}{A - C} \right) \tag{4.43}$$

(3) Major and minor ellipse semi-axes:

$$a = \sqrt{-\frac{\Delta}{a^* \times \delta}} \tag{4.44}$$

$$b = \sqrt{-\frac{\Delta}{b^* \times \delta}} \tag{4.45}$$

where,

$$\Delta = -A \times C + 2 \times B \times D \times F - C \times D^2 - A \times F^2 - B^2 \tag{4.46}$$

$$\delta = A \times C - B^2 \tag{4.47}$$

$$a^* = \frac{1}{2} \times \left( A + C - \sqrt{(A - C)^2 + 4 \times B^2} \right) \tag{4.48}$$

$$b^* = \frac{1}{2} \times \left( A + C + \sqrt{(A - C)^2 + 4 \times B^2} \right) \tag{4.49}$$

To fit the experimental data by the equation of ellipse, the least squares method is used to calculate all coefficients of the equation (4.40). As a result of this approach, all values of the coefficients can be calculated, and necessary data regarding the anisotropic properties of the tested material can be captured. One should note, that the Szczepiński anisotropic yield criterion for plane stress (Eq. (4.40)) can be turned into the von Mises anisotropic yield criterion by imposing D = F = 0 and the Hill criterion by imposing B = D = F = 0.

### 4.4.1 Key features of Szczepiński's criterion

Main features of the criterion can be summarized as follows:

- By introducing linear terms in the stress components, Szczepiński's criterion captures the asymmetric yielding behaviour of materials, which is essential for accurately modelling the Bauschinger effect.

- The criterion accounts for the anisotropic nature of materials, particularly those with texture-induced anisotropy, by including terms that reflect the directional dependence of yield strength.

- Szczepiński's criterion can be viewed as a generalization of the von Mises anisotropic yield criterion, extending its applicability to materials with deformation-induced anisotropy and kinematic hardening.

### 4.4.2 Applications and significance

Szczepiński's yield criterion has found applications in the analysis of metal forming processes, cyclic loading, and fatigue failure, where the Bauschinger effect and anisotropic behaviour play a significant role. It is particularly useful for materials such as rolled metals, textured alloys, and composites, which exhibit pronounced directional dependence in their mechanical properties. The criterion provides a more accurate prediction of yield surfaces and plastic deformation under complex loading conditions, making it a valuable tool for engineering design and material characterisation.

### 4.4.3 Limitations

While Szczepiński's criterion represents a significant advancement in plasticity theory, it has some limitations:

- The accurate determination of material constants ($k_{ij}$ and $b_{ij}$) requires extensive experimental data, which can be time-consuming and costly.

- The criterion is primarily designed for materials with texture-induced anisotropy and may not fully capture the behaviour of materials with more complex microstructures or pressure-dependent yielding.

- The inclusion of linear terms increases the mathematical complexity of the criterion, making it more challenging to implement in numerical simulations compared to simpler models like the von Mises criterion.

## 4.5 Concluding remarks

This chapter provides a comprehensive overview of various yield criteria used to describe the onset of plastic deformation in materials under complex stress states. The study traces the historical evolution of yield models from classical isotropic theories to advanced anisotropic models, highlighting the critical role of yield criteria in engineering applications. The chapter emphasizes that understanding yield behaviour is essential for accurate material performance predictions in structural, automotive, aerospace, and manufacturing industries.

The findings of this chapter stress that the choice of a suitable yield criterion depends on factors such as material anisotropy, loading conditions, and computational complexity. The chapter also acknowledges the ongoing advancements in yield modelling, particularly the integration of experimental methods and numerical simulations to refine existing models.

# Chapter 5

# Yield surface identification of CP-Ti

*This chapter presents the results of experimental investigations conducted on CP-Ti (Commercially Pure Titanium) following the methodology discussed in Chapter 3. Basic mechanical properties were characterised, including equivalent mechanical parameters under combined loading conditions, such as tension-torsion. The mechanical response of Titanium under multiaxial stress states was explored. The initial yield surface was determined from tests on the as-received material, followed by an analysis of subsequent yield surfaces after pre-deformation. Additionally, Electron Backscatter Diffraction (EBSD) analysis was performed to assess microstructural changes induced by pre-deformation. These findings contribute to understanding the deformation mechanics and anisotropic yield behaviour of Pure Titanium.*

## 5.1 Introduction

Titanium and its alloys have been widely used in significant engineering disciplines such as medicine [143], aerospace, and marine engineering [144], due to their high specific strength, corrosion resistance, high impact resistance, and other properties. However, the mechanical testing of these materials is still primarily performed under simple stress conditions in research and commercial facilities. The most common form of testing is tension and compression of solid cylindrical specimens. Such types of testing can only generate limited results concerning the mechanical strength and damage of materials in a single direction which does not simulate the real-world stress conditions encountered by materials in most engineering applications.

In recent years, many researchers have performed complex loadings on metals to investigate their behaviour under metal forming conditions. Combined tension/compression - torsion loading experiments have been conducted on Mg alloys using solid specimens [145,146] as well as thin-walled tubular specimens [147,148]. It should be stressed, however, that solid specimens are not adequate for these experiments since the shear stress and strain distributions along the specimen's radial direction are not uniform. For the rolled Mg alloy AZ31B, the maximum strength is in simple tension (300.1 MPa) and simple compression (297.2 MPa) whereas the lowest strength is in torsion with slight tension (169.3 MPa), and the strength in other loading paths falls in between. This can be attributed to enhanced tension twinning in the tension-torsion loading path [149]. Multiaxial loading tests performed on the sintered porous iron reveal, that strength during uniaxial loading conditions was slightly lower than that obtained under combined tension-torsion proportional loading tests with a maximum variation of 10%. Furthermore, the sintered iron exhibited significantly higher strength during non-proportional loading tests in comparison to that captured under proportional loading paths with a maximum aberration of 35%. Such behaviour indicates the presence of additional hardening [150]. One should highlight, that the evolution of damage in porous sintered metals follows a two-stage process. In the initial stage, plastic deformation primarily occurs at the pore edges, while in the subsequent stage, bulk deformation becomes the dominant mechanism. Notably, micro-cracks always originated from pores oriented with their major axis perpendicular to the direction of tensile loading [150,151]. Commercially pure copper has also been tested under

combined tension-torsion loading conditions [152]. The results showed, that the magnitude of tensile and shear stresses assessed at a given strain were significantly lower in the combined-loading conditions compared to the simple tension or pure torsion conditions, Figure 5.1. The ultimate tensile stress in the simple tension case ($\beta = 90^0$) was equal to 274 MPa, whereas, under pure torsion conditions ($\beta = 0^0$), shear stress was equal to 160 MPa. One should mention, that for combined loading conditions including tension-dominated loading ($\beta = 49.9^0$) and torsion-dominated loading ($\beta = 42.5^0$), the tensile stress of 210 MPa and 223 MPa and shear stress of 102 MPa and 141 MPa were obtained, respectively [153]. Furthermore, it has been observed, that the simultaneous tension-torsion deformation of pure copper leads to the formation of an ultrafine-grained microstructure with high-angle boundaries. The fractured surface of the specimens subjected to pure torsion exhibited ductile mode with oval cavities. However, under combined tension-torsion loading, the fracture mode transits to a mixed fracture pattern, featuring equiaxial dimples and oval cavities [153,154].
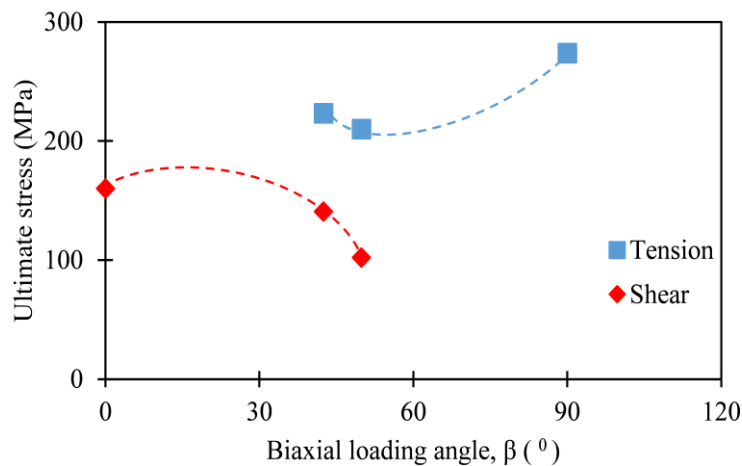


***Figure 5.1.*** *Variation of the ultimate stress under different states of stress of commercially pure copper [153].*

Fatigue life assessment of different materials had been performed under multi-axial proportional and non-proportional loading conditions [155,156]. Conventional uniaxial fatigue techniques frequently overestimate the fatigue life of engineering components, which might have adverse effects during their critical applications. Over the past few decades, multiaxial fatigue testing has been more important for the goal of a reliable and safe design. Additive manufactured IN718 nickel-based alloy shows slightly lower fatigue lifetimes in the perpendicular to the building direction during tests under combined proportional tension-torsion loading (5295 cycles) than during tension-compression (6081 cycles) and pure torsion (5442 cycles) loading conditions at the equivalent strain amplitude of 1%. It has been found [157], that fatigue lifetimes under non-proportional cyclic loading are significantly lower (maximum of 87% decrease) than those in proportional cyclic loading obtained at the same equivalent strain [157]. Unlike other metals, there have been very limited experimental investigations conducted on Ti and its alloys under complex stress loadings. Majority of these investigations did not involve an effect of the multiaxial loading on the mechanical properties, in particular, yield strength using the concept of yield surface.

The literature review performed in the area of materials and existing methods for yield surface identification enabled to highlight the novelty of this Thesis, which is mainly expressed by:

(a) a new database from investigations on CP-Ti alloy carried out under complex stress state;

(b) complex stress loading experiments to understand the physical mechanism accountable for plastic deformation caused by monotonic tension and monotonic tension assisted by cyclic torsion in the CP-Ti;

(c) application of the yield surface approach to assess the variation of mechanical properties in the as-received and pre-deformed material;

(d) identification of the optimal loading parameters under which tension of titanium could be performed under lower forces. This aspect is directly related to the potential applications in the industrial forming processes.

## 5.2 Materials and Methods

The material investigated in this research was CP-Ti alloy. The titanium bars are classified as grade 2 (3.7035/UNSR50400/ASTM B348 EN10204/3.1) and undergo a sequence of heat treatments. This includes a process of soft annealing at temperatures between 600°C and 700°C, followed by stress relief heat treatment within the range from 450°C to 600°C. The experimental investigations conducted on CP-Ti involved four stages following the methodology discussed in Chapter 3:

- determination of the basic mechanical properties of CP-Ti;
- introduction of the following plastic pre-deformation in the specimens:
    - (a) monotonic tension up to 1% permanent strain at constant strain rate of 5 x $10^{-6}$ $s^{-1}$.
    - (b) combination of monotonic axial tension up to 1% permanent strain at constant strain rate of 5 x $10^{-6}$ $s^{-1}$, and torsion-reverse-torsion cyclic loading for two magnitudes of strain amplitude (±0.2% and ±0.4%) at two different values of frequency (0.5 Hz and 1 Hz), Figure 5.2.
- determination of the initial yield surface of the as-received material and yield surfaces of the pre-deformed specimens;
- determination of the microstructure and texture evolution after pre-deformation.

The selection of plastic pre-deformation values was based on the material properties and experimental limitations, with the objective of attaining controlled deformation in the specimens. Strain gauges attached to the specimen's outer surface facilitated more accurate monitoring and control of pre-deformation strain than compared to depending only on the testing machine's crosshead movement. Attachment of stain gauges is explained in details in Chapter 3. A 1% axial pre-strain level was chosen based on the tensile stress-strain behaviour of CP-Ti and the operational range of the strain gauges, ensuring a consistent and limited plastic strain value. However, tests involving combined monotonic tension and cyclic torsion showed that CP-Ti was unable to achieve the 1% axial pre-strain value when the shear strain amplitude was ±0.8% and more at frequencies of 0.5 and 1 Hz, as shown in Figure 5.3. This result demonstrates that the response of CP-Ti is significantly influenced by the cyclic shear strain amplitude. At higher cyclic shear strain amplitudes, CP-Ti exhibits preferential plastic deformation in the shear direction, reducing axial strain accumulation. This effect is strengthened by its rate sensitivity and limited strain hardening, which increase resistance to axial plastic flow under multiaxial loading conditions. Consequently, to ensure stable pre-

deformation during bi-directional stress loading, cyclic shear strain amplitudes of ±0.2% and ±0.4% at frequencies of 0.5 Hz and 1 Hz were selected, enabling the specimens to reach the target axial strain level of 1%.
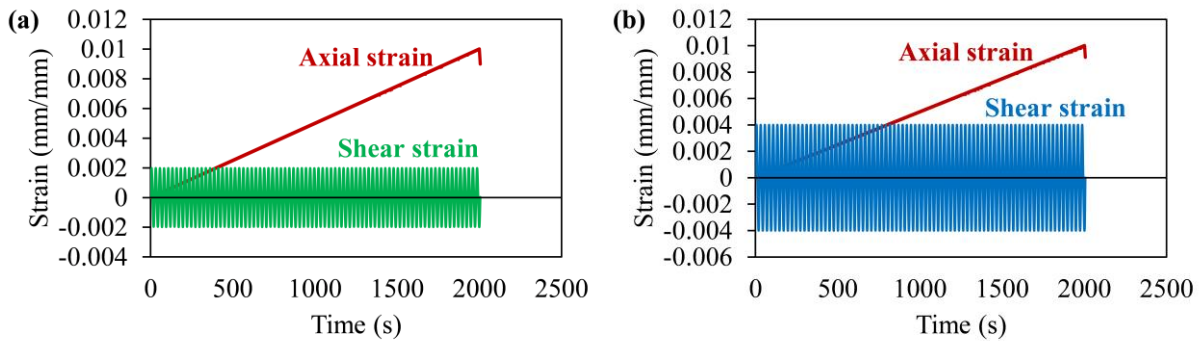


***Figure 5.2.*** *Strain controlled complex loading programme with monotonic axial tension and cyclic torsion with strain amplitudes of ±0.2% (a); and ±0.4% (b) at a frequency of 0.5 Hz.*
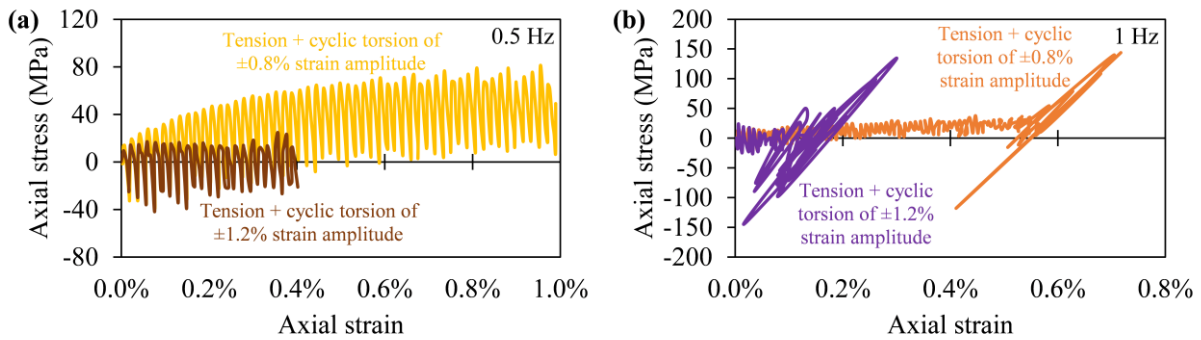


***Figure 5.3.*** *Response of CP-Ti in axial direction during monotonic tension assisted by the torsion-reverse torsion cycles of strain amplitude equal to: ±0.8% and ±1.2% and frequency of: (a) 0.5 Hz and (b) 1 Hz.*

Only one specimen was used to determine the initial and subsequent yield surfaces after pre-deformation. The specimens were loaded to the desired value of plastic strain and then linearly unloaded to zero stress state. Subsequently, yield points for each path at 0.01% and 0.005% plastic offset strains were determined. The yield surface was obtained by fitting the experimental yield points with the Szczepinski anisotropic yield equation [29] using the least squares method as discussed in Chapter 4.

## 5.3 Results and discussion

### 5.3.1 Identification of the basic mechanical parameters of the material

The room temperature tensile properties of CP-Ti can be determined on the basis of stress-strain curve (Figure 5.4a), they are listed in Table 5.1. Tensile tests were carried out using solid tubular and thin-walled tubular specimens. The variation of the results obtained in Figure 5.4a for both types of specimen was attributed to the specimen geometry differences. It is challenging to compare the findings given here with those in the available literature presented, since the mechanical properties of commercially pure titanium are significantly dependent on the microstructure, interstitial elements (O, N, C) concentration and manufacturing method. As the

reference, the yield and tensile strengths published in earlier studies [158–161] fall in the ranges of 170-550 MPa and 240-750 MPa, respectively. One can indicate, that the values of these parameters for the material tested are within those ranges.

*Table 5.1. The mechanical properties of CP-Ti.*

|  | 0.2% Yield strength [MPa] | Tensile strength [MPa] | Elongation [%] | Young's modulus [GPa] |
|---|---|---|---|---|
| Solid tubular specimen | 390 ($\pm$ 2) | 503 ($\pm$ 1) | 29 ($\pm$ 0) | 107 ($\pm$ 1) |
| Thin-walled tubular specimen | 400 ($\pm$ 3) | 531 ($\pm$ 1) | 37 ($\pm$ 1) | 100 ($\pm$ 1) |
| ASTM standard | 350 - 450 | > 485 | > 28 | 103 |

### 5.3.2 Equivalent mechanical parameters of the material tested under combined loading

Figure 5.4b shows the equivalent stress-strain curve for the comparison of material characteristics determined on the thin-walled tubular specimen subjected to tension (1), tension-torsion (2) and pure torsion (3). It can be observed from the Figure 5.4b that all three curves do not coincide themselves, i.e. material characteristics varies in different loading conditions for the same material. These differences are probably the result of initial anisotropy introduction to the material during the manufacturing process. This anisotropy will be further discussed in details using the yield surface of 'as-received' material in the section 5.3.4.
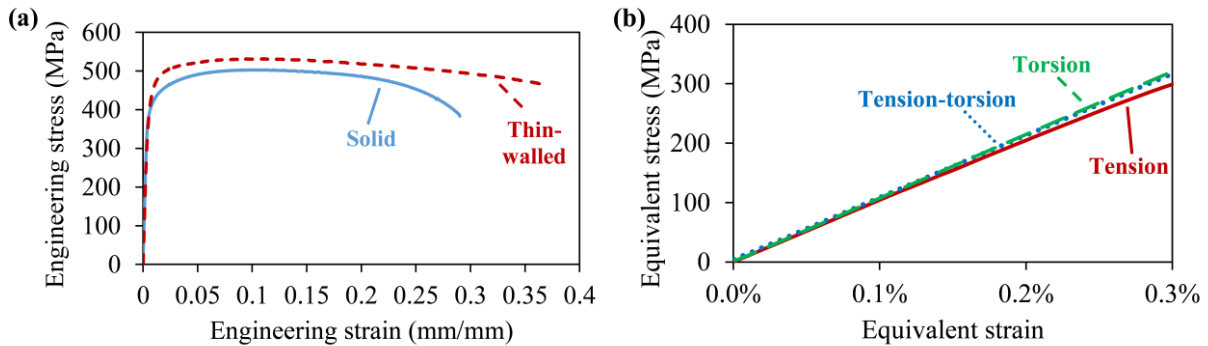


*Figure 5.4. Tensile stress-strain characteristics of solid tubular and thin-walled tubular specimen of CP-Ti (a); Comparison of material characteristics of pure titanium for different loading paths: simple tension; tension-torsion and pure torsion on thin-walled tubular specimen (b).*

### 5.3.3 Results of the material under complex loading

An influence of the cyclic torsion of different strain amplitudes and frequencies on the monotonic tension of CP-Ti was investigated. The main objectives of these tests were to introduce plastic pre-deformation of the material and to investigate variation of the tensile characteristics in the presence of torsion-reverse-torsion cycles. Figure 5.5a and Figure 5.5b clearly show that tensile characteristics of pure titanium significantly varies if tension is associated with cyclic torsion. A tendency of decreasing axial stress, looking like the softening effect, can be clearly observed with the progressive increase of the cyclic strain amplitude. Also,

an increase of the frequency led to the decrease of the axial stress. In the case of ±0.2% cyclic torsion strain amplitude and frequency of 0.5 Hz, the tensile stress for 0.2% axial strain decreased from 205 MPa to 181 MPa. For the same level of axial strain in the case of cyclic torsion strain amplitude of ±0.4% such decrease takes 110 MPa, Figure 5.5a. The effect is strengthened for higher value of frequency. The respective values of tensile stress at strain of 0.2% equal to 205 MPa, 178 MPa and 90 MPa, Figure 5.5b. The magnitude of axial stress dropped nearly 46% and 56% in the case of frequency equal to 0.5 Hz and 1 Hz, respectively, in comparison to that obtained at tension only for the axial strain equal to 0.2%.

This decrease in tensile stress is expected due to the introduction of shear stress indeed. To address the effect of shear stress on the equivalent stress in the three cases of loading, Figure 5.5c and Figure 5.5d provide the equivalent stress-strain curves. These curves depict the material's response under different loading conditions. The courses of equivalent stress-strain curves variation clearly demonstrate a softening effect in the material's response as the cyclic torsion strain amplitude increases. This further emphasizes an influence of shear stress on the material's behaviour during simultaneous tension.
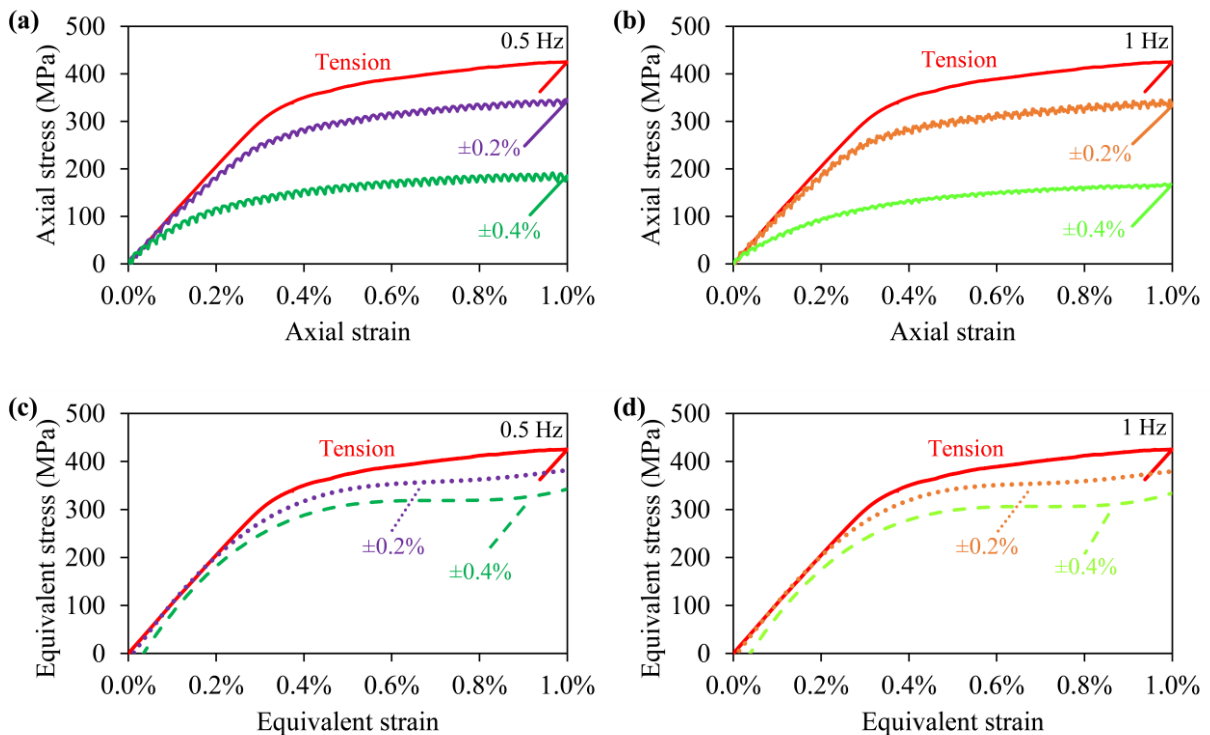


***Figure 5.5.*** *Comparison of standard tensile curve with tensile characteristics and curves representing equivalent stress captured during monotonic tension assisted by the torsion-reverse torsion cycles of strain amplitude equal to: ±0.2% and ±0.4% and frequency of: (a, c) 0.5 Hz and (b, d) 1 Hz.*

The aforementioned tendency of decreasing tensile stress is shown in Figure 5.6 for 0.5% axial strain at both cyclic torsion strain amplitude and frequency (Note that the 0% cyclic torsion strain amplitude represents monotonic tension). The same effect has also been reported for Mg-alloy (AZ31B) [149], commercially pure Cu [153] and aluminium alloy (Al-6061-T6) [162] due to typical reduction of the tension twining volume fraction in Mg alloy and shallow more elongated dimples on Cu fracture surface with the increase of cyclic torsion strain amplitude during combined tension-torsion loading.
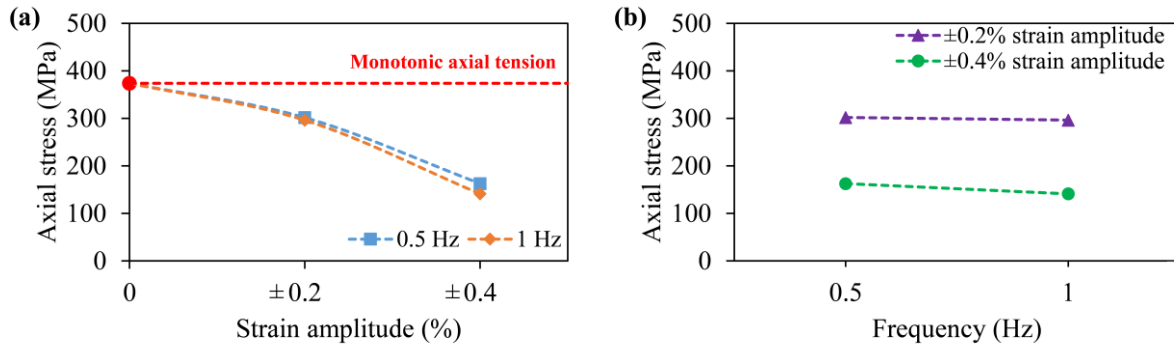
***Figure 5.6.*** *Variation of the tensile stress corresponding to the 0.5% axial strain value, in response to combined monotonic tension and cyclic torsion of strain amplitude equal to: ±0.2% and ±0.4% (a) and frequency of: 0.5 Hz and 1 Hz (b).*

### 5.3.4 Yield surface of the pure titanium in the as-received state

The yield points describing initial yield surface of CP-Ti were determined by loading-unloading of a single specimen in different strain directions (axial-shear strain) through the specified offset strain method. Figure 5.7 shows the pure titanium response in biaxial stress plane on the strain-controlled loading program discussed in Chapter 3. It can be observed, that there is negligible deviation from linearity during loading and unloading for each path. The total plastic strain was equal to 0.02%. The Poisson's ratio for all directions taken into account was equal to 0.3.
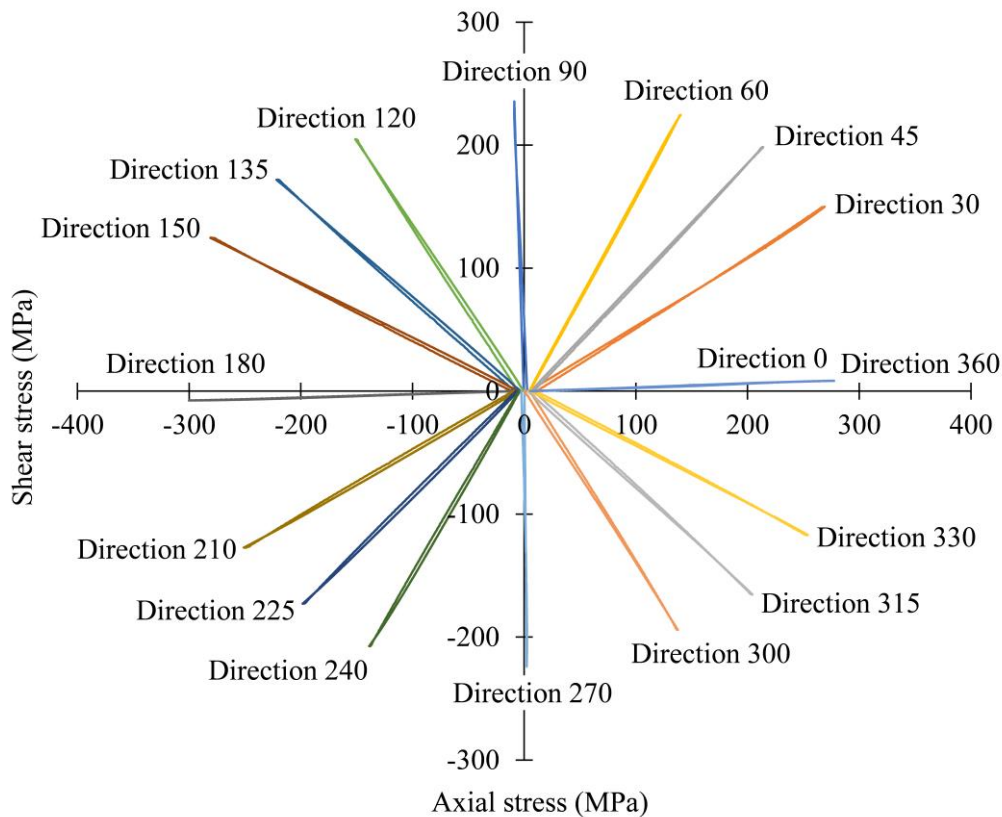


***Figure 5.7.*** *Stress responses to the strain-controlled loading program used for determination of the initial yield surface of CP-Ti.*

A graphical representation of the variation in the effective Young's modulus for the as-received pure titanium specimen under plane stress loading in various directions is shown in Figure 5.8. The maximum variation of this parameter is approximately 10%, which emphasizes the existence of texture even for the as-received material. The material texture can be identified by comparison of characteristics determined in all directions considered. CP- metals often exhibit directionality due to preferred texture or crystallographic orientation, as their crystal structures are frequently anisotropic [163]. In previous studies, it has been reported that the Young's moduli of aluminium and some hexagonal metals, such as titanium and magnesium, exhibit relatively uniform variation compared to other metals such as steels and copper, which exhibit a significant degree of anisotropy [164,165]. However, the differences in Young's modulus for different directions in plane stress alone do not provide a satisfactory explanation of the initial anisotropy observed in the as-received pure titanium specimen under examination.

Considering the low magnitude of the plastic strain probing involved in the study, such variation of the Young's modulus can have a significant impact on the results of yield surface, if only the Young's modulus of initial elastic curve is used for each stress direction. The authors have performed the experiment while using the initial elastic curve for each direction during plastic strain probing but the obtained results were deemed unacceptable. Specifically, for a limited plastic strain (0.02%) in each direction, which depends on the Young's modulus, a lesser equivalent strain was necessary in directions other than the initial one. The Young's modulus obtained for the initial direction is the lowest among the directions examined, as shown in Figure 5.8. When this variation of the Young's modulus ignored, specimen experienced a higher plastic strain in other directions than the pre-defined value. Therefore, to account for the elastic anisotropy in the estimation of plastic strain during probing in different stress directions, the effective Young's modulus specific to each respective direction is utilized. Through this approach, the authors sought to improve the accuracy and reliability of their analysis by considering the elastic anisotropy and its impact on the estimation of plastic strain during probing in various stress directions.
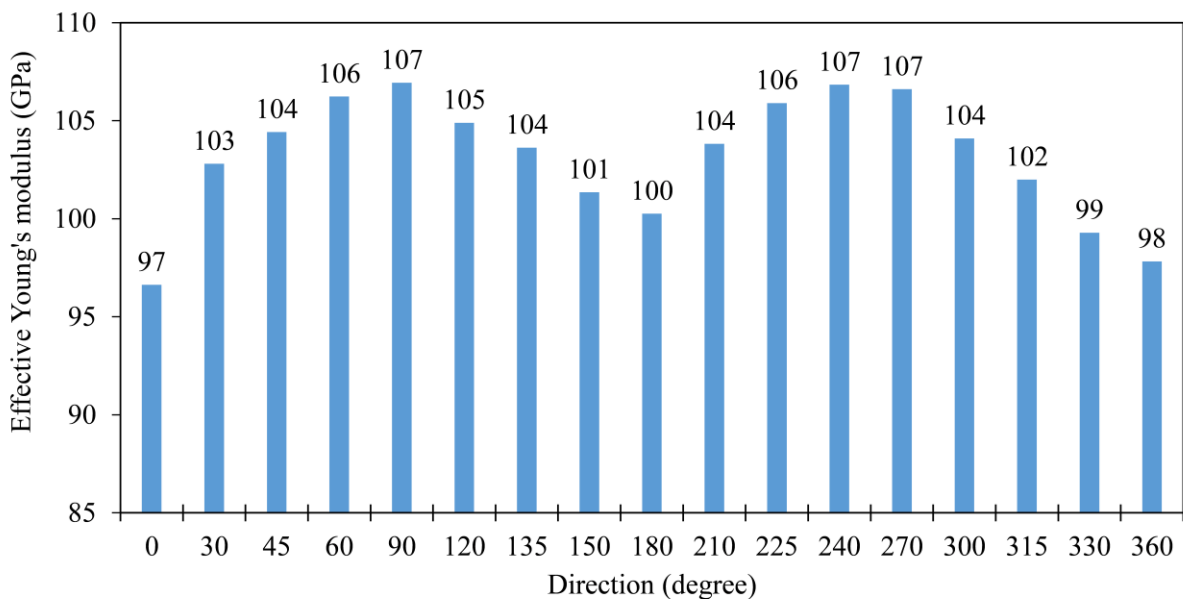


**Figure 5.8.** *Variation of the effective Young's modulus in different loading directions in the biaxial strain space for CP-Ti.*

The yield surfaces of the pure titanium in the as-received state were determined using a sequential loading procedure on a single specimen at 0.01% and 0.005% offset strain, as shown by the continuous line and dotted line, respectively, in Figure 5.9a. These yield surfaces show the dependence on the chosen definition of yield. After obtaining the yield loci for different directions from experimental results, ellipses were obtained by fitting the A, B, C, D, and F coefficients using a least squares evaluation method, as explained in Chapter 4. The main ellipse parameters for the initial yield surface of the titanium at both selected offset strain values are listed in Table 5.2. The results for the as-received state of the titanium indicate some level of initial anisotropy, as the yield surfaces are shifted in the compression direction and the axis ratios are significantly lower than 1.73 (the value for an isotropic material according to the von Misses-Huber yield condition).

***Table 5.2.*** *Five ellipse parameters that define the initial yield surface for CP-Ti.*

| Yield definition | Centre $(x_0, y_0)$ [MPa] | Rotation angle $(\emptyset)$ [Radian] | Semi-axes $(a, b)$ [MPa] | Axis ratio $(^a/_b)$ |
|---|---|---|---|---|
| 0.01% offset strain | -11.36, 1.15 | 0.14 | 293.61, 237.11 | 1.24 |
| 0.005% offset strain | -16.82, 1.99 | 0.22 | 270.25, 227.17 | 1.19 |
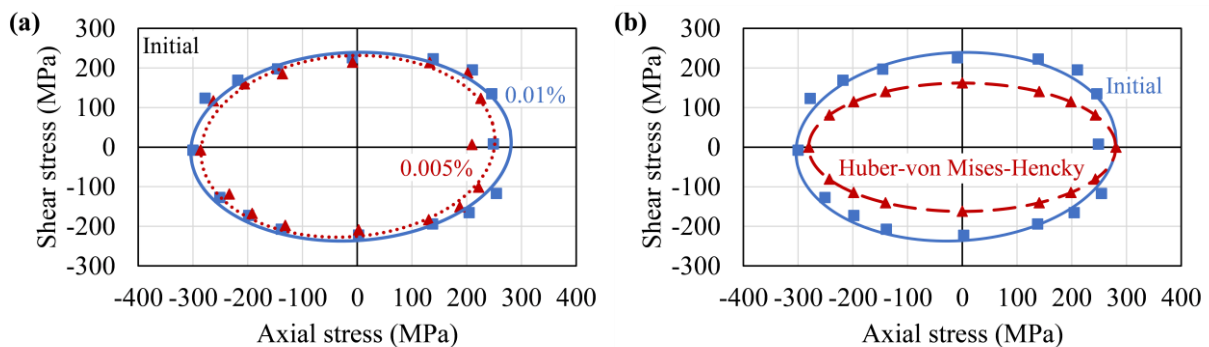


***Figure 5.9.*** *Yield surface of CP-Ti in the as-received state determined by least square fitting method of yield points (square and triangular points) obtained using a sequential loading technique for two values of plastic offset strain, 0.005% (dotted red line) and 0.01% (continuous blue line) (a); comparison of the initial yield surface (0.01% offset strain) of the CP-Ti (continuous blue line) with the yield surface assuming isotropic material (dashed red line) (b).*

In order to compare the yield surface of CP-Ti, an isotropic yield surface was determined by fixing the yield point in tension (direction 0) of the 0.01% offset initial yield surface of pure titanium. The isotropic yield surface was centred at the origin, had a zero-rotation angle, and had an axis ratio of 1.73 according to the von Misses-Huber yield criterion. Figure 5.9b shows the resulting yield surface. It can be observed from Figure 5.9b, that the initial anisotropy of the material is mainly a distinct hardening behaviour in the shear strength and that is likely a result of the thin-walled tubular specimen manufacturing process from solid specimen or material production process applied to the as-received state of the material.

### 5.3.5 Yield surface of the pure titanium in the pre-deformed state

The effect of monotonic tension and complex monotonic tension-cyclic torsion plastic pre-deformation on the mechanical parameters of CP-Ti was assessed based on the evolution of the initial yield surface. All pre-deformations of specimens were carried out until an axial strain of 1% was achieved. Subsequently, the yield surfaces of the pre-deformed specimens were determined using the same procedure as was previously used for the as-received specimen at a 0.01% offset strain.

The yield surface determined for 1% tensile pre-deformed titanium is shown in Figure 5.10 as a dashed line. The shape of the yield surface is similar to the initial one, but with an increase in the tensile direction. This indicates that monotonic tensile deformation has induced kinematic hardening of the titanium. The yield point increase in tension is about 45 MPa, which is approximately a 16% greater in comparison to the initial value.

Figure 5.11 shows the yield surfaces determined after plastic pre-deformation caused by monotonic tension assisted by torsion-reverse-torsion cyclic loading. These yield surfaces are plotted together with the initial yield surface (continuous line) of the material tested. The combined preloading leads to anisotropic hardening of the material. For the torsional strain amplitude of ±0.2%, the subsequent yield surface exhibits an increase of the tensile yield and a significant reduction of the compressive yield at frequency of 0.5 Hz (Figure 5.11a), which decreases in both directions when the frequency is increased to 1 Hz (Figure 5.11c).
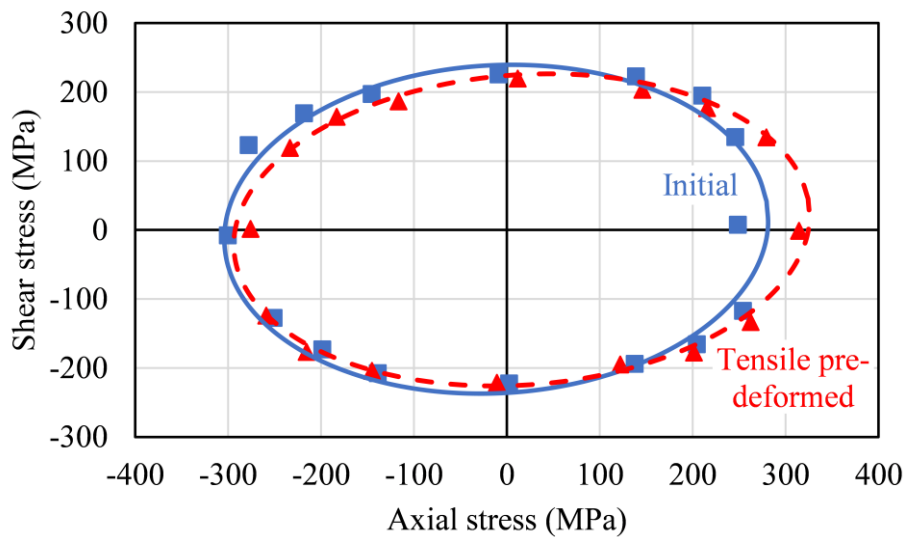


***Figure 5.10.*** *Comparison of the yield surface for pure titanium after tensile pre-deformation to the initial yield surface. Both were obtained at 0.01% offset strain.*

On the other hand, for the torsional strain amplitude of ±0.4%, the yield surface size of the pre-deformed material is reduced in both the compression and shear directions, but there is an increase in the tensile direction at a frequency of 0.5 Hz (Figure 5.11b). However, at an increased frequency of 1 Hz (Figure 5.11d), it is interesting to note that the compressive yield is nearly the same as that observed for the initial yield surface, with a further reduction in the shear yield stress. When the frequency is increased from 0.5 Hz to 1 Hz for monotonic tension assisted by cyclic torsion of strain amplitude equal to ±0.4%, the higher reduction of shear stress is compensated by an increase of axial stress. One should observe, that regardless the introduced

pre-deformation, including monotonic tension and combined tension-cyclic torsion, an increase of the tension stress and a decrease in shear stress at higher torsional strain magnitudes in the titanium could be found. Many studies have been conducted on the effects of pre-deformation on materials, but most of them focus on changes in cumulative mechanical properties [166,167], while only a few researchers have published the results related to changes of directional mechanical properties, specifically using the yield surface evolution approach [31,34]. Therefore, it is difficult to make an exact comparison to the findings of this work. A similar tendency of pronounced kinematic hardening after 1% tension pre-strain (shown in Figure 5.10) was also observed in P250GH and S235JR steel [168] and aluminium alloy (Al 6061-T6511) [32], and it was stated that the existence of incoherent, non-shearable precipitates, which serve as an obstacle to dislocation motion, may contribute to this effect. On the other hand, the evolution of the yield surface after monotonic tension assisted by cyclic torsion was rarely studied by researchers. The yield surface evolution of X10CrMoVNb9-1 steel and Cu 99.9 E copper [34] due to combined monotonic tension-cyclic torsion pre-deformation is in good agreement with the findings of this work, as the size of the subsequent yield surfaces is smaller in all directions except that representing pure tension.
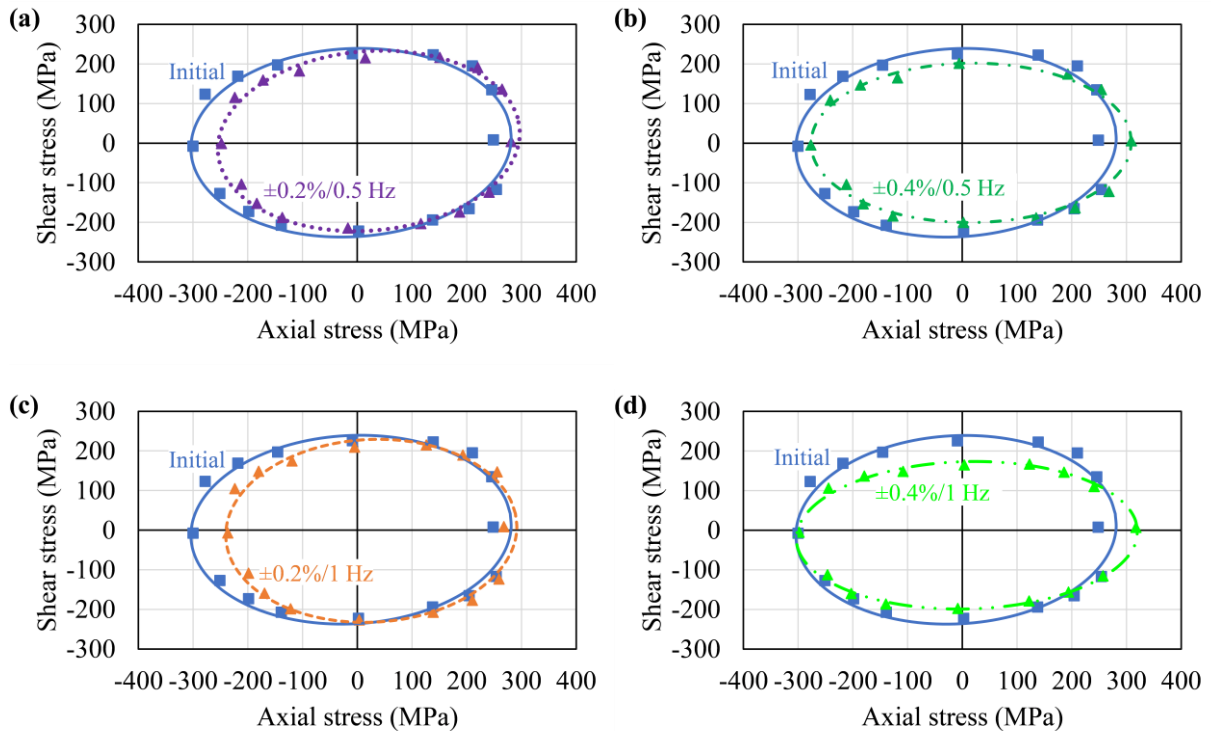


***Figure 5.11.*** *Comparison of the initial yield surface of CP-Ti to the yield surfaces of pre-deformed titanium due to combined monotonic tension and cyclic torsion of strain amplitude equal to: ±0.2% and ±0.4% and frequency of: 0.5 Hz (a, b) and 1 Hz (c, d), respectively.*

The least squares method was used to calculate the coefficients of the yield equation by fitting the experimental data. The yield surface equation coefficients (A, B, C, D, F) were taken to describe the ellipse representing the approximation yield surface of the tested material. The fitting errors obtained while minimizing the sum of squares of the distances of experimental points from the approximation curve were presented in the Table 5.3 for each yield surface determined.

***Table 5.3.*** *The fitting errors for the yield surfaces in as-received state and after pre-deformation caused by monotonic tension; combined monotonic tension with cyclic torsion of strain amplitude equal to: ±0.2% and ±0.4% at frequency of: 0.5 Hz and 1 Hz.*

| As-received | Monotonic tension deformed | ±0.2% at 0.5 Hz deformed | ±0.4% at 0.5 Hz deformed | ±0.2% at 1 Hz deformed | ±0.4% at 1 Hz deformed |
|---|---|---|---|---|---|
| 2.31E-01 | 5.73E-02 | 1.06E-01 | 1.07E-01 | 1.62E-01 | 5.01E-02 |

The fitting error values obtained for each yield surface were found as minimal, indicating an accurate match between the experimental data and fitted ellipse. Such low fitting errors confirm the suitability, accuracy and reliability of the yield surface equation as well as the quality of the yield surface approximation.
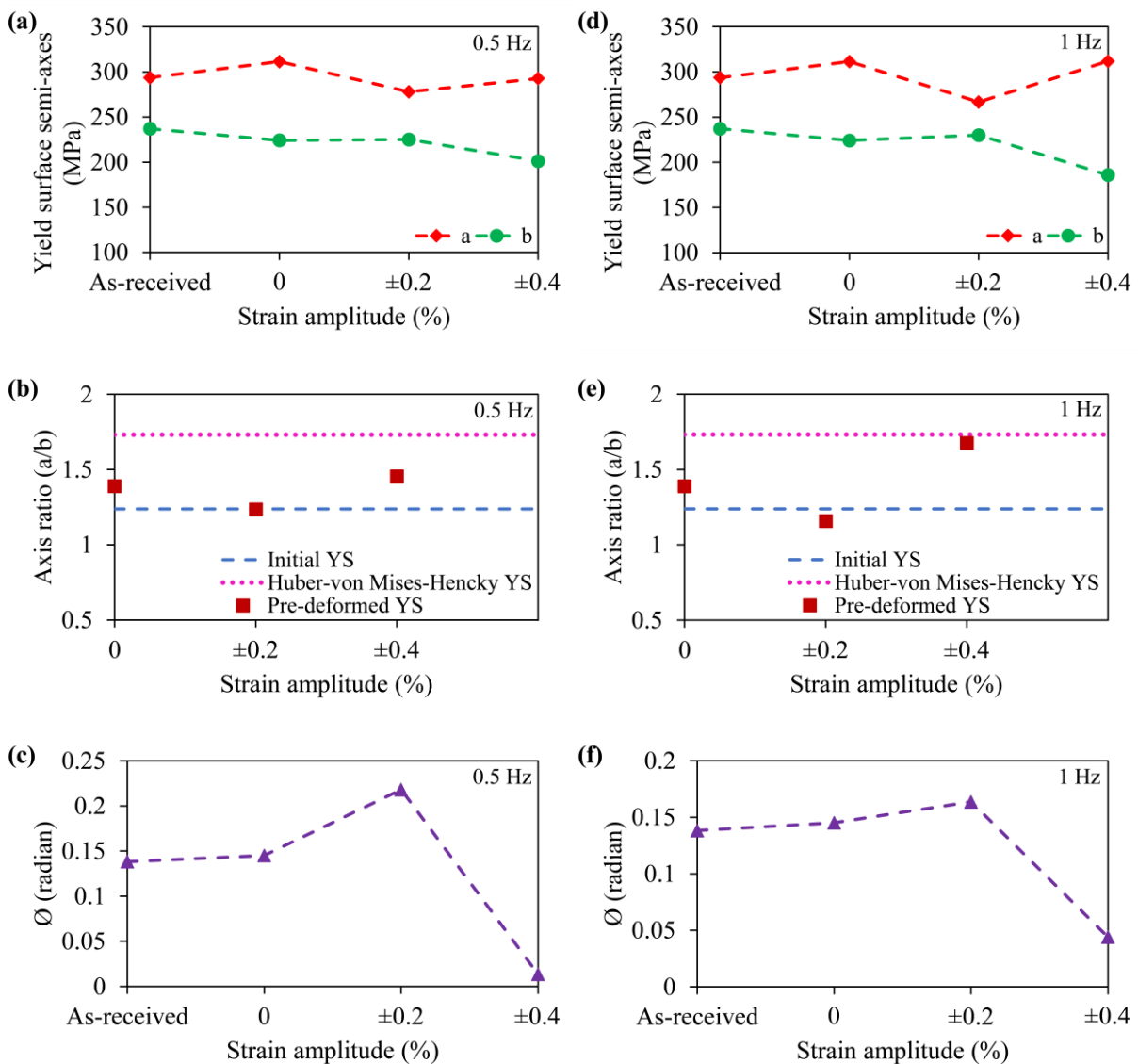


***Figure 5.12.*** *Variation of the yield surface parameters of CP-Ti due to pre-deformation caused by monotonic tension (0% strain amplitude); combined monotonic tension with cyclic torsion of strain amplitude equal to: ±0.2% and ±0.4% at frequency of: 0.5 Hz (a, b, c) and 1 Hz (d, e, f), respectively.*

Figure 5.12 illustrates the variation in the ellipse parameters that represent the yield surface (YS) of CP-Ti in the pre-deformed state. Pre-deformation caused by monotonic tension is denoted by 0% cyclic torsion strain amplitude. The axis ratio of the yield surface was compared to that representing the initial yield surface (Table 5.2) and Huber-von Mises-Hencky isotropic yield surface (HMH YS) (1.73) in Figure 5.12b and Figure 5.12e. The results indicate that the yield surface obtained following monotonic tension combined with a cyclic torsion strain amplitude of ±0.4% aligns more closely with the HMH yield criterion at both 0.5 Hz and 1 Hz frequencies compared to other material states (as-received or pre-deformed). This observation is further supported by the near-zero rotation angle (Ø) of the axes with respect of ($\sigma_{xx}$, $\tau_{xy}$) co-ordinate system, as shown in Figure 5.12c and Figure 5.12f.

Subsequently, the analysis of the centre of all the yield surfaces was performed (Figure 5.13). One should highlight the presence of back stress components which is often observed in materials that have undergone plastic deformation. Figure 5.13 shows, that the back-stress components are minimal in the as-received state, however, for the pre-deformed state they increased significantly. The back stress arises due to the formation of dislocations, which can block the movement of other dislocations and create areas of high stress in the material.
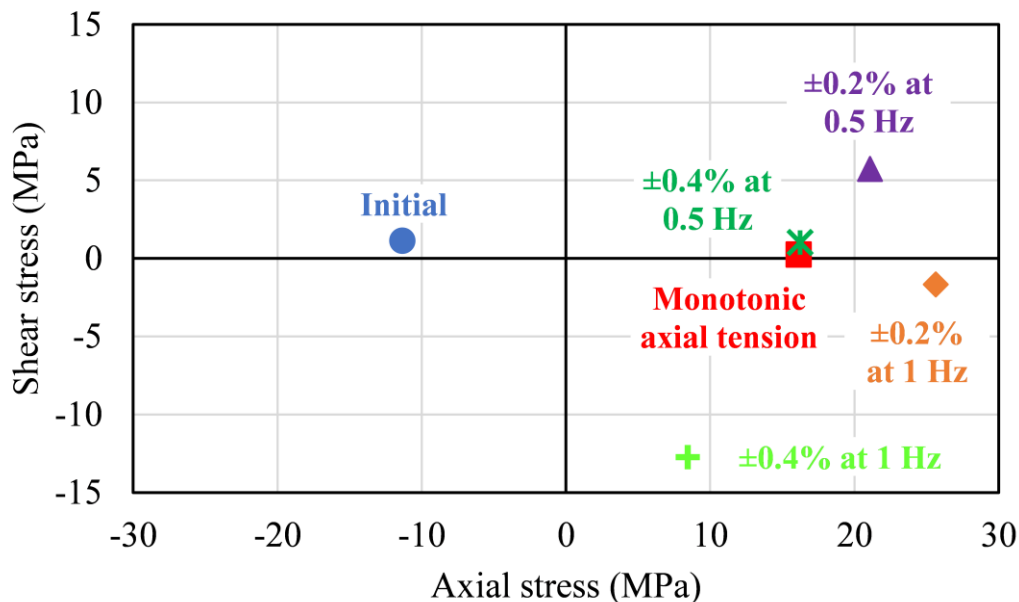


***Figure 5.13.*** *Analysis of the yield surface origin position of CP-Ti in the as-received state and after pre-deformation caused by monotonic tension; combined monotonic tension with cyclic torsion of strain amplitude equal to: ±0.2% and ±0.4% at frequency of: 0.5 Hz and 1 Hz.*

Figure 5.14 depicts a cumulative representation of the evolution of the initial yield surface in the axial-shear stress space that were obtained from experimental results following pre-deformation of the material at 0.5 Hz and 1 Hz. It can be observed, that the yield surfaces have distinct shapes on the one hand and the size of the subsequent yield surfaces decreases in the direction opposite to the pre-deformation loading on the other. As shown in Figure 5.14, the subsequent yield surface for monotonic tension exhibits the largest dimensions.
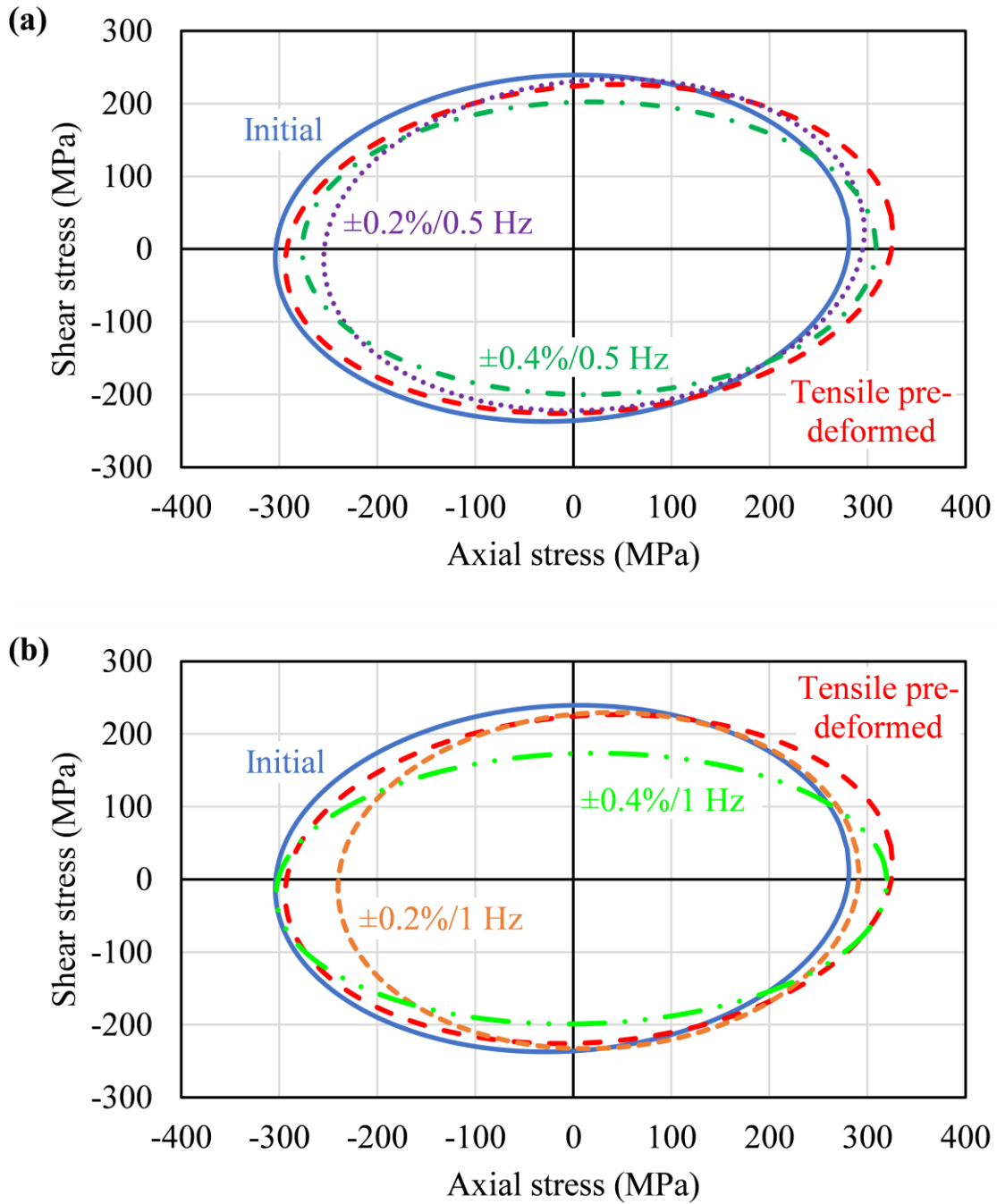
***Figure 5.14.*** *Evolution of the initial yield surface of CP-Ti due to pre-deformation caused by monotonic tension; monotonic tension assisted by cyclic torsion of strain amplitudes equal to: ±0.2% and ±0.4% at frequencies equal to 0.5 Hz (a) and 1 Hz (b).*

By examining Figure 5.14, it becomes evident that the pre-deformed material exhibits both:

- kinematic hardening towards the applied axial pre-deformation direction in comparison to the as-received material surface;

- kinematic softening after the introduction of cyclic torsion during monotonic tensile pre-deformation in comparison to the yield surface of the material deformed due to monotonic tension.

This is demonstrated by the decrease of subsequent yield loci compared to those for monotonic tensile pre-deformation. For example, the yield surface obtained after combined tension-cyclic torsion with a strain amplitude of ±0.2% pre-deformation exhibits a similar shear yield strength but a decrease of axial yield strength compared to that obtained for monotonic tension deformation. Conversely, in the case of combined tension-cyclic torsion with a strain amplitude of ±0.4% pre-deformation, the opposite trend is observed. Similar tendencies can be observed for both frequencies of 0.5 Hz and 1 Hz, respectively. The shape analysis of these subsequent yield surfaces reveals that the dimensions of the yield surface are dependent on the preloading direction.

### 5.3.6 Microstructural characteristics of the pure titanium in the as-received and pre-deformed state

The microstructure of titanium in its as-received state and its evolution after deformation was presented in the form of Inverse Pole Figure (IPF) maps and (0001) pole figures as shown in Figure 5.15 and Figure 5.16. Each map was related to the specific yield surface presented in Figure 5.14. The material of all specimens was fully recrystallized after pre-deformation and exhibited similar average grain size. In the as-received state of the material (Figure 5.15a and Figure 5.16a), two ED split basal texture could be observed. The stronger basal texture with most of the c-axes is inclined at + (20° – 55°) from the TD towards the ED with narrow distribution in the extrusion direction ED-TD plane and a weaker texture component with the c-axes inclined at – (45° – 60°) from TD towards ED. However, for the 1% tensile pre-deformation (Figure 5.15b and Figure 5.16b), both texture components with the c-axis tend to align parallel to the TD as inclination towards the ED decreased up to maximum of 30°. When material is deformed with combined tension-cyclic torsion with ±0.2% strain amplitude (Figure 5.15c and Figure 5.16c), the weaker texture component is intensified and its c-axis aligned more towards the TD. It should be noted, that the other texture component is weakened. However, with the increase of frequency from 0.5 Hz to 1 Hz (Figure 5.15e and Figure 5.16e), the previous weaker texture component disappeared and a new texture component with the c-axis distributed narrowly in the negative extrusion direction (-ED) – RD plane appears. Simultaneously, the stronger texture component shifts towards negative RD. One could observe a new basal texture with most of the c-axes aligned parallel to the TD and rest distributed in the positive ED-TD plane when pre-deformation caused by combined monotonic tension-cyclic torsion with ±0.4% strain amplitude was applied (Figure 5.15d and Figure 5.16d). In the case of ±0.4% strain amplitude at the frequency equal to 1 Hz (Figure 5.15f and Figure 5.16f), a significantly different grain orientation was observed. The basal texture was distributed widely with the c-axis in the whole ED-TD plane with 3 different high-intensity orientations. First, with most of the c-axes is inclined at – (50° – 68°) from the TD towards the ED; second, with the c-axis aligned to be parallel to the TD and third, with the c-axes inclined at + (45° – 50°) from the TD towards the positive ED-RD plane. These results clearly support the presence of anisotropy and evolution of the initial yield surface of CP-Ti due to pre-deformation, presented in Figure 5.14, as texture evolution and preferred grain orientation can be clearly observed in Figure 5.15 and Figure 5.16.
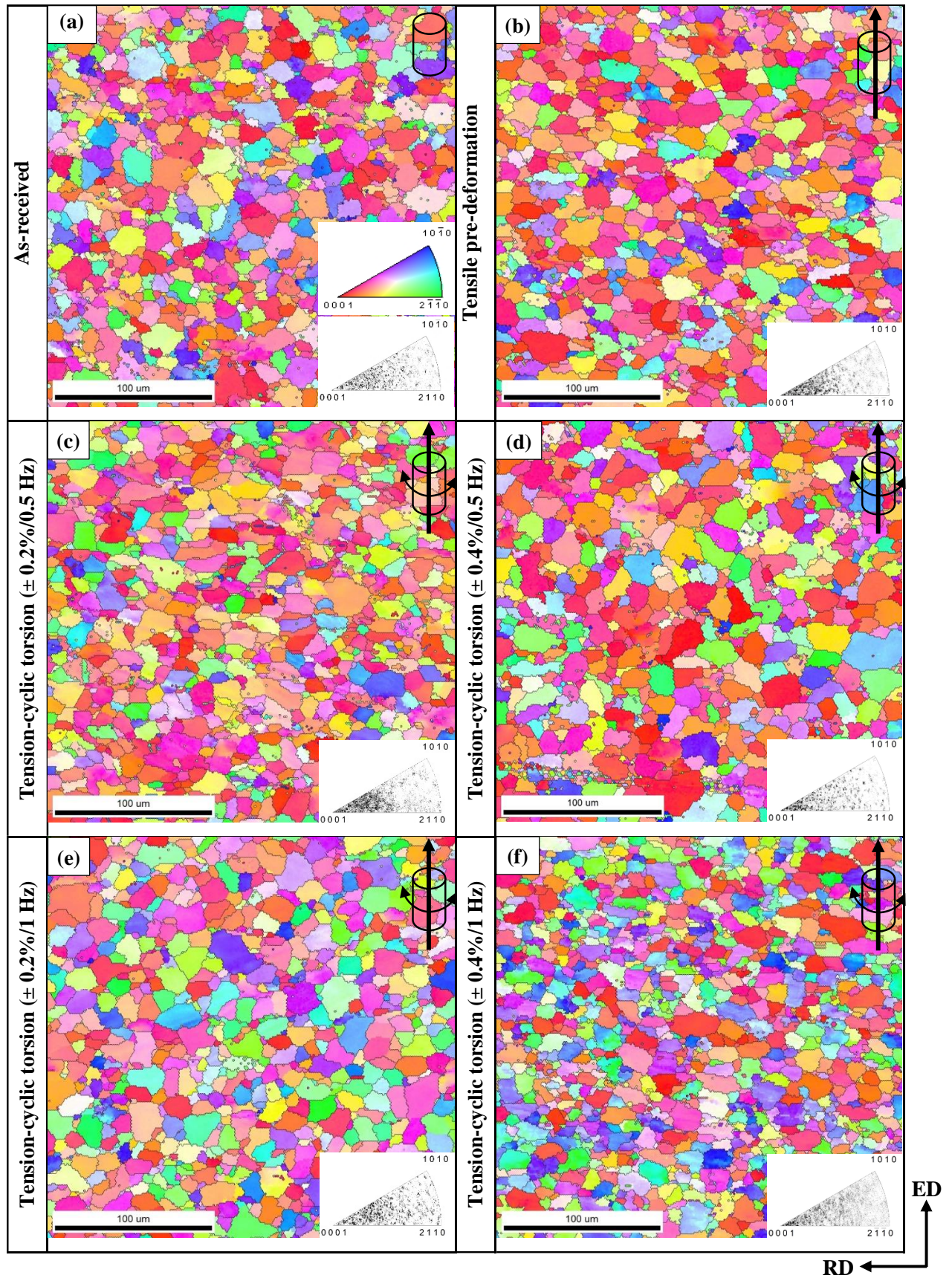
***Figure 5.15.*** *Inverse pole figure maps of the as-received material (a); after 1% monotonic tension (b); and monotonic tension with cyclic torsion of strain amplitudes equal to ±0.2% (c, e) and ±0.4% (d, f) at frequencies equal to 0.5 Hz (c, d) and 1 Hz (e, f).*
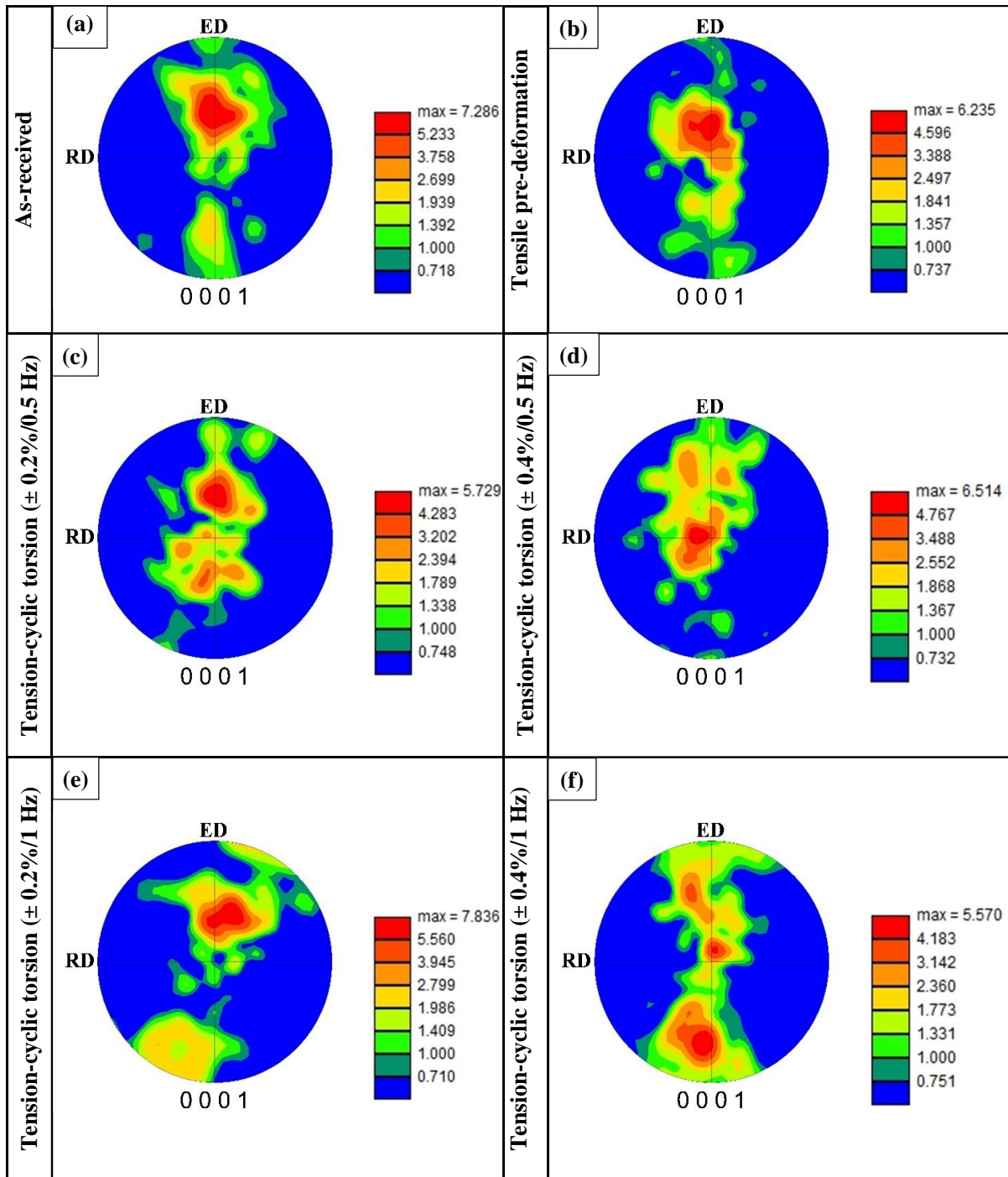
***Figure 5.16.*** *Pole figure maps of the as-received material (a); after 1% monotonic tension (b); and monotonic tension with cyclic torsion of strain amplitudes equal to ±0.2% (c, e) and ±0.4% (d, f) at frequencies equal to 0.5 Hz (c, d) and 1 Hz (e, f).*

## 5.4 Concluding remarks

Presented in this chapter, an experimental approach was performed to investigate the effect of monotonic tension and combined monotonic tension-cyclic torsion on the pure titanium behaviour using the single specimen method. The 0.01% plastic offset strain was adopted as yield definition. Such approach was found to be suitable for sequential probing paths during the

yield surface determination. The initial yield surface and its evolution reflecting the pre-deformation history were identified. The main conclusions were drawn as follows:

- Under complex stress states (tension + cyclic torsion), restructurization of the material is responsible for significant decrease of the normal stress. This reduction of the axial stress becomes more dominant with an increase of torsion strain amplitude and frequency.

- The initial yield surface of the as-received titanium for the 0.01% and 0.005% offset strain exhibits anisotropic behaviour and shows clear dependence of yield surfaces on the chosen definition of yield. The manufacturing process of the material or the specimen machining may have introduced the initial anisotropy.

- The size of subsequent yield surfaces after pre-deformation of the material were reduced in all directions, except of that representing the tension. This indicates, that the introduction of plastic anisotropy caused by the complex loading leads to significant softening in the direction opposite to axial loading.

- CP-Ti yield surface after tensile pre-deformation in comparison to the initial yield surface exhibits kinematic hardening towards the applied pre-deformation direction, while the same material after pre-deformation due to monotonic tension assisted by cyclic torsion shows kinematic softening when compared to the yield surface determined after monotonic tension pre-deformation.

- The low fitting error values obtained for each yield surface after fitting the experimental yield points in the Szczepiński anisotropic yield criterion confirmed the accuracy and quality of the yield surface approximation.

- The analysis of Inverse Pole Figure (IPF) maps and (0001) pole figures reveals a good agreement with the yield response of the as-received and pre-deformed CP-Ti, as texture evolution and preferred grain orientation can be clearly observed in the material.

# Chapter 6

# Yield surface identification of CP-Cu

*In this chapter the results of tests for commercially pure copper (CP-Cu), which methodology is discussed in the Chapter 3, are presented. Basic mechanical properties of CP-Cu were characterized under tensile loading. Additionally, the mechanical response of CP-Cu under multiaxial stress states, involving combined tension and cyclic torsion, was systematically explored. The initial yield surface of the as-received material and subsequent yield surfaces after pre-deformation were experimentally determined. The collective insights from these studies illustrate that the evolution of yield surfaces in pure copper is intricately linked to processing history, and pre-strain conditions. These findings offer a deeper understanding for optimizing the mechanical performance of copper in various applications, particularly in the field of materials science and engineering.*

## 6.1 Introduction

Copper, a versatile and highly conductive material, serves as a fundamental element in various engineering and industrial applications due to its exceptional mechanical, thermal, and electrical properties. Its alloys, such as bronze and brass, further expand its utility by enhancing characteristics such as strength, corrosion resistance, and wear resistance [169,170]. Copper and its alloys are extensively used in such industrial sectors as electronics, electrical engineering, construction, automotive, and aerospace. The mechanical properties of copper, such as ductility, toughness, high thermal conductivity (400 W/m·K), high electrical conductivity ($5.8 \times 10^7$ S/m), and low electrical resistivity ($1.72 \times 10^{-8}$ Ω), make it indispensable for manufacturing of heat exchangers, electrical wires, printed circuit boards, and architectural elements [171]. However, understanding the mechanical behaviour of copper under different manufacturing conditions and loading situations is crucial for optimizing its performance and reliability in these applications.

The mechanical properties of copper are closely related to its purity, microstructure, and the presence of alloying elements. Pure copper exhibits excellent ductility and thermal conductivity, with a tensile strength usually ranging between 200 and 300 MPa and an elongation at break of up to 50% in annealed conditions [172,173]. Its yield strength is comparatively lower, approximately 70 MPa in pure, annealed form, but can be significantly enhanced through alloying and work-hardening [172,174]. For example, copper-zinc alloys (brass) provide improved strength and machinability, with yield strengths reaching up to 600 MPa, while copper-tin alloys (bronze) are favoured for their corrosion resistance and higher tensile strength, reaching up to 700 MPa [175–177].

Applications in the electrical industry demand high conductivity, which necessitates minimal alloying. In contrast, structural and mechanical applications prioritize strength and wear resistance, often achieved through alloying with elements like aluminium, titanium, silicon, or nickel [178–180]. The interplay of these properties underlines the need for a detailed understanding of the material's mechanical behaviour during various manufacturing processes.

Manufacturing techniques significantly influence the mechanical properties of copper and its alloys. Processes such as casting, forging, extrusion, rolling, and additive manufacturing introduce variations in grain size, texture, and residual stress, which affect yield strength and deformation behaviour [169,181]. Several studies have investigated the impact of pre-deformation and manufacturing techniques on the mechanical properties of copper and its alloys. Pre-deformation, such as cold rolling or tension, modify the microstructure of copper by inducing dislocations and work hardening.

- For example, Stepanov et al. [182] demonstrated the effect of cold rolling on the microstructure and mechanical properties of copper processed via equal channel angular pressing (ECAP). It reveals that cold rolling transforms the equiaxed grains formed during ECAP into a lamellar structure. This process enhances yield strength by 100 MPa due to reduced boundary spacing, aligning with the Hall-Petch relationship. Additionally, dynamic restoration increases high-angle boundary fractions, reflecting microstructural refinement and strengthening.

- Singh Sivam et al. [183] examined unidirectional rolling (UDR) and cross-rolling (CR) of pure copper, revealing distinct mechanical responses. UDR achieves higher tensile strength (324 MPa) and hardness (98.2 HV) compared to CR (310 MPa and 95.4 HV, respectively) at a true strain of 2.77. UDR induces elongated grains and higher stored energy (0.69 J/g), while CR forms equiaxed grains with reduced anisotropy and lower stored energy (0.54 J/g). These microstructural changes, driven by deformation modes, explain the variations in mechanical properties.

- Research by Pan et al. [184] revealed significant enhancement in mechanical properties of pure copper processed with low-angle dislocation boundaries (LADBs). Initial coarse-grained (CG) copper had a yield strength of 61 MPa, tensile strength of 231 MPa, and a fatigue endurance limit of 50 MPa (fatigue ratio 0.24). After LADBs introduction, dislocation-cell-structured (DC) copper exhibited a yield strength of 372 MPa, tensile strength of 374 MPa, and a fatigue endurance limit of 130 MPa (fatigue ratio 0.35). This improvement is attributed to nanoscale dislocation patterns, reducing surface roughening and enhancing cyclic loading resistance.

The study of yield strength and yield surface evolution in copper and its alloys has been an active area of research. This analysis of copper enables the design of components that can withstand multiaxial stresses encountered in practical applications, such as piping systems, automotive heat exchangers, and structural elements in buildings.

- Mair and Pugh [5] analysed thin-walled tubes of annealed copper pre-strained to values of 1.3%, 4.7%, and 8.5% in tension and 0.25%, 1.5%, and 3% in torsion. The results demonstrated yield locus expansions and cross-effects in both cases, such as tensile pre-strain increased torsional yield stress and torsional pre-strain increased yield stress in tension, contrary to expectations of isotropic hardening. The torsional pre-strain displayed a significant Bauschinger effect, with the magnitude increasing with the increase of the pre-strain level.

- Hecker [11] investigated yield surface evolution in annealed OFHC copper subjected to biaxial stress. Specimens pre-strained via axial tension and internal pressure showed significant yield surface distortions and directional anisotropy at small proof strain ($5\mu\varepsilon$) levels. Initial yield surface expanded and translated in the direction of pre-strain either in axial or circumferential pre-strain and, for biaxial pre-strains, distorted in the vicinity

of the loading point. Larger proof strains (2000με) mitigated these effects, resulting in isotropic expansion.

- Dietrich and Kowalewski [26] explored impact of pre-deformation on the yield surface of 99.9% pure copper subjected to pre-strains up to 5% and 15% due to tensile creep at 523K and monotonic tension at ambient temperature. The investigations revealed that initial yield surfaces align with the isotropic Huber-Mises criterion, but even minor plastic deformation introduces anisotropy. Pre-strain causes disproportionate increase in yield surface axes, with monotonic loading inducing greater shifts than creep due to elevated-temperature exposure. Additionally, the major-to-minor axis ratio of the yield surface decreases significantly with small plastic pre-strain and stabilizes for higher pre-deformation for both pre-strain cases. These findings emphasize the role of deformation mechanisms in altering yield surface geometry and material anisotropy. It can be attributed to stress-induced texture development and subgrain formation that extended creep life and yield strength, with secondary creep rates reduced significantly for pre-strained copper.

- Helling et al. [22] analysed multiaxial yield loci in 70:30 brass under torsional pre-strains ranging from 2.4% to 32%. Severe distortions and strong directional memory effects were observed, with yield surface translations up to 80% in comparison to initial yield locus. Microstructural findings showed pronounced twin boundary motion and strain-induced grain refinement, contributing to yield locus shifts. The study also investigated the effects of directionality on yield surface distortion, i.e., the orientation of the flattened region on the yield locus. Results indicate that yield surface distortion is largely independent of the pre-stress path but is significantly influenced by the pre-strain path, with the final pre-strain direction exerting a dominant effect. These results emphasized the sensitivity of brass to pre-strain direction and magnitude.

- A recent research conducted by Liu et al. [185] investigates the yielding behaviour of TU00 pure copper under strain rates ranging from $10^{-3}$/s to $10^{3}$/s using servo-hydraulic axial-torsional testing machine and combined tension-torsion Hopkinson bar system for dynamic tension-torsion tests. Yield stress increased significantly with the strain rate, from 120 MPa to 190 MPa, highlighting the strain rate dependency. The modified Hill yield criterion, incorporating strain rate effects, provided the most accurate predictions of yield points, while emphasizing that strain rate hardening is anisotropic with notable differences in tensile and torsional responses. A universal strain rate hardening model integrating the Johnson-Cook constitutive framework effectively described the work hardening behaviour of copper under complex stress states, aligning well with experimental data and demonstrating the limitations of uniaxial tensile tests alone for describing the strain hardening behaviour of TU00 copper.

Despite substantial progress has been made in understanding the mechanical behaviour and yield surface evolution of copper and its alloys, there are still several gaps remain. The effects of complex pre-deformation, and multiaxial stress loading on the yield surface evolution have not been fully studied. Therefore, the main aim of this chapter is to experimentally determine the initial yield surface of CP-Cu alloy, followed by subsequent yield surfaces reflecting plastic pre-deformation. The pre-deformation was introduced by monotonic tension and combined monotonic tension – cyclic torsion. By advancing the understanding of yield surface evolution, this research seeks to provide insights for optimizing copper's mechanical performance in various engineering applications.

## 6.2 Materials and Methods

The material investigated in this research was CP-Cu alloy. The copper bars used in this study were obtained in the M1E-Z4 condition, which corresponds to the Cu-ETP (M1E; E-Cu58) state. This state was achieved by annealing the copper bars at temperatures ranging from 350°C to 600°C. The experimental investigations conducted on CP-Cu involved three stages following the methodology discussed in Chapter 3:

- determination of the basic mechanical properties of CP-Cu;
- introduction of the following plastic pre-deformation in the specimens:
  - (a) monotonic tension up to 1% permanent strain at constant strain rate of 5 x $10^{-6}$ $s^{-1}$.
  - (b) combination of monotonic axial tension up to 1% permanent strain at constant strain rate of 5 x $10^{-6}$ $s^{-1}$, and torsion-reverse-torsion cyclic loading for two magnitudes of strain amplitude (±0.1% and ±0.2%) at two different values of frequency (0.5 Hz and 1 Hz), Figure 6.1.
- determination of the initial yield surface of the as-received material and yield surfaces after pre-deformation.

The selection of plastic pre-deformation values was based on the material properties and experimental limitations. A 1% axial pre-strain level was chosen based on the tensile stress-strain behaviour of CP-Cu and the operational range of the strain gauges, ensuring a consistent and limited plastic strain value. However, test involving combined monotonic tension and cyclic torsion showed that CP-Cu achieved very limited value of axial stress (15 MPa) at the 1% axial pre-strain value when the shear strain amplitude was ±0.4% at frequency of 0.5 Hz, as shown in Figure 6.2. This result demonstrates that the response of CP-Cu is significantly sensitive to the magnitude of cyclic shear strain amplitude. Consequently, in order to ensure stable pre-deformation during bi-directional stress loading, cyclic shear strain amplitudes of ±0.1% and ±0.2% at frequencies of 0.5 Hz and 1 Hz were selected, enabling the specimens to reach the target axial strain level of 1%.
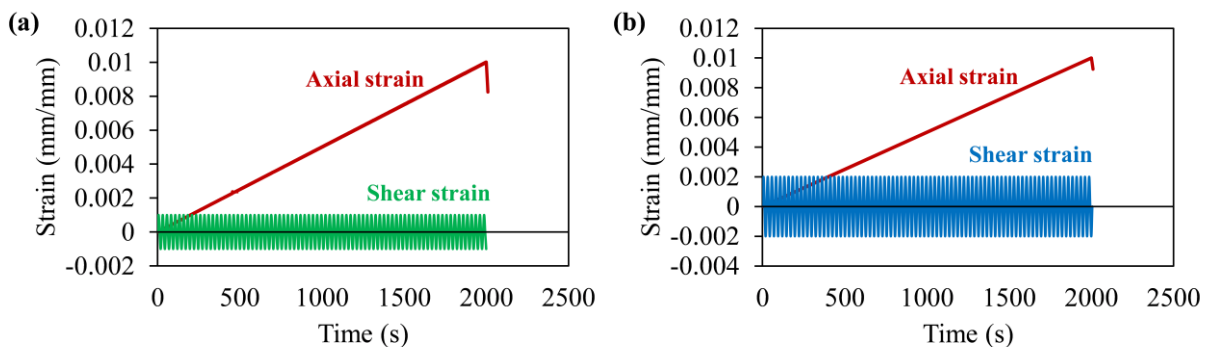


***Figure 6.1.*** *Strain controlled complex loading programme with monotonic axial tension and cyclic torsion with strain amplitudes of ±0.1% (a); and ±0.2% (b) at a frequency of 0.5 Hz.*
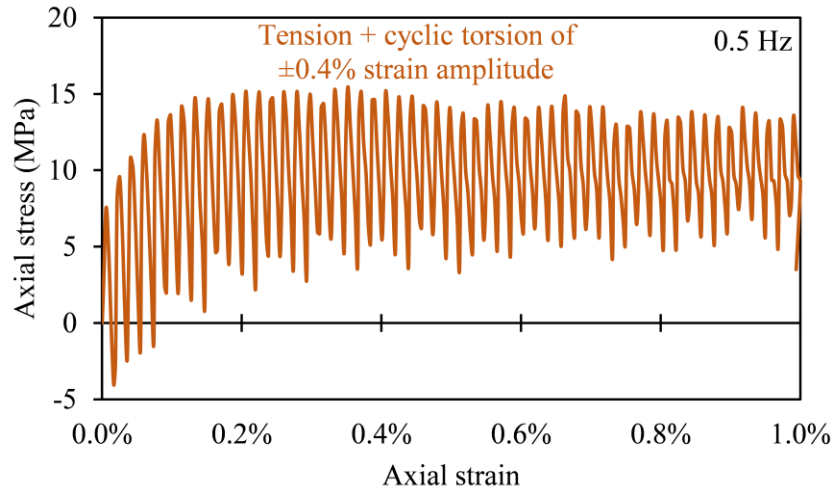
***Figure 6.2.*** *Response of CP-Cu in axial direction during combined tension-cyclic torsion.*

## 6.3 Results and discussion

### 6.3.1 Basic mechanical parameters of the material

Tensile tests were performed on solid tubular and thin-walled samples (discussed in Chapter 3) at room temperature at constant strain rate of 0.005 s^{-1}. Figure 6.3a presents the engineering stress-strain curve of CP-Cu and its tensile properties are listed in Table 6.1. The minor variations in tensile results shown in Figure 6.3a for both solid tubular and thin-walled specimens can be attributed to differences in specimen geometry, which may influence stress distribution and deformation characteristics. Comparing these findings with existing literature is challenging, as the mechanical properties of commercially pure copper are highly sensitive to factors such as grain size, purity, processing, and heat treatment conditions. For reference, previous studies [172,186] report yield strengths ranging from 70 to 300 MPa and tensile strengths between 150 and 450 MPa, depending on these variables. The yield and tensile strength values obtained in this study fall within these ranges, suggesting consistency with established trends while also emphasizing the inherent variability in mechanical properties due to processing conditions. These findings highlight the necessity of considering microstructural and processing differences when interpreting mechanical behaviour.
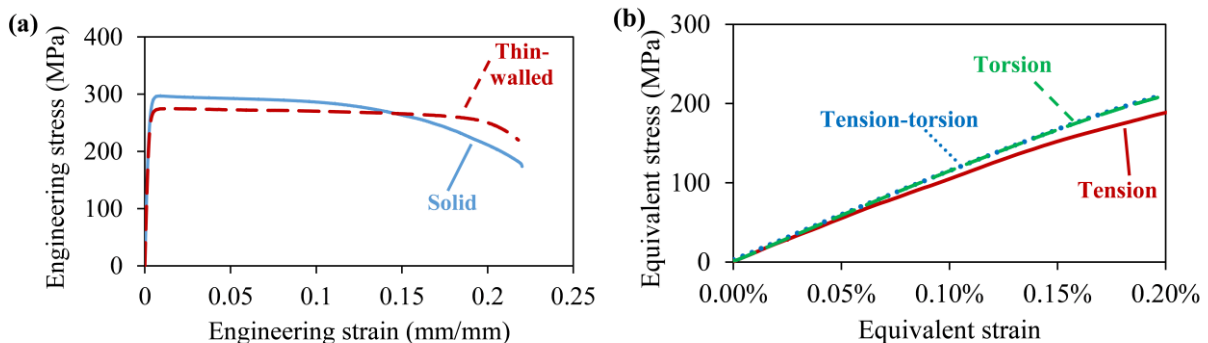


***Figure 6.3.*** *Tensile stress-strain characteristics of solid tubular and thin-walled tubular specimen of CP-Cu (a); Comparison of material characteristics of pure copper for different loading paths: simple tension; tension-torsion and pure torsion on thin-walled tubular specimen (b).*

***Table 6.1.*** *The mechanical properties of commercially pure copper.*

|  | 0.2% Yield strength [MPa] | Tensile strength [MPa] | Elongation [%] | Young's modulus [GPa] |
|---|---|---|---|---|
| Solid specimen | 286 (± 2) | 297 (± 1) | 22 (± 1) | 112 (± 1) |
| Tubular specimen | 264 (± 2) | 274 (± 1) | 21 (± 1) | 110 (± 1) |
| ASTM standard (C11000) [187] | 69-365 | 221-455 | 4-55 | - |

**6.3.2 Equivalent mechanical parameters of the material tested under combined loading**

Figure 6.3b presents the equivalent stress-strain curves comparing the material behaviour of thin-walled tubular specimens subjected to tension, tension-torsion, and pure torsion. The stress-strain curves for torsion and tension-torsion loading closely overlap, whereas the curve for tension loading deviates significantly from other two loadings, which indicates that the same material exhibits distinct mechanical responses under different loading conditions. These variations can likely be attributed to the initial anisotropy introduced during the manufacturing process, which affects how the material accommodates different stress states. This anisotropy influences the deformation mechanisms, leading to differences in stress distribution and strain accumulation under various loading paths. A more detailed analysis of this anisotropy will be provided in Section 6.3.4, focusing on the yield surface characterisation of the 'as-received' material. Understanding these differences is essential for accurately predicting material behaviour in complex loading scenarios.

**6.3.3 Results of the material under complex loading**

The influence of the cyclic torsion with varying strain amplitudes and frequencies on the monotonic tensile of CP-Cu was investigated. The primary objectives were to induce plastic pre-deformation and examine changes in tensile characteristics under torsion-reverse-torsion cycling. Figure 6.4a and Figure 6.4b demonstrate that the tensile characteristics of CP-Cu is significantly affected when tension is combined with cyclic torsion. A clear softening effect is observed, characterised by a decrease in axial stress as the cyclic strain amplitude increases. Additionally, an increase in cyclic torsion frequency further amplifies this decrease of the axial stress. For a cyclic torsion strain amplitude of ±0.1% at frequency of 0.5 Hz, the tensile stress at 0.2% axial strain decreased from 188 MPa to 163 MPa. When the cyclic torsion strain amplitude increased to ±0.2% at the same frequency, the decrease was more pronounced (80 MPa) at the same level of axial strain (Figure 6.4a). The effect became even more significant at higher frequency. For example, at ±0.2% cyclic torsion strain amplitude and 1 Hz frequency, the tensile stress dropped from 188 MPa to 64 MPa, representing a 66% reduction compared to tension-only condition at 0.2% axial strain (Figure 6.4b).
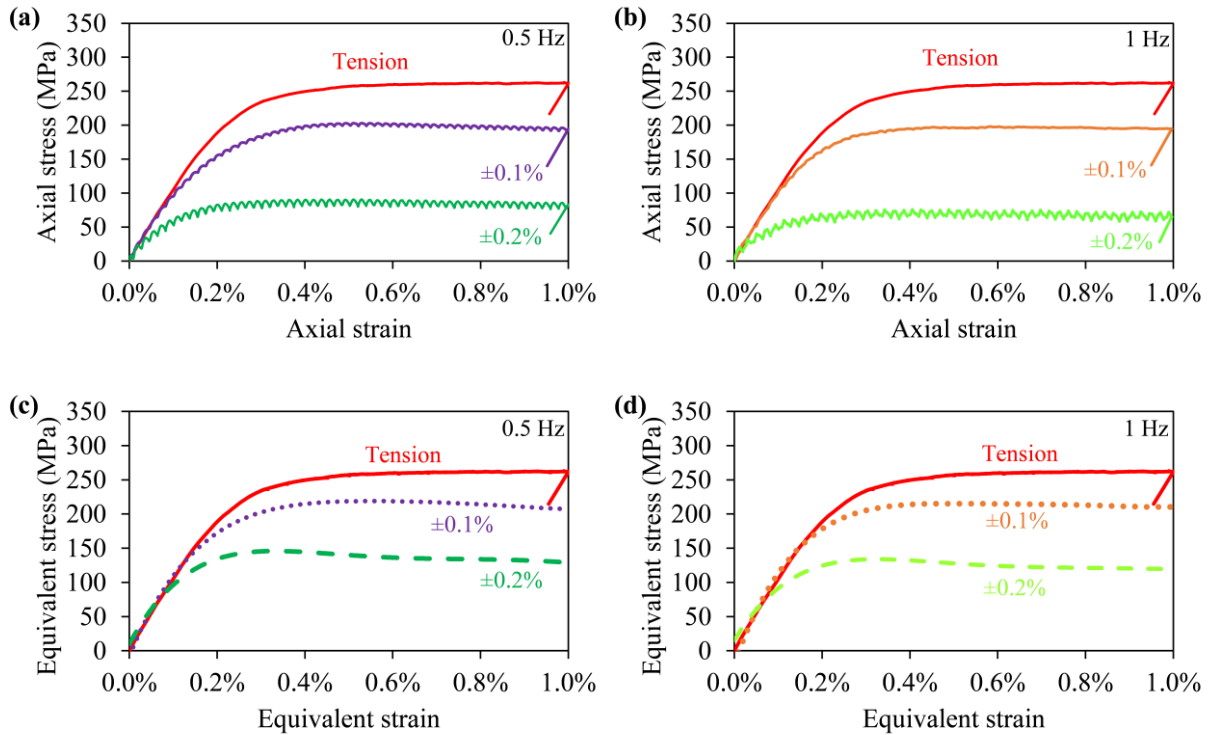
***Figure 6.4.*** *Comparison of standard tensile curve with tensile characteristics and curves representing equivalent stress captured during monotonic tension assisted by the torsion-reverse torsion cycles of strain amplitude equal to: ±0.1% and ±0.2% and frequency of: (a, c) 0.5 Hz and (b, d) 1 Hz.*

This decrease in tensile stress is consistent with the influence of shear stress introduced during cyclic torsion. To better understand the effect of shear stress and evaluate the equivalent stress under the three loading scenarios, Figure 6.4c and Figure 6.4d present the equivalent stress-strain curves. These curves provide a comprehensive representation of the material's response under combined tension and torsion. The equivalent stress-strain curves clearly demonstrate a pronounced softening effect in CP-Cu as the cyclic torsional strain amplitude increases. This trend aligns with the reduction in axial stress observed in Figure 6.4a and Figure 6.4b, suggesting that shear stress significantly alters the material's behaviour. The progressive reduction in equivalent stress at higher strain amplitudes highlights the combined effects of axial and torsional deformation, where shear stress introduces additional dislocation motion, enhancing plastic flow and reducing the material's load-bearing capacity.

The observed trend of tensile stress decrease with increasing cyclic torsion is further illustrated in Figure 6.5 for 0.5% axial strain, evaluated across different cyclic torsion strain amplitudes and frequencies. Notably, the case of 0% cyclic torsion strain amplitude corresponds to monotonic tension, serving as a baseline (Figure 6.5a). The results clearly demonstrate a significant reduction in tensile stress with increasing cyclic torsion strain amplitude. In contrast, the impact of increasing cyclic torsion frequency on tensile stress is comparatively less pronounced during combined loading (Figure 6.5b). This suggests that the amplitude of shear strain plays a dominant role in altering the stress state of copper by introducing additional shear deformation and facilitating plastic flow, whereas the role of frequency is primarily to modulate the rate at which these effects accumulate. The softening effect was also observed in CP-Ti with the increase of cyclic torsion strain amplitude and frequency during combined tension-torsion,

as explained in Chapter 5. These results indicate that the combination of cyclic torsion and tension leads to significant material softening, likely due to the accumulation of dislocation interactions and the microstructural evolution under complex loading. The severity of the softening effect increases with both strain amplitude and frequency, emphasizing the need to account for such interactions when predicting the mechanical performance of CP-Cu in applications involving combined loading conditions.
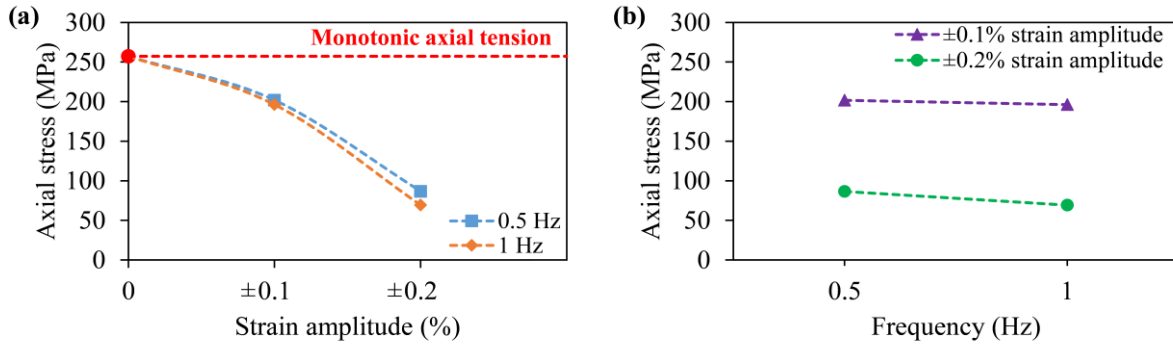


***Figure 6.5.*** *Variation of the tensile stress corresponding to the 0.5% axial strain value, in response to combined monotonic tension and cyclic torsion of strain amplitude equal to: ±0.1% and ±0.2% (a) and frequency of: 0.5 Hz and 1 Hz (b).*

### 6.3.4 Yield surface of pure copper in the as-received state

The yield points defining the initial yield surface of commercially pure copper were determined using a loading-unloading method in various strain directions (axial and shear) via the specified offset strain approach. Figure 6.6 illustrates the response of CP-Cu in a biaxial stress plane under the strain-controlled loading program detailed in Chapter 3. The loading and unloading paths show negligible deviation from linearity across all directions, indicating minimal plastic deformation during the probing of initial yield surface. The total plastic strain observed was 0.02%, and the Poisson's ratio for all evaluated directions was consistently nearly 0.3, suggesting uniform elastic behaviour.

Figure 6.7 presents the variation of the effective Young's modulus for the as-received CP-Cu under plane stress state across different directions. The Young's modulus in the axial tension direction (0 and 360) was found to be the lowest, while in other direction, it varied slightly, with differences of 4-5 GPa. This variation highlights the presence of texture in the material, even in its as-received state. Such texture, resulting from manufacturing processes, induces elastic anisotropy, which influences the mechanical response in different directions.

To accurately account for this anisotropy in estimating limited plastic strain (0.02%) during biaxial probing, direction-specific effective Young's modulus values were applied as outlined in Chapter 5. The observed directional differences align with the anisotropic nature of commercially pure metals, which often exhibit crystallographic textures due to their processing history [163]. The slight differences in Young's modulus alone cannot fully explain the initial anisotropy evident in the as-received specimen. This highlights the necessity of considering additional factors, such as yield surfaces, residual stresses and microstructural heterogeneities, to fully characterise the anisotropic behaviour of CP-Cu.
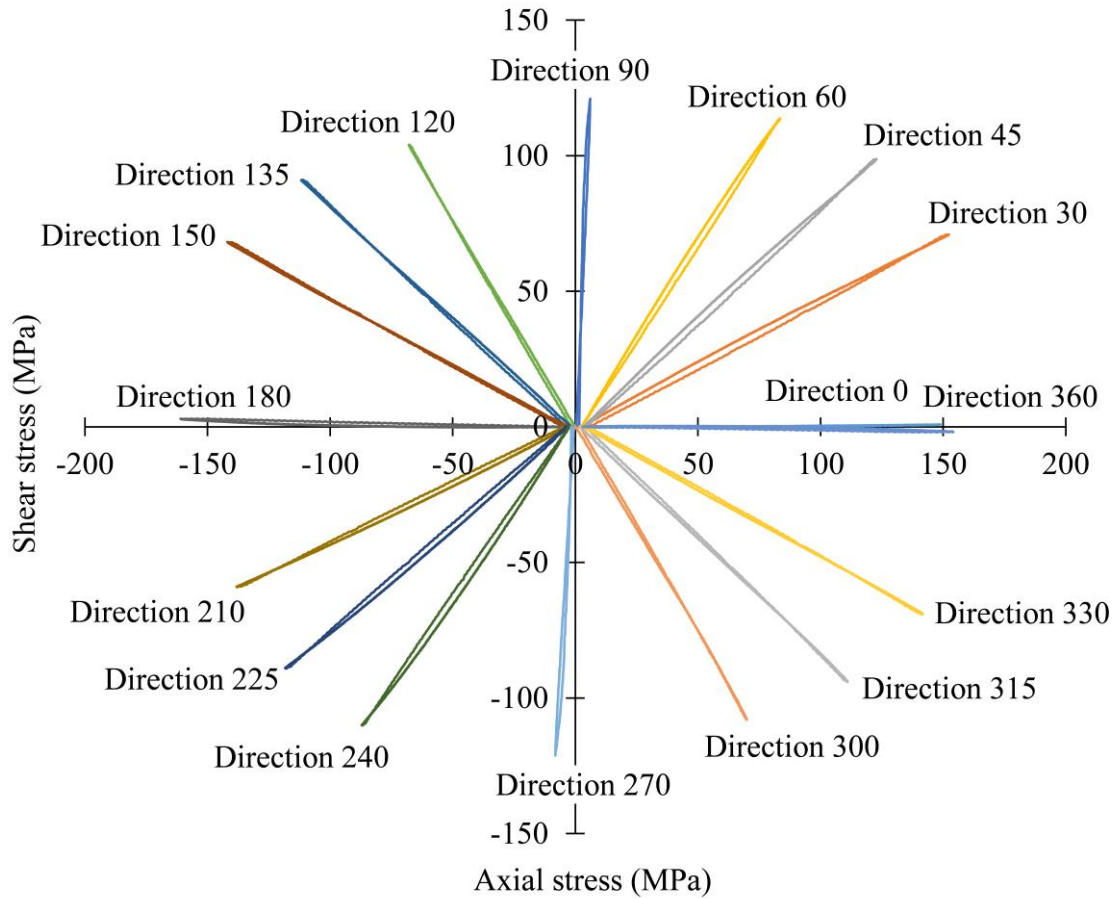
**Figure 6.6.** *Stress responses to the strain-controlled loading program used for determination of the initial yield surface of CP-Cu.*
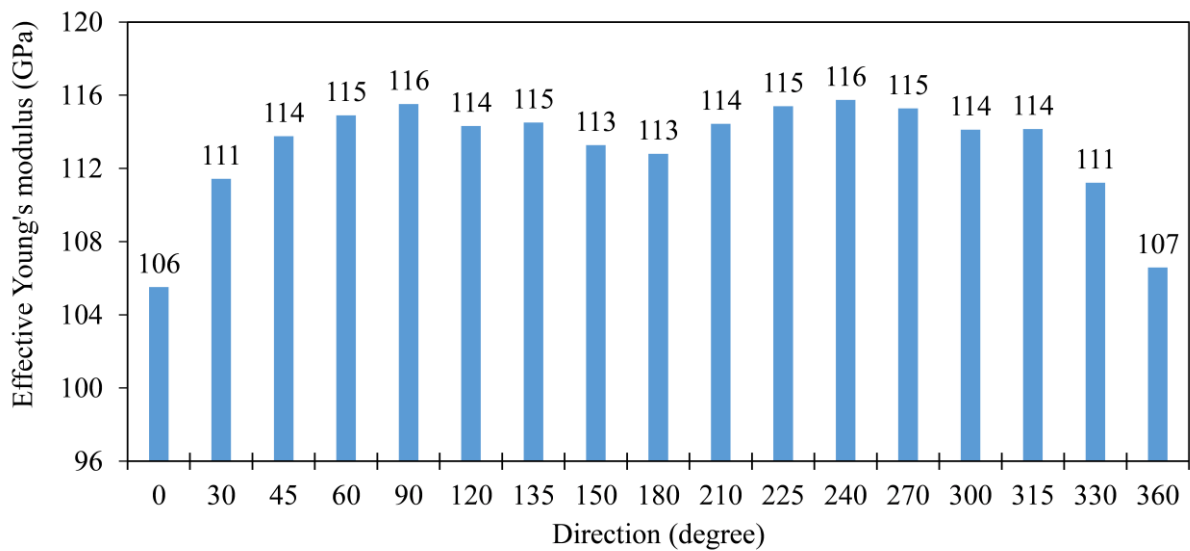


**Figure 6.7.** *Variation of the effective Young's modulus in different loading directions in the biaxial strain space for CP-Cu.*

The yield surfaces of the pure copper in the as-received state were determined using a sequential loading procedure at offset strain values of 0.01% and 0.005%, as shown in Figure 6.8a. These yield surfaces demonstrate a clear dependence on the chosen yield definition. After experimentally determining the yield points in various directions, ellipses were fitted using coefficients (A, B, C, D, and F) calculated via the least squares evaluation method, as detailed in Chapter 4. The primary parameters of these ellipses are summarized in Table 6.2, indicating that the centre of the yield surface is nearly aligned with the origin (0, 0) of the biaxial stress plane, with negligible rotation.
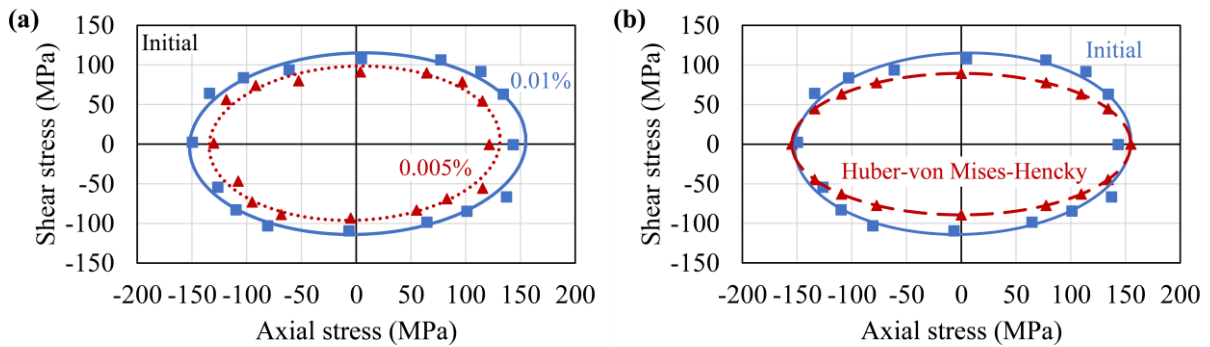


***Figure 6.8.** Yield surface of CP-Cu in the as-received state determined by least square fitting method of yield points (square and triangular points) obtained using a sequential loading technique for two values of plastic offset strain, 0.005% (dotted red line) and 0.01% (continuous blue line) (a); comparison of the initial yield surface (0.01% offset strain) of the CP-Cu (continuous blue line) with the yield surface assuming isotropic material (dashed red line) (b).*

Despite this alignment, some degree of initial anisotropy was evident, as the axis ratios of the yield surfaces were 1.34 and 1.37—significantly lower than the isotropic value of 1.73 predicted by the von Mises-Huber yield criterion. This deviation highlights the anisotropic behaviour of the as-received material.

To further investigate the material's initial anisotropy, the yield surface of CP-Cu for 0.01% offset strain was compared with the isotropic yield surface, anchored by the yield point in tension (direction 0). Figure 6.8b illustrates this comparison, showing that the axial yield stress of the as-received CP-Cu aligns with the isotropic yield surface, while noticeable deviations occur in the shear stress direction. This discrepancy confirms the presence of initial anisotropy in the as-received material.

The observed initial anisotropy is attributed to distinct hardening behaviour in shear strength, which likely results from the manufacturing processes applied to the material, such as the conversion of a solid specimen into a thin-walled tubular geometry or specific production methods used during material preparation. These processes induce microstructural variations, residual stresses, and texture development, which collectively contribute to the anisotropic response of CP-Cu.

*Table 6.2. Five ellipse parameters that define the initial yield surface for CP-Cu.*

| Yield definition | Centre $(x_0, y_0)$ [MPa] | Rotation angle $(\emptyset)$ [Radian] | Semi-axes $(a, b)$ [MPa] | Axis ratio $(^a/_b)$ |
|---|---|---|---|---|
| 0.01% offset strain | 1.36, 0.60 | 0.07 | 153.78, 114.44 | 1.34 |
| 0.005% offset strain | -1.45, 1.26 | 0.08 | 133.09, 97.17 | 1.37 |

### 6.3.5 Yield surface of pure copper in the pre-deformed state

The influence of monotonic tension and combined monotonic tension-cyclic torsion pre-deformation on the mechanical parameters of commercially pure copper was investigated by analysing the evolution of the initial yield surface. All pre-deformation experiments were conducted until the specimens reached an axial strain of 1%. Subsequently, the yield surfaces of the pre-deformed specimens were determined using the same 0.01% offset strain methodology as applied to the as-received material.
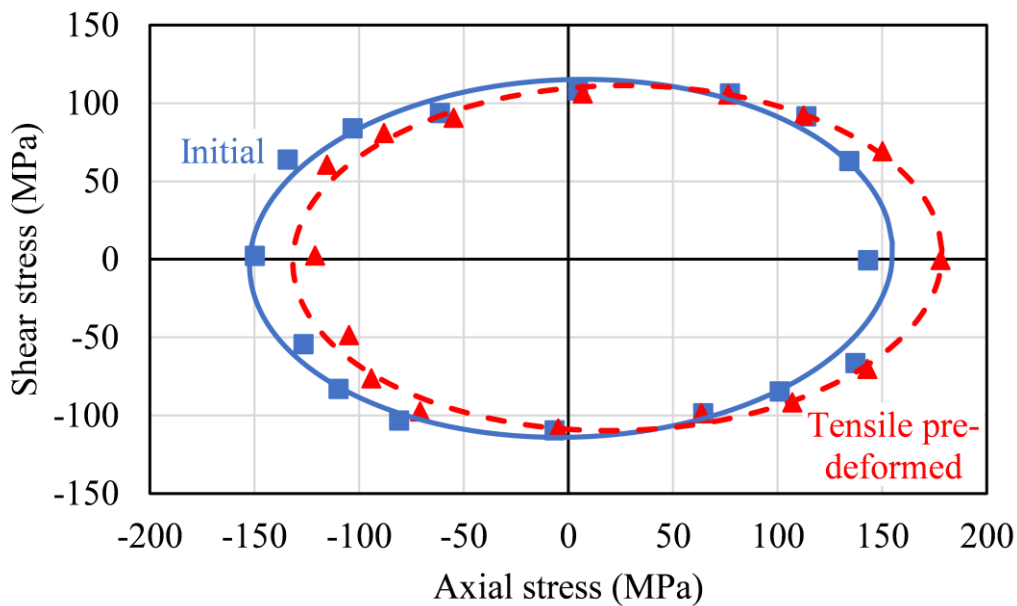


*Figure 6.9. Comparison of the yield surface for pure copper after tensile pre-deformation to the initial yield surface. Both were obtained at 0.01% offset strain.*

Figure 6.9 illustrates the yield surface for CP-Cu after 1% tensile pre-deformation compared to the initial yield surface. While the overall shape of the yield surface remains similar to the initial one, a noticeable translation in the tensile direction is observed. This shift indicates that monotonic tensile deformation has induced kinematic hardening in the pre-strain direction. The increase in the tensile yield point is approximately 35 MPa, representing a 24% enhancement over the initial yield point. This kinematic hardening effect can be attributed to the accumulation of dislocations and rearrangement of microstructural features during tensile pre-deformation, which results in an increase in material resistance to further plastic deformation

in the pre-strain direction. The translation of the yield surface, rather than a uniform expansion, suggests that the material retains some degree of anisotropy following pre-deformation. This behaviour is consistent with the dislocation motion being predominantly oriented along the tensile direction, which reinforces the material's strength and shifts the yield surface correspondingly.

Figure 6.10 presents the yield surfaces of CP-Cu after pre-deformation caused by monotonic tension combined with torsion-reverse-torsion cyclic loading. These yield surfaces are compared with the initial yield surface of the as-received material (continuous line). The combined preloading induces anisotropic hardening or softening, depending on the torsional strain amplitude and frequency applied during pre-deformation.

For a torsional strain amplitude of ±0.1% at a frequency of 0.5 Hz, the tensile yield stress increases by approximately 46 MPa compared to the initial yield surface, while yield stresses in other directions remain largely unchanged (Figure 6.10a). A similar trend is observed when the frequency is increased to 1 Hz (Figure 6.10c), suggesting that low-amplitude cyclic torsion predominantly reinforces the material in the axial stress direction.

Conversely, for a torsional strain amplitude of ±0.2% at 0.5 Hz, the yield surface exhibits a reduction in the shear stress direction by 32-38 MPa, while axial stress values remain comparable to those of the initial yield surface (Figure 6.10b). Increasing the frequency to 1 Hz produces similar results, with a decrease in shear stress and negligible change in axial stress (Figure 6.10d). This indicates that higher torsional strain amplitudes primarily weaken the material in the shear direction without significantly affecting axial properties.
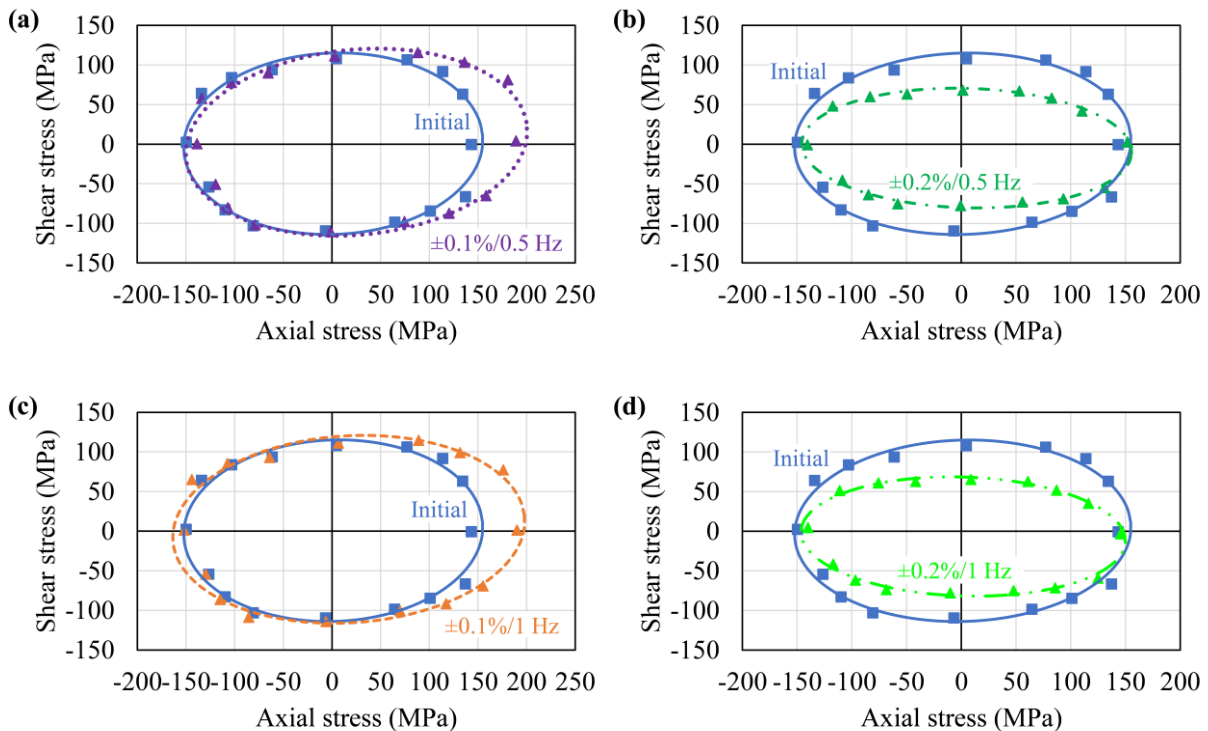


***Figure 6.10.*** *Comparison of the initial yield surface of CP-Cu to the yield surfaces of pre-deformed copper due to combined monotonic tension and cyclic torsion of strain amplitude equal to: ±0.1% and ±0.2% and frequency of: 0.5 Hz (a, b) and 1 Hz (c, d), respectively.*

When the frequency increases from 0.5 Hz to 1 Hz for either torsional strain amplitude (±0.1% or ±0.2%), the yield surface changes remain consistent, emphasizing that cyclic torsion strain amplitude has a more pronounced impact on yield surface evolution than frequency. Regardless of the pre-deformation conditions, the compressive yield stress values exhibit minimal variation compared to the initial state, indicating that compressive response is less sensitive to combined tension-cyclic torsion pre-deformation.

These findings highlight the complex interplay of strain amplitude, frequency, and stress direction in determination of the anisotropic evolution of the yield surface. The behaviour of CP-Cu under combined preloading reflects its unique response, which may be influenced by factors such as dislocation interactions, texture development, and strain path. Although similar studies have explored yield surface evolution in different materials, the variations in material properties, microstructures, and loading conditions make direct comparisons challenging. This highlights the importance of tailored investigations for specific materials and preloading scenarios to fully understand their mechanical responses.

**Table 6.3.** *The fitting errors for the yield surfaces in as-received state and after pre-deformation caused by monotonic tension; combined monotonic tension with cyclic torsion of strain amplitude equal to: ±0.1% and ±0.2% at frequency of: 0.5 Hz and 1 Hz.*

| As-received | Monotonic tension deformed | ±0.1% at 0.5 Hz deformed | ±0.2% at 0.5 Hz deformed | ±0.1% at 1 Hz deformed | ±0.2% at 1 Hz deformed |
|---|---|---|---|---|---|
| 1.95E-01 | 1.01E-01 | 1.58E-01 | 7.18E-02 | 1.63E-01 | 8.77E-02 |

The coefficients of the Szczepiński yield equation (A, B, C, D, F) were calculated using the least squares method to fit the experimental data and describe the elliptical yield surface of the tested material. This approach minimizes the sum of squares of the distances between the experimental yield points and the approximation curve, ensuring an optimal representation of the yield surface. Table 6.3 summarizes the fitting errors for each yield surface determined during the analysis. The fitting error values were minimal across all cases, demonstrating a high degree of accuracy in matching the experimental data with the fitted ellipses. These low errors validate the reliability and precision of the Szczepiński anisotropic yield criterion in approximating the yield behaviour of the material. The accuracy of the fitting not only confirms the robustness of the Szczepiński model but also highlights its ability to account for the material's anisotropy effectively. By closely representing the experimental data, the model captures the features of yield surface evolution, such as the influence of pre-deformation, stress directionality, and anisotropic hardening or softening effects. This agreement further highlights the suitability of the Szczepiński criterion for characterising the complex mechanical behaviour of the tested material under multiaxial stress states, providing a reliable foundation for predictive modelling and material design.
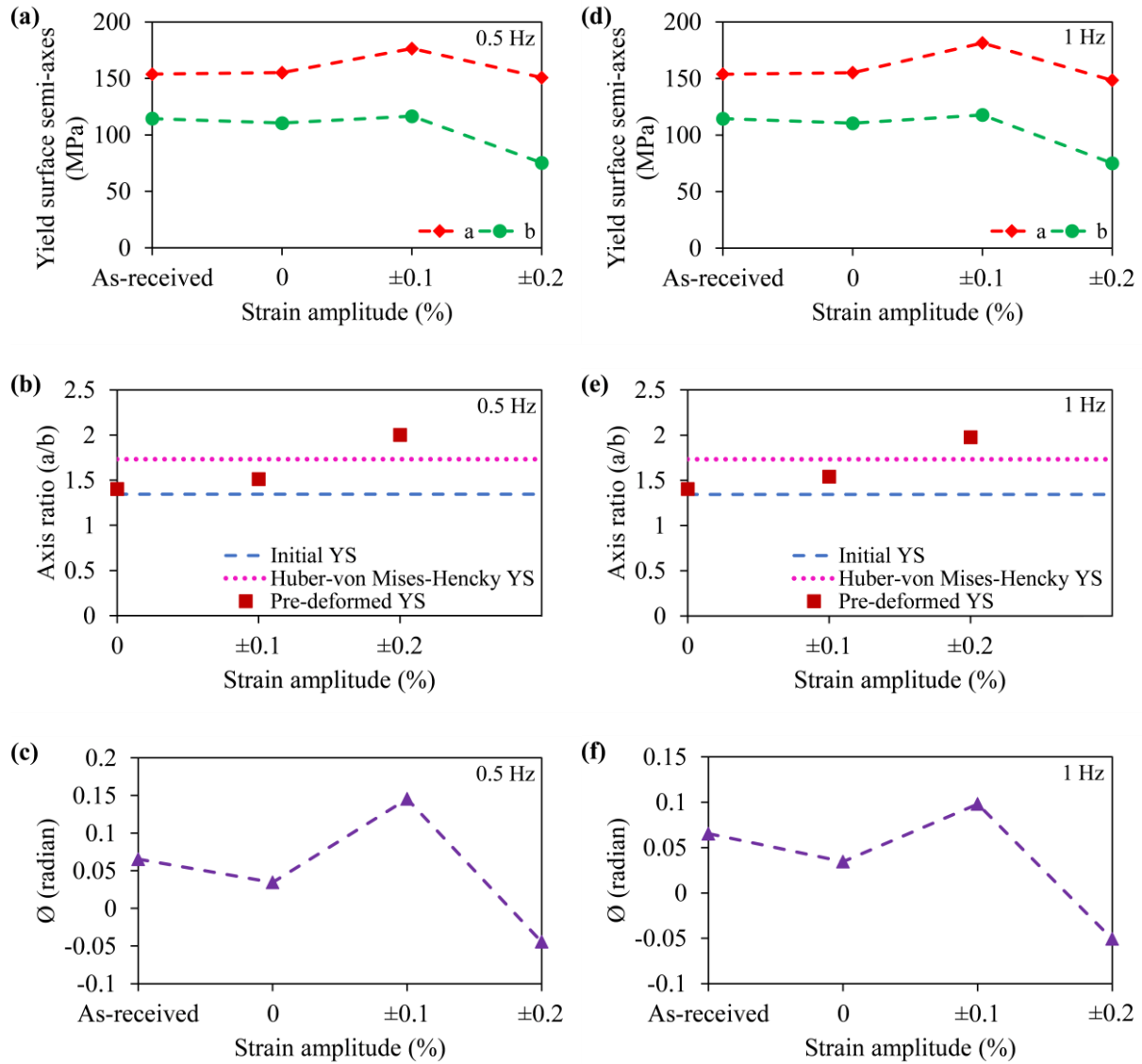
***Figure 6.11.*** *Variation of the yield surface parameters of CP-Cu due to pre-deformation caused by monotonic tension (0% strain amplitude); combined monotonic tension with cyclic torsion of strain amplitude equal to: ±0.1% and ±0.2% at frequency of: 0.5 Hz (a, b, c) and 1 Hz (d, e, f), respectively.*

Figure 6.11 highlights the evolution of the elliptical parameters representing the yield surface (YS) of CP-Cu in the pre-deformed state compared to the as-received state. Pre-deformation through monotonic tension, represented by 0% cyclic torsion strain amplitude, shows minimal deviations in the axis ratio relative to the initial yield surface (1.34). However, combined tension-cyclic torsion pre-deformation significantly alters the axis ratio, with higher values observed at both 0.5 Hz and 1 Hz cyclic torsion frequencies (Figure 6.11b and Figure 6.11e). The highest axis ratio, reaching 2, occurs after pre-deformation with a cyclic torsion strain amplitude of ±0.2% at 0.5 Hz, indicating substantial anisotropic behaviour.

The rotation angle (Ø) of the YS axes with respect to the $(\sigma_{xx}, \tau_{xy})$ coordinate system further reflects the influence of pre-deformation. As shown in Figure 6.11c and Figure 6.11f, monotonic tension pre-deformation results in near-zero rotation, signifying minimal distortion in the YS orientation. In contrast, combined tension-cyclic torsion pre-deformation induces

distinct rotations: positive angles (counter-clockwise) for a cyclic torsion strain amplitude of ±0.1% and negative angles (clockwise) as the strain amplitude increases to ±0.2% at both 0.5 Hz and 1 Hz frequencies. These rotations highlight the directional sensitivity of anisotropic behaviour induced by cyclic torsion and its dependence on strain amplitude.

Figure 6.12 further analyses the YS centre positions, emphasizing the role of back stress components in pre-deformed materials. In the as-received state, the YS centre aligns closely with the origin, reflecting minimal back stress. However, pre-deformation through monotonic tension and combined tension-cyclic torsion at ±0.1% strain amplitude shows a significant shift in the YS centre, indicating elevated back stress. In contrast, combined tension-cyclic torsion at higher strain amplitudes (±0.2%) results in minimal back stress, suggesting a redistribution of internal stresses. The observed back stress arises from dislocation interactions, including the accumulation of geometrically necessary dislocations (GNDs) and their ability to impede further dislocation motion. These interactions create localized high-stress regions that influence the material's plastic behaviour. The findings emphasize the interplay between dislocation structures, strain amplitude, and stress state in shaping the yield surface evolution of CP-Cu.
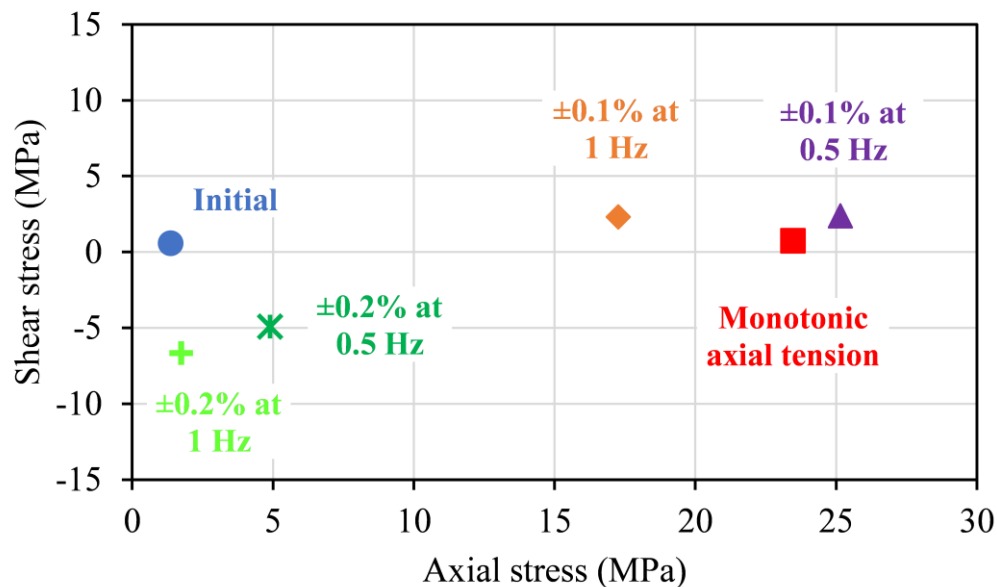


***Figure 6.12.** Analysis of the yield surface centre position of CP-Cu in the as-received state and after pre-deformation caused by monotonic tension; combined monotonic tension with cyclic torsion of strain amplitude equal to: ±0.1% and ±0.2% at frequency of: 0.5 Hz and 1 Hz.*

Figure 6.13 presents a comprehensive visualization of the evolution of the initial yield surface in the axial-shear stress space, derived from experimental data following material pre-deformation at frequencies of 0.5 Hz and 1 Hz. The results reveal distinct yield surface shapes and significant variations in their dimensions depending on the pre-deformation loading conditions. For monotonic tension combined with cyclic torsion at a strain amplitude of ±0.1%, the yield surfaces at both frequencies exhibit the largest dimensions among all loading conditions. This indicates that cyclic torsion, even at a low strain amplitude, induces pronounced hardening effects in the material.
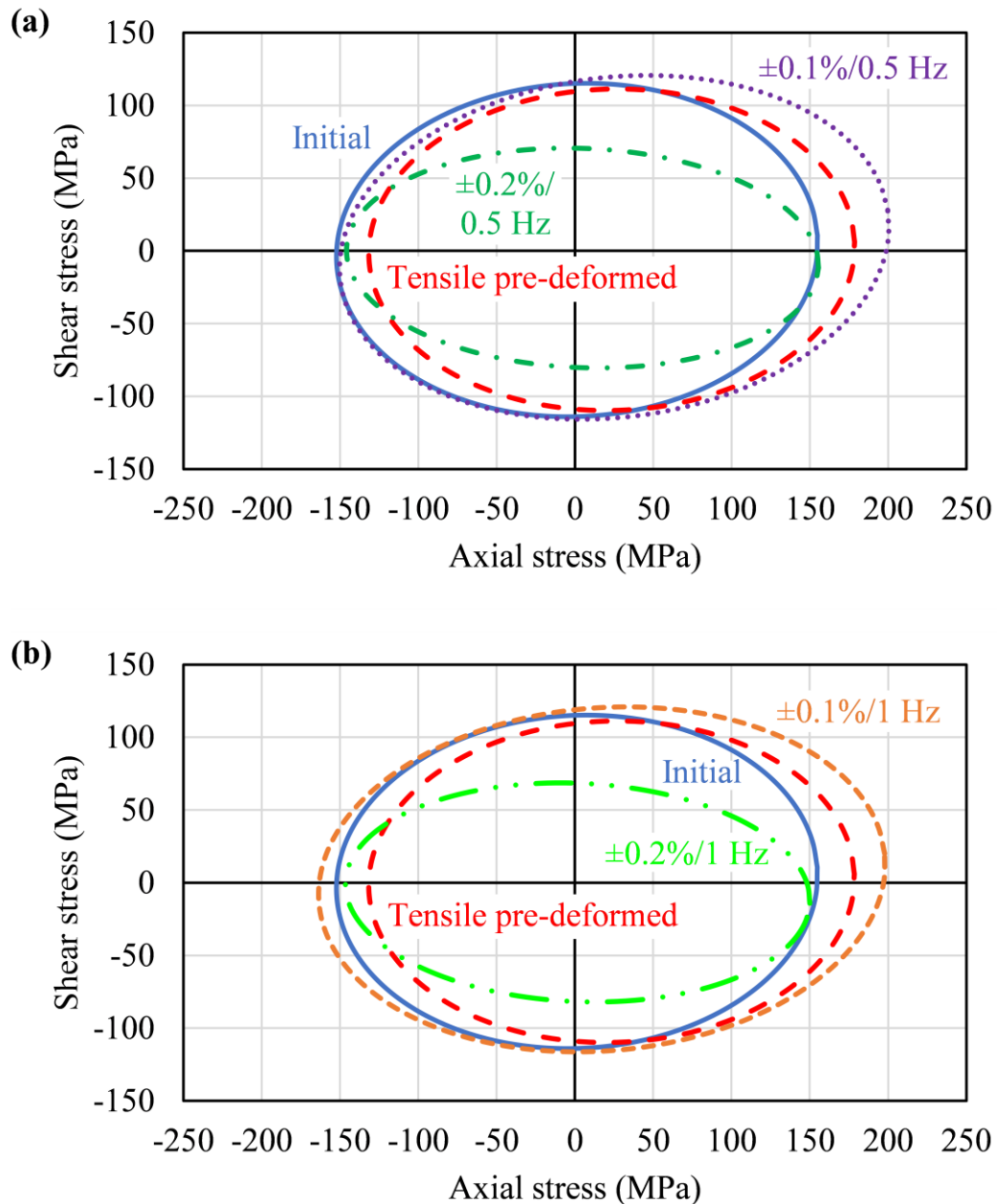
***Figure 6.13.*** *Evolution of the initial yield surface of CP-Cu due to pre-deformation caused by monotonic tension; monotonic tension assisted by cyclic torsion of strain amplitudes equal to: ±0.1% and ±0.2% at frequencies equal to 0.5 Hz (a) and 1 Hz (b).*

A detailed examination of the yield surfaces highlights two primary hardening mechanisms:

**Kinematic Hardening:** After monotonic tension pre-deformation, the yield surface shifts in the direction of axial pre-deformation. This translation indicates kinematic hardening, which reflects the material's increased resistance to plastic flow in the pre-deformation direction, likely due to the accumulation of dislocations and directional stress-induced anisotropy.

**Isotropic Hardening:** When cyclic torsion (±0.1% strain amplitude) is introduced during monotonic tensile pre-deformation, nearly an isotropic hardening is observed in comparison to

monotonic tensile pre-deformed yield surface. This is demonstrated by the expansion of the yield loci compared to those resulting from monotonic tension alone. The presence of a small cyclic torsion facilitates a more distributed microstructural rearrangement, leading to an overall increase in material strength across all stress directions. This effect is consistent across both frequencies (0.5 Hz and 1 Hz), emphasizing that strain amplitude, rather than frequency, is the dominant factor influencing isotropic hardening.

Furthermore, the analysis of yield surface shapes highlights a clear dependency on the preloading direction. The directional nature of pre-deformation, whether simply axial or combined with torsional components, governs the stress distribution and subsequent yield surface dimensions. Axial preloading emphasizes anisotropic hardening effects, while the addition of small torsional components promotes a more uniform strengthening across stress states considered. However, a larger torsional component during axial preloading led to anisotropic softening. These findings emphasize the complex relationships between preloading conditions, strain path, and resulting hardening/softening mechanisms. Understanding these effects is essential for accurately modelling the mechanical behaviour of CP-Cu and optimizing its performance in applications involving multiaxial loading and pre-deformed states.

## 6.4 Concluding remarks

The comprehensive investigation of the yield surface evolution for commercially pure copper under monotonic tension and combined tension-cyclic torsion loading has provided valuable insights into its mechanical response and hardening/softening behaviour. The key findings are summarized below:

- Pre-deformation, whether through monotonic tension or combined tension-cyclic torsion, significantly changes the shape, size, and position of the yield surface. Monotonic tension induces kinematic hardening, expressed by a translation of the yield surface in the pre-strain direction, while combined tension-cyclic torsion (±0.1% strain amplitude) introduces anisotropic hardening, in comparison to the initial yield loci. Higher torsional strain amplitude during pre-deformation (±0.2%) leads to anisotropic softening, especially in the shear stress direction, reflecting the complex interplay between loading direction and strain path.
- Cyclic torsion strain amplitude significantly impacts the material's mechanical response, especially for higher amplitudes (±0.2%) it causes pronounced softening effects, that can be attributed to increased dislocation interactions and microstructural rearrangements. Conversely, cyclic torsion frequency has a comparatively lesser impact, with yield surface evolution remaining consistent across frequencies (0.5 Hz and 1 Hz). This underscores strain amplitude as the dominant factor influencing the hardening or softening mechanisms in CP-Cu.
- The initial yield surface of the as-received copper for the 0.01% and 0.005% offset strain exhibits anisotropic behaviour, as evidenced by yield surface deviations from the isotropic Huber-von Mises-Hencky (HMH) criterion and shows clear dependence of yield surfaces on the chosen definition of yielding. This anisotropy may arise from manufacturing processes of the material or the specimen machining that induce crystallographic textures, residual stresses, and microstructural heterogeneities. Variations of the Young's modulus across loading directions further confirm elastic

anisotropy, indicating careful consideration of these factors when modelling material behaviour.

- The Szczepiński anisotropic yield criterion, fitted using the least squares method, effectively captured the experimental yield surfaces with minimal fitting errors. This model accurately represents anisotropic and isotropic hardening effects, providing a robust framework for predicting the mechanical response of CP-Cu under multiaxial stress states. Its reliability emphasizes the importance of advanced yield criteria in modelling of complex material behaviour.

# Chapter 7

# Yield surface identification of Ti-Cu bimetal

*This chapter explores the mechanical behaviour and microstructural changes in Ti-Cu bimetal under different loading conditions. Experiments were conducted in uniaxial and biaxial stress states to understand the material's response. The chapter begins with an overview of the basic mechanical properties of the material and progresses to its behaviour under combined loading conditions, including tension-torsion. Detailed insights into Ti-Cu bimetal's complex response to multiaxial stresses are provided. The initial yield surface of the as-received material was presented, followed by a study of how the yield surface evolves after pre-deformation. The chapter concludes with EBSD analysis, which reveals how pre-deformation affects the material's grain structure and texture. This study may provide potential implications on the physical mechanism accountable for plastic deformation and the evolution of yield surfaces in HCP/FCC bimetallic structures.*

## 7.1 Introduction

The main objective in the design of structural metals is to manufacture high-strength materials characterised by improved the yield and ultimate strengths. Both these mechanical parameters immensely rely on the primary mechanisms of plastic deformation and evolving microstructure under loading conditions taken into account. In recent years, bimetals or two-phased nano-layered metals have been extensively investigated due to tremendous opportunities to replace costly and rare metals used in the industrial applications [188]. Bimetals demonstrated higher strength and mechanical stability as compared to their component metals at extreme temperature and pressure environments [189]. This unique behaviour of bimetals cannot be explained by a simple volumetric average property of the component metals.

A demand for bimetal joints made of two dissimilar metals has increased in many industrial applications due to the advantages of bimetal's attributes. As a result, it was anticipated, that such set of joints would be very useful in a variety of applications, including those involving the transportation sectors (automobile, rail, and aviation) as well as smaller, more frequently used items like saucepans for example [190,191]. Such joint configurations can be fabricated using a conventional processing techniques, like a diffusion bonding [192], friction welding [193], explosive welding [194], and soldering [195]. The mechanical properties of bimetals are significantly affected by the choice of fabrication technology and component materials. Therefore, it is necessary to investigate the behaviour of the bimetal formed during the combining process of metal layers, not only in uni-axial stress state, but also, under complex stress states in order to simulate the conditions of real-world applications.

There have been numerous studies examining the mechanical properties of bimetal layered materials. Chen et al. [188] fabricated a bimetallic laminated steel structure (multi-interface) by using wire arc additive manufacturing (WAAM). Such structure exhibited an improved tensile property as compared to the single-material structures of 304 stainless steel (SS) and low-carbon steel (LCS). Specifically, the tensile strength along the building direction was found to

be 154% and 163% for 304 SS and LCS, respectively. The tensile strength in the direction perpendicular to that of building one was slightly higher, i.e. 173% and 184% for 304 SS and LCS, respectively. The improved tensile properties were attributed to the increased metal solidification nucleation rate and the formation of fine grains at both the low-carbon steel layer and interface, as well as the presence of martensite at the 304 stainless steel layer [188]. The fabrication of a single-interface bimetallic structure, combining LCS and SS316L, using WAAM technique, was characterised by enhanced yield strength (320 MPa) along the build direction as compared to the individual constituents (295 MPa and 280 MPa for LCS and SS316L, respectively). However, the tensile strength of the WAAM-bimetal (482 MPa) was found to be in between that of WAAM-LCS (435 MPa) and WAAM-SS316L (580 MPa) [196]. Nevertheless, both yield and tensile strengths of the WAAM- single interface bimetal were lower than those observed in various welded LCS-austenitic SS bimetals formed through gas tungsten arc, friction stir, and electron beam welding [197–199]. Heat treatment of the WAAM-bimetal led to a significant improvement of the yield strength (25%) and tensile strength (35%) as compared to the as-deposited state [196]. These improvements were attributed to the ferrite-to-ferrite-bainite transformation in LCS and ferrite-to-austenite transformation in SS316L [196,200]. A bimetallic structure fabricated by the SS316L and Inconel 625 using WAAM system had almost identical tensile strength (600 MPa) to that of the SS316L, however, lower than that of Inconel 625 (650 MPa) [201]. Steel-nickel bimetal fabricated using WAAM also exhibited improved tensile strength of 634 MPa in comparison to that of constituent metals (steel, 537 MPa and nickel, 455 MPa), due to formation of the interlocking microstructure at the interface as well as the strengthening of solid solutions from the mixing of Fe and Ni [202].

Copper alloy - Austenitic stainless steel (SS316L) bimetallic structure fabricated using laser powder bed fusion (L-PBF) processing exhibited an average mechanical properties between those of the Cu alloy and SS316L, Figure 7.1 [203]. A higher strength of the bimetal in comparison to the copper alloy was associated to the formation of strong interface bonded due to interconnected network of steel and copper across the interface. Similar results also have been reported for copper-maraging steel bimetal, fabricated by L-PBF technique [191]. A bimetallic structure consisting of Inconel 718 and copper alloy (GRCop-84), fabricated using the Laser Engineered Net Shaping (LENS[TM]) technique, exhibited shear and compressive yield strengths of 220 MPa and 232 MPa, respectively. These values represent significant increases of approximately 100% and 43%, respectively, when compared to the corresponding strengths of the GRCop-84 base material. In contrast, the shear and compressive yield strengths of monolithic Inconel 718 were equal to 653 MPa and 712 MPa, respectively. The enhanced strength of the bimetallic structure relative to GRCop-84 is primarily attributed to the improved interfacial bonding, which results from the formation of a nickel-copper single-phase solid solution within the metallurgical bonding region [204]. In the case of bimetallic material consisting of aluminium alloy (Al6061) and mild steel, which was metallurgically bonded together using rotary friction welding, the structure exhibited maximum tensile strength of 136 MPa, which was 65% of the Al6061 base material (209 MPa) [205]. Similarly, the friction-welded bimetal consisting of aluminium alloy (AA6063-T6) and stainless steel (SS 304L) had reduced yield and tensile strengths of 156 MPa and 195 MPa, respectively. The values correspond to approximately 63% and 72%, respectively, of the strengths of AA6063-T6 base material [206]. The friction-welded titanium alloy (Ti-6Al-4V) – LCS bimetal exhibited the tensile strength equivalent to 100% of the LCS base metal's strength under specific conditions of high friction pressure, forge pressure and friction time [207]. The aforementioned material

properties depend on the processing parameters. These parameters play a critical role in facilitating interatomic diffusion between the distinct materials, as a joining mechanism for achieving effective bonding. The formation of intermetallic compounds at the interface, which promotes localized brittle fracture, is a dominant factor for the observed lower joint strengths. Such compounds are well known for their potential to induce degradation of mechanical properties [207,208].

Bimetals fabricated at nanoscale multilayer metallic (NMM) compositions have demonstrated ultra-high strength in comparison to their bulk constituents, such as in Ag-Nb [209], Al-Ti [210], Cu-Nb [211], Mg-Nb [212], Cu-Ni [213], Ag-Fe and Ag-Ni [214]. In particular, the strength of nanoscale multi-layered bimetals is three-to-ten times greater than that of their coarse-layered counterparts with layer thicknesses ranging from 10 μm to 1000 μm. The strength of NMM bimetals increases initially as the layer thickness decreases to tens of nanometres, and reaches a maximum value at the critical layer thickness, following the Hall-Petch relationship [215,216]. However, as the layer thickness continues to decrease, the strength tends to reach a plateau or experiences softening, depending on the nature of the interfaces [217].
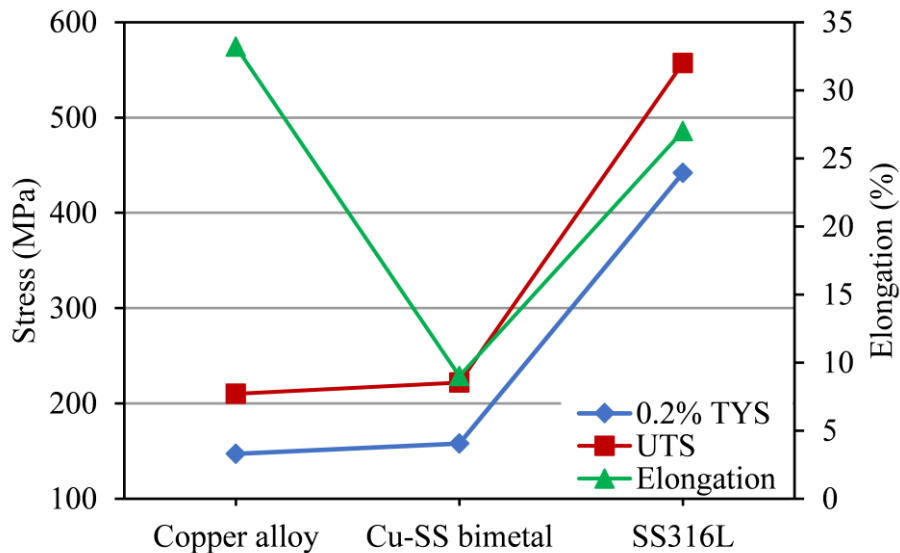


***Figure 7.1.*** *Comparison of mechanical properties of Cu alloy-SS316L bimetal with its constituent metals [203].*

It should be emphasized, that effect of plastic pre-deformation introduced through the uniaxial or complex loadings modes upon bimetallic structures remains a considerably unexplored domain. Till now, the primary focus of bimetal research has predominantly revolved around the optimization of its synthesis, either to take benefit on the distinctive properties of the constituent base materials or to selectively improve the overall properties of one of the base components. A recent investigation was carried out on the bimetallic aluminium – copper and steel – aluminium structures to describe the effect of plastic pre-straining, performed by the application of Equal Channel Angular Pressing-Drawing (ECAP-drawing). The results showed, that following four successive straining cycles (a cumulative 13.33% reduction in diameter) of ECAP-drawing for the Al-Cu bimetal led to the enhancement of yield strength from 198 MPa to 515 MPa. Correspondingly, the tensile strength increased from 302 MPa to 689 MPa [218]. In the case of steel-aluminium bimetal, these properties increased from 260 MPa to 465 MPa

and 370 MPa to 690 MPa, respectively, after two iterative strain cycles (a cumulative 10% reduction in diameter) [219]. Such significant increments in the material strengths were mainly attributed to the grain refinement of materials after each pass and segregation of dislocations at the grain boundaries [218].

In this chapter, a variation of mechanical properties of the as-received and plastic pre-deformed Ti-Cu bi-material was assessed. The yield surface approach was applied, since an evolution of the initial yield surface well illustrates the characteristics of plastic deformation. Numerous investigations have experimentally examined an evolution of subsequent yield surfaces for different single materials, such as Aluminium alloys [3,4,12,20,21,30–32,99,220–225], Magnesium alloys [94,96,145,226–228], Titanium [1], Copper [5,11,25,26,185,229], Brass [6,20,22,230], Steels [23,24,27,28,34,168,223,231,232] and Inconel 718 [98]. However, author is aware of only one paper, by R. Uscinowicz [233], that experimentally determined the yield surface of bimetallic structure (Al-Cu) and its evolution after uni-axial tensile plastic pre-strain. In this chapter, the yield surfaces of Ti-Cu bimetal in the as-received and after either monotonic uni-axial tension or simultaneous application of monotonic uni-axial tension – torsion - reverse torsion plastic pre-deformation, are presented.

There are four important reasons of the Ti-Cu bimetallic system investigations in this chapter.

(1) Ti and Cu together exhibit multifunctional physical properties as titanium has excellent corrosion resistance and highest strength-to-density ratio [234], whereas, copper is ductile, malleable and has a very high electric and thermal conductivity [235].

(2) Prior studies on bimetallic structures are mainly focused on the improvement of its synthesis process and uniaxial mechanical properties. However, there is still a gap of comprehensive investigation of these bimetals under complex stress state.

(3) To the author's knowledge, there are no such prior research available related to the yield surface identification of Ti-Cu bimetal and its evolution due to plastic pre-deformation under complex loading.

(4) Furthermore, apart from mechanical experiments, the EBSD measurements was performed to reveal the deformation mechanisms responsible for yield surface evolution. The combination of the mechanical tests and microstructural investigations on bimetallic structures is thus important as the material behaviour under complex loading could be somehow explained by the detailed observations.

## 7.2 Materials and Methods

As-received material in the form of bimetallic solid rod consisting of two dissimilar component materials of a 9.4 mm diameter commercially pure copper (CP-Cu) core and a 1.6 mm thick shell of commercially pure titanium (CP-Ti) was investigated in this research. Initial bimetallic (Ti-Cu) rod with a nominal diameter of 12.6 mm and a length of 6 m was obtained by hot-extrusion of copper rod in titanium shell. The Ti-Cu bimetallic rod was hydrostatically extruded at the temperature of 700°C, which allows for obtaining sufficiently high bonding strength without intermetallic compound at the interface. The bimetallic rod was not subjected to any heat treatment process after the extrusion. As reported in the literature [236,237], when the extrusion temperature was between 800°C and 900°C the formation of intermetallic compounds

were observed at the interface of Ti-Cu which resulted in the reduction of bonding strength. Additionally, structural degradation at the interface of Ti-Cu has been reported due to the formation of intermetallic compounds after short-term annealing at temperature range from 600°C to 900°C [238]. A scanning electron microscope (SEM) micrographs of the contact zone of Ti and Cu layers are shown in Figure 7.2. There was no variation in microstructure and bonding quality along the hoop direction of the bimetal rod as could be observed in Figure 7.2. The representative SEM images were presented for three locations marked I, II and III. It was observed, that there was a permanent connection of Ti and Cu metals without a transition layer and with no debonding nor significant differences in the joint area. Furthermore, chemical composition analysis was performed along the yellow line in area II to confirm the narrow joint area. As can be observed, there is no notable diffusion between titanium and copper since the reversible content of each element of almost 100% could be found. The similar observations were performed in several places of the bimetal rod and since there was no significant difference, only representative results were shown.
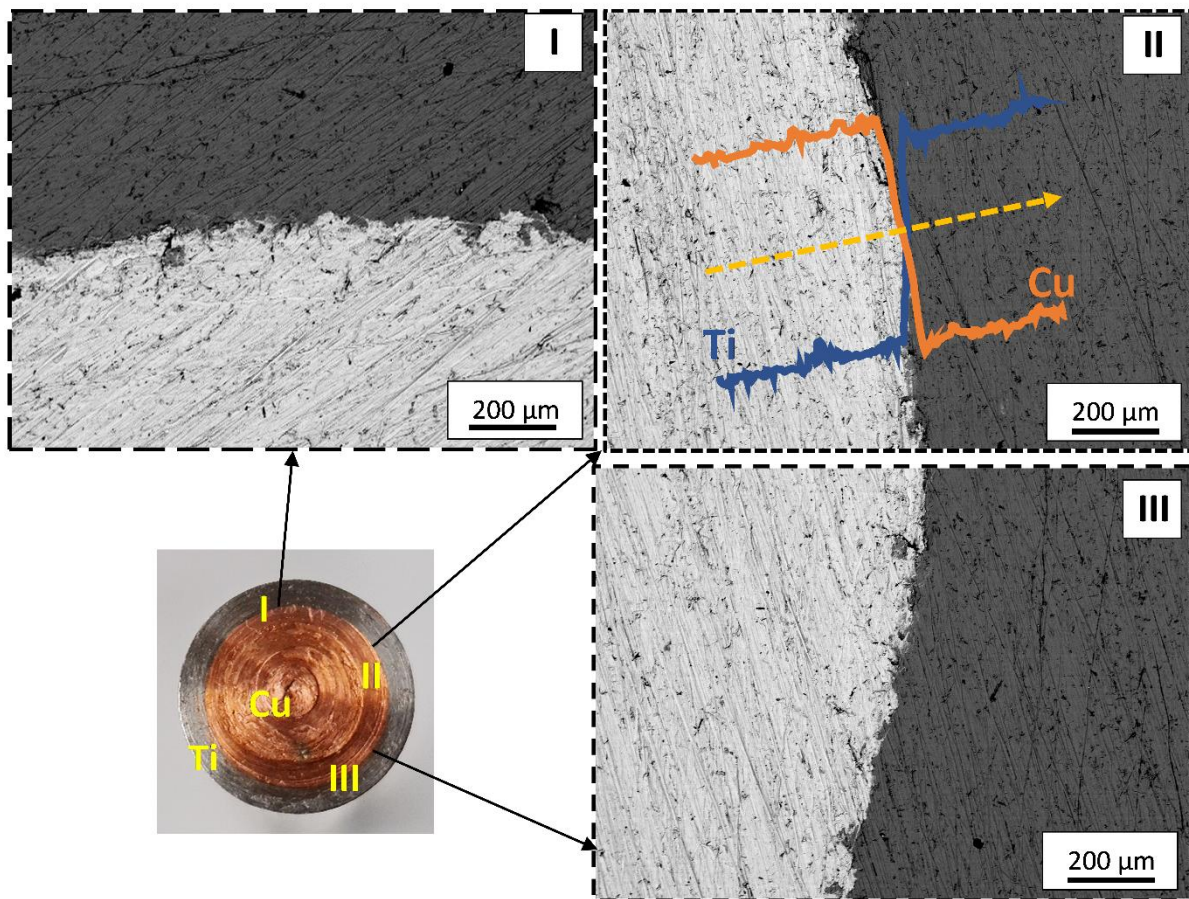


***Figure 7.2.*** *SEM micrographs for the bonding quality examination in the hoop direction of Ti-Cu bimetal at various points in the as-received state.*

Thin-walled tubular specimens were subjected to monotonic tensile loading as well as combination of monotonic tension – cyclic torsion. The main specimen dimensions were as following: gauge length of 16 mm, inner diameter of 8.4 mm, an outer diameter of 10.4 mm and an average thickness of 0.5 mm with variation of ±17 μm of each material in the gauge section, as shown in Figure 7.3. The specimens were machined from the bimetallic rod of 12.6 mm diameter. Vishay 120 Ω strain gages were bonded in the middle of the outer surface of

gauge section of the tubular specimens to measure and control axial, shear and hoop strain components. Due to torsional loading on the tubular specimens, the shear strain has a gradient across the thickness in the elastic range. It varies linearly from minimum value at the internal surface of the tube to the maximum one on its external surface. Despite the shear strain distribution is usually assumed to be uniform across the thickness if it is small, it should be noted that the external surface of the thin-walled tubular specimen represents a location of the most critical part. In order to mitigate the impact of strain gradient, the thickness of each metal in the gauge area was minimized to the maximum extent possible for conducting the experiment.
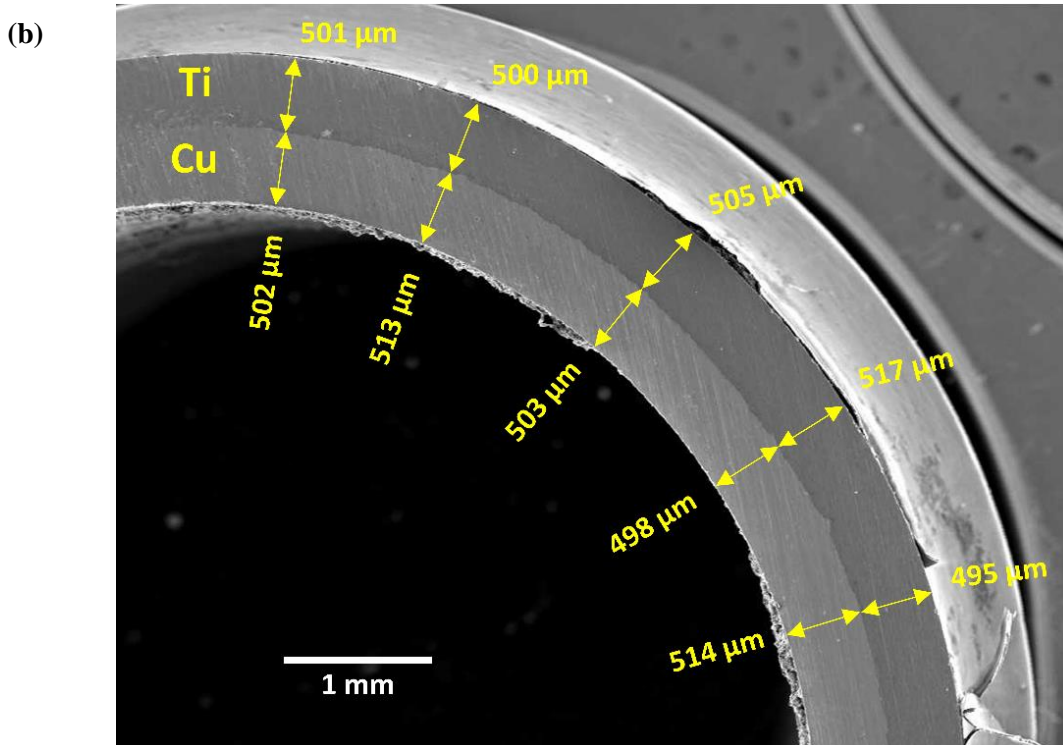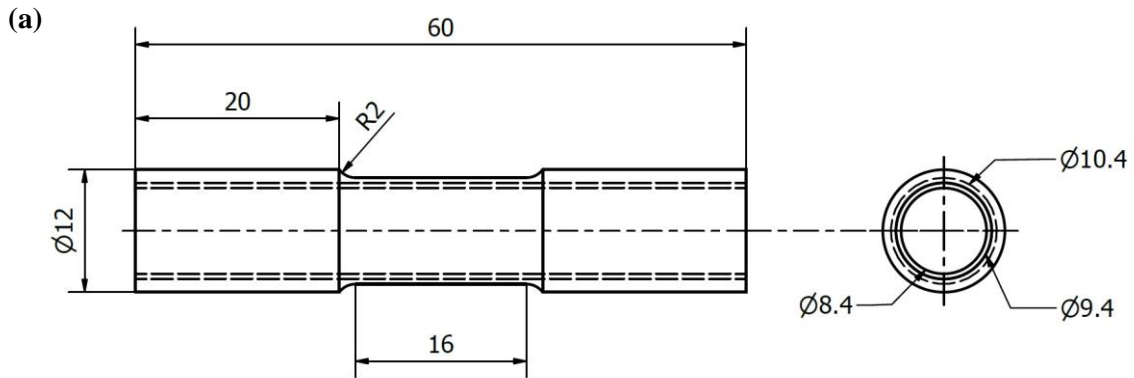


***Figure 7.3.*** *Engineering drawing of the thin-walled tubular specimen (All dimensions are in millimetres) (a); SEM micrograph with the thickness measurement of Ti and Cu at various points in the middle of gauge section of the thin-walled tubular specimen (b).*

The experimental investigations involved four stages following the methodology discussed in Chapter 3:

(1) determination of the basic mechanical properties of Ti-Cu bimetal;

(2) introduction of the following plastic pre-deformation in the specimens:

 (a) monotonic tension up to 1% permanent strain at constant strain rate of 5 x $10^{-6}$ $s^{-1}$.

 (b) combination of monotonic axial tension up to 1% permanent strain at constant strain rate of 5 x $10^{-6}$ $s^{-1}$, and torsion-reverse-torsion cyclic loading for two magnitudes of strain amplitude (±0.1% and ±0.15%) at two different values of frequency (0.5 Hz and 1 Hz), Figure 7.4.

(3) determination of the initial yield surface of the as-received material and yield surfaces of the pre-deformed material;

(4) determination of the microstructure and texture evolution after pre-deformation.
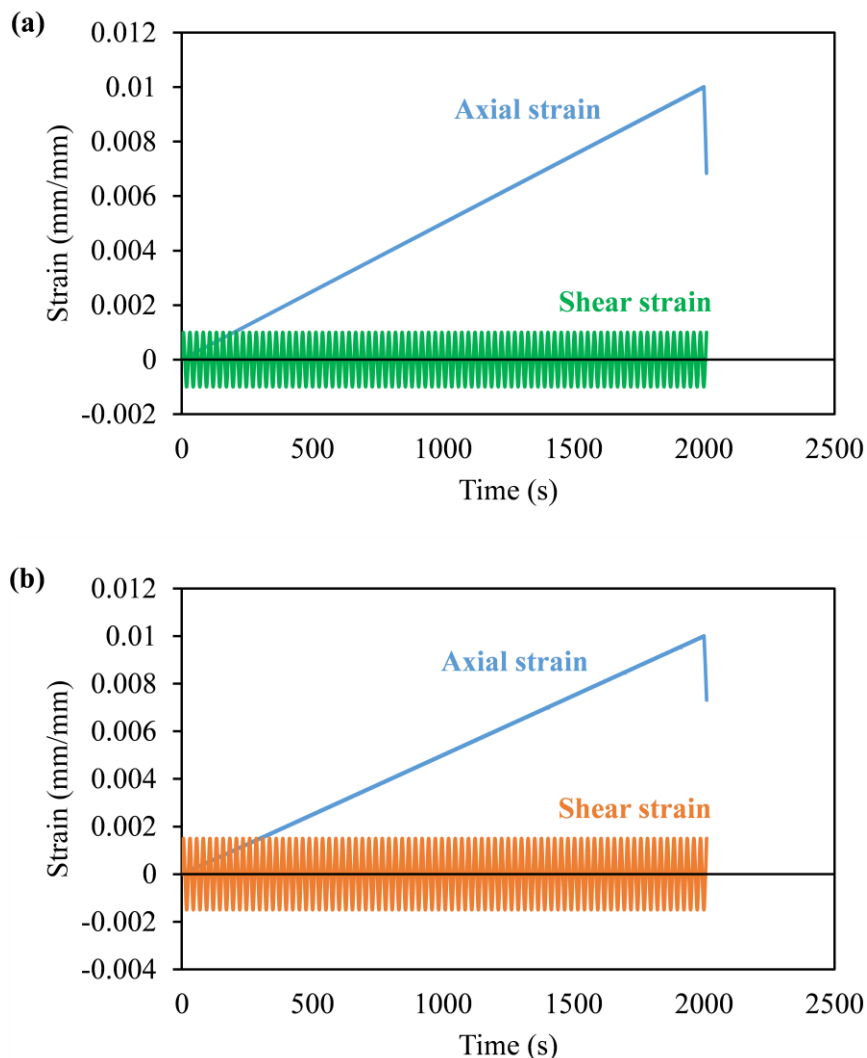


*Figure 7.4. Strain controlled complex loading programme with combined monotonic tension-cyclic torsion with strain amplitudes equal to ± 0.1% (a); and ± 0.15% (b) at a frequency of 0.5 Hz.*

The selection of pre-strain parameters was influenced by material characteristics and experimental constraints with the objective of ensuring controlled deformation of the specimens. The selection of a 1% axial pre-strain level was based on the tensile stress-strain characteristics of the Ti-Cu bimetal and the strain gauge's operational range to ensure a limited axial plastic pre-strain value. Thorough investigation of combined monotonic tension with cyclic torsion for different values of the shear strain amplitude, revealed that bimetal failed to get the desired axial strain level, reaching up to shear strain amplitude of ±0.4% (and ±0.8%) at frequency of 0.5 Hz (Figure 7.5). It shows that the interface of bimetal is very sensitive to the values of cyclic shear strain amplitude. Therefore, to introduce a stable pre-deformation level during the bi-directional stress loading conditions, the magnitude of cyclic shear strain amplitude was taken to be equal to ±0.1% and ±0.15% and frequency of 0.5 Hz and 1 Hz. Under these loading conditions axial deformation up to 1% could be successfully executed.
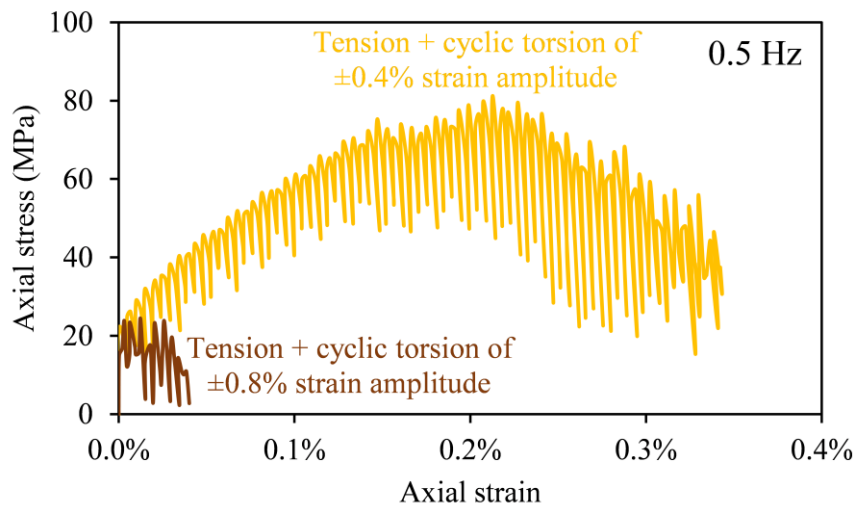


*Figure 7.5. Response of Ti-Cu bimetal in axial direction during monotonic tension assisted by the torsion-reverse torsion cycles of strain amplitude equal to: ±0.4% and ±0.8% and frequency of 0.5 Hz.*

## 7.3 Results and discussion

### 7.3.1 Basic mechanical parameters of the material

The basic mechanical properties governing the elastic and plastic properties of the Ti-Cu bimetal were determined using data captured from uniaxial monotonic tensile tests. The values obtained from these tests were extremely important in the experimental planning for pre-deformation processes and probing of yield surfaces. Tensile tests were performed on the Ti-Cu bimetal specimen, and its constituents' metals, namely titanium (Ti) and copper (Cu), independently. The tensile properties of the Ti-Cu bimetal, along with CP-Ti and CP-Cu, were determined on the basis of their respective stress-strain curves (Figure 7.6a) and they were listed in Table 7.1. The constituent metals undergo different heat treatment processes in comparison to the Ti-Cu bimetallic material. Data in Table 7.1 enables direct comparison with that of CP-Ti and CP-Cu, as reported in Chapters 5 and 6. Based on the tensile test results, some insightful parallels could be drawn for strength characteristics between the constituent materials and the bimetal. It became evident, that the bimetal's tensile yield and ultimate strengths fell within the spectrum defined by copper and titanium, each serving as reference materials to set the baseline

for strength characteristics within the bimetal. The yield strength of bimetal was about 43% higher and 6% lower than Cu and Ti, respectively. However, the ultimate strength was about 50% higher and 23% lower of them. This notable improvement in the strength of the bimetal was necessary in ensuring the mechanical reliability of the joint and was attributed to the accumulation of particles and elemental diffusion near the interface [204]. One can indicate however, that the ductility of bimetal was lower than its constituent metals. Similar results have been also reported for Al-Cu bimetallic joint processed using rolling after heating the metals [233].

***Table 7.1.*** *The mechanical properties of bimetal and its constituent metals.*

| Material | 0.2% Yield strength [MPa] | Tensile strength [MPa] | Elongation [%] | Young's modulus [GPa] |
|---|---|---|---|---|
| Bimetal (Ti-Cu) | 377 ($\pm$ 2) | 410 ($\pm$ 1) | 18 ($\pm$ 0) | 106 ($\pm$ 1) |
| Titanium | 400 ($\pm$ 3) | 531 ($\pm$ 1) | 37 ($\pm$ 1) | 100 ($\pm$ 1) |
| Copper | 264 ($\pm$ 2) | 274 ($\pm$ 1) | 21 ($\pm$ 1) | 110 ($\pm$ 1) |

Figure 7.7 shows the fractography of the Ti-Cu bimetal, CP-Ti and CP-Cu specimens, fractured during uniaxial tensile testing. Since titanium exhibited almost doubled elongation as copper (Figure 7.6a), the fracture behaviour of bimetal was different. It could be observed, that the thickness of the titanium part of the specimen is relatively uniform, while that for the copper varies due to the elongated neck observed in the axial direction, as shown in Figure 7.7a. One should mention, that both materials exhibit ductile behaviour (Figure 7.7b and Figure 7.7c) when the specimens of constituent metals are deformed separately. The fracture areas of both, titanium and copper, are characterised by dimples and micro-voids formed during plastic deformation. Because the bimetal consists of materials of different strength properties, the copper is starting to fracture much earlier than titanium. Such behaviour leads to the debonding of two metals since the hydrostatic extrusion process enables a bond which is able to withstand the shear of ~150MPa [238].

### 7.3.2 Equivalent mechanical parameters of the material tested under combined loading

The material characteristics were systematically compared to the Ti-Cu bimetal specimen, which was subjected to distinct loading conditions: uniaxial tension, tension-torsion, and pure torsion. The equivalent stress-strain curves in Figure 7.6b represent these results. All three curves in Figure 7.6b start at the origin, uniaxial tension and tension-torsion curves nearly coincide, whereas, pure torsion curve differs a little. Notably, the values of Young's modulus in various loading directions presented in Figure 7.11, underline that the lowest Young's modulus is associated with pure torsion loading. This observation signifies the intrinsic variability in material characteristics under different loading conditions for the Ti-Cu bimetal. These differences are presumably attributed to the initial anisotropy introduced into the material during the manufacturing process.
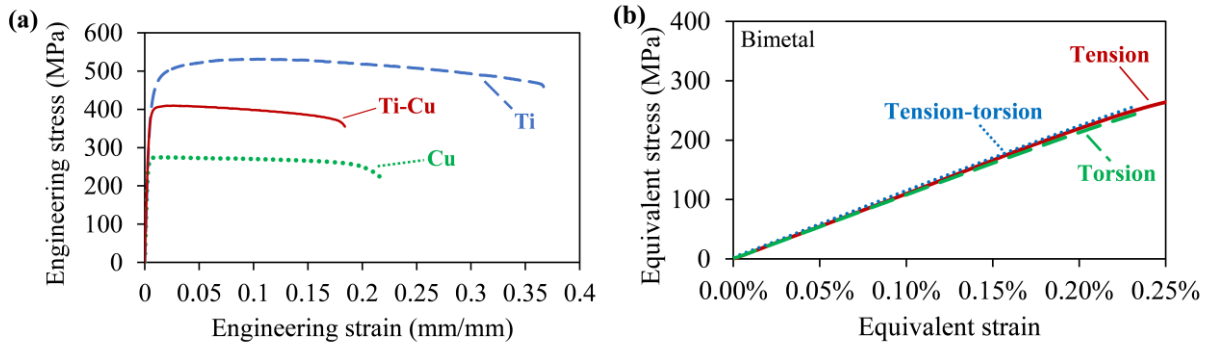
**Figure 7.6.** *Tensile stress-strain characteristics of Ti-Cu bimetal; and its constituent metals (a); Comparison of material characteristics of bimetal for different loading paths (b).*
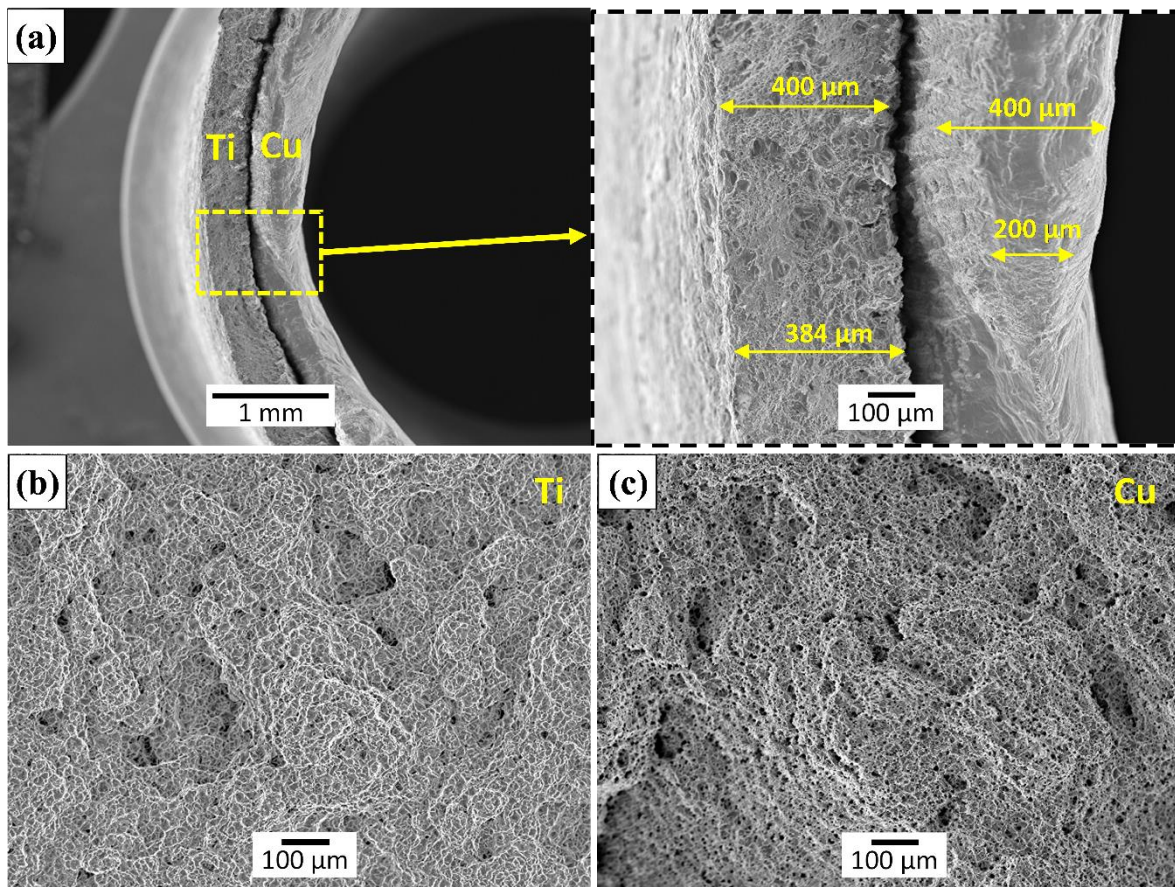


**Figure 7.7.** *SEM micrographs of the tensile deformed Ti-Cu bimetal with magnified view (a); the tensile deformed CP-Ti (b) and CP-Cu (c).*

### 7.3.3 Material behaviour under complex cyclic loading

The study examined how the Ti-Cu bimetal behaved under monotonic stress when subjected to cyclic torsion with a range of strain amplitudes and frequencies. Two primary objectives of these experimental investigations can be indicated: to induce plastic pre-deformation within the material, and to examine the changes in tensile characteristics resulting from the application of torsion-reverse-torsion cycles. As shown in Figure 7.8a and Figure 7.8b, a clear tendency of decreasing tensile stress can be observed when tension is combined with cyclic torsion of

increasing strain amplitude. Also, an increase of the frequency resulted in decrease of the tensile stress.

The corresponding equivalent stress-strain curves were shown in Figure 7.8c and Figure 7.8d in order to better explain the effect of shear stress on the equivalence of stress states among the three distinct loading scenarios. It is evident from the trajectories of the equivalent stress-strain curves, that bimetal demonstrate a softening effect as the amplitude of cyclic torsional strain increases.
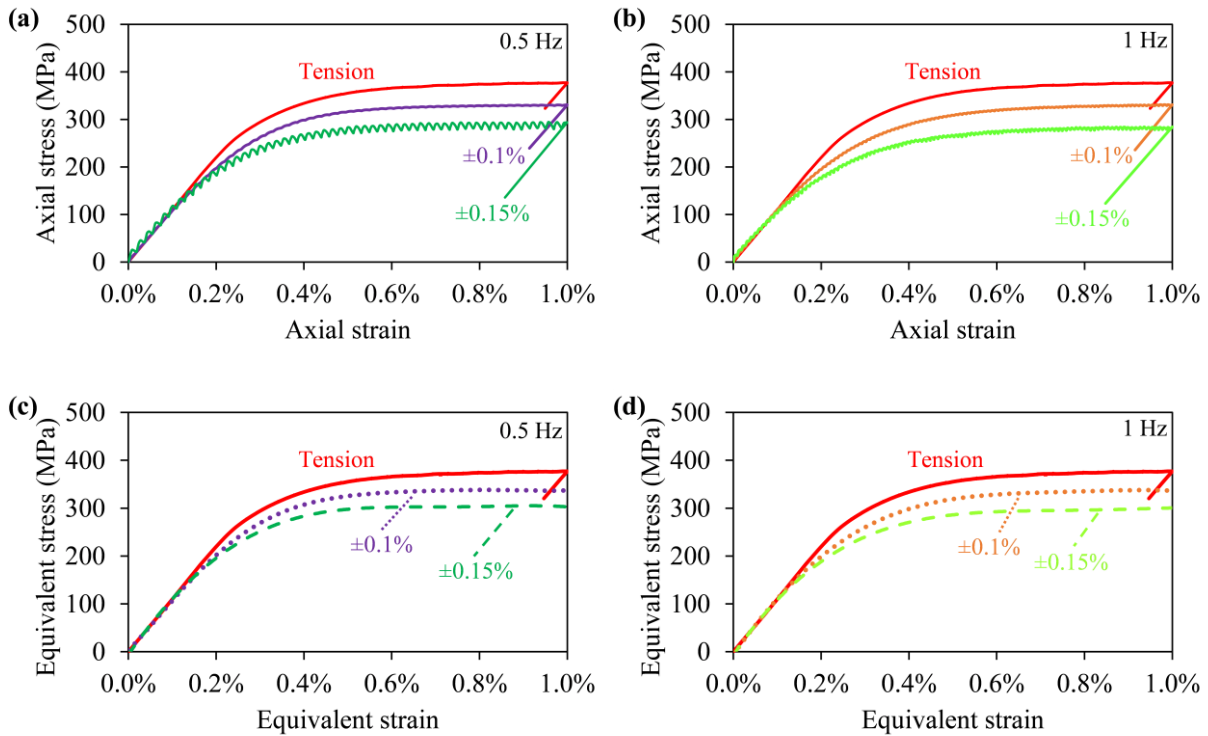


***Figure 7.8.*** *Material characteristics of Ti-Cu bimetal subjected to: monotonic tension only and simultaneous application of monotonic tension with cyclic torsion with strain amplitude equal to: ± 0.1% and ± 0.15% at frequency of 0.5 Hz (a, c) and 1 Hz (b, d), respectively.*

Figure 7.9 depicts a decreasing trend of tensile stress at axial strain equal to 0.5% for all values of cyclic strain amplitude and frequency taken into account, as was previously discussed. It should be noted, that the monotonic tension was represented by 0% strain amplitude as shown in Figure 7.9a. It can be observed, that the tensile stress for 0.5% axial strain reduces itself from an initial value of 355 MPa to 316 MPa in the case of ±0.1% cyclic torsion strain amplitude and frequency equal to 0.5 Hz. For the same level of axial strain and cyclic torsion strain amplitude of ±0.15%, it was equal to 273 MPa, Figure 7.9a. Notably, this effect becomes increasingly pronounced under higher values of frequency. At frequency equal to 1 Hz, the respective tensile stress values were 355 MPa, 308 MPa, and 263 MPa, Figure 7.9a. The magnitude of axial stress demonstrates a substantial decrease, amounting to nearly 23% and 26%, respectively, for frequency values of 0.5 Hz and 1 Hz, when compared to that obtained under axial tension only, for axial strain of 0.5%. The same effect has been reported for commercially pure Ti [1] and commercially pure Cu [153], and was attributed to the development of specific crystallographic

textures in titanium and more elongated sallow dimples on the copper fracture surface during combined tension-torsion loading.
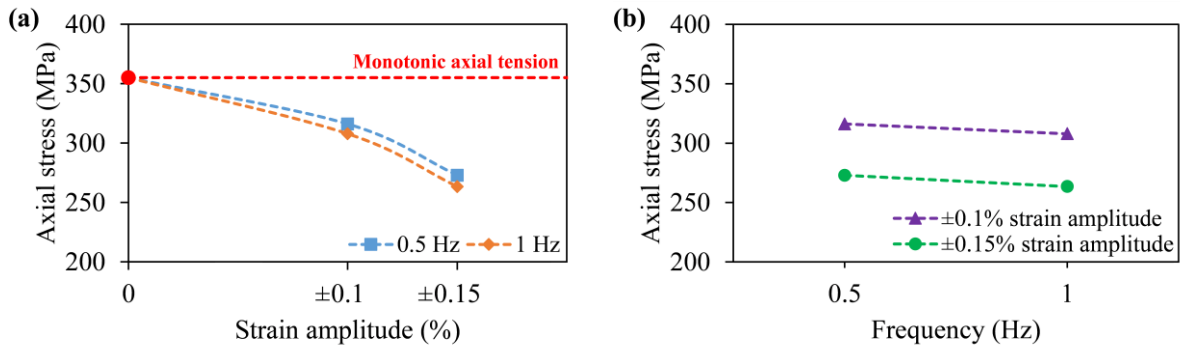


***Figure 7.9.*** *Effects of combined monotonic tension and cyclic torsion on the tensile stress at 0.5% axial strain, in response of strain amplitude equal to: ± 0.1% and ± 0.15% (a) and frequency of: 0.5 Hz and 1 Hz (b).*

### 7.3.4 Determination of the yield surface for bimetal in the as-received state

Determination of yield points characterising the initial yield surface of the Ti-Cu bimetal involved a sequential probing procedure of loading and unloading of a single specimen along different directions in the plane strain state, applying a designated plastic offset strain method. Figure 7.10 elucidates the bimetallic response within the biaxial stress plane in the context of a strain-controlled loading program, as specified in Chapter 3. Notably, the experimental results obtained in both the loading and unloading stages along each considered strain path showed a conspicuous absence of substantial deviations from linearity. Additionally, it is important to note, that the plastic strain incurred along each path during these investigations was equal to 0.02%.

Elastic properties of the tested bimetal and its constituent metals (pure titanium and copper) were presented in the form of effective Young's modulus values obtained for each specific direction (Figure 7.11). These values were different depending on the loading direction in the strain plane considered. The value of Young's modulus of Ti-Cu bimetal exhibited a maximum in the direction of 180°, which corresponded to the pure compression. On the other hand, the lowest value of Young's modulus was observed during pure torsion (direction 270°). Although the discrepancy between the minimum and maximum values of this parameter was approximately 9%, which from a practical point of view can be considered as small, it nevertheless highlights the presence of the material texture even in the as-received state. Determination of material texture relies on a comprehensive analysis of characteristics across all considered directions. The potential reason of the Young's modulus values dispersion was associated with strongly oriented texture.

Additionally, Figure 7.11 shows that the effective Young's modulus of Ti-Cu bimetal is close to or slightly higher than that of pure Cu under pure axial loading (tension and compression). This suggests that the Cu layer primarily governs the mechanical response in axial-dominated directions. In contrast, under pure torsional and reverse torsional loading, the bimetal's Young's modulus closely matches that of pure Ti, indicating that the Ti component controls the response in shear-dominated directions. In intermediate loading directions, the stiffness of the bimetal transitions between those of its constituents, reflecting a direction-dependent mechanical

behaviour. Pure Ti demonstrates notable anisotropy, with lower Young's modulus values in pure axial directions and higher values under torsional loading, highlighting its greater stiffness in shear. Pure Cu, meanwhile, shows relatively consistent Young's modulus values across all directions, with a mild anisotropic response and generally higher stiffness than Ti. The Ti-Cu bimetal effectively blends the mechanical characteristics of both metals, which underscores its potential advantage in applications involving complex or multidirectional stresses.
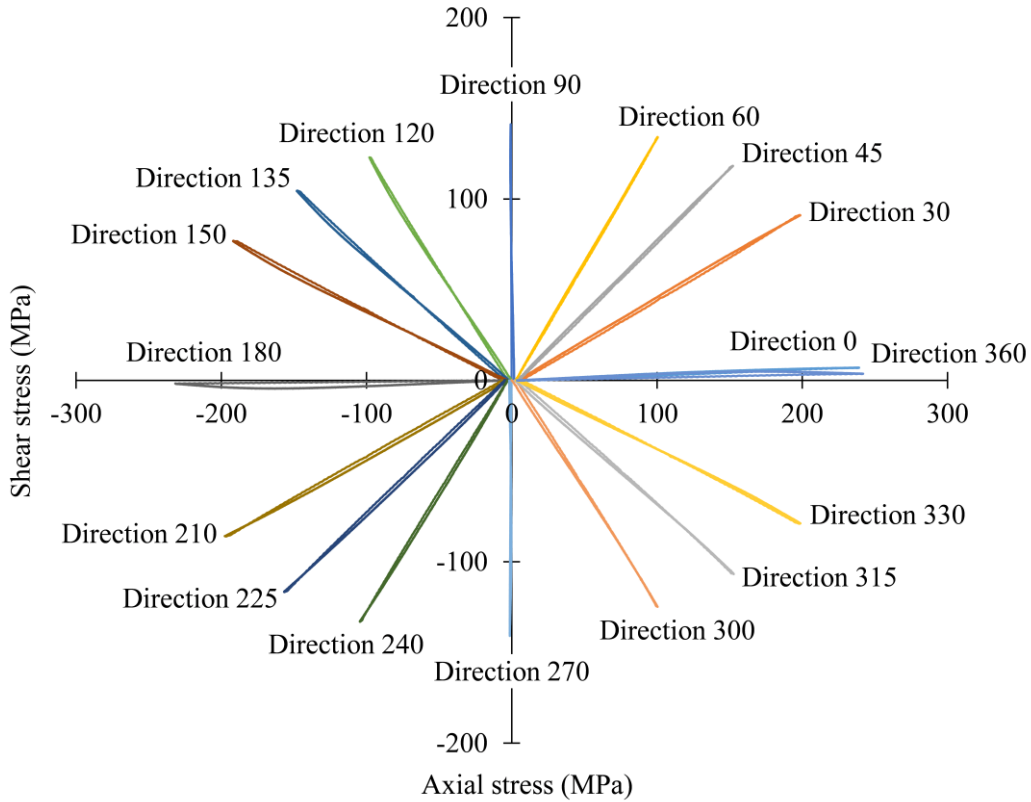


**Figure 7.10.** *Stress response to the sequential probing program used for determination of the yield surface for the Ti-Cu bimetal in the as-received state.*
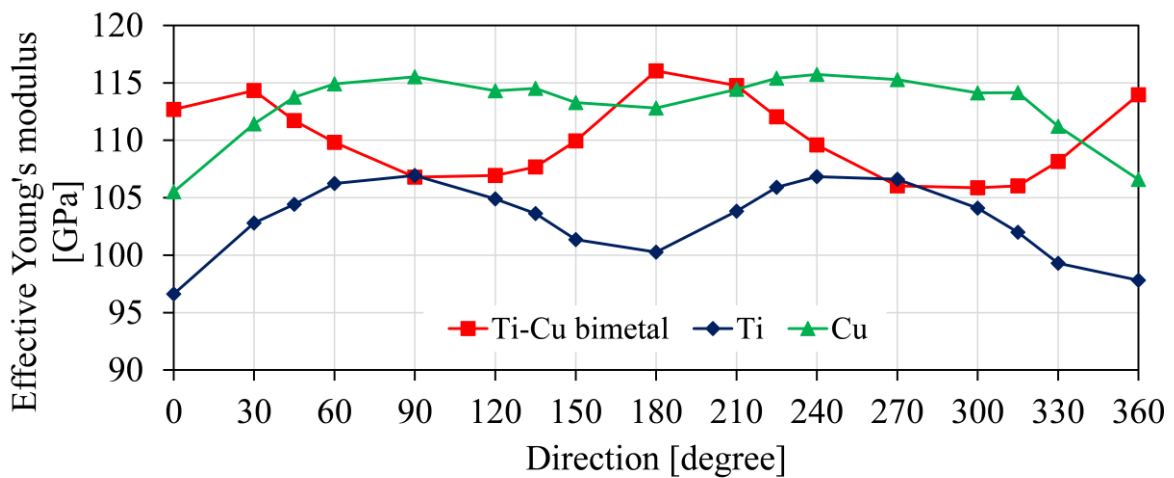


**Figure 7.11.** *Directional variation of effective Young's modulus for Ti-Cu bimetal, pure Ti, and pure Cu under axial-shear loading conditions.*

For the relatively low magnitude of plastic strain introduced in the study, such variations in the Young's modulus can exert a notable influence on the results of yield surface analysis, particularly when a single Young's modulus value from the monotonic tension would be applied for all loading directions taken into account. To accurately account for this anisotropy in estimating limited plastic strain (0.02%) during biaxial probing, direction-specific effective Young's modulus values were applied as outlined in Chapter 5.

The yield surfaces of the as-received Ti-Cu bimetal were shown in Figure 7.12a as ellipses. They were determined by fitting the yield points using the least square method in the Szczepinski anisotropic yield equation [29] obtained at 0.005% and 0.01% plastic offset strain in each loading directions of the biaxial plane. The yield surfaces determined demonstrate an impact of the selected yield point definition. The yield stress at 0.01% plastic offset strain was found to be 221.25 MPa in tension and -200.8 MPa in compression. It exposes the presence of tension-compression asymmetry in the Ti-Cu bimetal. The yield stresses in torsion and reverse torsion were equal to 141.08 MPa and -140.77 MPa, respectively, for same offset strain. Similar results have also been reported in the literature [94,226]. The parameters characterising the ellipses are presented in Table 7.2. They represent the initial yield surfaces of the Ti-Cu bimetal, corresponding to both selected offset strain values. The yield surfaces of the bimetal in the as-received state are shifted in the tension direction, and the axis ratios are considerably lower than 1.73, which is the value for the isotropic material according to the Huber – von Mises – Hencky yield criterion [108,109,118]. Such behaviour indicates an occurrence of the initial anisotropy.

**Table 7.2.** *Ellipse parameters for the initial yield surface of Ti-Cu bimetal.*

| Definition of yielding | Centre $(x_0, y_0)$ [MPa] | Rotation angle $(\emptyset)$ [Radian] | Semi-axes $(a, b)$ [MPa] | Axis ratio $(^a/_b)$ |
|---|---|---|---|---|
| 0.01% offset strain | 8.25, -1.76 | 0.11 | 225.31, 145.64 | 1.55 |
| 0.005% offset strain | 4.78, 0.03 | 0.16 | 205.18, 146.10 | 1.40 |
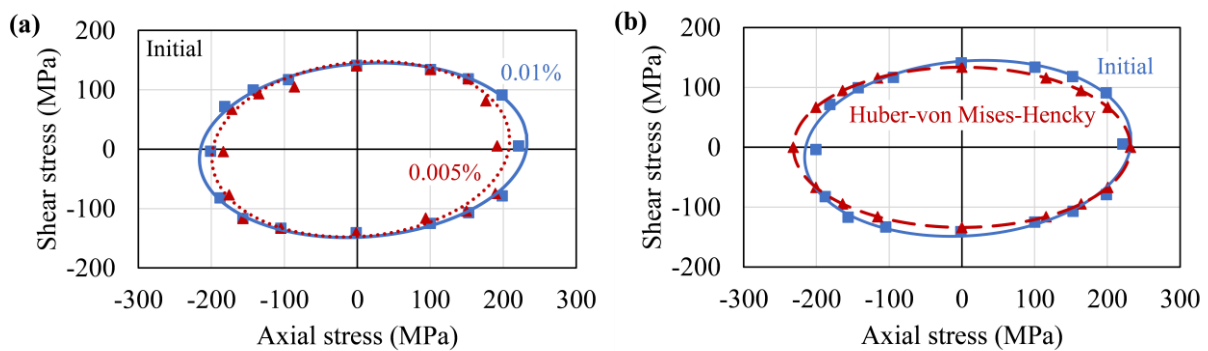


**Figure 7.12.** *Yield surfaces of Ti-Cu bimetal in the 'as-received' state with yield points (square and triangular points) obtained for 0.01% and 0.005% plastic offset strains (a); Initial yield surface (0.01% offset strain) of the Ti-Cu bimetal compared with the Huber-von Mises-Hencky isotropic yield locus (b).*

The theoretical isotropic yield surface was determined in order to perform precise comparison with the yield surface of Ti-Cu bimetal captured experimentally. It was achieved by aligning the yield point in tension (designated as direction 0) with that of the 0.01% offset for the initial yield surface of bimetal. According to the Huber – von Mises – Hencky yield criterion, the resulting isotropic yield surface is centred at the origin, displayed a zero-degree rotation angle, and maintained the axis ratio of 1.73. Figure 7.12b shows how the isotropic yield surface was configured. It can be observed, that the broken line representing the predicted Huber – von Mises – Hencky yield locus is nearly similar to that obtained experimentally for the Ti-Cu bimetal, except of the compression direction. It reflects a characteristic softening that corresponds to the compressive strength reduction. Such behaviour can be attributed to the preferred texture or grain orientation in the as-received state of bimetal.
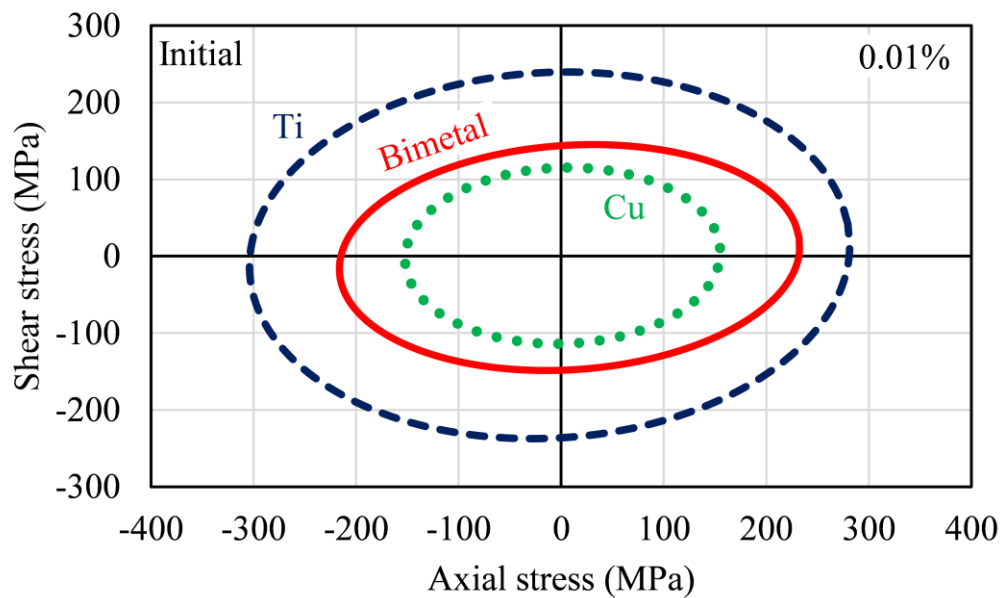


**Figure 7.13.** *Initial yield loci of Ti-Cu bimetal, CP-Ti, and CP-Cu obtained for 0.01% plastic offset strain.*

Figure 7.13 shows a comparison of the initial yield surface of Ti-Cu bimetal with those of CP-Ti and CP-Cu, as reported in Chapters 5 and 6. Each yield surface corresponds to the onset of plastic deformation for 0.01% plastic offset strain. The yield surface of CP-Ti is the largest, indicating that it has the highest yield strength among the three materials in both axial and shear directions. In contrast, CP-Cu has the smallest yield surface, reflecting its lower yield strength in both loading modes. The Ti-Cu bimetal exhibits a yield surface that lies between those of its constituents, showing intermediate yield strength characteristics. This intermediate yielding highlights the synergistic effect of combining Ti and Cu, where the bimetal inherits the higher axial strength of Ti and moderate shear strength closer to Cu. Additionally, the results suggest that the Ti-Cu bimetal can be effectively engineered for improved performance under multiaxial loading conditions. This combined response offers a favourable balance of mechanical strength, economic efficiency, and application versatility that surpasses what either CP-Ti or CP-Cu can achieve individually.

**7.3.5 Determination of the yield surface for the pre-deformed material**

The subsequent yield loci were determined for 0.01% plastic offset strain in tension-torsion stress space following monotonic tension and various combinations of the tension-cyclic torsion plastic pre-deformation, using the same procedure as applied to the material in the as-received state. An effect of plastic pre-deformation on the bimetal was evaluated based on the evolution of the initial yield surface. All specimens were subjected to pre-deformation until they reached an axial strain of 1%.

The yield locus and yield points corresponding to bimetal subjected to 1% tensile pre-deformation is presented in Figure 7.14, as denoted by the dashed line and triangles. It can be clearly seen, that the shape of the yield surface exhibits significant shift towards the tensile direction, i.e. direction of prior deformation. It indicates, that the application of monotonic tensile deformation led to the induction of kinematic hardening within the bimetallic structure. Specifically, the yield point in tension increased from 221 MPa to 288 MPa and that in compression decreased from -201 MPa to - 150 MPa, representing close to 30% and 25% variation in comparison to the initial values, respectively.
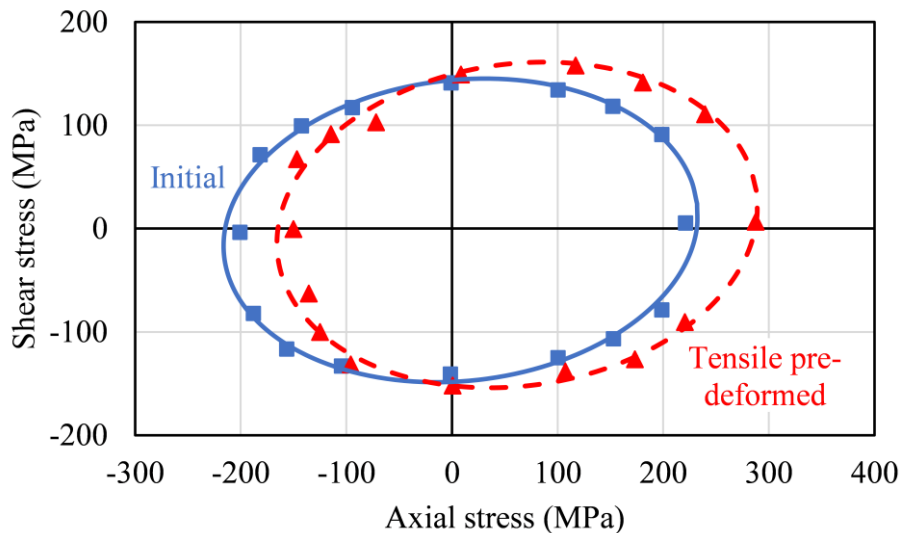


*Figure 7.14. Comparison of the yield surfaces for tensile pre-deformed Ti-Cu bimetal and the same material in the as-received state.*

Figure 7.15 illustrates the fitted yield loci and experimentally obtained yield points of plastically pre-deformed Ti-Cu bimetal due to monotonic tension assisted by torsion-reverse-torsion of various strain amplitudes and frequencies. These subsequent yield surfaces were shown in comparison to the initial yield surface of the tested material (represented by a continuous line). The results identified clear anisotropic softening of the bimetal. Specifically, for the cyclic torsional strain amplitude equal ±0.1% at frequency of 0.5 Hz (Figure 7.15a) and 1 Hz (Figure 7.15c), the subsequent yield surfaces exhibited a decrease of 14% in the tensile yield stress for both cases and a decrease of 17% and 20% in the compressive yield stress, respectively, as compared to those representing the initial yield point values. It has to be indicated however, that the yield stresses in torsion and reverse torsion exhibited an equal slight reduction of 6% for both values of cyclic loading frequency applied in this work.
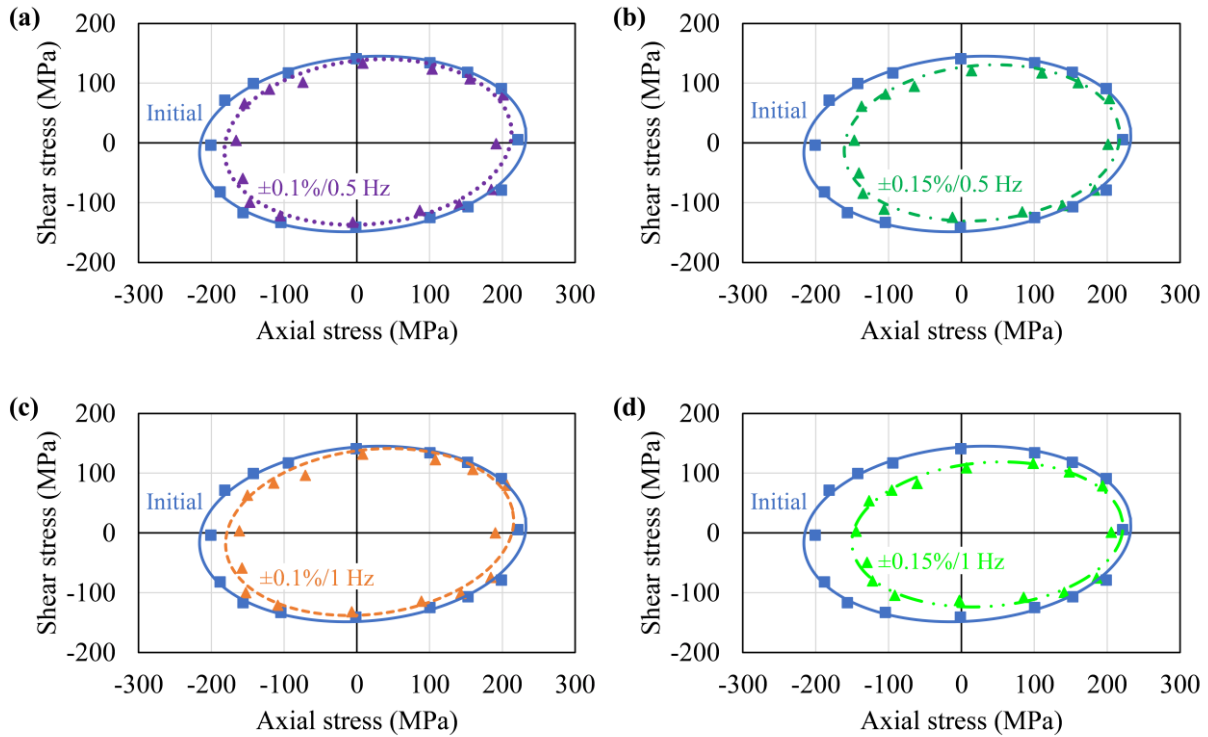
***Figure 7.15.*** *Comparative analysis of the initial yield surface of the Ti-Cu bimetal with the yield surfaces of the same bimetal subjected to pre-deformation through the combined monotonic tension and cyclic torsion of strain amplitude equal to ±0.1% and ±0.15% at frequencies of 0.5 Hz (a, b) and 1 Hz (c, d), respectively.*

When the cyclic strain amplitude was increased from ±0.1% to ±0.15% for monotonic tension assisted by cyclic torsion pre-deformation, the size of the yield surfaces were reduced in all directions, however, more dominantly in the compressive direction, at frequency of 0.5 Hz (Figure 7.15b) and 1 Hz as well (Figure 7.15d). A decrease of the tensile yield stresses was 9% and 7% at 0.5Hz and 1 Hz, respectively, whereas of the compressive yield stresses 27% and 28%, respectively. Additionally, yield stresses in torsion and reverse torsion showed an equal decrease of nearly 13% for monotonic tension assisted by cyclic torsion of strain amplitude equal to ±0.15% at frequency of 0.5 Hz (Figure 7.15b) and nearly 22% decrease in both stresses at an increased frequency of 1 Hz (Figure 7.15d). One should note that, regardless of the level of pre-deformation introduced through combined monotonic tension-cyclic torsion, a significant decrease of the compressive yield stress and noticeable reduction of the shear yield stress were observed in the Ti-Cu bimetal, particularly for higher cyclic torsion strain amplitude. The rate of anisotropic softening increased with the increase of combined pre-deformation level. Despite many previous investigations performed on the impact of pre-deformation on materials, relatively few studies explored this phenomenon from the perspective of yield surface evolution. A similar tendency of kinematic hardening variation after 1% tensile pre-strain (Figure 7.14) was observed in CP-Ti [1], various steels [168] and Al-alloys [32]. This behaviour was attributed to factors such as preferred texture and the presence of non-shearable, incoherent precipitates, which hinder the dislocation motion. It has to be emphasised, that the effects associated to influence of monotonic tension assisted by cyclic torsion on the yield surface has received relatively limited attention up to now. The softening effect identified by subsequent yield surfaces was also observed in other materials, including 18G2A low alloy

steel [28] and A336 GR5 structural steel [33], following the application of cyclic pre-strain history.

The experimentally obtained yield points were fitted by the Szczepinski yield function [29] using the least squares method to describe the ellipse representing the approximate yield surface of the tested material. In Table 7.3, the fitting errors, computed through the minimization of the sum of squares of the distances of the experimental yield points from the approximated yield surface, were presented for each of the yield surfaces determined. These fitting error values, in each case, were found to be exceptionally minimal. This observation indicates a precise match between the experimental data and the fitted elliptical approximation. The consistently low fitting errors confirm the suitability and high accuracy of the yield surface equation, as well as the overall quality of the yield surface approximation.

**Table 7.3.** *The fitting errors associated with the yield surfaces for the material in the as-received state and the same material after subsequent pre-deformation resulting from monotonic tension, as well as combined monotonic tension with cyclic torsion of strain amplitude equal to: ±0.1% and ±0.15% at frequency of: 0.5 Hz and 1 Hz.*

| As-received | Monotonic tension deformed | ±0.1% at 0.5 Hz deformed | ±0.15% at 0.5 Hz deformed | ±0.1% at 1 Hz deformed | ±0.15% at 1 Hz deformed |
|---|---|---|---|---|---|
| 6.69E-02 | 1.06E-01 | 2.43E-01 | 1.93E-01 | 2.84E-01 | 1.78E-01 |

Figure 7.16 provides the variation in the parameters characterising the elliptical shape of the yield surface (YS) for the Ti-Cu bimetal in the pre-deformed state. It should be noted, that pre-deformation due to monotonic tension is represented by 0% strain amplitude as shown in Figure 7.16. The results present, that the semi-axes (a, b) of the yield surface of material pre-deformed due to monotonic tension increased to 228.73 MPa and 155.65 MPa in comparison to that of the as-received state (225.31 MPa, 145.64 MPa), suggesting a positive cross-effect. On the other hand, these values decreased after the combined pre-deformation at both frequencies considered (0.5 Hz and 1 Hz) (Figure 7.16a and Figure 7.16d).

The axis ratio of the subsequent yield surfaces was compared with two reference frameworks: the initial yield surface, as presented in Table 7.2, and the Huber – von Mises – Hencky isotropic yield surface. Such comparison was presented in Figure 7.16b and Figure 7.16e. It could be observed, that the axis ratio of the yield surface was nearly constant after all pre-deformation level considered, except of that determined after monotonic tension-cyclic torsion with strain amplitude of ±0.15% at 1 Hz, which closely resembles the axis ratio of as-received state. The rotation angle (Ø) of the yield surface axes with respect to the axial-shear stress co-ordinate system showed the variation with pre-deformation level. The maximum value of 0.19 radian rotation was observed after the monotonic tension assisted by cyclic torsion with strain amplitude of ±0.1% at frequency of 1 Hz (Figure 7.16c and Figure 7.16f).
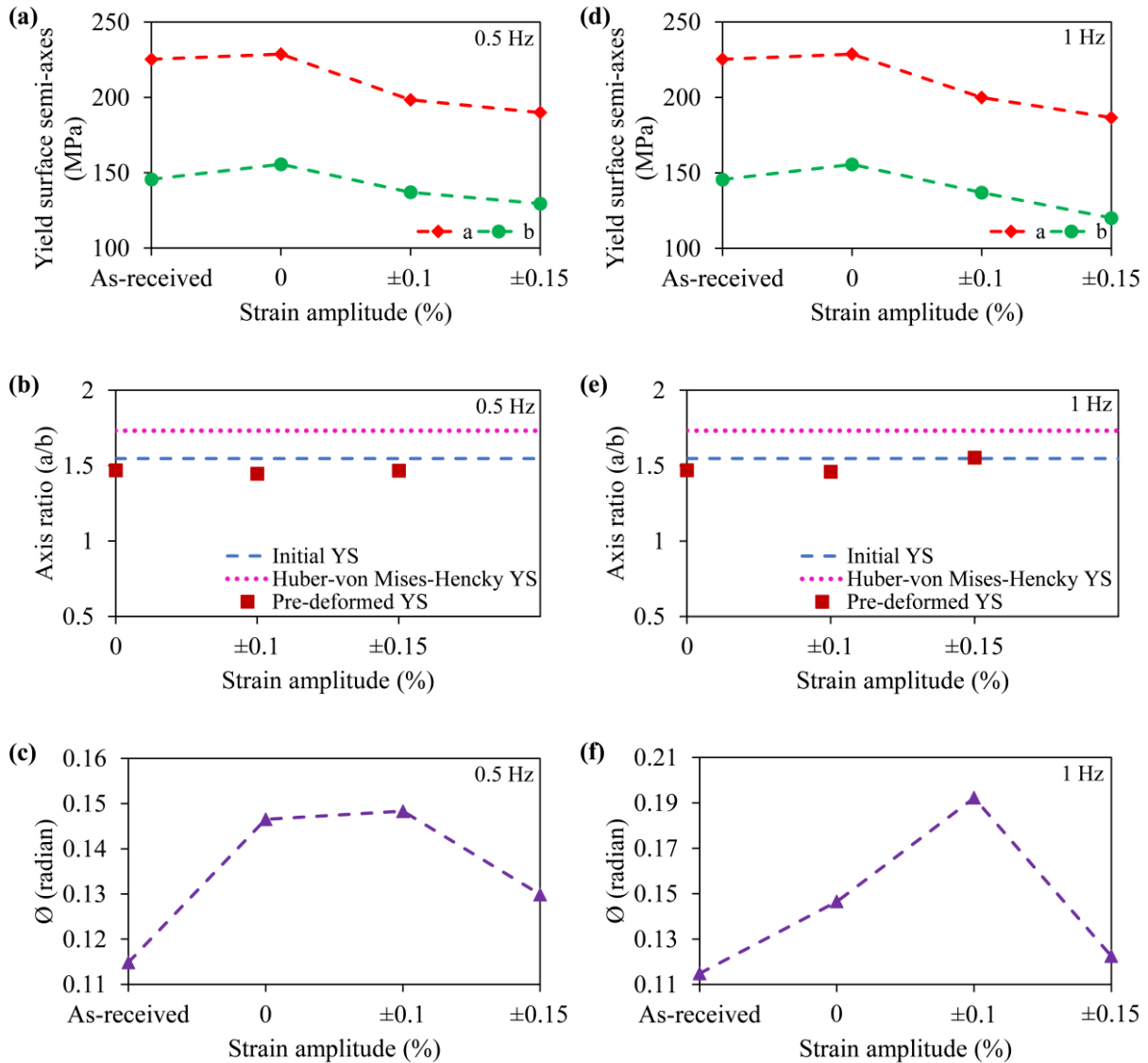
***Figure 7.16.*** *Variation of the yield surface parameters of Ti-Cu bimetal due to pre-deformation by monotonic tension (0% strain amplitude); combined monotonic tension with cyclic torsion of strain amplitude equal to: ±0.1% and ±0.15% at frequency of: 0.5 Hz (a, b, c) and 1 Hz (d, e, f), respectively.*

Subsequently, a study of origin position variation of the initial yield surface was carried out taking into account all yield surfaces determined, as shown in Figure 7.17. When a material undergoes plastic deformation, the existence of back stress components can be often observed, which can be highlighted by the position of the centre of yield surface from the origin. The result shows that, in all cases, the centres of the yield surfaces are consistently oriented in the tensile direction. The back-stress components were minimal for the bimetal in the as-received state (8.25 MPa in tensile direction, -1.76 MPa in reverse torsion direction), however, it displayed a significant increase for the material after loading history. The most pronounced back stress components, reaching 64.84 MPa in tensile direction and 3.44 MPa in torsional direction, were observed in the case of bimetal pre-strained up to 1% due to monotonic tension. Such effect can be attributed to the creation of high stress area in the material due to the formation of new dislocations which as a consequence, impede the movement of existing dislocations, contributing to the increase of back stress components observed.
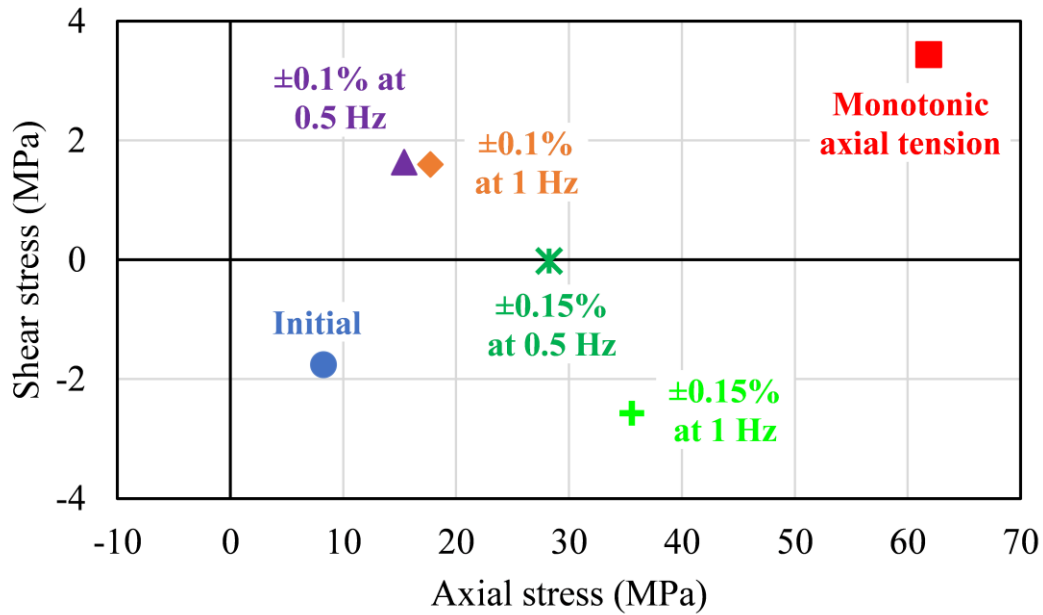
***Figure 7.17.*** *Analysis of the origin position of the yield surfaces of Ti-Cu bimetal in the as-received state and resulting from pre-deformation caused by monotonic tension; combined monotonic tension-cyclic torsion of strain amplitude equal to: ±0.1% and ±0.15% at frequencies of 0.5 Hz and 1 Hz.*

Figure 7.18 provides a comprehensive visualization of the initial yield surface evolution in the axial-shear stress space, following various level of pre-deformation of the Ti-Cu bimetal. It was observed, that each yield surface has a distinct shape and the size of subsequent yield surfaces decreases in the compressive direction, which is the opposite of that representing the tensile pre-deformation of bimetal. The yield surface of bimetal after 1% monotonic tension pre-deformation exhibited the largest dimensions. By examining Figure 7.18a and Figure 7.18b, it becomes evident that:

- monotonic tension pre-deformation leads to the kinematic hardening in the same direction as that used during pre-deformation;

- combined monotonic tension-cyclic torsion pre-deformation leads to the kinematic softening in all directions and it becomes more prominent with the increase of torsional strain amplitude.

One could observe the impact of an increase of cyclic torsional strain amplitude on the yield surface in Figure 7.18. The yield surface obtained after monotonic tension-cyclic torsion with a strain amplitude of ±0.15% pre-deformation exhibits a similar tensile yield stress compared to that obtained for ±0.1% torsional strain amplitude. On the other hand, a significant decrease in all other stress directions could be found. Similar tendencies can be observed for both frequencies (0.5 Hz and 1 Hz) used in the pre-deformation process. An examination of the shape of these subsequent yield surfaces elucidates, that the dimensions of the yield surface are dependent upon the nature of the pre-deformation process.
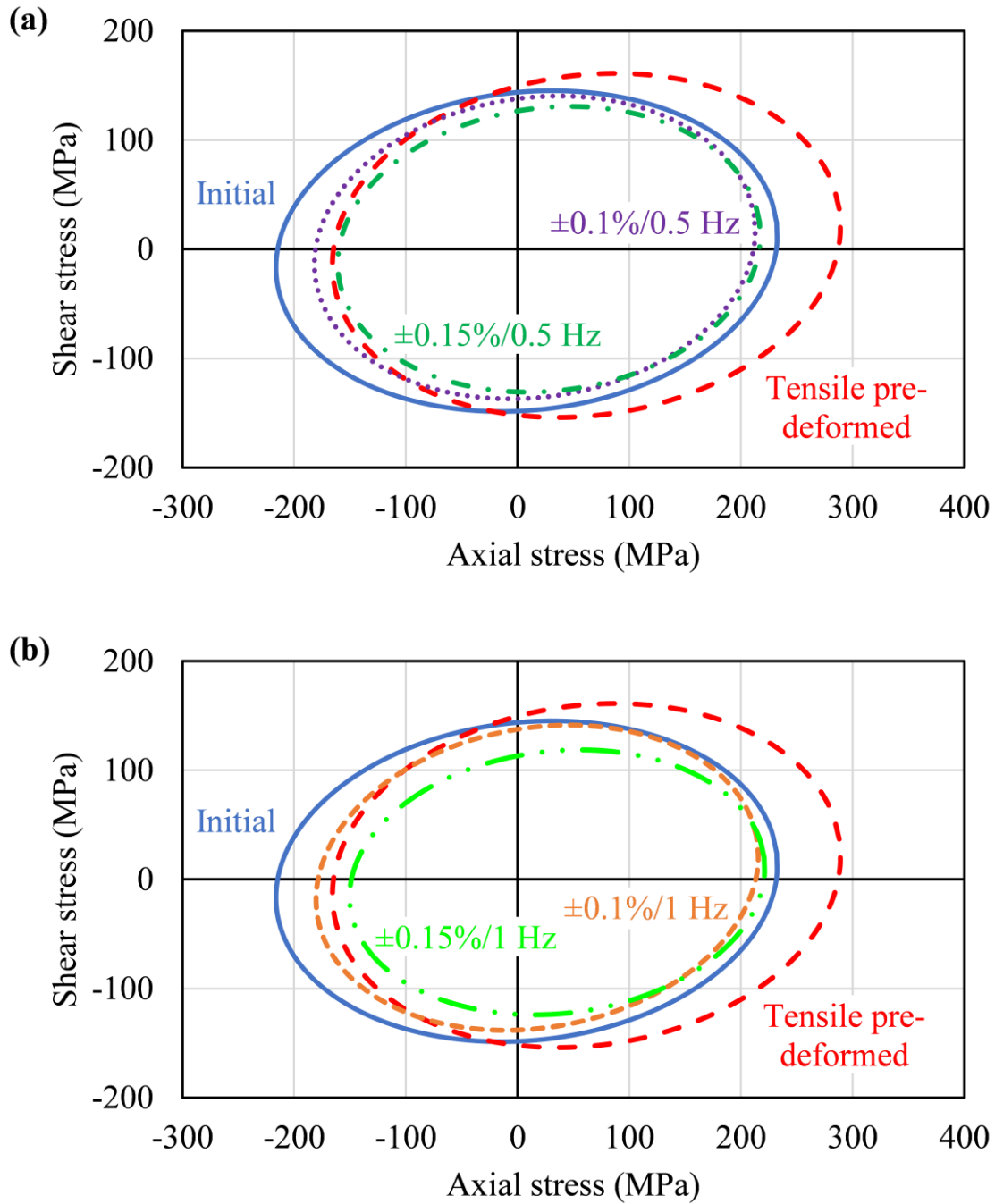
**Figure 7.18.** *Evolution of the initial yield surface of Ti-Cu bimetal due to pre-deformation caused by monotonic tension and tension-cyclic torsion with strain amplitudes of ±0.1% and ±0.15% at frequency values equal to 0.5 Hz (a) and 1 Hz (b), respectively.*

The reported yield surface evolution reflecting the effect of plastic pre-deformation of Ti-Cu bimetal is compared with those of copper and titanium present in the literature. The 99.9% pure copper exhibited isotropic hardening effect after plastic pre-deformation by means of monotonic tension up to 5% and 15% axial strain [26], whereas CP-Ti exhibited kinematic hardening for 1% tensile pre-deformation [1], which is similar to the reported kinematic hardening effect observed in the Ti-Cu bimetal after 1% monotonic plastic pre-deformation. In the case of plastic pre-deformation caused by monotonic tension assisted by cyclic torsion, CP-Cu and CP-Ti showed hardening in tensile yield stress direction and softening in all other stress

directions for strain amplitudes varying from ±0.2% to ±0.7% [1,34]. Conversely, the reported Ti-Cu bimetal exhibited a softening effect in all biaxial stress directions under similar loading conditions.

These findings emphasize the importance of doing experimental analysis to comprehend the plastic behaviour of bimetals, as it cannot be solely predicted based on the behaviour of their constituent metals. The plastic behaviour of bimetals is extensively controlled by parameters such as the bonding quality, thickness of each metal and variations in microstructure at the interfaces of both metals.

### 7.3.6 Microstructural characteristics of the Ti-Cu bimetal in the as-received state and after loading history induced

EBSD results at solid-solid bonded Ti-Cu interface were presented in Figure 7.19 and Figure 7.20. The figures reveal the nature of grain structure and texture evolution in the form of Inverse Pole Figure (IPF) maps, as well as (001) and (0001) pole figures in the as-received state of bimetal and after its deformation. The planes with the three typical miller indices $\{001\}$, $\{101\}$, $\{111\}$ for copper, and $\{0001\}$, $\{2\overline{11}0\}$, $\{10\overline{1}0\}$ for titanium were displayed in RGB (red, green and blue) colours, respectively. Each map was related to the specific yield surface presented in Figure 7.18. All specimens were fully recrystallized after the plastic pre-deformation.

The microstructure of the as-received bimetal was characterised by the finer grains near interface and coarse structure far from it in copper, embedded with many twins. More or less equal sized grains with a high number of deformation twins were found in titanium, as presented in Figure 7.19a. Additionally, the fine equiaxed grains were observed at the interface zone, which was in a span of average 7-8 μm width. The size of the grains was uniform in the deformed Ti-Cu interface (Figure 7.19a). By comparing the grain maps of the as-received state (Figure 7.19a) and 1% tensile pre-deformed state (Figure 7.19b), it was evident, that tensile pre-deformation leads to a refined grain size with elongated grains along the tensile loading direction in copper. Also, the copper grains were more deformed and merged with the interface. The width of Ti-Cu bimetal interface increased up to the average value of 34 μm (Figure 7.19b). The fine grain structure implies, that severe plastic deformation creates more nucleating sites that leads to the grain refinement. When bimetal was deformed under combined tension-cyclic torsion (Figures 7.19c, d, e, f), the average grain size of copper increased with the increase of strain amplitude and frequency in comparison to the prior deformation due to tension, only (Figure 7.19b). The grain map (Figure 7.19e) demonstrates that the pre-deformation caused by combined monotonic tension-cyclic torsion with ±0.1% strain amplitude at frequency equal to 1 Hz enlarges the grain size of copper and elongates the grains in a spoke-wise pattern. The interface zone in bimetal deformed due to combination of tension assisted by cyclic torsion with ±0.1% strain amplitude at 0.5 Hz frequency (Figure 7.19c) decreased in comparison to the bimetal deformed due to tension, only (Figure 7.19b). However, with the increase of strain amplitude and frequency, an opposite effect can be observed, i.e. the width of the interface zone increased. One can also observe, that with the increase of cyclic shear strain amplitude from ±0.1% (Figure 7.19c) to ±0.15% (Figure 7.19d) at the frequency equal to 0.5 Hz, the size of grains at the interface transformed from fine to ultrafine. Similar trend can also be observed at the higher frequency equal to 1 Hz (Figure 7.19e and Figure 7.19f). In the case of titanium, more or less similar average grain sizes were obtained for all bimetal states considered. It means, that all types of pre-deformation applied do not affect significantly the grain structure

of titanium. Such behaviour was also reported in previous work for the experimental program performed under higher magnitudes of prior deformation [1].

When examining the deformation characteristics of the Ti-Cu bimetallic interface, it is evident that increasing the amplitude of cyclic shear strain from ±0.1% (Figure 7.19c) to ±0.15% (Figure 7.19d) at a frequency of 0.5 Hz results in a greater amount of recrystallization at the interface. This, in turn, leads to a greater degree of material softening reflected by adequate sizes of the yield surface. This phenomenon becomes more pronounced as the frequency is further increased from 0.5 Hz to 1 Hz (Figure 7.19e and Figure 7.19f).

The microstructural evolution observed on the boarder of two metals is mainly driven by the shear strain magnitude and frequency as the width of interface is changing significantly when different conditions are applied. Considering the physical mechanisms, one can indicate two microstructural changes that may affect the yielding: grain refinement resulting from recrystallization, and formation of twins and new grains due to activation of different slip systems. These features should be analysed for both, constituent materials as well as for the interface. It should be stressed, that the as-received material was characterised by the relatively narrow interface zone, which expanded when the deformation was applied. Theoretically, the higher shear strain magnitude and frequency, the more slip systems should be activated because of the notable interaction between two metals. Such behaviour is well observed in the interface zone, as the application of frequency equal to 1 Hz lead to the expansion of the interface zone due to recrystallization and subsequent formation of fine grain structure. It is easy to notice the occurrence of twins near the transition zone after deformation. Their share is significantly higher in titanium, than copper, which means, that copper is not that sensitive for frequency changes. The YS identification showed in Figure 7.15 exposes a negligible effect of frequency on yielding behaviour, while some differences could be observed when different shear strain amplitude magnitudes are considered. It should be stressed, that such behaviour could not be directly explained by the microstructural changes in bimetallic structure. Interestingly, the growth of copper grains could be observed, when shear strain magnitude of ±0.15% at frequency 0.5 Hz was utilized, as well as for both strain values at frequency of 1 Hz. Such grain growth could be associated with heat dissipation and temperature changes due to notable interaction between two metals during deformation. Since the temperature was not monitored during the test, the future studies should include such direction in order to investigate in detail the effect of temperature on microstructural evolution when complex loading conditions are applied. Based on the EBSD analysis and mechanical response of bimetallic specimens, one should conclude, that mainly shear strain magnitude affects the yielding. The higher strain magnitude is, the more prominent microstructural changes are observed. These involved activations of more slip systems, leading to the material recrystallization and subsequent softening observed mainly in the RD direction.
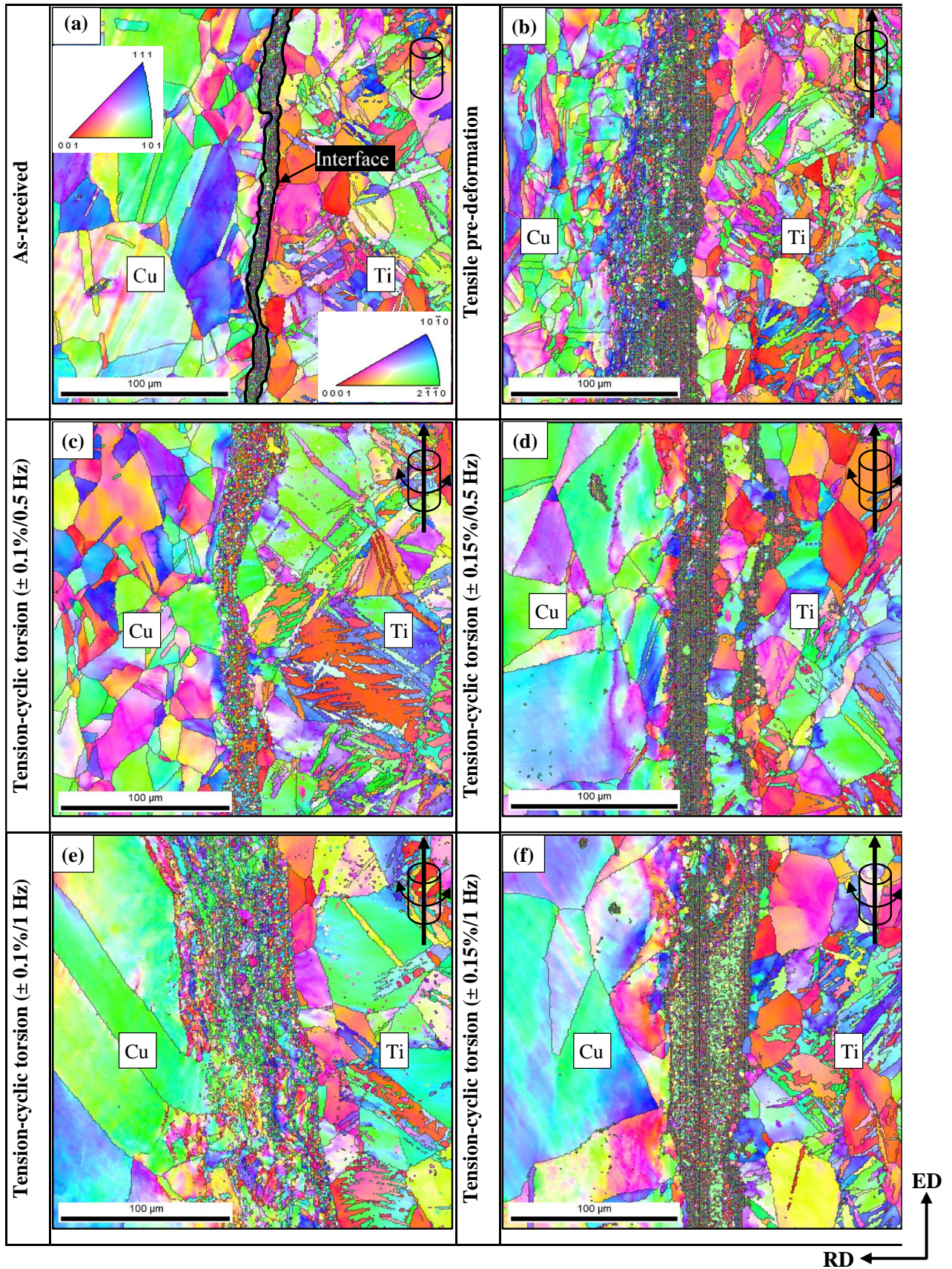
***Figure 7.19.*** *Inverse pole figure (IPF) maps of the as-received material (a); after monotonic tension to 1% (b); and monotonic tension with cyclic torsion of strain amplitudes equal to ±0.1% (c, e) and ±0.15% (d, f) at frequencies equal to 0.5 Hz (c, d) and 1 Hz (e, f).*
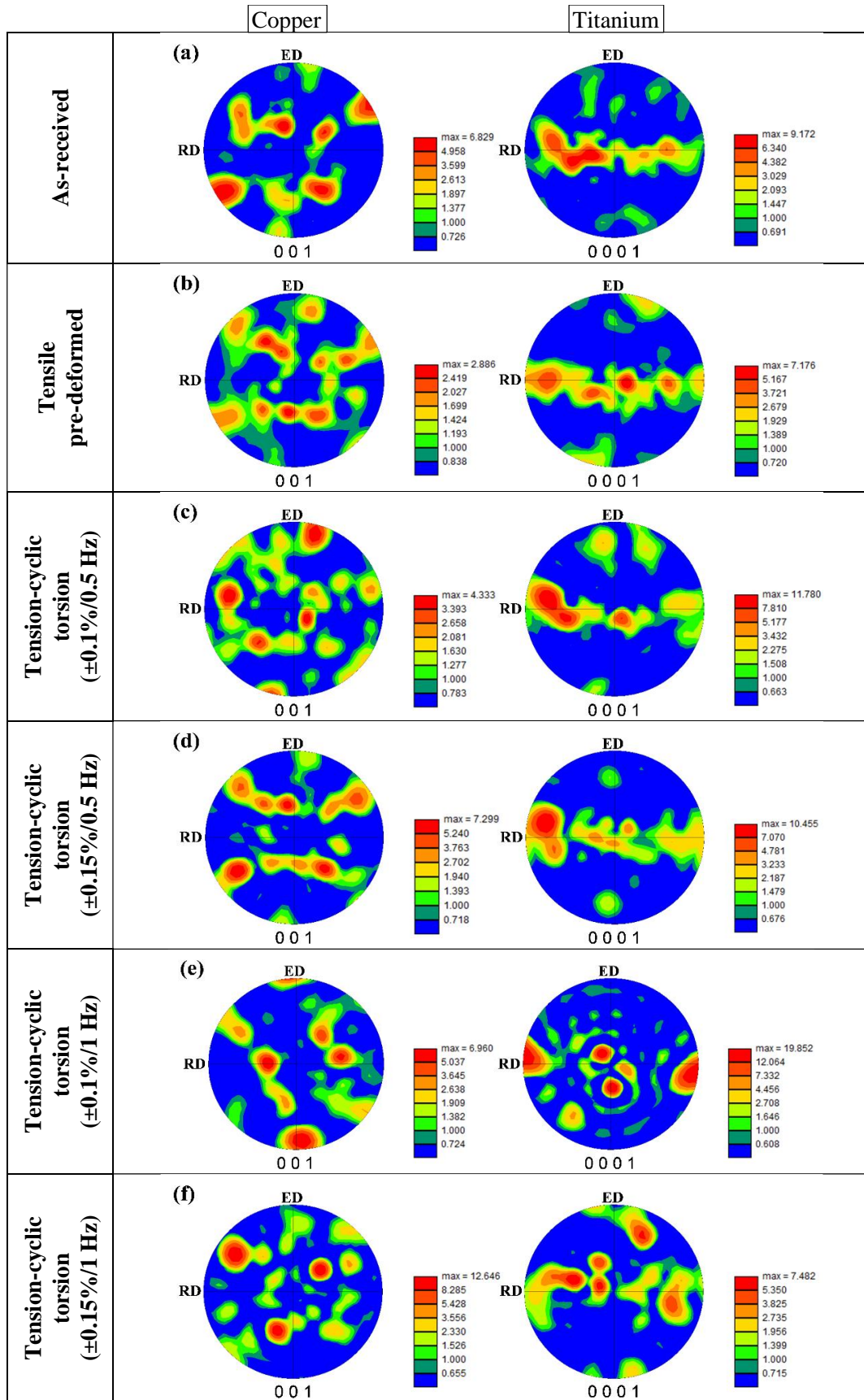
**Figure 7.20.** *Pole figure maps of the as-received material (a); after monotonic tension to 1% (b); monotonic tension assisted by cyclic torsion of strain amplitudes equal to ±0.1% (c, e) and ±0.15% (d, f) at frequencies equal to 0.5 Hz (c, d) and 1 Hz (e, f).*

As it can be seen from the (001) pole figures in Figure 7.20, the copper has a nearly random texture in all states. More interestingly, a texture or crystallographic orientation of copper near the interface was dominant in <101> and <111> directions (Figure 7.19), that can be also observed in Figure 7.20, as the high intensity points located in those areas of the pole figures were found. In the case of combined tension-cyclic torsion with ±0.1% strain amplitude at frequencies equal to 0.5 Hz (Figure 7.20c) and 1 Hz (Figure 7.20e), the closed-packed <001> direction was also distinguished.

Evolution of the titanium crystallographic textures recorded on basal plane (0001) in the extrusion plane (ED-RD) was presented in Figure 7.20. The pole figure of titanium (0001) near the interface illustrates the RD split basal texture for the bimetal in the as-received state (Figure 7.20a). The basal texture with c-axis of the majority of grains is inclined at an angle of ± (20° – 60°) from the TD towards the RD. More interestingly, the texture shows, that the c-axis of grains near the interface are preferentially oriented perpendicularly to the extrusion direction. Figure 7.20b represents the pole figures after the 1% tensile pre-deformation. It reveals a development of the RD split basal texture with the c-axes widely distributed in the whole RD-TD plane, since a line in the pole figure represents the plane. However, a weaker texture component with the c-axes oriented almost in parallel to the ED appeared as well. When bimetal was deformed by combined monotonic tension assisted by cyclic torsion with ±0.1% strain amplitude at 0.5 Hz frequency (Figure 7.20c), two stronger basal textures were observed; first one with the c-axes inclined at (40° – 80°) from the TD towards the RD and the second one with the c-axes in parallel to the TD. Also, some weaker basal texture aligned in parallel to the - RD and ED still occurred in the microstructure. However, with the increase of strain amplitude from ±0.1% to ±0.15% at 0.5 Hz frequency (Figure 7.20d), the weaker texture component parallel to the ED disappeared and the RD split basal texture with most of the grains reoriented their c-axis in parallel to the RD. One could notice a stronger basal texture with the c-axes aligned in parallel to the ± RD and TD; weaker basal texture distributed non-uniformly in the plane parallel to the ED-RD plane when the pre-deformation was induced by combined tension and cyclic torsion with ±0.1% strain amplitude at 1 Hz frequency (Figure 7.20e). Based on the pole figure of material after the ±0.15% cyclic strain amplitude at the frequency equal to 1 Hz (Figure 7.20f), the basal texture was observed for 3 different high-intensity orientations. First, with narrow distribution of the c-axes inclined at (20° – 50°) from the TD towards the positive ED-RD plane; second, with the c-axes inclined at (50° – 60°) from the TD towards negative RD, and third, with the c-axes inclined at (64° – 78°) from the TD towards ED – (-RD) plane.

The texture intensities are represented by the colour scale bar corresponding to each pole figures. It is evident from the pole figures in Figure 7.20, that the intensity value is considerably lower for the bimetal deformed by monotonic tension (Figure 7.20b) in comparison to the same material in the as-received state (Figure 7.20a). This is mainly due to the significant changes in microstructure induced by the tensile pre-deformation. However, when bimetal was deformed due to combination of the monotonic tension and cyclic torsion, the intensity gradually increased in copper with the increase of strain amplitudes at both values of frequency taken into account. It reached a maximum of 12.6 in the case of material subjected to tension assisted by cyclic torsion with ±0.15% strain amplitude at frequency equal to 1 Hz (Figure 7.20f). An opposite trend can be observed in titanium for which the peak intensity value equal to 19.9 was obtained for ±0.1% strain amplitude at frequency of 1 Hz (Figure 7.20e). Such increase in intensity value indicates a development of the stable orientation after combined pre-

deformation towards (001) and (0001) crystallographic planes of the Ti-Cu bimetal specimens in the extrusion plane (ED-RD).

In summary, the plastic pre-deformation process of Ti-Cu bimetal leads to a texture evolution, preferred grain orientation and changes in grain structure, more dominantly in copper. The internal misorientation within the grains is also evident through the colour variations in individual grain interior. It is worth to note, that after loading histories applied to pre-deform the bimetal tested, the interfaces of Ti-Cu were still intacting. These results clearly support an evolution of the initial yield surface of bimetal due to prior deformation illustrated in Figure 7.18.

## 7.4 Concluding remarks

In this chapter, a pioneer investigations of the evolution of initial yield surface reflecting plastic pre-deformation of the Ti-Cu bimetal were performed. An experimental procedure was selected to investigate the effect of monotonic tension and combined tension-cyclic torsion pre-deformation on the mechanical properties of the bimetal. Initial and subsequent yield loci of the Ti-Cu bimetal were systematically investigated after various pre-deformation levels using the single specimen approach with 0.01% plastic offset strain as definition of yield point. The main findings can be summarized as follows:

- The mechanical properties of bimetal lie in between those of its constituent metals. The tensile yield and ultimate strengths were approximately 43% and 50% higher than those of copper, respectively.

- Cyclic torsion applied during monotonic tension caused a significant decrease of tensile stress. The tensile stress reduction becomes greater with an increase of torsional strain amplitude and frequency.

- The initial yield surface of the as-received Ti-Cu bimetal exhibited anisotropy, which was clearly identified by its comparison to the Huber – von Mises – Hencky isotropic yield surface. A tension-compression asymmetry can be easily observed on the initial yield surface.

- Kinematic hardening along pre-strain direction and positive cross-effect were identified for the pre-strained bimetal on the basis of subsequent yield surface following 1% monotonic tensile pre-deformation in comparison to the as-received state, whereas, kinematic softening was found after the combined pre-deformation due to monotonic tension assisted by cyclic torsion. Effect of kinematic softening became more prominent with the increase of cyclic torsion strain amplitude and frequency.

- EBSD analysis performed on the pre-deformed specimens revealed, that only shear strain magnitude of the combined pre-deformation condition affects the yielding behaviour of bimetallic structure. The higher strain magnitude is leading to notable microstructural changes involving activation of more slip systems which in turn cause material recrystallization and subsequent softening in the radial direction.

# Chapter 8

# Yield surface identification of AM SS316L

*In this chapter the mechanical behaviour of wrought SS316L and LPBF-printed SS316L in XY, ZX, and Z orientations are studied, focusing on the evolution of yield surfaces, stress-strain responses, and plastic deformation under uniaxial and multi-axial loading conditions. The results demonstrate the impact of printing orientation, anisotropy, and tensile plastic pre-straining on yield surface contraction, hardening mechanisms, and material anisotropy. By addressing these objectives, this chapter contributes to the broader understanding of additively manufactured materials and their application in engineering designs, facilitating the development of optimized manufacturing protocols and predictive modelling frameworks for SS316L components.*

## 8.1 Introduction

Stainless steel 316L (SS316L) belongs to the materials of an austenitic structure. It is widely used in such industries as aerospace, medical, and energy due to its exceptional combination of mechanical properties, corrosion resistance, and biocompatibility [239]. These properties make it a preferred material for critical applications like implants, structural components, and chemical processing equipment. Most often used chemical composition of SS316L is presented in Figure 8.1. The low carbon content of SS316L minimizes carbide precipitation, enhancing its weldability and resistance to intergranular corrosion. Furthermore, SS316L exhibits excellent ductility and toughness across a broad temperature range, making it suitable for environments where mechanical stress and chemical reaction coexist [240]. In biomedical applications, SS316L is employed for manufacturing surgical tools and orthopaedic implants due to its non-reactive surface and superior strength. In the power engineering sector, it is used for components exposed to high-pressure and high-temperature conditions, such as heat exchangers and reactor vessels. Its combination of low thermal conductivity, high melting point, limited sensitivity to oxygen absorption, and high absorptivity in infrared, also makes SS316L ideal for additive manufacturing (AM) techniques, such as Laser Powder Bed Fusion (LPBF), enabling the fabrication of intricate geometries and optimized designs tailored to specific applications [241].

Traditional manufacturing methods, including casting, forging, and machining, have been historically employed to process SS316L. However, these methods often result in material wastage and limitations in geometric complexity. The emergence of AM has revolutionized the production of SS316L components. AM for SS316L encompasses different technologies such as Powder Bed Fusion (PBF), Directed Energy Deposition (DED), Fused Deposition Modeling (FDM), and Binder Jetting (BJ) [242]. The selection of the appropriate printing technology and parameters is crucial for ensuring a successful process during which crack-free components with extremely low porosity can be manufactured [243]. Therefore, it is essential to apply optimized process parameters to achieve the required mechanical properties since they are strongly dependent on the AM process strategy applied [244]. LPBF involves selectively melting fine metal powders layer by layer using a high-energy laser, facilitating near-net-shape

manufacturing and reducing material waste. Moreover, LPBF offers the flexibility to produce customized components with intricate internal structures that are challenging to achieve with conventional techniques [245]. Despite its advantages, LPBF introduces unique challenges, including residual stresses, anisotropic mechanical properties, and variations in microstructure. These factors significantly influence the mechanical behaviour of SS316L, including its yield strength, ductility, and overall performance. Addressing these challenges requires a comprehensive understanding of the material's mechanical properties and their dependence on the printing orientation and post-processing conditions.
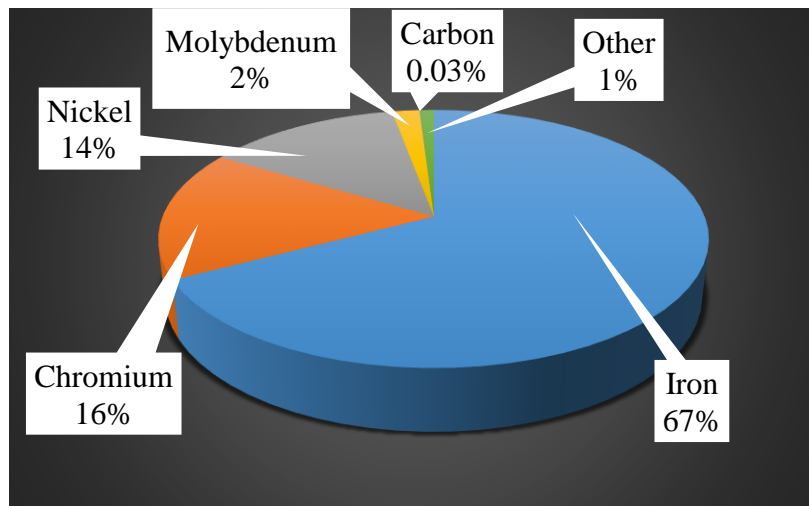


***Figure 8.1.** Chemical composition of SS316L.*

The mechanical characterisation of materials is still primarily performed using uniaxial testing methods in research and commercial facilities. Uniaxial tensile tests conducted on SS316L manufactured using Selective Laser Melting (SLM) [246], Directed Laser Deposition (DLD) [247], Laser Engineered Net Shaping (LENS) [248], and High-Power Direct Laser Deposition [249] have demonstrated superior mechanical properties in the horizontal and 45° orientations compared to the vertical orientation. One should highlight, that uniaxial testing methods provide only limited data concerning the mechanical strength and damage of materials in a single direction which does not simulate the real-world multiaxial stress conditions encountered by materials in most engineering applications. To fully understand all aspects of material's behaviour, such as initial texture or anisotropy, yield surface determination in the biaxial or triaxial stress space is important. Determination of the yield surface of SS316L is crucial for predicting its performance under complex loading conditions, especially in safety-critical applications such as pressure vessels, aerospace structures, and medical implants. Yield surface analysis enables identification of anisotropy and directional dependencies in mechanical behaviour, which are particularly pronounced in additively manufactured materials. For LPBF-fabricated SS316L, the anisotropy in mechanical properties arises from the layer-by-layer building process, resulting in heterogeneous microstructures and residual stress distributions.

The yield strength of SS316L is a critical parameter dictating its performance in structural applications. For LPBF-fabricated components, the yield strength varies with printing orientation due to the anisotropic microstructure. Lavery et al., [250] reported yield strength of 325 MPa, and 415 MPa for samples printed along vertical and horizontal directions, respectively. Moreover, on post-processing treatment such as hot isostatic pressing (HIP) they

demonstrated that it reduced anisotropy by homogenizing the microstructure and relieving residual stresses, achieving yield strength values of approximately 225 MPa in both directions.

Kumar et al., [251] examined the mechanical properties of SS316L produced via binder jetting (BJ) and LPBF, highlighting changes due to microstructural variations. The yield strength increased from 273 MPa (wrought) to 511 MPa, and 430 MPa (LPBF) in vertical and horizontal printed specimens, respectively, due to fine cellular structures, while BJ exhibited a lower yield strength equal to 198 MPa in both printed directions due to higher porosity. These findings suggest that while LPBF enhances strength, it shows considerable anisotropy, whereas BJ SS316L leads to isotropic through microstructural advantages. This anisotropy necessitates a thorough understanding of the yield surface of AM SS316L, which describes the combination of stress states under which a material begins to flow plastically.

Yield surface analysis has been extensively studied for isotropic and anisotropic materials. However, the available literature on the experimental identification of yield surface for additively manufactured stainless steel 316L is still limited. Somlo et al. [252] presented a computing attempt to determine yield surfaces for additively manufactured metals, austenitic stainless steel 316L and titanium alloy Ti-6Al-4V, through crystal plasticity modelling. Although some experimental papers devoted to the identification of yield surface based on the uniaxial or biaxial tensile tests of the 316L stainless steel manufactured by selective laser melting could be found, they are not considering printing orientation [253,254].

The experimental studies on yield surface identification for AM materials are also important from the modelling point of view. In the last decade, crystal plasticity has become an indispensable tool for establishing a connection between the microstructure of materials and their macroscopic mechanical strength [252]. It allows for a detailed description of the plastic deformation mechanisms of different AM materials including SS316L. It should be stressed, that despite having the same chemical composition, such material exhibits distinct mechanical properties as compared to its wrought form [239,241,247–249]. Therefore, it is of the highest importance to reveal the deformation mechanisms to further implement them into the material model to precisely predict its behaviour. At larger scales, the heterogeneous microstructure of AM metals can be described using a homogeneous elastic-plastic material model [252]. An anisotropic yield function is usually employed to govern the plastic behaviour, and it can be determined through crystal plasticity simulations or directly from the experiments. There are numerous anisotropic yield criteria available, each utilizing quadratic or non-quadratic yield functions with varying numbers of adjustable parameters. Generally, the complexity and flexibility of a yield function increase with the number of parameters it incorporates. However, calibrating multiple parameters requires extensive experimental testing.

While significant progress has been made in understanding the mechanical behaviour of SS316L, gaps remain in the comprehensive yield surface characterisation of LPBF-fabricated components, particularly concerning their anisotropy and the influence of printing orientation. This study aims to:

- Investigate the yield surface of LPBF SS316L with respect to three different printing orientations.
- Comparison of the yield surface of LPBF SS316L with that of wrought material.
- Assess the impact of plastic pre-deformation on the evolution of initial yield surface.

## 8.2 Materials and Methods

The SS316L was additively manufactured by using the Renishaw AM 250 system with powder feedstock supplied by the same company. The Renishaw AM 250 is a Laser Powder Bed Fusion (LPBF) additive manufacturing system designed for high-precision metal 3D printing, as shown in Figure 8.2. It features a 200 W fibre laser, offering high precision with a 70 µm focal diameter, and 1070 nm wavelength, along with a $250 \times 250$ mm build area, up to 365 mm deep. The inert atmosphere generation creates a vacuum before backfilling with high-purity argon, ensuring a high-quality build environment with minimal argon consumption and reduced oxidation. This system supports all qualified metals, including titanium and aluminium, making it ideal for aerospace and biomedical applications.

***Table 8.1.*** *Process parameters applied during additive manufacturing*

| Region | Layer thickness [µm] | Hatch distance [mm] | Beam Comp [mm] | Focal point [mm] | Power [W] | Point distance [µm] | Exposure time [µs] | Scan speed [mm/s] | Energy density [J/mm³] |
|---|---|---|---|---|---|---|---|---|---|
| Volume Fill Hatch | 50 | 0.11 | 0.025 | 0 | 195 | 60 | 80 | 750 | 47.27 |
| Scanning strategy | | | | Meander | | | | | |

The round bars of diameter and length equal to 13 mm and 70 mm, respectively, were printed in three orientations (Z – vertical, XY – horizontal, ZX – 45°) (Figure 8.3) following the process parameters presented in Table 8.1. Figure 8.4 shows a schematic of one of the half build plates, with a detailed view of the meander scanning strategy. After the AM process, the as-built specimens were subjected to stress relief using a 470°C soak for 6 hours whilst still attached to the build plate following standards. The bars were then wire cut from the build plate and subsequently machined to achieve the thin-walled tubular specimen geometry discussed in Chapter 3. Both, the inner and outer surfaces of the specimens were machined using the same turning parameters.

The experimental investigations involved four stages following the methodology discussed in Chapter 3:

(1) determination of the basic mechanical properties of wrought and AM SS316L;

(2) determination of the initial yield surfaces of wrought and as-printed SS316L;

(3) introduction of tensile pre-deformation in the specimens at 0.35%, 0.5%, and 0.8% plastic strain;

(4) determination of subsequent yield surfaces of the plastic pre-deformed specimens.

Only one specimen was used to determine the subsequent yield surfaces after tensile pre-deformation at several levels of plastic strains. The specimens were loaded to the desired value of plastic strain and then linearly unloaded to zero stress state. Subsequently, yield points were determined by the technique specified in Chapter 3. Based on the stress-strain characteristic,

the yield points for each path at 0.001% and 0.005% plastic offset strains were determined. The yield surface was obtained by fitting the experimental yield points with the Szczepinski anisotropic yield equation [29] using the least squares method as discussed in Chapter 4.



***Figure 8.2.*** *The Renishaw Additive Manufacturing 250 system (works on the LPBF technology).*
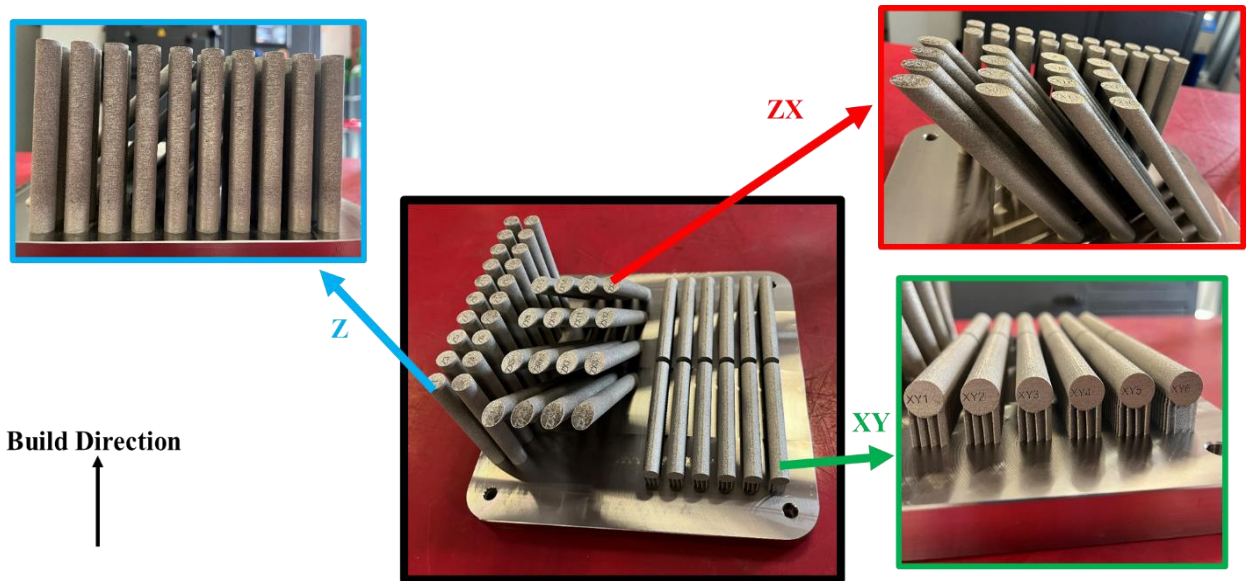


***Figure 8.3.*** *Printing orientation of specimens on the build plate.*
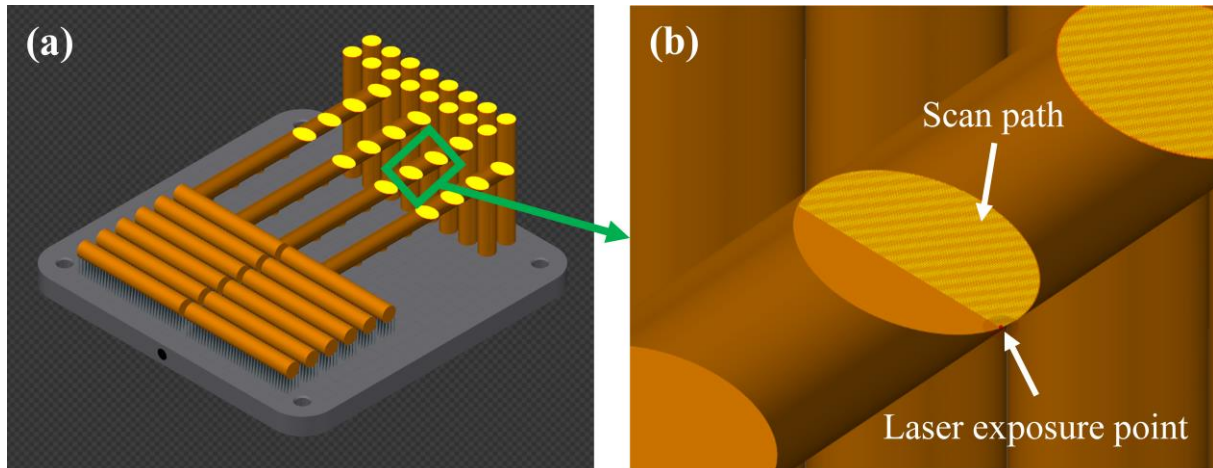
***Figure 8.4.*** *Build plate half way through printing (a); and enlarge view of the meander scanning strategy.*

## 8.3 Results and discussion

### 8.3.1 Basic mechanical parameters of the material

The engineering stress vs strain curves of wrought and three different printing orientations of SS316L are presented in Figure 8.5. All tubular specimens were subjected to uniaxial tensile conditions at room temperature. Tensile strength is essential for assessing a quality of the build part. The yield strength (0.2% YS), ultimate tensile strength (UTS), elongation at failure (EL) and Young modulus (E) are presented in Table 8.2. The results show that the specimens printed in the horizontal direction exhibit slightly higher mechanical properties compared to those printed in the vertical and inclined orientations. The horizontal printing orientation resulted in a 9.5% increase in YS and an 8% increase of UTS compared to the vertical orientation. An increase of 82% in EL was also observed. These results align with previous studies [246] on the same SLM process and various printing orientations, as well as for components manufactured using LENS [248]. Notably, SLM-printed SS316L in the Z direction can exhibit elongation equal to more than 20%, depending on heat treatment, though the Z direction shows greater variability compared to the XY printed specimens [255].

This anisotropy arises from the layer-by-layer manufacturing process, where the microstructural characteristics and interlayer bonding significantly impact mechanical performance [249]. In horizontally printed samples, the loading direction is parallel to the sliced layers, allowing the scanning tracks to act as reinforcing fibers, thereby improving mechanical strength. In contrast, when the orientation is vertical, the loading direction aligns perpendicular to the sliced layers, which resulted in lower tensile properties by weakening the metallurgical bonds between the layers.

In Table 8.2, the comparison of the mechanical properties of SS316L shows that LPBF-processed specimens of this work in XY, ZX and Z orientations have lower tensile characteristics than those of the wrought one. It has to be indicated that these results are much higher in comparison to those reported in literature, where different techniques were used to produce the SS316L specimens.
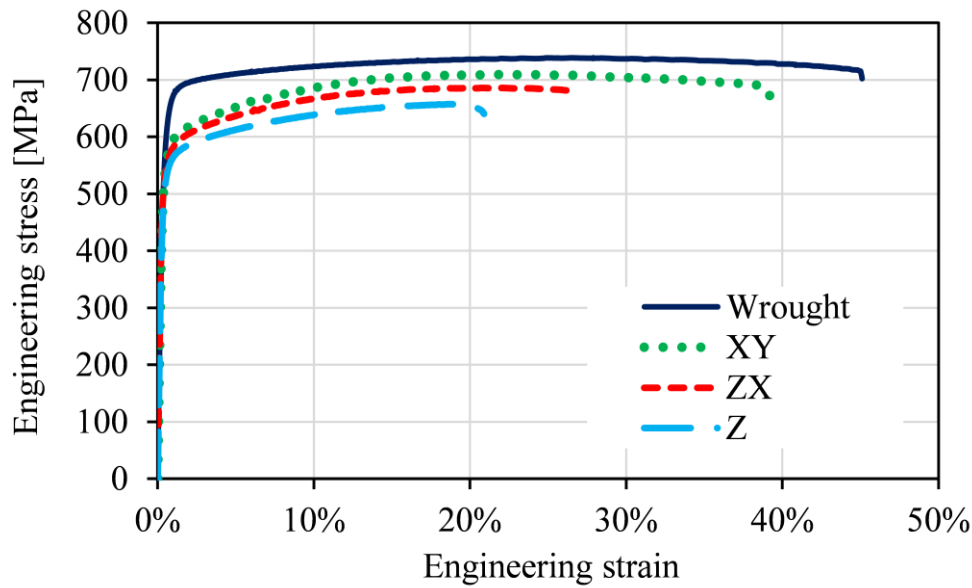
***Figure 8.5.*** *Standard tensile characteristics of the additively manufactured and wrought SS316L.*

***Table 8.2.*** *Comparison of the mechanical properties of wrought and AM SS316L.*

| Material | | 0.2% YS [MPa] | UTS [MPa] | EL [%] | E [GPa] |
|---|---|---|---|---|---|
| Wrought (current work) | | 610 | 740 | 45 | 178 |
| XY (current work) | | 553 | 713 | 40 | 182 |
| ZX (current work) | | 540 | 685 | 25 | 193 |
| Z (current work) | | 505 | 660 | 22 | 185 |
| Wire arc additive manufacturing [256] | XY | 262 | 580 | 34 | - |
| | Z | 252 | 676 | 39 | - |
| Electron beam powder bed fusion [257] | XY | 396 | 652 | 31 | - |
| | Z | 334 | 572 | 29 | - |
| Laser directed energy deposition [258] | XY | 530 | 670 | 34 | - |
| Cast [259] | | 262 | 552 | 55 | - |
| Wrought [259] | | 170-310 | 480-623 | 30-40 | - |

Previous studies have demonstrated that LPBF can induce preferred crystallographic orientation and texture along the build direction, influenced by scanning strategy; however, its effect can vary depending on processing parameters and material system [260–262]. A research by Casati et al., [263] found no significant texture in LPBF-processed SS316L using a meander

scanning strategy with a 67° rotation of the scanning direction after each layer. This rotation modifies thermal gradient directions, preventing texture formation and ensuring an isotropic polycrystalline structure. The additive manufacturing parameters used in this work are similar to the previous study. Therefore, the lack of a pronounced grain orientation in the samples suggests that variations in mechanical behaviour are primarily attributed to microstructural features. It is well known that microstructural defects such as micro-segregation, oxidation, inclusions, and melting defects are more prevalent at interlayer boundaries perpendicular to the build direction [264]. These defects act as stress concentrators, potentially reducing strength and ductility. Since interlayer boundaries in vertically printed samples are oriented orthogonally to the loading direction, stress concentration at these interfaces leads to earlier yielding, reduced strength, and lower elongation at failure. Conversely, in horizontal samples, these boundaries align parallel to the loading direction, minimizing stress localization and enhancing mechanical performance. Thus, this difference in positioning of layer boundaries relative to the loading axis is a key factor in the anisotropic behaviour of LPBF-processed SS316L.

**8.3.2 Equivalent mechanical parameters of the material tested under combined loading**

Figure 8.6 presents the equivalent stress-strain curves, comparing the mechanical behaviour of wrought SS316L and LPBF-printed specimens in XY, ZX, and Z orientations under tension, tension-torsion, and pure torsion loading conditions. In wrought SS316L, the stress-strain responses for torsion and tension-torsion loading are close to each other, whereas the tensile curve deviates significantly (Figure 8.6a), indicating different deformation mechanisms. A similar trend is observed in Z-oriented printed specimens (Figure 8.6d), suggesting that the building direction influences mechanical behaviour.
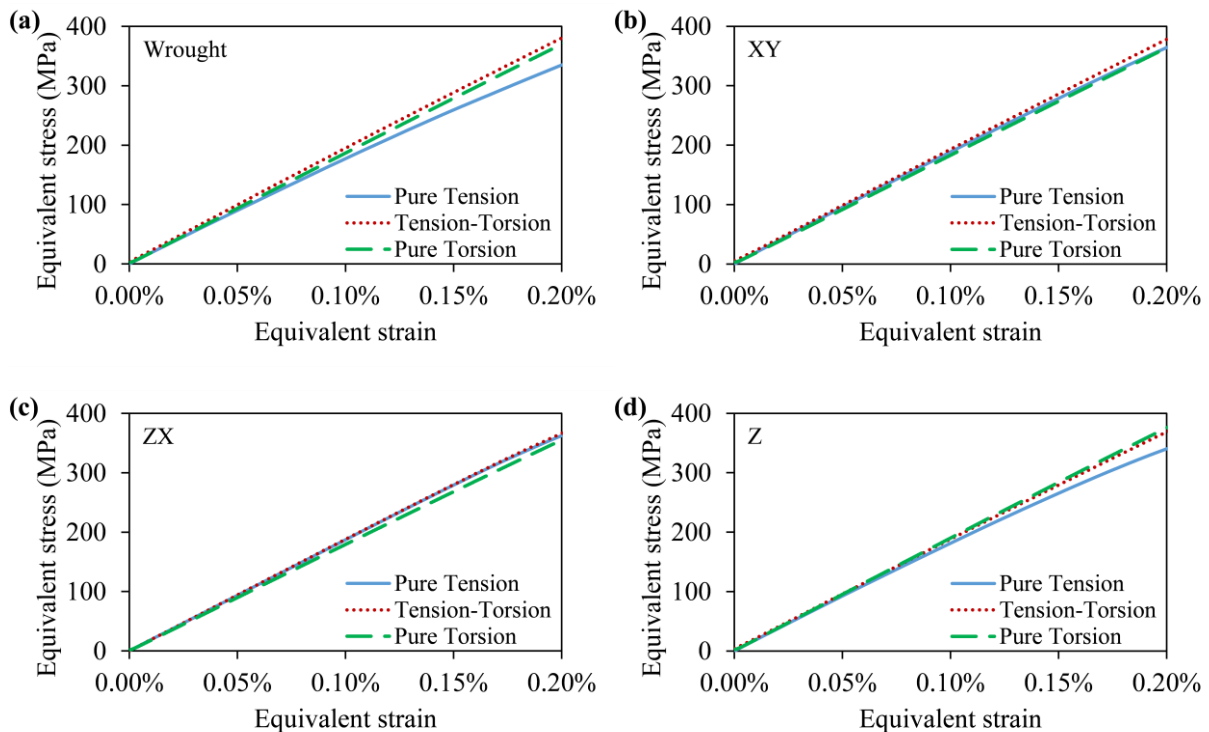


***Figure 8.6.*** *Comparison of material characteristics of SS316L for different loading paths: pure tension; tension-torsion and pure torsion on thin-walled tubular specimens of: (a) wrought steel; (b); (c) and (d) printed steel along XY; ZX and Z orientations, respectively.*

In contrast, XY- and ZX-oriented specimens show minimal deviation between loading conditions at limited effective strain values, implying a more uniform response (Figure 8.6b and Figure 8.6c). These findings demonstrate that the same material can exhibit distinct mechanical responses depending on the loading conditions, primarily due to the initial anisotropy present in the material. This anisotropy affects stress accommodation, strain localization, and overall deformation behaviour, leading to variations in stress distribution under different loading paths. A more detailed analysis of this anisotropic behaviour will be provided in Section 8.3.4, focusing on the yield surface characterisation of the as-printed material. Understanding of these differences is important for accurate prediction of material performance under complex loading scenarios, particularly in applications requiring multi-axial loading resistance.

### 8.3.3 Results of the material under tensile pre-deformation

The stress-strain and plastic strain curves of wrought SS316L and LPBF-printed SS316L specimens (in XY, ZX, and Z orientations) subjected to cyclic loading-unloading tensile tests for the purpose of plastic pre-strain (0.35%, 0.5%, and 0.8%), reveal key insights into their mechanical behaviour, as shown in Figure 8.7. These results provide a detailed understanding of elastic-plastic deformation, strain recovery, and residual plasticity, essential for predicting material performance under repeated loading conditions.

As it can be observed from Figure 8.7, all specimens demonstrate a smooth, continuous stress-strain response with a well-defined elastic-plastic transition. Each curve initially exhibits an elastic region followed by plastic deformation, where stress increases non-linearly. Whereas, after unloading to zero stress, the material does not return to its original strain but retains permanent plastic deformation (as seen by the shift in strain values for different curves). Upon unloading executed after different levels of plastic pre-strain, the wrought SS316L exhibits strong elastic recovery with residual plastic strain (Figures 8.7a and 8.7b), highlighting its superior work hardening and uniform deformation capability. The plastic strain accumulation per cycle is relatively low, suggesting greater microstructural stability and reduced dislocation pile-up, making it highly suitable for applications requiring excellent fatigue resistance. In contrast, the LPBF-printed specimens show notable differences in their cyclic stress-strain behaviour due to anisotropy and process-induced microstructural heterogeneities. The LPBF specimens display increased plastic strain accumulation per loading cycle with weak strain recovery potential, indicating a lower resistance to plastic deformation compared to the wrought specimen. The XY and ZX orientations show comparable mechanical behaviour, while the Z orientation exhibits significantly reduced mechanical performance, emphasizing the role of layer orientation and microstructural integrity in determining the cyclic stress-strain response. Compared to the wrought material, the LPBF-specimens show a lower yield point, suggesting a degree of microstructural softening due to the laser scanning strategy and heat accumulation.

### 8.3.4 Yield surface of SS316L in the as-received state

The stress-strain dependence for the as-received wrought and as-printed SS316L was investigated in each of the 17 distinct stress paths in a narrow plastic strain range to determine the yield points for further calculations of the yield surface. The yield points were determined using a loading-unloading method in various strain directions (being a different combinations of axial and shear loads) via the specified offset strain approach. Figure 8.8 illustrates the responses of SS316L in a biaxial stress plane under the strain-controlled loading program

detailed in Chapter 3. The loading and unloading paths show negligible deviation from linearity across all directions, indicating minimal plastic deformation during the probing of initial yield surface. The total plastic strain observed was 0.015%, and the Poisson's ratio equal to 0.25 was used for calculations along all evaluated directions.
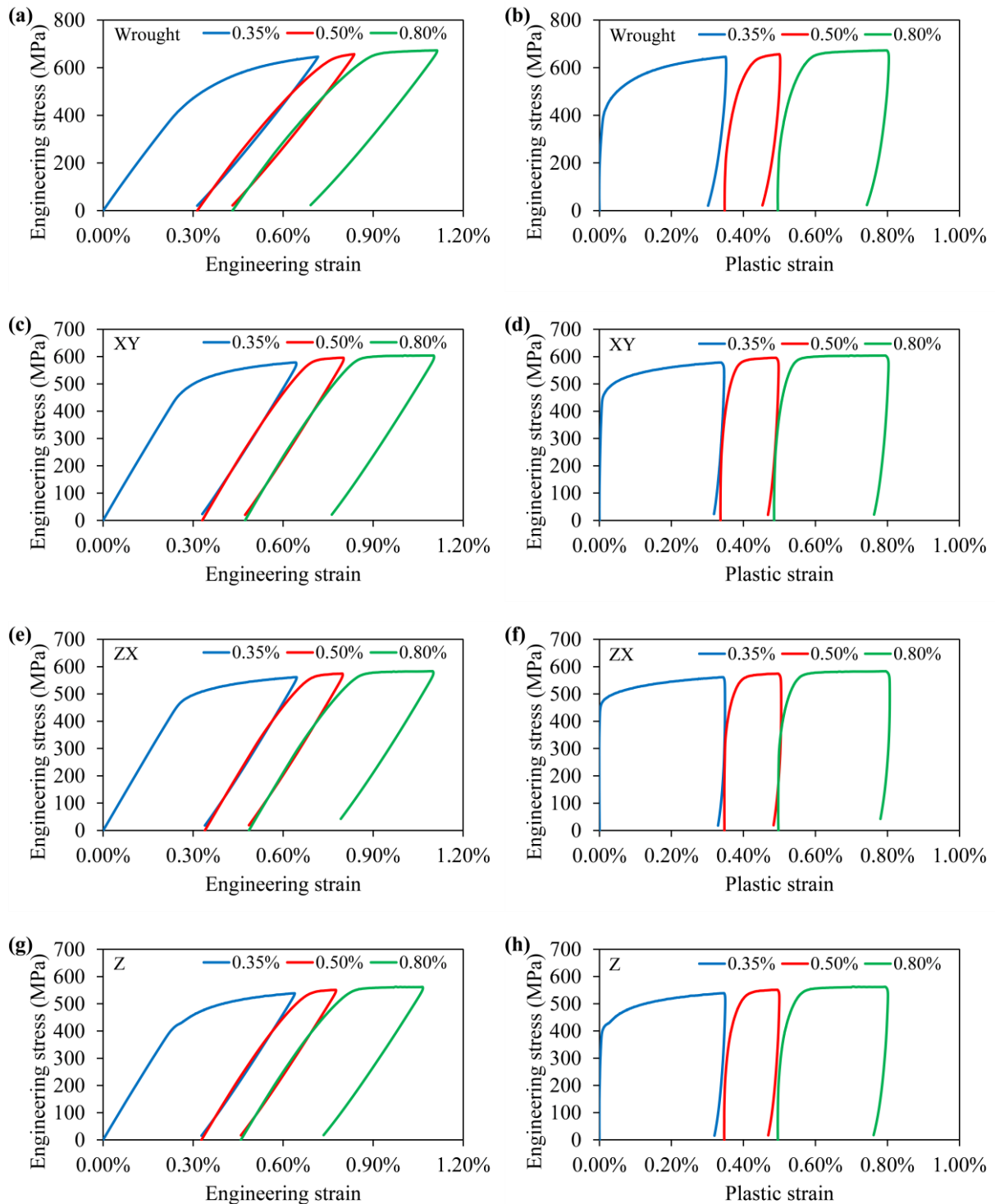


***Figure 8.7.*** *Material response of tensile plastic pre-deformation and unloading after different values of plastic strain for: wrought steel (a, b); and printed steel along XY (c, d); ZX (e, f) and Z (g, h) orientations, respectively.*
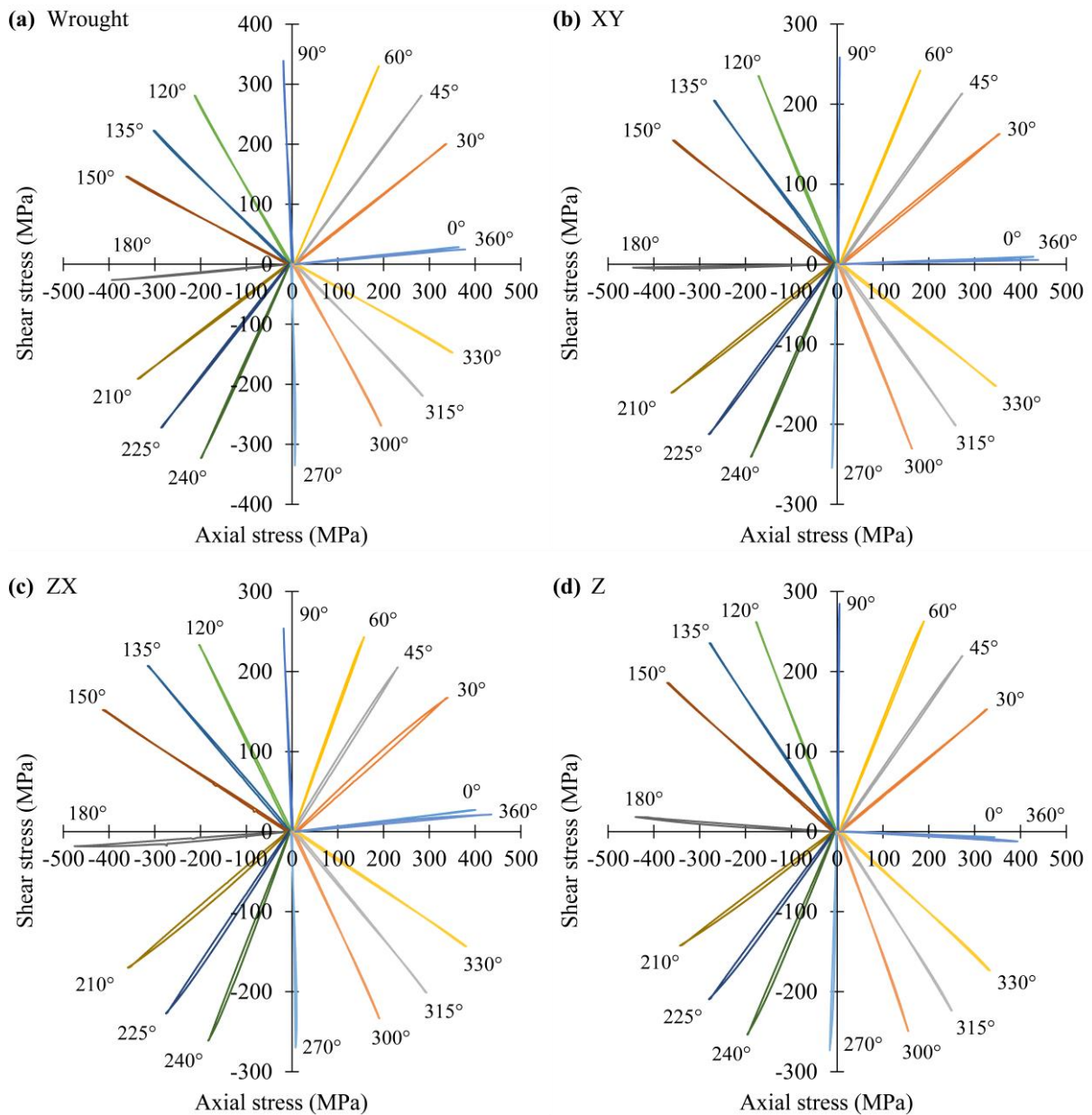
***Figure 8.8.*** *Stress responses to the strain-controlled loading program used for determination of the initial yield surface of SS316L.*

The yield points of the as-received wrought and as-printed SS316L were determined at offset strain values of 0.001% and 0.005% for each stress path, as shown in Figure 8.9. After experimentally determination of the yield points in various directions, ellipses were fitted via the least squares method using the Szczepinski anisotropic yield equation, as detailed in Chapter 4. The primary parameters of these ellipses are summarized in Table 8.3. The ellipses representing yield surfaces demonstrate a clear dependence on the chosen yield definition. For the wrought SS316L, the yield surfaces at 0.001% and 0.005% offset strains (Figure 8.9a) show a relatively symmetric and smooth distribution of yield points in the axial-shear stress plane. The axis ratio is nearly 1 for yield surface at 0.005% offset strain. The yield surfaces of LPBF-printed SS316L specimens exhibit a slightly asymmetric distribution of yield points, with a broader spread along the axial stress axis compared to the shear stress axis. This suggests that the material exhibits higher resistance to the axial deformation than that to the shear one. Additionally, the yield points of as-printed SS316L, determined at offset strain values of

0.001% and 0.005%, exhibit close proximity along the shear stress axis. In contrast, along the axial stress axis, the yield points for these two offset strain definitions are significantly separated, indicating a greater sensitivity to yield definition in axial loading conditions.
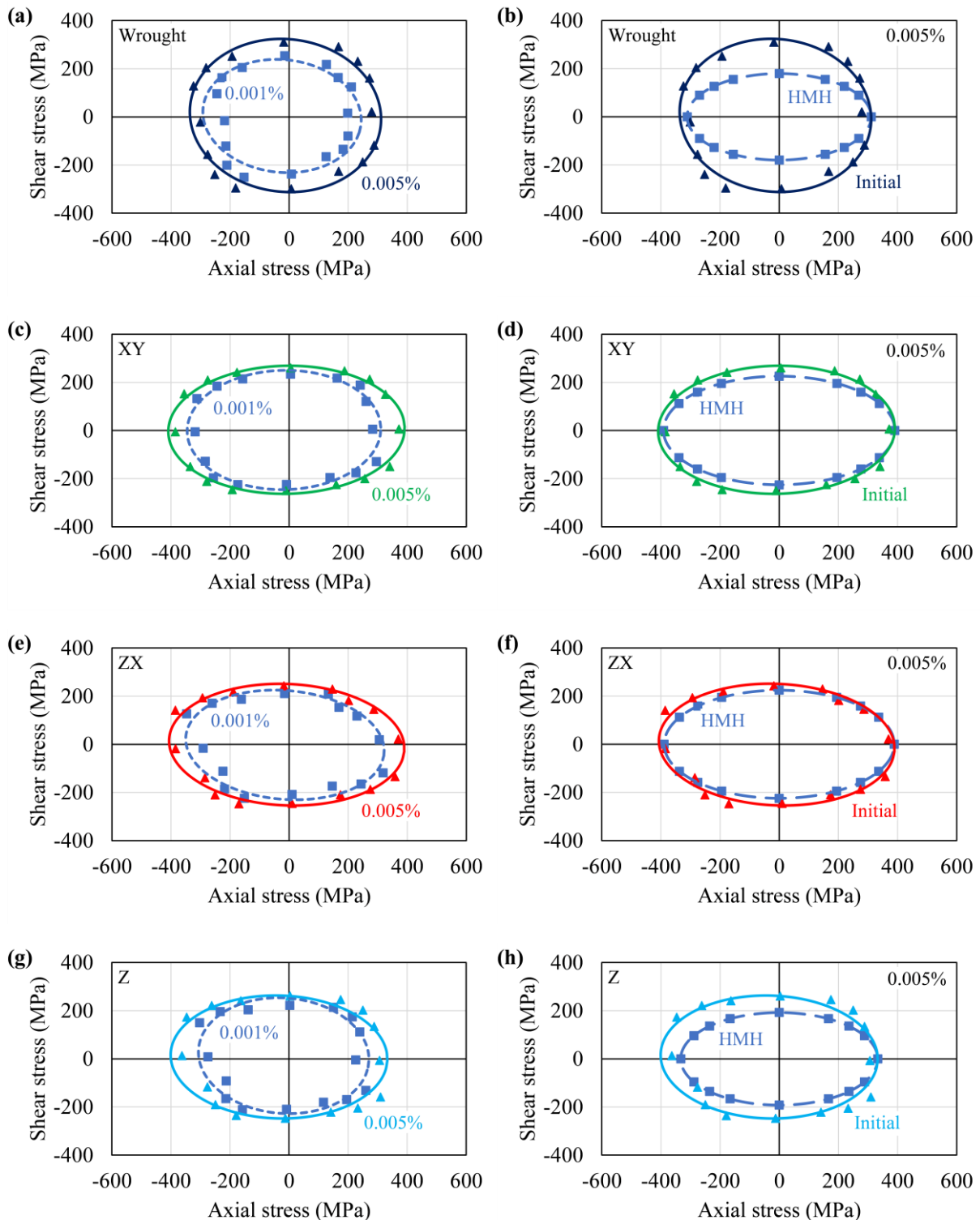


***Figure 8.9.*** *Yield surfaces of SS316L in the 'as-received' state with yield points obtained for 0.005% and 0.001% plastic offset strains (a, c, e, g); Initial yield surface (0.005% offset strain) of the SS316L compared with the Huber-von Mises-Hencky (HMH) isotropic yield locus (b, d, f, h).*

The initial yield surface determined at 0.005% offset strain is compared with the Huber-von Mises-Hencky (HMH) isotropic yield locus, which assumes material isotropy (Figures 8.9b, 8.9d, 8.9f, 8.9h). The HMH isotropic yield surface is drawn by fixing the experimentally obtained yield point in tension. The initial yield surface of wrought SS316L deviates more noticeably from the HMH isotropic yield locus, particularly in the shear stress region. This deviation confirms the presence of initial anisotropy in the as-received state of wrought SS316L. The observed initial anisotropy is attributed to distinct hardening behaviour in shear strength, which likely results from the manufacturing processes applied to the material. In the case of XY- and ZX- orientations a close agreement with the HMH locus was obtained, suggesting near-isotropic behaviour. In contrast, in the Z orientation, the yield surface deviates from the HMH isotropic yield locus, in the compressive and the shear stress regions. This deviation suggests that the material's yielding in the Z orientation is influenced by the layered microstructure, which may introduce directional strengthening mechanisms such as grain boundary strengthening or texture effects. The Z orientation, being parallel to the build direction, may exhibit different deformation mechanisms compared to the XY and ZX orientations, leading to significant variations of yield points. Since the yield surface axis ratios of the printed materials (1.51 – XY, 1.58 – ZX, 1.44 – Z) are lower than the same ratio for the isotropic material according to the HMH yield condition (1.73), an occurrence of some initial anisotropy was confirmed.

Furthermore, the deviations from the HMH isotropic yield locus observed in the LPBF-printed specimens suggest that conventional yield criteria may not be sufficient to predict accurately the yield behaviour of AM materials. This highlights a need for development of the advanced yield criteria that account for the anisotropic microstructure and directional dependence of mechanical properties in AM materials.
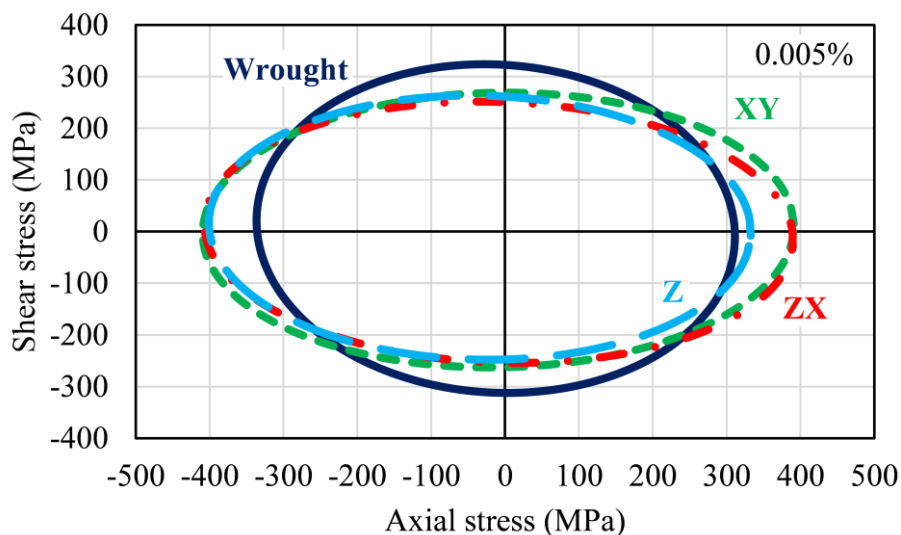


***Figure 8.10.*** *Comparison of the initial yield surfaces for three printing orientations and the same material in the wrought state for 0.005% plastic offset strain.*

Yield surfaces obtained for 0.005% plastic offset strain of wrought and AM SS316L in three directions were compared in Figure 8.10. The yield stress at this offset strain was found to be 280 MPa (wrought), 372 MPa (XY), 370 MPa (ZX), 307 MPa (Z) in tension and -301 MPa (wrought), -385 MPa (XY), -385 MPa (ZX), -363 MPa (Z) in compression. It exposes the

presence of tension-compression asymmetry in the initial state of materials. The yield stresses in torsion and reverse torsion were equal to 310 MPa, 260 MPa, 243 MPa, 261 MPa and -299 MPa, -250 MPa, -246 MPa, -247 MPa, respectively, for the same offset strain. It can be observed that the tensile yield strength at 0.005% plastic offset strain of wrought SS316L is lower than those of AM 316L, which is contrary to the results obtained for the conventional tensile strength (0.2% offset strain), reported in the Figure 8.5 and Table 8.2. This is due to the effect of the selected yield point definition, as Figure 8.11 shows the stress-strain response of materials under tensile loading at smaller strain value. A close-up view of the tensile curves shows that the samples built using LPBF technology have a higher stress values at the very initial stage of elastic deformation in comparison to the wrought material (Figure 8.11).
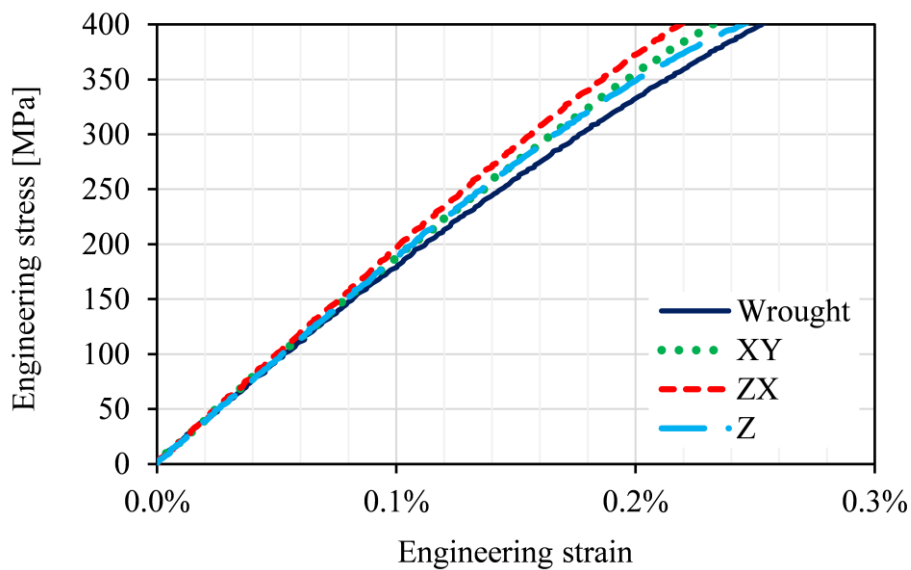


**Figure 8.11.** *Tensile characteristics of the additively manufactured and wrought SS316L for limited strain range.*

It can be observed in Figure 8.10, that the sizes of yield surfaces elaborated for LPBF specimens increased along tensile and compressive directions and shrunk in directions where torsion was applied, as compared to the specimen in wrought, as-received conditions. Such behaviour was probably associated with material anisotropy, and thus, different textures [265] and crystal structures [252]. The shape of yield surfaces for all printing orientations strongly indicates the texture presence [266]. However, it could be observed, that the specimen built in the Z orientation exhibits a notable shift of yield surface centre in the compression direction in comparison to that of other specimens (Table 8.3). It should be emphasised, that the anisotropic character of mechanical properties in AM SS316L is directly attributed to texture. However, as reported by Casati et al. [263], no significant texture was observed in the vertical and horizontal printed SS316L utilizing the LPBF process with a meander scanning strategy, incorporating a 67° rotation of the scanning direction after each layer. Therefore, considering the differences in mechanical properties due to the intrinsic anisotropy at different printing orientations, one should indicate an undoubtful effects of microstructure, melt pool, and temperature gradient that are directly related to such issues. Recent studies by Liu et al. [267] have shown, that a depth of the melt pool and remelting time interval can effectively control the grain size and dislocation density of SS316L manufactured by using dual-laser powder bed fusion. With the adoption of a 50 ms time interval, an increase of about 43 MPa in ultimate tensile strength could be achieved. During the LPBF-M process, the overlap of melt track boundaries could be found.

The occurrence of such partial remelting between subsequent scanning tracks leads to the creation of a melting trajectory that exceeds the size of the laser spot due to the penetration depth being larger than the layer thickness [268]. Consequently, there is a remelting of the previous layer. This phenomenon enables grain growth in parallel or perpendicular orientations to the build direction in different dimensions, contributing to the anisotropic mechanical property [268,269]. Furthermore, it has been observed, that columnar grains grow in the direction of the temperature gradient, which also may affect the mechanical response of material when it is deformed along the printing orientation.

**Table 8.3.** *Ellipse parameters for the initial yield surface of SS316L for 0.005% plastic offset strain.*

| Material | Centre $(x_0, y_0)$ [MPa] | Rotation angle $(\emptyset)$ [Radian] | Semi-axes $(a, b)$ [MPa] | Axis ratio $(a/b)$ |
|---|---|---|---|---|
| Wrought | -12.63, 5.83 | -0.61 | 329.11, 312.65 | 1.05 |
| XY | -9.07, 3.14 | 0.03 | 400.34, 265.93 | 1.51 |
| ZX | -8.32, -1.39 | -0.07 | 398.93, 251.89 | 1.58 |
| Z | -34.05, 7.60 | -0.04 | 367.12, 255.28 | 1.44 |

The variation in the effective Young's modulus for wrought SS316L and LPBF-printed SS316L specimens in XY, ZX, and Z orientations has been analysed across multiple loading paths within the axial-shear stress plane. As shown in Figure 8.12, the results demonstrate a clear dependency of the Young's modulus on both the material processing route and the loading direction applied. For the wrought SS316L specimen, the effective Young's modulus varies between approximately 170 GPa and 190 GPa, with notable oscillations across different loading directions. The highest stiffness is observed near 45° and 225°, whereas the lowest modulus values are recorded around 150° and 330°. This anisotropic behaviour in the wrought material, while more pronounced than in the LPBF-printed samples, may arise due to strongly oriented texture introduced during manufacturing processes. The XY- and ZX- oriented specimens exhibited similar trend of variation of the effective Young's modulus as observed in the wrought specimen. An opposite trend was observed in the Z-oriented specimen. The XY- and ZX-oriented specimens maintain a relatively high values of the Young's modulus (186–191 GPa) in the axial loading directions, however, show a reduction near 120° and 300°. This behaviour suggests that the XY- and ZX- oriented specimens retain significant stiffness in the loading paths dominated by axial tension and compression but exhibit reductions in the effective stiffness under shear-dominated conditions. The Z- oriented specimens display a relatively low fluctuation being within the range from 181 GPa to 191 GPa. The stronger modulus variation suggests that the mechanical response in the LPBF-printed SS316L is more sensitive to the underlying grain orientation, defect distribution, and residual stress accumulation, which may result from the repeated laser scanning and subsequent cooling cycles.
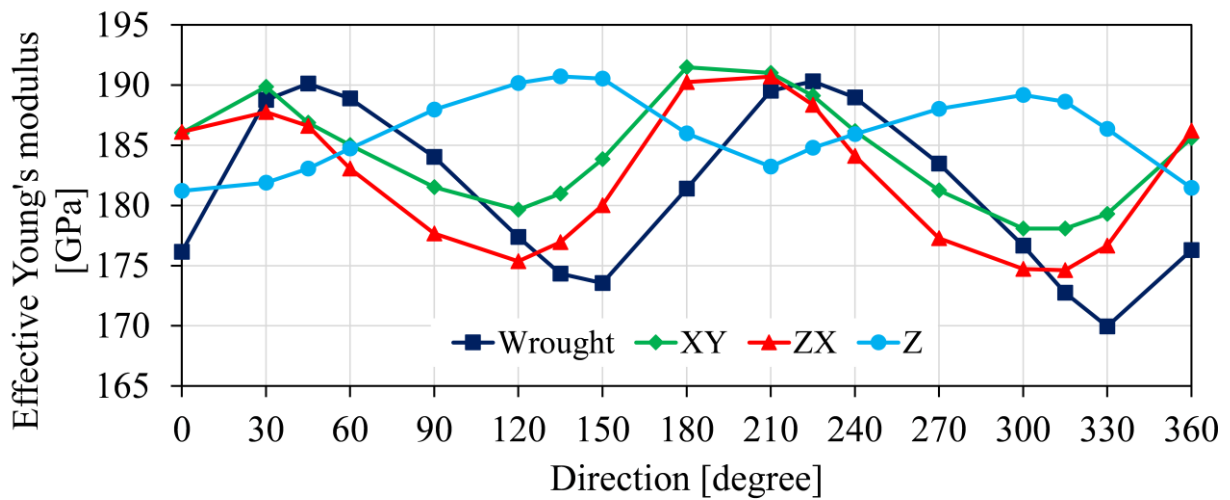
***Figure 8.12.*** *The effective Young's modulus values of the SS316L in various loading directions of the strain plane considered.*

### 8.3.5 Evolution of the initial yield surface reflecting pre-deformation

The analysis of the subsequent yield surfaces in the axial-shear stress plane for both wrought and LPBF-printed SS316L in different orientations provides critical insights into the material's mechanical response under plastic deformation. The results presented in Figure 8.13 provide the evolution of yield surfaces obtained for the as-received state of wrought SS316L and the as-printed specimens in XY, ZX, and Z orientations using LPBF. The yield surfaces changes were studied for three strain levels of the tensile plastic pre-deformation: 0.35%, 0.5%, and 0.8%. All yield surfaces were determined for 0.001% plastic offset strain. This method ensures an accurate representation of the plastic behaviour and its evolution due to prior deformation.

The initial yield surface evolution of the wrought SS316L specimen due to the tensile plastic pre-deformation (Figure 8.13a) demonstrates a reduction of its dimensions, particularly in the compression and shear stress directions. Such contraction signifies strain softening effect in directions orthogonal to the pre-deformation loading path, reflecting the kinematic character of softening. It means that while plastic deformation strengthens the material in the tensile direction, it reduces the yield stress in the transverse and shear directions, likely due to anisotropic dislocation interactions. Notably, at 0.35% plastic strain, the yield surface exhibits its smallest size, demonstrating an immediate softening effect. As the pre-strain increases to 0.5%, the yield surface undergoes a relatively symmetric and uniform expansion, indicating a shift towards isotropic hardening. At this stage, the yield stress surpasses that of the initial yield surface in the tensile direction. However, a further increase in plastic strain to 0.8% results in a minor softening compared to 0.5%, although the yield stress remains higher than that at 0.35% obtained. Additionally, the yield surfaces rotate, with the major axis oriented approximately 24° clockwise relative to the tensile stress direction applied, suggesting a redistribution of internal stresses and possible back stress effects.
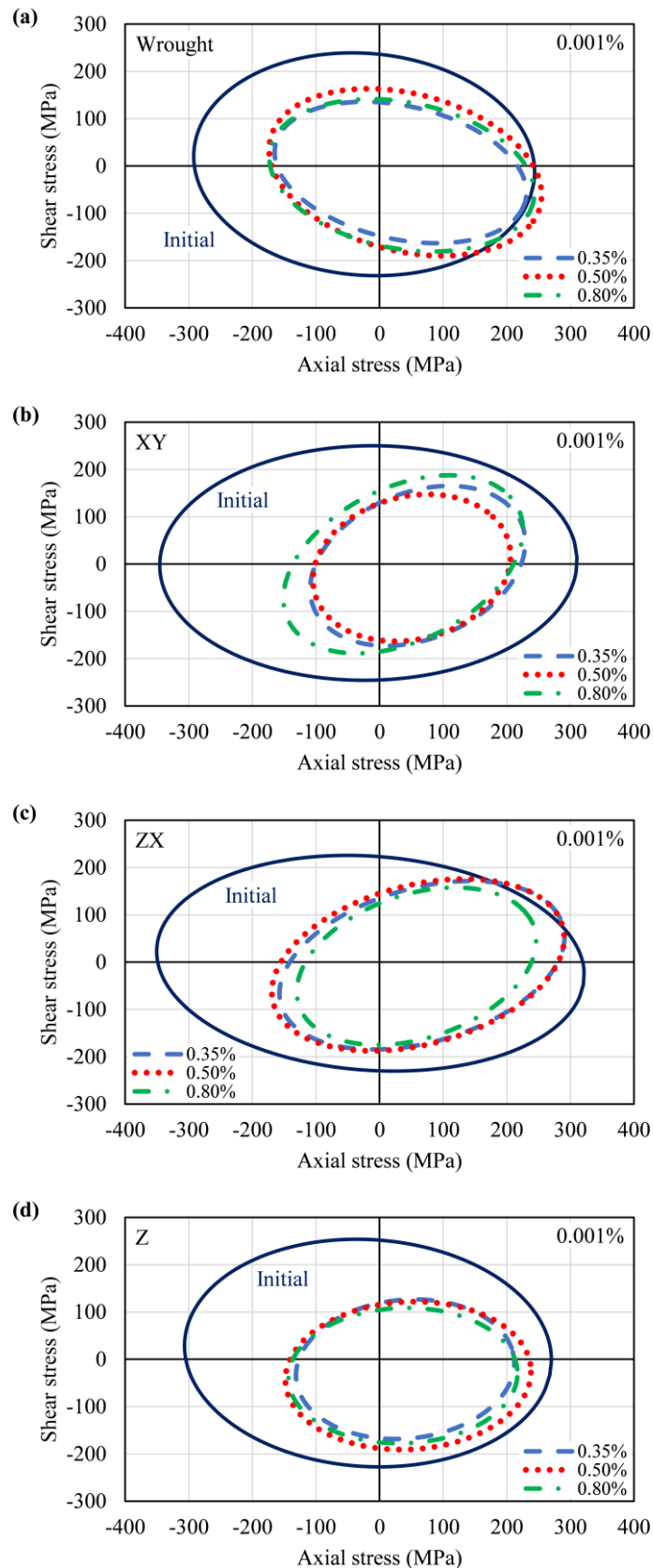
***Figure 8.13.*** *Comparative analysis of the initial yield surfaces of the SS 316L with the yield surfaces of the same material subjected to pre-deformation through the monotonic tension up to plastic pre-strain equal to 0.35%, 0.5%, and 0.8% for: (a) wrought steel.; (b); (c) and (d) printed steel along XY; ZX and Z orientations, respectively.*

The LPBF-printed SS316L specimen in the XY orientation (Figure 8.13b) exhibits an anisotropic yield surface evolution following tensile plastic pre-deformation. The contraction of the yield surface is non-uniform, with the centre shifting slightly towards the positive axial stress direction at 0.35% plastic strain. The centre shift from the initial yield surface origin suggests a preferential softening opposite to the applied tensile stress, which may be attributed to the residual stress state and microstructural anisotropy inherent in LPBF processing. Among the yield surfaces for pre-deformed material, the largest dimensions exhibit that after 0.8% prior plastic deformation, whereas the smallest ones that after 0.5% plastic pre-deformation. Despite this variation, all yield surfaces obtained after tensile pre-deformation remain smaller than the initial yield surface, emphasizing the persistent influence of microstructural anisotropy and potential texture-induced effects. Furthermore, the major axes of these yield surfaces rotate approximately 45° counter-clockwise with respect to the applied tensile pre-deformation direction, signifying a complex interaction between strain-induced softening and the anisotropic grain morphology of the LPBF-printed material.

The ZX-oriented LPBF-printed SS316L specimen (Figure 8.13c) displays a comparable response to the XY orientation, particularly in terms of the rotational behaviour of the subsequent yield surfaces. The major axes of these yield surfaces also undergo a counter-clockwise rotation of approximately 30°. However, some notable differences are observed in these yield surfaces with increasing plastic pre-deformation. The yield surfaces after 0.35% and 0.5% plastic pre-deformation exhibit nearly identical characteristics, with higher yield stress levels than the initial yield surface along certain stress paths. This suggests that the material retains a substantial degree of strain hardening along specific directions at lower pre-strain levels. However, after 0.8% plastic pre-strain, the yield surface exhibits a noticeable contraction, becoming the smallest among all pre-strain levels considered in this research. This behaviour may be associated with strain localization effects, microstructural evolution, and the potential onset of damage mechanisms that reduce the material's ability to sustain further plastic deformation. The distinct evolution of yield surfaces in this orientation highlights the influence of layer-wise grain structure and residual stress distribution, which govern the hardening and softening characteristics of LPBF-printed materials.

The yield surface evolution for LPBF-printed SS316L in the Z orientation (Figure 8.13d) further emphasizes the influence of plastic pre-straining on material anisotropy. After tensile plastic pre-straining, a general softening trend is observed, with a lowest degree of this effect occurring after 0.5% plastic pre-deformation. At 0.35% plastic pre-strain, the yield surface contracts in an almost isotropic manner while slightly shifting towards the positive axial stress direction, indicative of uniform softening with a minor directional bias. With an increase of pre-strain to 0.5%, the yield surface expands compared to the 0.35% condition, demonstrating a transient hardening effect. However, at 0.8% plastic pre-strain, the yield surface closely resembles that at 0.35%, suggesting that strain hardening and subsequent recovery effects may balance each other out at higher plastic strains. These findings indicate that the Z-oriented LPBF specimens exhibit a complex interplay between strain hardening, residual stress relaxation, and microstructural anisotropy, which collectively influence the mechanical response under plastic deformation.

Khan et al. [30] investigated the yield surfaces at 0.001% plastic offset strain after unloading through linear, bi-linear and non-linear path to zero stress from the 6% true tensile strain for a very low work hardening  aluminium alloy (Al-6061-T6511) and showed contraction along the

prior loading direction with plastic deformation. However, in another study by Khan et al. [31] on subsequent yield surfaces of a high work hardening aluminium alloy (annealed Al-1100) after unloading from 16% tensile pre-strain showed expansion, positive cross-effect, and translation in the pre-loading direction. Also, Ishikawa [27] determined the subsequent yield surfaces after complete unloading on an initially isotropic SUS 304 steel using 0.005% plastic offset strain. The results showed that approximately 0.4% tensile plastic pre-strain lead to the contraction of the yield surface along the axial stress direction. Therefore, it can be concluded from the published results that the behaviour of subsequent yield surface depends on the material type, pre-deformation level, and the definition of yielding. In this study, the evolution of initial yield surface of wrought SS316L displays a more predictable hardening-softening sequence, with a relatively symmetric yield surface evolution and a clear transition from softening to isotropic hardening. In contrast, the LPBF-printed specimens exhibit pronounced texture, with distinct yield surface shapes, orientations, and hardening/softening effects depending on the build direction.

The experimentally determined yield points for both the initial and plastically pre-deformed states of wrought SS316L and LPBF-printed SS316L in XY, ZX, and Z orientations were fitted using the Szczepinski yield function. The fitting procedure employed the least squares method to describe an elliptical approximation of the yield surface for each tested material condition. Table 8.4 presents the fitting errors, calculated as the sum of the squared distances between the experimentally obtained yield points and the corresponding points on the fitted yield surface. The results indicate that these fitting errors were consistently minimal across all cases, demonstrating a strong correlation between the experimental yield data and the derived elliptical yield surface approximation. The exceptionally low fitting errors not only validate the appropriateness of the Szczepinski yield function in describing the yield surface at different pre-strain levels but also highlight the reliability of the experimental measurements and data processing techniques employed in this study. The results suggest that the identified yield function parameters can be effectively incorporated into finite element modelling (FEM) frameworks for accurate simulations of the mechanical response of SS316L under complex loading conditions.

***Table 8.4.*** *The fitting errors associated with the yield surfaces for the materials tested.*

| Material | Initial | 0.35% deformed | 0.5% deformed | 0.8% deformed |
|---|---|---|---|---|
| Wrought | 0.329 | 0.420 | 1.32 | 0.873 |
| XY | 0.271 | 0.311 | 0.418 | 0.430 |
| ZX | 0.514 | 0.385 | 0.271 | 0.399 |
| Z | 0.658 | 0.589 | 1.04 | 0.669 |

Figure 8.14 provides a comprehensive analysis of the evolution of the yield surface parameters for wrought SS316L and LPBF-printed SS316L in the XY, ZX, and Z orientations under varying levels of tensile plastic pre-deformation (0.35%, 0.5%, and 0.8% plastic strain). The major semi-axis of the yield surface exhibits a general decreasing trend with introduction of tensile plastic pre-strain across all material conditions (Figure 8.14a). Initially, the major semi-axis values for the different materials vary significantly, with wrought SS316L exhibiting the

lowest value (270 MPa), while LPBF-printed specimens display higher initial values in the XY (328 MPa), ZX (338 MPa), and Z (290 MPa) orientations. With the introduction of plastic pre-strain, the major semi-axis decreases, particularly in the LPBF-printed specimens the reduction is most pronounced. After 0.35% plastic pre-strain, the XY-oriented specimen experiences the greatest decrease, approximately 41% lower than its initial value. As plastic pre-strain increases to 0.5%, the major semi-axis of the XY specimen continues to decline, while the wrought and other orientations exhibit a slight increase, indicating different strain hardening responses among orientations taken into account. However, after 0.8% plastic pre-strain, the trend reverses, with the major semi-axis stabilizing or slightly recovering in some cases. By this stage, the major semi-axis was reduced to 215 MPa in wrought SS316L, 222 MPa in XY, 206 MPa in ZX, and 180 MPa in Z. The relatively slower rate of decrease observed in the wrought SS316L suggests that it undergoes a more stable softening process, while the LPBF-printed specimens exhibit a greater susceptibility to yield surface contraction, likely due to their distinct microstructural characteristics.
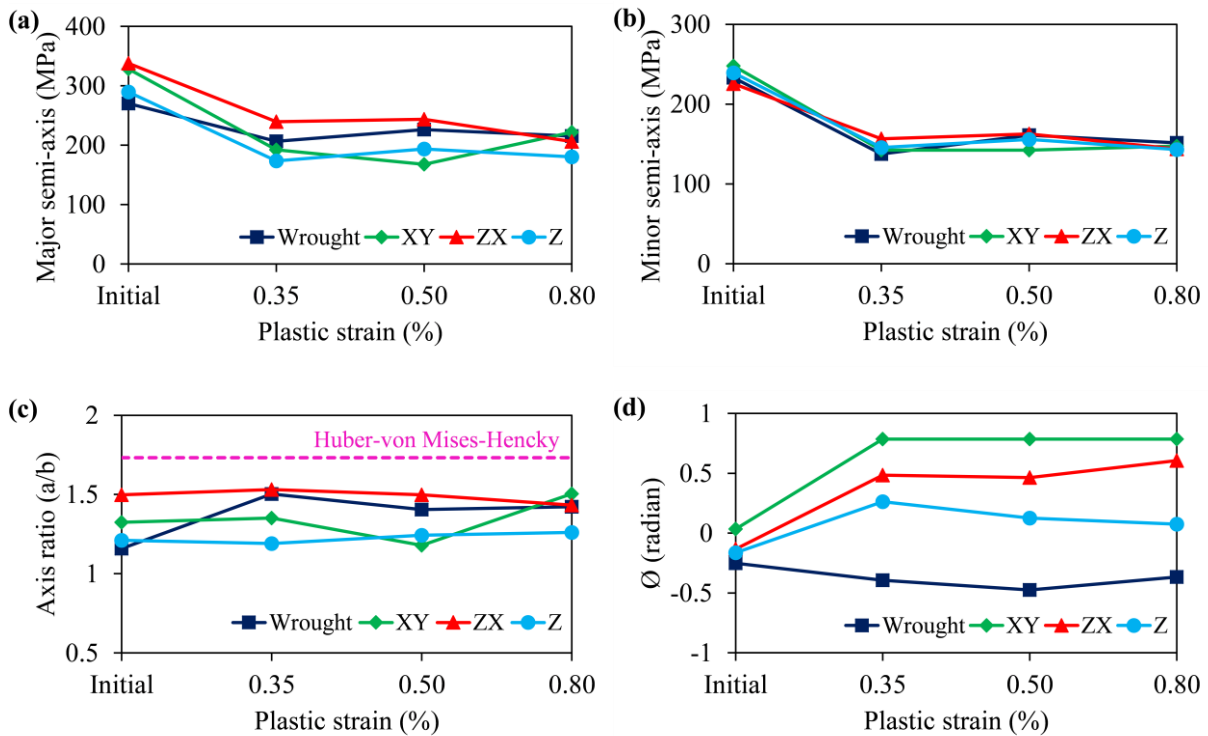


*Figure 8.14. Variation of the yield surface parameters of SS316L due to pre-deformation by monotonic tension up to plastic strain equal to: 0.35%, 0.5%, and 0.8%, respectively.*

The minor semi-axis variations are shown in Figure 8.14b. It can be observed, that initially all materials exhibit relatively similar minor semi-axis values, ranging between 226 MPa and 248 MPa. However, upon applying 0.35% plastic pre-strain, all materials experience a significant decrease in their minor semi-axis values, reflecting softening effects. At 0.5% plastic pre-strain, a slight increase is observed in the wrought, ZX, and Z specimens, suggesting localized strain hardening effects. However, after 0.8% plastic pre-strain, a further decrease occurs. In the XY orientation, the minor semi-axis remains nearly constant. Interestingly, at this stage, the minor semi-axis values for all materials converge within a narrow range from 143 to 151 MPa, indicating that despite initial differences in processing and orientation, all specimens exhibit similar minimum yield strengths after undergoing significant plastic deformation. This suggests

that plastic pre-straining leads to a homogenisation effect in the yield surface characteristics, particularly in shear-dominated stress directions.

The axis ratio, which represents quotient of the major to minor semi-axes and reflects the shape evolution of the yield surface, also varies with increasing plastic pre-strain, as shown in Figure 8.14c. For wrought SS316L, the axis ratio increases from 1.16 in the initial state to 1.5 for 0.35% plastic pre-strain, then decreases slightly to 1.4 for 0.5% plastic pre-strain before rising again to 1.42 for 0.8% plastic pre-strain. This behaviour suggests that tensile pre-deformation may lead to a homogeneous microstructure, which results in a partial isotropic recovery with plastic pre-strains. In contrast, the LPBF-XY specimen maintains a nearly constant axis ratio of around 1.34 in the initial and 0.35% plastic pre-strain states, but after 0.5% plastic pre-strain, it undergoes a significant drop to 1.18 before increasing again to 1.5 after 0.8% plastic pre-strain. This abrupt variation suggests a more complex interaction between strain softening and hardening mechanisms in the XY orientation, possibly due to its process-dependent microstructural features. The LPBF-ZX and LPBF-Z orientations exhibit relatively stable values of the axis ratio of approximately 1.48 and 1.23, respectively, throughout the plastic pre-straining process, indicating a more consistent anisotropic response in these orientations. Notably, the axis ratio for all tested materials remains lower than the theoretical value of 1.73 for the perfect Huber–von Mises–Hencky isotropic yield surface, indicating significant anisotropic effects in both wrought and LPBF-printed SS316L.

The rotation angle (Ø), measured with respect to the x-axis (axial stress) to the major semi-axis of the yield surface, exhibits notable differences between wrought and LPBF-printed SS316L (Figure 8.14d). For wrought SS316L, the major semi-axis undergoes a progressive clockwise rotation as the tensile plastic pre-strain increases, as evidenced by an increasing negative rotation angle. This suggests that plastic deformation induces a systematic reorientation of the yield surface, likely due to evolving dislocation structures and strain path effects. In contrast, LPBF-printed specimens display counter-clockwise rotation (positive rotation angle) with increasing plastic pre-strain, indicating a fundamentally different response to plastic deformation compared to the wrought material. Interestingly, the rotation angle remains close to zero in the initial state of the LPBF-XY specimen and after 0.8% plastic pre-strain in the LPBF-Z specimen, suggesting that in these specific conditions, the yield surface remains aligned with the principal stress axes. It should be noted, that the most significant change in rotation occurs in the LPBF-XY orientation, where the rotation angle increases from 0 radians in the initial state to 0.79 radians (approximately 45 degrees) after plastic pre-straining, highlighting a pronounced anisotropic effect in this orientation.

The anisotropic nature of the LPBF specimens leads to significant variations in major and minor semi-axes evolution, axis ratio trends, and yield surface rotation. These findings highlight fundamental differences in the mechanical response of conventionally processed and additively manufactured SS316L, providing crucial insights into their strain-hardening/softening behaviour and anisotropic plasticity.

Although the yield surface concept is commonly known, the experimental identification of yield surfaces for additively manufactured materials can be treated as a relatively new approach used in mechanics to characterise the material behaviour subjected to complex loading in stress states separating the elastic and plastic ranges [265,270,271]. One should emphasize, that research in this area is mainly limited to numerical investigations through crystal plasticity [265,270] and

anisotropic [271,272] models. Even though experimental data is used to validate or calibrate the model, it is mainly based on the uniaxial tensile test results. The approach presented in this research is thus important as it provides the experimental data for AM SS316L for which the yield surfaces were determined for three different printing orientations. Future studies should involve the combination of numerical and experimental approaches to establish a new model, which could be validated through data obtained in this research.

## 8.4 Concluding remarks

This chapter provides a comprehensive analysis of the mechanical behaviour of wrought SS316L and LPBF-printed SS316L in XY, ZX, and Z orientations, focusing on their yield surface evolution, strain-hardening mechanism, and anisotropic behaviour under tensile plastic pre-deformation. To the author's knowledge, there are no such prior study available related to experimental investigation of yield surface and its evolution reflecting prior deformation for additively manufactured SS316L. The yield surfaces were determined employing a single specimen approach and sequential probing technique for the plastic offset strain equal to 0.001% and 0.005%. Additionally, tensile plastic pre-deformation at 0.35%, 0.5%, and 0.8% plastic strain was introduced to all materials. The findings highlight key differences between the conventionally manufactured and additively manufactured materials, with significant implications for their structural applications. The main findings can be summarized as follows:

- The layer-by-layer additive manufacturing process introduces directional dependencies in mechanical properties, affecting the strength, stiffness, and plasticity of the material. The Z-oriented specimens exhibit the lowest mechanical performance, primarily due to weaker interlayer bonding, while the XY and ZX orientations show relatively higher yield strength and more uniform hardening behaviour during uniaxial tensile tests. The wrought SS316L shows the highest mechanical properties among all specimens.

- The loading-unloading cyclic behaviour in LPBF-printed SS316L is highly dependent on printing orientation, with wrought SS316L outperforming all LPBF orientations in terms of elastic recovery and reduced plastic strain accumulation. These results highlight the importance of build orientation, post-processing, and accurate anisotropic modelling for structural reliability of AM components in high-cycle loading applications.

- The initial yield surfaces obtained at 0.005% plastic offset strain demonstrate that the yield strengths of LPBF-printed specimens were increased along axial stress direction, but reduced along shear stress one, in comparison to the wrought SS316L. Such behaviour was associated with a certain form of material anisotropy representing different textures and crystal structures.

- The subsequent yield surfaces obtained at 0.001% plastic offset strain reflecting tensile plastic pre-strain exhibits softening of the wrought and LPBF-printed SS316L specimens. A degree of this effect depends on the material morphology and pre-strain level.

- The minimal discrepancies between experimental yield points and fitted yield surfaces show the ability of the Szczepinski yield function to capture the evolution of yield surfaces at different pre-strain levels. This signify the utilization of a precise mathematical approximations to characterise yield surfaces, particularly for anisotropic materials such as LPBF-printed SS316L, where microstructural variations contribute to directional differences in plasticity.

# Chapter 9

# Conclusions and future work

*The chapter provides a comprehensive overview of the key findings and contributions of the Thesis. It summarizes the achieved objectives outlined in the introductory chapter, highlighting their significance and impact. Additionally, the chapter proposes potential directions for future work, offering ideas and recommendations to extend and enhance the study in subsequent research efforts.*

## 9.1 Conclusions

The doctoral Thesis presents an experimental investigation of the yield surface identification of functional materials and its evolution reflecting plastic pre-deformation under monotonic and complex loadings. The material investigated are CP-Ti, CP-Cu, Ti-Cu bimetal, wrought SS316L, and LPBF-printed SS316L (in XY, ZX, and Z orientations). Pre-deformation was introduced in the materials by monotonic tension and/or combined tension-cyclic torsion loadings until a pre-defined value. The level of pre-deformation was dependent on material characteristics and experimental constraints with the objective of ensuring controlled deformation of the specimens. Yield points were determined for initial and pre-deformed states of materials using sequential probes in the plane stress state, where strain-controlled loading was applied until a limited plastic strain was reached, followed by stress-controlled unloading. The procedure was performed along 17 strain paths (from 0° to 360° in defined angular increments) in the axial-shear strain plane. Yield points using plastic offset strain method were determined from each stress-strain curve. The yield surfaces were obtained by fitting the experimental yield points to the Szczepinski anisotropic yield equation using the least squares method. Yield surface characterisation provides valuable insights into the material's deformation mechanisms, presence of anisotropy, and guiding the optimization of manufacturing parameters and post-processing treatments to enhance performance.

The key findings can be summarised in the following way:

1. **Influence of monotonic and combined loadings on mechanical response:**
   Under combined monotonic tension and cyclic torsion, notable variations in mechanical behaviour were observed. In CP-Ti, cyclic torsion led to a significant reduction of normal stress, particularly as torsional strain amplitude increased from ±0.2% to ±0.4% and frequency varied from 0.5 Hz to 1 Hz. In CP-Cu, cyclic torsion strain amplitude significantly impacts the material's mechanical response, with higher amplitudes (±0.2%) induced pronounced softening, whereas cyclic torsion frequency had a lesser impact. The tensile properties of Ti-Cu bimetal lie in between those of its constituent metals. Bimetal showed a 43% higher tensile yield strength and a 50% increase in ultimate strength compared to CP-Cu. However, combined loading caused a reduction in tensile strength, which became more pronounced with increased torsional strain amplitude and frequency. In SS316L, the additive manufacturing process introduced directional dependencies, leading to reduced tensile properties in Z-oriented specimens

compared to XY- and ZX-oriented, due to weaker interlayer bonding. The wrought SS316L shows the highest tensile properties among all SS316L specimens.

2. **Initial yield surface and anisotropy:**
   The initial yield surface exhibited significant anisotropy in all investigated materials—CP-Ti, CP-Cu, Ti-Cu bimetal, and SS316L. The initial yield surfaces of CP-Ti and CP-Cu showed clear dependence on the chosen yield definition (0.01% and 0.005% plastic offset strain), with observed initial anisotropic behaviour attributed to distinct hardening in shear strength linked to manufacturing processes of the materials or the specimens machining that induce crystallographic textures, residual stresses, and microstructural heterogeneities. Ti-Cu bimetal exhibited tension-compression asymmetry in the initial yield surface (0.01% and 0.005% plastic offset strain), while LPBF-printed SS316L revealed an increased yield strengths along axial stress direction, but reduced along shear stress direction, in comparison to the wrought SS316L (0.001% and 0.005% plastic offset strain). Such behaviour was associated with a certain form of material anisotropy representing different textures and crystal structures. These anisotropic characteristics must be carefully considered in material modelling and application.

3. **Evolution of initial yield surface (hardening and softening mechanisms):**
   Pre-deformation led to hardening and softening effects in different materials. CP-Ti and CP-Cu experienced kinematic hardening under monotonic tension, shifting the yield surface in the pre-strain direction, while combined tension-cyclic torsion (±0.2% and ±0.4% strain amplitudes) in CP-Ti introduced hardening along pure tension direction and softening in all other directions. In CP-Cu, combined tension-cyclic torsion at ±0.1% strain amplitude led to anisotropic hardening, whereas at ±0.2% strain amplitude, softening effects were dominant. Ti-Cu bimetal exhibited kinematic hardening along pre-strain direction and positive cross-effect following 1% tensile pre-deformation but showed significant kinematic softening under cyclic torsion-assisted tension, especially at higher strain amplitudes. For SS316L, tensile plastic pre-strain of 0.35%, 0.5%, and 0.8% led to the material softening, that was dependent on the material morphology.

4. **Microstructural and texture evolution:**
   Microstructural analysis confirmed the correlation between material behaviour and texture evolution. In CP-Ti, Inverse Pole Figure (IPF) maps and (0001) pole figures highlighted preferred grain orientations, reflecting the yield response of the as-received and pre-deformed material. Ti-Cu bimetal exhibited notable microstructural changes due to activation of additional slip systems under higher cyclic torsional strain amplitudes of combined pre-deformation, leading to recrystallization and radial softening.

5. **Validation of Szczepinski anisotropic yield criterion:**
   In order to avoid corners in yield surface a methodology of sequential probes (Figure 3.13) for yield points was adopted. The Szczepiński anisotropic yield criterion provided accurate yield surface approximations for all materials, with minimal fitting errors, validating its effectiveness in capturing complex multiaxial stress states. This is particularly important when analysing the evolution of yield surfaces under different pre-strain conditions, as it enables a quantitative assessment of the directional hardening or softening mechanisms that govern the material's response. The versatility of the proposed yield description was also shown by application to materials with different manufacturing process and crystal structures. As examples of CP-Ti, CP-Cu, Ti-Cu bimetal, and wrought SS316L were manufactured through conventional methods,

whereas, LPBF-printed SS316L was additively manufactured in three various orientations, where microstructural variations contributed to directional differences in plasticity. Materials with various crystal structures investigated are: - a face centered cubic (FCC)-structure type material – CP-Cu, SS316L, a hexagonal close packed (HCP)-structure type material – CP-Ti and HCP-FCC bimetallic (Ti-Cu) structure. The minimal discrepancies between experimental and fitted surfaces for these materials suggest the robustness of the proposed methodology for characterising the yield behaviour. Additionally, accurate yield surface models are integral to finite element simulations, ensuring reliable predictions of component behaviour under operational loads.

These findings provide a deeper understanding of how pre-deformation, strain amplitude, and stress states interact to influence the mechanical properties and yield surface evolution of functional materials. Such insights are necessary for optimal design and performance of components in engineering applications where multiaxial loading and pre-deformed states are common. The study highlights the importance of customizing loading conditions to achieve desired mechanical characteristics, particularly in applications involving anisotropic materials.

## 9.2 Suggestions for future work

A number of aspects involved in the material selection, microstructural analysis, modelling and simulation that could be further explored are listed below:

1. Experimental identification of yield surface analysis of the additional functional materials following the methodology used in the Thesis. Each material responds differently when subjected to complex loading in stress states and it cannot be predicted based on the uniaxial tests only.
2. Experimental identification of yield surfaces in a tri-axial stress state using tubular specimens under combined loading of axial, torsion, and internal pressure.
3. Development of a program of monotonic tensile loading in combination with cyclic loading on the cruciform testing machine in order to determine an effect of symmetrical tension-compression cycles on the tensile characteristic to be determined in the perpendicular direction with respect to the cyclic loading.
4. Study of the bimetallic structures with varying ratio of the thicknesses of the two layers, and also of the different conditions (texture and deformation) of the two layers.
5. Study of the additional additively manufactured materials and effect of various printing parameters (power source, scan pattern, layer thickness, hatch distance, scanning speed, and build orientation) on their yield surfaces and evolution reflecting plastic pre-deformation.
6. Microstructural analysis of CP-Cu, wrought SS316L, and LPBF-printed SS316L (in XY, ZX, and Z orientations) specimens in initial and plastic pre-deformed states for texture analysis.
7. Development of potential finite element modelling (FEM) frameworks for accurate simulations that can describe the observed effect of pre-deformation on mechanical response of materials during complex loading conditions.

# References

[1] Dubey, V. P., Kopec, M., Łazińska, M., and Kowalewski, Z. L., 2023, "Yield Surface Identification of CP-Ti and Its Evolution Reflecting Pre-Deformation under Complex Loading," International Journal of Plasticity, **167**, p. 103677. https://doi.org/10.1016/j.ijplas.2023.103677.

[2] Kopec, M., Dubey, V. P., Pawlik, M., Wood, P., and Kowalewski, Z. L., 2024, "Experimental Identification of Yield Surface for Additively Manufactured Stainless Steel 316L under Tension–Compression-Torsion Conditions Considering Its Printing Orientation," Manufacturing Letters, **41**, pp. 28–32. https://doi.org/10.1016/j.mfglet.2024.07.003.

[3] Naghdi, P. M., Essenburg, F., and Koff, W., 1958, "An Experimental Study of Initial and Subsequent Yield Surfaces in Plasticity," Journal of Applied Mechanics, **25**(2), pp. 201–209. https://doi.org/10.1115/1.4011745.

[4] Ivey, H. J., 1961, "Plastic Stress–Strain Relations and Yield Surfaces for Aluminium Alloys," Journal of Mechanical Engineering Science, **3**(1), pp. 15–31. https://doi.org/10.1243/JMES_JOUR_1961_003_005_02.

[5] Mair, W. M., and Pugh, H. L. D., 1964, "Effect of Pre-Strain on Yield Surfaces in Copper," Journal of Mechanical Engineering Science, **6**(2), pp. 150–163. https://doi.org/10.1243/JMES_JOUR_1964_006_025_02.

[6] Miastkowski, J., and Szczepiński, W., 1965, "An Experimental Study of Yield Surfaces of Prestrained Brass," International Journal of Solids and Structures, **1**(2), pp. 189–194. https://doi.org/10.1016/0020-7683(65)90026-0.

[7] Szczepiński, W., and Miastkowski, J., 1968, "An Experimental Study of the Effect of the Prestraining History on the Yield Surfaces of an Aluminium Alloy," Journal of the Mechanics and Physics of Solids, **16**(3), pp. 153–162. https://doi.org/10.1016/0022-5096(68)90024-0.

[8] Marjanović, R., and Szczepiński, W., 1975, "On the Effect of Biaxial Cyclic Loading on the Yield Surface of M-63 Brass," Acta Mechanica, **23**(1), pp. 65–74. https://doi.org/10.1007/BF01177669.

[9] Williams, J. F., and Svensson, N. L., 1970, "Effect of Tensile Prestrain on the Yield Locus of 1100-f Aluminium," Journal of Strain Analysis, **5**(2), pp. 128–139. https://doi.org/10.1243/03093247V052128.

[10] Williams, J. F., and Svenssoon, N. L., 1971, "Effect of Torsional Prestrain on the Yield Locus of 1100-F Aluminium," Journal of Strain Analysis, **6**(4), pp. 263–272. https://doi.org/10.1243/03093247V064263.

[11] Hecker, S. S., 1971, "Yield Surfaces in Prestrained Aluminum and Copper," Metall Trans, **2**(8), pp. 2077–2086. https://doi.org/10.1007/BF02917534.

[12] Phillips, A., and Juh-Ling, T., 1972, "The Effect of Loading Path on the Yield Surface at Elevated Temperatures," International Journal of Solids and Structures, **8**(4), pp. 463–474. https://doi.org/10.1016/0020-7683(72)90017-0.

[13] Phillips, A., Liu, C. S., and Justusson, J. W., 1972, "An Experimental Investigation of Yield Surfaces at Elevated Temperatures," Acta Mechanica, **14**(2), pp. 119–146. https://doi.org/10.1007/BF01184853.

# References

[14] Phillips, A., Tang, J. L., and Ricciuti, M., 1974, "Some New Observations on Yield Surfaces," Acta Mechanica, **20**(1), pp. 23–39. https://doi.org/10.1007/BF01374960.

[15] Phillips, A., and Ricciuti, M., 1976, "Fundamental Experiments in Plasticity and Creep of Aluminum—Extension of Previous Results," International Journal of Solids and Structures, **12**(3), pp. 159–171. https://doi.org/10.1016/0020-7683(76)90060-3.

[16] Phillips, A., and Moon, H., 1977, "An Experimental Investigation Concerning Yield Surfaces and Loading Surfaces," Acta Mechanica, **27**(1), pp. 91–102. https://doi.org/10.1007/BF01180078.

[17] Phillips, A., and Lee, C. W., 1979, "Yield Surfaces and Loading Surfaces. Experiments and Recommendations," International Journal of Solids and Structures, **15**(9), pp. 715–729. https://doi.org/10.1016/0020-7683(79)90069-6.

[18] Phillips, A., and Kawahara, W. A., 1984, "The Effect of Thermal Loading on the Yield Surface of Aluminium. An Experimental Investigation," Acta Mechanica, **50**(3), pp. 249–270. https://doi.org/10.1007/BF01170964.

[19] Phillips, A., and Lu, W., 1984, "An Experimental Investigation of Yield Surfaces and Loading Surfaces of Pure Aluminum With Stress-Controlled and Strain-Controlled Paths of Loading," Journal of Engineering Materials and Technology, **106**(4), pp. 349–354. https://doi.org/10.1115/1.3225729.

[20] Phillips, A., and Das, P. K., 1985, "Yield Surfaces and Loading Surfaces of Aluminum and Brass: An Experimental Investigation at Room and Elevated Temperatures," International Journal of Plasticity, **1**(1), pp. 89–109. https://doi.org/10.1016/0749-6419(85)90015-4.

[21] Stout, M. G., Martin, P. L., Helling, D. E., and Canova, G. R., 1985, "Multiaxial Yield Behavior of 1100 Aluminum Following Various Magnitudes of Prestrain," International Journal of Plasticity, **1**(2), pp. 163–174. https://doi.org/10.1016/0749-6419(85)90027-0.

[22] Helling, D. E., Miller, A. K., and Stout, M. G., 1986, "An Experimental Investigation of the Yield Loci of 1100-0 Aluminum, 70:30 Brass, and an Overaged 2024 Aluminum Alloy After Various Prestrains," Journal of Engineering Materials and Technology, **108**(4), pp. 313–320. https://doi.org/10.1115/1.3225888.

[23] Wu, H. C., and Yeh, W. C., 1991, "On the Experimental Determination of Yield Surfaces and Some Results of Annealed 304 Stainless Steel," International Journal of Plasticity, **7**(8), pp. 803–826. https://doi.org/10.1016/0749-6419(91)90019-U.

[24] Kim, K. H., 1992, "Evolution of Anisotropy during Twisting of Cold Drawn Tubes," Journal of the Mechanics and Physics of Solids, **40**(1), pp. 127–139. https://doi.org/10.1016/0022-5096(92)90282-7.

[25] Khan, A. S., and Wang, X., 1993, "An Experimental Study on Subsequent Yield Surface after Finite Shear Prestraining," International Journal of Plasticity, **9**(8), pp. 889–905. https://doi.org/10.1016/0749-6419(93)90056-V.

[26] Dietrich, L., and Kowalewski, Z. L., 1997, "Experimental Investigation of an Anisotropy in Copper Subjected to Predeformation Due to Constant and Monotonic Loadings," International Journal of Plasticity, **13**(1), pp. 87–109. https://doi.org/10.1016/S0749-6419(97)00002-8.

[27] Ishikawa, H., 1997, "Subsequent Yield Surface Probed from Its Current Center," International Journal of Plasticity, **13**(6), pp. 533–549. https://doi.org/10.1016/S0749-6419(97)00024-7.

[28] Kowalewski, Z. L., and Śliwowski, M., 1997, "Effect of Cyclic Loading on the Yield Surface Evolution of 18G2A Low-Alloy Steel," International Journal of Mechanical Sciences, **39**(1), pp. 51–68. https://doi.org/10.1016/0020-7403(96)00016-1.

[29] Szczepinski, W., 1993, "On Deformation-Induced Plastic Anisotropy of Sheet Metals," Archives of Mechanics, **45**(1), pp. 3–38.

[30] Khan, A. S., Kazmi, R., Pandey, A., and Stoughton, T., 2009, "Evolution of Subsequent Yield Surfaces and Elastic Constants with Finite Plastic Deformation. Part-I: A Very Low Work Hardening Aluminum Alloy (Al6061-T6511)," International Journal of Plasticity, **25**(9), pp. 1611–1625. https://doi.org/10.1016/j.ijplas.2008.07.003.

[31] Khan, A. S., Pandey, A., and Stoughton, T., 2010, "Evolution of Subsequent Yield Surfaces and Elastic Constants with Finite Plastic Deformation. Part II: A Very High Work Hardening Aluminum Alloy (Annealed 1100 Al)," International Journal of Plasticity, **26**(10), pp. 1421–1431. https://doi.org/10.1016/j.ijplas.2009.07.008.

[32] Khan, A. S., Pandey, A., and Stoughton, T., 2010, "Evolution of Subsequent Yield Surfaces and Elastic Constants with Finite Plastic Deformation. Part III: Yield Surface in Tension–Tension Stress Space (Al 6061–T 6511 and Annealed 1100 Al)," International Journal of Plasticity, **26**(10), pp. 1432–1441. https://doi.org/10.1016/j.ijplas.2009.07.007.

[33] Dietrich, L., and Socha, G., 2012, "Accumulation of Damage in A336 GR5 Structural Steel Subject to Complex Stress Loading," Strain, **48**(4), pp. 279–285. https://doi.org/10.1111/j.1475-1305.2011.00821.x.

[34] Kowalewski, Z. L., Szymczak, T., and Maciejewski, J., 2014, "Material Effects during Monotonic-Cyclic Loading," International Journal of Solids and Structures, **51**(3), pp. 740–753. https://doi.org/10.1016/j.ijsolstr.2013.10.040.

[35] Froustey, C., and Lataillade, J. L., 2008, "Influence of Large Pre-Straining of Aluminium Alloys on Their Residual Fatigue Resistance," International journal of fatigue, **30**(5), pp. 908–916.

[36] Giacometti, E., Guyot, P., Baluc, N., and Bonneville, J., 2001, "Plastic Behaviour of Icosahedral Al–Cu–Fe Quasicrystals: Experiment and Modelling," Materials Science and Engineering: A, **319**, pp. 429–433.

[37] Kang, M., Aono, Y., and Noguchi, H., 2007, "Effect of Prestrain on and Prediction of Fatigue Limit in Carbon Steel," International journal of fatigue, **29**(9–11), pp. 1855–1862.

[38] Mall, S., Nicholas, T., and Park, T. W., 2003, "Effect of Predamage from Low Cycle Fatigue on High Cycle Fatigue Strength of Ti-6Al-4V," International journal of fatigue, **25**(9–11), pp. 1109–1116.

[39] Ratchev, P., Verlinden, B., Smet, P. D., and Houtte, P. V., 1998, "Effect of Cooling Rate and Predeformation on the Precipitation Hardening of an Al-4.2 Wt.% Mg-0.6 Wt.% Cu Alloy," Scripta materialia, **38**(8), pp. 1195–1201.

[40] Robertson, L. T., Hilditch, T. B., and Hodgson, P. D., 2008, "The Effect of Prestrain and Bake Hardening on the Low-Cycle Fatigue Properties of TRIP Steel," International journal of fatigue, **30**(4), pp. 587–594.

[41] Hansen, V., Gjønnes, J., and Skjervold, S. R., 2001, "Effect of Predeformation and Preaging at Room Temperature in Al–Zn–Mg–(Cu, Zr) Alloys," Materials Science and Engineering: A, **303**(1–2), pp. 226–233.

[42] Whittaker, M. T., and Evans, W. J., 2009, "Effect of Prestrain on the Fatigue Properties of Ti834," International journal of fatigue, **31**(11–12), pp. 1751–1757.

[43] Piao, M., Otsuka, K., Miyazaki, S., and Horikawa, H., 1993, "Mechanism of the As Temperature Increase by Pre-Deformation in Thermoelastic Alloys," Materials Transactions, JIM, **34**(10), pp. 919–929.

[44] Piao, M., Miyazaki, S., and Otsuka, K., 1992, "Characteristics of Deformation and Transformation in Ti44Ni47Nb9 Shape Memory Alloy," Materials Transactions, JIM, **33**(4), pp. 346–353.

[45] Duerig, T. W., Melton, K. N., and Stöckel, D., 2013, Engineering Aspects of Shape Memory Alloys, Butterworth-heinemann.

[46] Melton, K. N., Proft, J. L., and Duerig, T. W., 1988, "Wide Hysteresis Shape Memory Alloys Based on the Ni–Ti–Nb System," Proceedings of the MRS International Meeting on Advanced Materials., pp. 165–170.

[47] Meng, X. L., Cai, W., Chen, F., and Zhao, L. C., 2006, "Effect of Aging on Martensitic Transformation and Microstructure in Ni-Rich TiNiHf Shape Memory Alloy," Scripta materialia, **54**(9), pp. 1599–1604.

[48] Zhao, L. C., Duerig, T. W., Justi, S., Melton, K. N., Proft, J. L., Yu, W., and Wayman, C. M., 1990, "The Study of Niobium-Rich Precipitates in a Ni□ Ti□ Nb Shape Memory Alloy," Scripta Metallurgica et Materialia, **24**(2), pp. 221–225.

[49] Yang, Y., Zhan, L., and Liu, C., 2020, "Pre-Deformation Effect on Stress-Relaxation Ageing Behavior and Mechanical Properties of AA2219 Alloy," International Journal of Lightweight Materials and Manufacture, **3**(1), pp. 73–76.

[50] Wang, N., Zhuang, L., and Zhang, J., 2019, "Effect of Pre-Deformation on the Mechanical Properties of Pre-Aging AA7093," IOP Conference Series: Materials Science and Engineering, IOP Publishing, p. 33083.

[51] Hirsch, J., 2014, "Recent Development in Aluminium for Automotive Applications," Transactions of Nonferrous Metals Society of China, **24**(7), pp. 1995–2002.

[52] Hu, T., Xiao, W., Wang, F., Li, Y., Lyu, S., Zheng, R., and Ma, C., 2018, "Improving Tensile Properties of Mg-Sn-Zn Magnesium Alloy Sheets Using Pre-Tension and Ageing Treatment," Journal of Alloys and Compounds, **735**, pp. 1494–1504.

[53] Park, S. H., Hong, S. G., and Lee, C. S., 2013, "In-Plane Anisotropic Deformation Behavior of Rolled Mg–3Al–1Zn Alloy by Initial {10–12} Twins," Materials Science and Engineering: A, **570**, pp. 149–163.

[54] Suh, B. C., Kim, J. H., Bae, J. H., Hwang, J. H., Shim, M. S., and Kim, N. J., 2017, "Effect of Sn Addition on the Microstructure and Deformation Behavior of Mg-3Al Alloy," Acta Materialia, **124**, pp. 268–279.

[55] Park, S. H., Hong, S. G., Lee, J. H., Kim, S. H., Cho, Y. R., Yoon, J., and Lee, C. S., 2017, "Effects of Pre-Tension on Fatigue Behavior of Rolled Magnesium Alloy," Materials Science and Engineering: A, **680**, pp. 351–358.

[56] Wang, J. T., Liu, J. Q., Tao, J., Su, Y. L., and Zhao, X., 2008, "Effect of Grain Size on Mechanical Property of Mg–3Al–1Zn Alloy," Scripta Materialia, **59**(1), pp. 63–66.

[57]   Syed, B., Geng, J., Mishra, R. K., and Kumar, K. S., 2012, "[0 0 0 1] Compression Response at Room Temperature of Single-Crystal Magnesium," Scripta Materialia, **67**(7–8), pp. 700–703.

[58]   Choi, S. H., Shin, E. J., and Seong, B. S., 2007, "Simulation of Deformation Twins and Deformation Texture in an AZ31 Mg Alloy under Uniaxial Compression," Acta Materialia, **55**(12), pp. 4181–4192.

[59]   Zheng, K. Y., Dong, J., Zeng, X. Q., and Ding, W. J., 2008, "Effect of Pre-Deformation on Aging Characteristics and Mechanical Properties of a Mg–Gd–Nd–Zr Alloy," Materials Science and Engineering: A, **491**(1–2), pp. 103–109.

[60]   Serra, A., Bacon, D. J., and Pond, R. C., 2002, "Twins as Barriers to Basal Slip in Hexagonal-Close-Packed Metals," Metallurgical and materials transactions A, **33**(13), pp. 809–812.

[61]   Serra, A., and Bacon, D. J., 1995, "Computer Simulation of Screw Dislocation Interactions with Twin Boundaries in HCP Metals," Acta metallurgica et materialia, **43**(12), pp. 4465–4481.

[62]   Ahmad, I. R., Jing, X., and Shu, D. W., 2014, "Effect of Temperature on the Mechanical Behaviour of Magnesium Alloy AZ91D in the Range between −30 °C and 250 °C," International Journal of Mechanical Sciences, **86**, pp. 34–45. https://doi.org/10.1016/j.ijmecsci.2014.04.010.

[63]   Mehmanparast, A., Davies, C. M., Dean, D. W., and Nikbin, K. M., 2013, "The Influence of Pre-Compression on the Creep Deformation and Failure Behaviour of Type 316H Stainless Steel," Engineering Fracture Mechanics, **110**. https://doi.org/10.1016/j.engfracmech.2013.08.006.

[64]   Davies, C. M., Dean, D. W., Mehmanparast, A. N., and Nikbin, K. M., 2010, "Compressive Pre-Strain Effects on the Creep and Crack Growth Behaviour of 316H Stainless Steel," Pressure Vessels and Piping Conference, pp. 323–330.

[65]   Anderson, T. L., 2017, Fracture Mechanics: Fundamentals and Applications, CRC press.

[66]   He, J., Liu, T., Xu, S., and Zhang, Y., 2013, "The Effects of Compressive Pre-Deformation on Yield Asymmetry in Hot-Extruded Mg–3Al–1Zn Alloy," Materials Science and Engineering: A, **579**, pp. 1–8.

[67]   Lee, W. T., Ding, S. X., Sun, D. K., Hsiao, C. I., Chang, C. P., Chang, L., and Kao, P. W., 2011, "Deformation Structure of Unidirectionally Compressed Ultrafine-Grained Mg-3Al-1Zn Alloy," Metallurgical and Materials Transactions A, **42**(9), pp. 2909–2916.

[68]   Barnett, M. R., 2001, "Influence of Deformation Conditions and Texture on the High Temperature Flow Stress of Magnesium AZ31," Journal of Light Metals, **1**(3), pp. 167–177.

[69]   Sarker, D., and Chen, D. L., 2014, "Dependence of Compressive Deformation on Pre-Strain and Loading Direction in an Extruded Magnesium Alloy: Texture, Twinning and de-Twinning," Materials Science and Engineering: A, **596**, pp. 134–144.

[70]   Hong, S. G., Park, S. H., and Lee, C. S., 2010, "Role of {10–12} Twinning Characteristics in the Deformation Behavior of a Polycrystalline Magnesium Alloy," Acta Materialia, **58**(18), pp. 5873–5885.

[71] Li, N., Wang, J., Misra, A., Zhang, X., Huang, J. Y., and Hirth, J. P., 2011, "Twinning Dislocation Multiplication at a Coherent Twin Boundary," Acta Materialia, **59**(15), pp. 5989–5996.

[72] Sarker, D., and Chen, D. L., 2013, "Texture Transformation in an Extruded Magnesium Alloy under Pressure," Materials Science and Engineering: A, **582**, pp. 63–67.

[73] Zhu, Y. T., Wu, X. L., Liao, X. Z., Narayan, J., Kecskés, L. J., and Mathaudhu, S. N., 2011, "Dislocation–Twin Interactions in Nanocrystalline Fcc Metals," Acta Materialia, **59**(2), pp. 812–821.

[74] Hong, S. G., Park, S. H., and Lee, C. S., 2010, "Enhancing the Fatigue Property of Rolled AZ31 Magnesium Alloy by Controlling {10-12} Twinning-Detwinning Characteristics," Journal of Materials Research, **25**(4), pp. 784–792.

[75] Park, S. H., Hong, S. G., Lee, J. H., and Lee, C. S., 2012, "Multiple Twinning Modes in Rolled Mg–3Al–1Zn Alloy and Their Selection Mechanism," Materials Science and Engineering: A, **532**, pp. 401–406.

[76] Park, S. H., Hong, S. G., and Lee, C. S., 2013, "Enhanced Stretch Formability of Rolled Mg–3Al–1Zn Alloy at Room Temperature by Initial {10–12} Twins," Materials Science and Engineering: A, **578**, pp. 271–276.

[77] Wang, Y. N., and Huang, J. C., 2007, "The Role of Twinning and Untwinning in Yielding Behavior in Hot-Extruded Mg–Al–Zn Alloy," Acta materialia, **55**(3), pp. 897–905.

[78] Cho, J. H., Jeong, S. S., Kim, H. W., and Kang, S. B., 2013, "Texture and Microstructure Evolution during the Symmetric and Asymmetric Rolling of AZ31B Magnesium Alloys," Materials Science and Engineering: A, **566**, pp. 40–46.

[79] Dallmeier, J., Huber, O., Saage, H., Eigenfeld, K., and Hilbig, A., 2014, "Quasi-Static and Fatigue Behavior of Extruded ME21 and Twin Roll Cast AZ31 Magnesium Sheet Metals," Materials Science and Engineering: A, **590**, pp. 44–53.

[80] Kleiner, S., and Uggowitzer, P. J., 2004, "Mechanical Anisotropy of Extruded Mg–6% Al–1% Zn Alloy," Materials Science and Engineering: A, **379**(1–2), pp. 258–263.

[81] Cáceres, C. H., Sumitomo, T., and Veidt, M., 2003, "Pseudoelastic Behaviour of Cast Magnesium AZ91 Alloy under Cyclic Loading–Unloading," Acta Materialia, **51**(20), pp. 6211–6218.

[82] Kang, J. Y., Bacroix, B., and Brenner, R., 2012, "Evolution of Microstructure and Texture during Planar Simple Shear of Magnesium Alloy," Scripta Materialia, **66**(9), pp. 654–657.

[83] Wang, C., Li, F., Li, J., Dong, J., and Xue, F., 2014, "Microstructure Evolution, Hardening and Thermal Behavior of Commercially Pure Copper Subjected to Torsion Deformation," Materials Science and Engineering: A, **598**, pp. 7–14.

[84] Ungár, T., Tóth, L. S., Illy, J., and Kovács, I., 1986, "Dislocation Structure and Work Hardening in Polycrystalline Ofhc Copper Rods Deformed by Torsion and Tension," Acta Metallurgica, **34**(7), pp. 1257–1267.

[85] Jie, L. I. U., Fuguo, L. I., and Han, C., 2018, "Influences of Pre-Torsion Deformation on Microstructure and Mechanical Properties of Pure Titanium Subjected to Subsequent Tension Deformation," Chinese Journal of Aeronautics, **31**(4), pp. 837–844.

[86] Zhang, H., Huang, G., Wang, L., and Li, J., 2012, "Improved Formability of Mg–3Al–1Zn Alloy by Pre-Stretching and Annealing," Scripta Materialia, **67**(5), pp. 495–498.

[87] Xin, Y., Wang, M., Zeng, Z., Huang, G., and Liu, Q., 2011, "Tailoring the Texture of Magnesium Alloy by Twinning Deformation to Improve the Rolling Capability," Scripta Materialia, **64**(10), pp. 986–989.

[88] Xin, Y., Zhou, X., and Liu, Q., 2013, "Suppressing the Tension–Compression Yield Asymmetry of Mg Alloy by Hybrid Extension Twins Structure," Materials Science and Engineering: A, **567**, pp. 9–13.

[89] Song, B., Xin, R., Chen, G., Zhang, X., and Liu, Q., 2012, "Improving Tensile and Compressive Properties of Magnesium Alloy Plates by Pre-Cold Rolling," Scripta Materialia, **66**(12), pp. 1061–1064.

[90] Guo, N., Luan, B., and Liu, Q., 2013, "Influence of Pre-Torsion Deformation on Microstructures and Properties of Cold Drawing Pearlitic Steel Wires," Materials & Design, **50**, pp. 285–292.

[91] Wei, Y., Li, Y., Zhu, L., Liu, Y., Lei, X., Wang, G., Wu, Y., Mi, Z., Liu, J., and Wang, H., 2014, "Evading the Strength–Ductility Trade-off Dilemma in Steel through Gradient Hierarchical Nanotwins," Nature communications, **5**(1), pp. 1–8.

[92] Guo, N., Song, B., Guo, C., Xin, R., and Liu, Q., 2015, "Improving Tensile and Compressive Properties of Magnesium Alloy Rods via a Simple Pre-Torsion Deformation," Materials & Design, **83**, pp. 270–275.

[93] Chouksey, M., and Basu, S., 2021, "Exploration of Subsequent Yield Surfaces through Unit Cell Simulations," International Journal of Solids and Structures, **219–220**, pp. 11–22. https://doi.org/10.1016/j.ijsolstr.2021.02.004.

[94] Iftikhar, C. M. A., Brahme, A., Inal, K., and Khan, A. S., 2022, "An Evolution of Subsequent Yield Loci under Proportional and Non-Proportional Loading Path of 'as-Received' Extruded AZ31 Magnesium Alloy: Experiments and CPFEM Modeling," International Journal of Plasticity, **151**, p. 103216. https://doi.org/10.1016/j.ijplas.2022.103216.

[95] Kowalewski, Z. L., Dietrich, L., and Turski, K., 2001, "The Effects Observed in Engineering Materials after Annealing and Ageing Processes," Journal of Materials Processing Technology, **119**(1), pp. 165–173. https://doi.org/10.1016/S0924-0136(01)00955-4.

[96] Iftikhar, C. M. A., and Khan, A. S., 2021, "The Evolution of Yield Loci with Finite Plastic Deformation along Proportional and Non-Proportional Loading Paths in an Annealed Extruded AZ31 Magnesium Alloy," International Journal of Plasticity, **143**, p. 103007. https://doi.org/10.1016/j.ijplas.2021.103007.

[97] Holmedal, B., 2019, "Bauschinger Effect Modelled by Yield Surface Distortions," International Journal of Plasticity, **123**, pp. 86–100. https://doi.org/10.1016/j.ijplas.2019.07.009.

[98] Gil, C. M., Lissenden, C. J., and Lerch, B. A., 1999, "Yield of Inconel 718 by Axial-Torsional Loading at Temperatures up to 649°C," Journal of Testing and Evaluation, **27**(5), pp. 327–336. https://doi.org/10.1520/jte12233j.

[99] Iftikhar, C. M. A., Li, Y. L., Kohar, C. P., Inal, K., and Khan, A. S., 2021, "Evolution of Subsequent Yield Surfaces with Plastic Deformation along Proportional and Non-Proportional Loading Paths on Annealed AA6061 Alloy: Experiments and Crystal

Plasticity Finite Element Modeling," International Journal of Plasticity, **143**, p. 102956. https://doi.org/10.1016/j.ijplas.2021.102956.

[100] Tozawa, Y., 1978, "Plastic Deformation Behavior under Conditions of Combined Stress," Mechanics of Sheet Metal Forming: Material Behavior and Deformation Analysis, D.P. Koistinen, and N.-M. Wang, eds., Springer US, Boston, MA, pp. 81–110. https://doi.org/10.1007/978-1-4613-2880-3_4.

[101] Haigh, B. P., 1920, "The Strain Energy Function and the Elastic Limit," Engineering, **109**, pp. 158–160.

[102] Westergaard, H. M., 1920, "On the Resistance of Ductile Materials to Combined Stresses in Two or Three Directions Perpendicular to One Another," Journal of the Franklin Institute, **189**(5), pp. 627–640. https://doi.org/10.1016/S0016-0032(20)90373-3.

[103] Timoshenko, S., 1983, History of Strength of Materials: With a Brief Account of the History of Theory of Elasticity and Theory of Structures, Courier Corporation.

[104] Paul, B., 1968, "Generalized Pyramidal Fracture and Yield Criteria," International Journal of Solids and Structures, **4**(2), pp. 175–196. https://doi.org/10.1016/0020-7683(68)90010-3.

[105] Yu, M. H., 2018, Unified Strength Theory and Its Applications, Springer, Singapore. https://doi.org/10.1007/978-981-10-6247-6.

[106] Coulomb, C. A., 1773, "Essai Sur Une Application Des Regles de Maximis et Minimis a Quelques Problemes de Statique Relatifs a l'architecture (Essay on Maximums and Minimums of Rules to Some Static Problems Relating to Architecture," Academy of Royal Science Memorial Physics, **7**, pp. 343–382. [Online]. Available: https://trid.trb.org/View/124803. [Accessed: 26-Feb-2025].

[107] Tresca, H., 1864, "Mémoire sur l'écoulement des corps solides soumis à de fortes pressions," C. R. Acad. Sci. Paris, **59**, pp. 754–758.

[108] Huber, M. T., 1904, "Specific Work of Deformation as a Measure of Material Effort (in Polish: Właściwa Praca Odkształcenia Jako Miara Wytężenia Materyału)," Towarzystwo Politechniczne.

[109] Mises, R. V., 1913, "Mechanik Der Festen Körper Im Plastisch- Deformablen Zustand," Nachrichten von der Gesellschaft der Wissenschaften zu Göttingen, Mathematisch-Physikalische Klasse, **1913**, pp. 582–592. [Online]. Available: http://dml.mathdoc.fr/item/GDZPPN002503697/. [Accessed: 29-Jan-2024].

[110] Mohr, O., 1900, "Welche Umstände Bedingen Die Elastizitätsgrenze Und Den Bruch Eines Materials," Zeitschrift des Vereins Deutscher Ingenieure, **46**, pp. 1524–1530.

[111] Hill, R., 1948, "A Theory of the Yielding and Plastic Flow of Anisotropic Metals," Proceedings of the Royal Society of London. Series A. Mathematical and Physical Sciences, **193**(1033), pp. 281–297. https://doi.org/10.1098/rspa.1948.0045.

[112] Yu, M., 1983, "Twin Shear Stress Yield Criterion," International Journal of Mechanical Sciences, **25**(1), pp. 71–74. https://doi.org/10.1016/0020-7403(83)90088-7.

[113] Guest, J. J., 1900, "On the Strength of Ductile Materials under Combined Stress," The London, Edinburgh, and Dublin Philosophical Magazine and Journal of Science, **50**(302), pp. 69–132. https://doi.org/10.1080/14786440009463892.

[114] Mohr, O., 1914, "Abhandlungen Aus Dem Gebiete Der Technischen Mechanik," Ernst Berlin, **2**, pp. 1–20.

[115] Nadai, A., and Hodge, P. G., Jr., 1963, "Theory of Flow and Fracture of Solids, Vol. II," Journal of Applied Mechanics, **30**(4), p. 640. https://doi.org/10.1115/1.3636654.

[116] Labuz, J. F., and Zang, A., 2012, "Mohr–Coulomb Failure Criterion," Rock Mech Rock Eng, **45**(6), pp. 975–979. https://doi.org/10.1007/s00603-012-0281-7.

[117] Jones, R. M., 2009, Deformation Theory of Plasticity, Bull Ridge Corporation.

[118] Hencky, H., 1924, "Zur Theorie Plastischer Deformationen Und Der Hierdurch Im Material Hervorgerufenen Nachspannungen," ZAMM - Journal of Applied Mathematics and Mechanics / Zeitschrift für Angewandte Mathematik und Mechanik, **4**(4), pp. 323–334. https://doi.org/10.1002/zamm.19240040405.

[119] Mises, R. V., 1928, "Mechanik Der Plastischen Formänderung von Kristallen," ZAMM - Journal of Applied Mathematics and Mechanics / Zeitschrift für Angewandte Mathematik und Mechanik, **8**(3), pp. 161–185. https://doi.org/10.1002/zamm.19280080302.

[120] Drucker, D. C., and Prager, W., 1952, "Soil Mechanics and Plastic Analysis or Limit Design," Quart. Appl. Math., **10**(2), pp. 157–165. https://doi.org/10.1090/qam/48291.

[121] Prager, W., 1953, "On the Use of Singular Yield Conditions and Associated Flow Rules," Journal of Applied Mechanics, **20**(3), pp. 317–320. https://doi.org/10.1115/1.4010700.

[122] Larsson, P. L., and E. Giannakopoulos, A., 1998, "Tensile Stresses and Their Implication to Cracking at Pyramid Indentation of Pressure-Sensitive Hard Metals and Ceramics," Materials Science and Engineering: A, **254**(1), pp. 268–281. https://doi.org/10.1016/S0921-5093(98)00752-7.

[123] Ivorra, S., Irles Más, R., Estevan, L., Adam Martínez, J. M., Pallarés Rubio, F. J., and Ferrer, B., 2010, Drucker-Prager Yield Criterion Application to Study the Behavior of CFRP Confined Concrete under Compression.

[124] Deng, J. R., Tang, X. C., Mo, Y. H., Meng, L. Y., and Yao, X. H., 2023, "The Drucker–Prager Criterion-Based Plasticity Theory of Amorphous Alloys under the Complex Stress States," Journal of Non-Crystalline Solids, **616**, p. 122453. https://doi.org/10.1016/j.jnoncrysol.2023.122453.

[125] Öztekin, E., Pul, S., and Hüsem, M., 2016, "Experimental Determination of Drucker-Prager Yield Criterion Parameters for Normal and High Strength Concretes under Triaxial Compression," Construction and Building Materials, **112**, pp. 725–732. https://doi.org/10.1016/j.conbuildmat.2016.02.127.

[126] Luo, Y., and Kang, Z., 2013, "Layout Design of Reinforced Concrete Structures Using Two-Material Topology Optimization with Drucker–Prager Yield Constraints," Struct Multidisc Optim, **47**(1), pp. 95–110. https://doi.org/10.1007/s00158-012-0809-1.

[127] Hill, R., 1979, "Theoretical Plasticity of Textured Aggregates," Mathematical Proceedings of the Cambridge Philosophical Society, **85**(1), pp. 179–191. https://doi.org/10.1017/S0305004100055596.

[128] Hill, R., 1990, "Constitutive Modelling of Orthotropic Plasticity in Sheet Metals," Journal of the Mechanics and Physics of Solids, **38**(3), pp. 405–417. https://doi.org/10.1016/0022-5096(90)90006-P.

[129] Sun, L., Du, K., Ren, Y., Hou, Y., You, J., Dong, L., Zhang, L., Dong, H., Li, X., and Yuan, X., 2025, "A New Coupled Yield Criterion Focusing on the Precise Description of Anisotropic Behavior under Broader Stress States: Modeling, Validation, and Convexity Analysis," International Journal of Solids and Structures, **313**, p. 113251. https://doi.org/10.1016/j.ijsolstr.2025.113251.

[130] Hosford, W. F., 1972, "A Generalized Isotropic Yield Criterion," Journal of Applied Mechanics, **39**(2), pp. 607–609. https://doi.org/10.1115/1.3422732.

[131] Logan, R. W., and Hosford, W. F., 1980, "Upper-Bound Anisotropic Yield Locus Calculations Assuming ⟨111⟩ -Pencil Glide," International Journal of Mechanical Sciences, **22**(7), pp. 419–430. https://doi.org/10.1016/0020-7403(80)90011-9.

[132] Barlat, F., and Lian, K., 1989, "Plastic Behavior and Stretchability of Sheet Metals. Part I: A Yield Function for Orthotropic Sheets under Plane Stress Conditions," International Journal of Plasticity, **5**(1), pp. 51–66. https://doi.org/10.1016/0749-6419(89)90019-3.

[133] Barlat, F., Lege, D. J., and Brem, J. C., 1991, "A Six-Component Yield Function for Anisotropic Materials," International Journal of Plasticity, **7**(7), pp. 693–712. https://doi.org/10.1016/0749-6419(91)90052-Z.

[134] Barlat, F., Brem, J. C., Yoon, J. W., Chung, K., Dick, R. E., Lege, D. J., Pourboghrat, F., Choi, S.-H., and Chu, E., 2003, "Plane Stress Yield Function for Aluminum Alloy Sheets—Part 1: Theory," International Journal of Plasticity, **19**(9), pp. 1297–1319. https://doi.org/10.1016/S0749-6419(02)00019-0.

[135] Barlat, F., Aretz, H., Yoon, J. W., Karabin, M. E., Brem, J. C., and Dick, R. E., 2005, "Linear Transfomation-Based Anisotropic Yield Functions," International Journal of Plasticity, **21**(5), pp. 1009–1039. https://doi.org/10.1016/j.ijplas.2004.06.004.

[136] Gurson, A. L., 1977, "Continuum Theory of Ductile Rupture by Void Nucleation and Growth: Part I—Yield Criteria and Flow Rules for Porous Ductile Media," Journal of Engineering Materials and Technology, **99**(1), pp. 2–15. https://doi.org/10.1115/1.3443401.

[137] Tvergaard, V., 1982, "On Localization in Ductile Materials Containing Spherical Voids," Int J Fract, **18**(4), pp. 237–252. https://doi.org/10.1007/BF00015686.

[138] Tvergaard, V., and Needleman, A., 1984, "Analysis of the Cup-Cone Fracture in a Round Tensile Bar," Acta Metallurgica, **32**(1), pp. 157–169. https://doi.org/10.1016/0001-6160(84)90213-X.

[139] Needleman, A., 1972, "Void Growth in an Elastic-Plastic Medium," Journal of Applied Mechanics, **39**(4), pp. 964–970. https://doi.org/10.1115/1.3422899.

[140] Zhang, H., Diehl, M., Roters, F., and Raabe, D., 2016, "A Virtual Laboratory Using High Resolution Crystal Plasticity Simulations to Determine the Initial Yield Surface for Sheet Metal Forming Operations," International Journal of Plasticity, **80**, pp. 111–138. https://doi.org/10.1016/j.ijplas.2016.01.002.

[141] Inal, K., Mishra, R. K., and Cazacu, O., 2010, "Forming Simulation of Aluminum Sheets Using an Anisotropic Yield Function Coupled with Crystal Plasticity Theory," International Journal of Solids and Structures, **47**(17), pp. 2223–2233. https://doi.org/10.1016/j.ijsolstr.2010.04.017.

[142] Zamiri, A., Pourboghrat, F., and Barlat, F., 2007, "An Effective Computational Algorithm for Rate-Independent Crystal Plasticity Based on a Single Crystal Yield

Surface with an Application to Tube Hydroforming," International Journal of Plasticity, **23**(7), pp. 1126–1147. https://doi.org/10.1016/j.ijplas.2006.10.012.

[143] Alipal, J., Mohd Pu'ad, N. A. S., Nayan, N. H. M., Sahari, N., Abdullah, H. Z., Idris, M. I., and Lee, T. C., 2021, "An Updated Review on Surface Functionalisation of Titanium and Its Alloys for Implants Applications," Materials Today: Proceedings, **42**, pp. 270–282. https://doi.org/10.1016/j.matpr.2021.01.499.

[144] Teschke, M., Moritz, J., Telgheder, L., Marquardt, A., Leyens, C., and Walther, F., 2022, "Characterization of the High-Temperature Behavior of PBF-EB/M Manufactured γ Titanium Aluminides," Prog Addit Manuf, **7**(3), pp. 471–480. https://doi.org/10.1007/s40964-022-00274-x.

[145] Shi, B., Peng, Y., Yang, C., Pan, F., Cheng, R., and Peng, Q., 2017, "Loading Path Dependent Distortional Hardening of Mg Alloys: Experimental Investigation and Constitutive Modeling," International Journal of Plasticity, **90**, pp. 76–95. https://doi.org/10.1016/j.ijplas.2016.12.006.

[146] Wang, H., Zhang, X., Wu, W., Liaw, P. K., An, K., Yu, Q., and Wu, P., 2022, "On the Torsional and Coupled Torsion-Tension/Compression Behavior of Magnesium Alloy Solid Rod: A Crystal Plasticity Evaluation," International Journal of Plasticity, **151**, p. 103213. https://doi.org/10.1016/j.ijplas.2022.103213.

[147] Nazari Tiji, S. A., Park, T., Asgharzadeh, A., Kim, H., Athale, M., Kim, J. H., and Pourboghrat, F., 2020, "Characterization of Yield Stress Surface and Strain-Rate Potential for Tubular Materials Using Multiaxial Tube Expansion Test Method," International Journal of Plasticity, **133**, p. 102838. https://doi.org/10.1016/j.ijplas.2020.102838.

[148] Shi, B., Yang, C., Peng, Y., Zhang, F., and Pan, F., 2022, "Anisotropy of Wrought Magnesium Alloys: A Focused Overview," Journal of Magnesium and Alloys, **10**(6), pp. 1476–1510. https://doi.org/10.1016/j.jma.2022.03.006.

[149] Carneiro, L., Yu, Q., and Jiang, Y., 2022, "An Experimental Study of the Mechanical Behavior of Rolled AZ31B Magnesium Alloy under Combined Axial-Torsion Loading," International Journal of Plasticity, **155**, p. 103319. https://doi.org/10.1016/j.ijplas.2022.103319.

[150] Ma, S., Markert, B., and Yuan, H., 2017, "Multiaxial Fatigue Life Assessment of Sintered Porous Iron under Proportional and Non-Proportional Loadings," International Journal of Fatigue, **97**, pp. 214–226. https://doi.org/10.1016/j.ijfatigue.2017.01.005.

[151] Straffelini, G., and Fontanari, V., 2011, "Stress State Dependent Fracture Behaviour of Porous PM Steels," Engineering Fracture Mechanics, **78**(6), pp. 1067–1076. https://doi.org/10.1016/j.engfracmech.2010.12.009.

[152] Zhao, C., Li, F., Li, J., Ma, X., Wan, Q., and Tong, T., 2017, "Influence of Deformation Stress Triaxiality on Microstructure and Microhardness of Pure Copper Processed by Simultaneous Torsion and Tension," J. of Materi Eng and Perform, **26**(8), pp. 4104–4111. https://doi.org/10.1007/s11665-017-2797-1.

[153] Zhou, J., Xu, Y., Lopez, M. A., Farbaniec, L., Patsias, S., Macdougall, D., Reed, J., Petrinic, N., Eakins, D., Siviour, C., and Pellegrino, A., 2022, "The Mechanical Response of Commercially Pure Copper under Multiaxial Loading at Low and High Strain Rates," International Journal of Mechanical Sciences, **224**, p. 107340. https://doi.org/10.1016/j.ijmecsci.2022.107340.

## References

[154] Li, J., Li, F., Zahid Hussain, M., Wang, C., and Wang, L., 2014, "Micro-Structural Evolution Subjected to Combined Tension–Torsion Deformation for Pure Copper," Materials Science and Engineering: A, **610**, pp. 181–187. https://doi.org/10.1016/j.msea.2014.04.083.

[155] Song, W., Liu, X., Xu, J., Fan, Y., Shi, D., Khosravani, M. R., and Berto, F., 2021, "Multiaxial Low Cycle Fatigue of Notched 10CrNi3MoV Steel and Its Undermatched Welds," International Journal of Fatigue, **150**, p. 106309. https://doi.org/10.1016/j.ijfatigue.2021.106309.

[156] Zhu, S. P., Yu, Z. Y., Correia, J., De Jesus, A., and Berto, F., 2018, "Evaluation and Comparison of Critical Plane Criteria for Multiaxial Fatigue Analysis of Ductile and Brittle Materials," International Journal of Fatigue, **112**, pp. 279–288. https://doi.org/10.1016/j.ijfatigue.2018.03.028.

[157] Jin, S., Pei, C., Yuan, H., and Markert, B., 2022, "Multi-Axial Fatigue Life Assessment of Additively Manufactured Nickel-Based Superalloys," International Journal of Fatigue, **163**, p. 107049. https://doi.org/10.1016/j.ijfatigue.2022.107049.

[158] Attar, H., Calin, M., Zhang, L. C., Scudino, S., and Eckert, J., 2014, "Manufacture by Selective Laser Melting and Mechanical Behavior of Commercially Pure Titanium," Materials Science and Engineering: A, **593**, pp. 170–177. https://doi.org/10.1016/j.msea.2013.11.038.

[159] Bajoraitis, R., 1988, "Forming of Titanium and Titanium Alloys," ASM Handbook, pp. 838–848.

[160] Bathini, U., Srivatsan, T. S., Patnaik, A., and Quick, T., 2010, "A Study of the Tensile Deformation and Fracture Behavior of Commercially Pure Titanium and Titanium Alloy: Influence of Orientation and Microstructure," J. of Materi Eng and Perform, **19**(8), pp. 1172–1182. https://doi.org/10.1007/s11665-010-9613-5.

[161] Mouritz, A. P., 2012, Introduction to Aerospace Materials, Elsevier.

[162] Scales, M., Tardif, N., and Kyriakides, S., 2016, "Ductile Failure of Aluminum Alloy Tubes under Combined Torsion and Tension," International Journal of Solids and Structures, **97–98**, pp. 116–128. https://doi.org/10.1016/j.ijsolstr.2016.07.038.

[163] Omale, J. I., Ohaeri, E. G., Tiamiyu, A. A., Eskandari, M., Mostafijur, K. M., and Szpunar, J. A., 2017, "Microstructure, Texture Evolution and Mechanical Properties of X70 Pipeline Steel after Different Thermomechanical Treatments," Materials Science and Engineering: A, **703**, pp. 477–485. https://doi.org/10.1016/j.msea.2017.07.086.

[164] Hutchinson, B., 2015, "Critical Assessment 16: Anisotropy in Metals," Materials Science and Technology, **31**(12), pp. 1393–1401. https://doi.org/10.1179/1743284715Y.0000000118.

[165] Nakajima, H., 2007, "Fabrication, Properties and Application of Porous Metals with Directional Pores," Progress in Materials Science, **52**(7), pp. 1091–1173. https://doi.org/10.1016/j.pmatsci.2006.09.001.

[166] Ghafari, E., and Rezaeepazhand, J., 2020, "Isogeometric-Based Cross-Sectional Analysis of Pre-Twisted Composite Beams," Thin-Walled Structures, **146**, p. 106424. https://doi.org/10.1016/j.tws.2019.106424.

[167] Qvale, K., Hopperstad, O. S., Reiso, O., Tundal, U. H., Marioara, C. D., and Børvik, T., 2021, "An Experimental Study on Pre-Stretched Double-Chamber 6000-Series

Aluminium Profiles Subjected to Quasi-Static and Dynamic Axial Crushing," Thin-Walled Structures, **158**, p. 107160. https://doi.org/10.1016/j.tws.2020.107160.

[168] Štefan, J., Parma, S., Marek, R., Plešek, J., Ciocanel, C., and Feigenbaum, H., 2021, "Overview of an Experimental Program for Development of Yield Surfaces Tracing Method," Applied Sciences, **11**(16), p. 7606. https://doi.org/10.3390/app11167606.

[169] Zhang, W. J., Huang, L., Mi, X. J., Xie, H. F., Feng, X., and Ahn, J. H., 2024, "Researches for Higher Electrical Conductivity Copper-Based Materials," cMat, **1**(1), p. e13. https://doi.org/10.1002/cmt2.13.

[170] Yang, K., Wang, Y., Guo, M., Wang, H., Mo, Y., Dong, X., and Lou, H., 2023, "Recent Development of Advanced Precipitation-Strengthened Cu Alloys with High Strength and Conductivity: A Review," Progress in Materials Science, **138**, p. 101141. https://doi.org/10.1016/j.pmatsci.2023.101141.

[171] Vahedi Nemani, A., Ghaffari, M., Sabet Bokati, K., Valizade, N., Afshari, E., and Nasiri, A., 2024, "Advancements in Additive Manufacturing for Copper-Based Alloys and Composites: A Comprehensive Review," Journal of Manufacturing and Materials Processing, **8**(2), p. 54. https://doi.org/10.3390/jmmp8020054.

[172] Guschlbauer, R., Momeni, S., Osmanlic, F., and Körner, C., 2018, "Process Development of 99.95% Pure Copper Processed via Selective Electron Beam Melting and Its Mechanical and Physical Properties," Materials Characterization, **143**, pp. 163–170. https://doi.org/10.1016/j.matchar.2018.04.009.

[173] Li, M., and Zinkle, S. J., 2012, "Physical and Mechanical Properties of Copper and Copper Alloys," Comprehensive Nuclear Materials, Elsevier, pp. 667–690. https://doi.org/10.1016/B978-0-08-056033-5.00122-1.

[174] Lai, Z., Mai, Y., Song, H., Mai, J., and Jie, X., 2022, "Heterogeneous Microstructure Enables a Synergy of Strength, Ductility and Electrical Conductivity in Copper Alloys," Journal of Alloys and Compounds, **902**, p. 163646. https://doi.org/10.1016/j.jallcom.2022.163646.

[175] Semih, Ö., and Recep, A., 2023, "Investigation of Microstructure, Machinability, and Mechanical Properties of New-Generation Hybrid Lead-Free Brass Alloys," High Temperature Materials and Processes, **42**(1), p. 20220263. https://doi.org/10.1515/htmp-2022-0263.

[176] Scudino, S., Unterdörfer, C., Prashanth, K. G., Attar, H., Ellendt, N., Uhlenwinkel, V., and Eckert, J., 2015, "Additive Manufacturing of Cu–10Sn Bronze," Materials Letters, **156**, pp. 202–204. https://doi.org/10.1016/j.matlet.2015.05.076.

[177] Wu, X. X., San, X. Y., Gong, Y. L., Chen, L. P., Li, C. J., and Zhu, X. K., 2013, "Studies on Strength and Ductility of Cu–Zn Alloys by Stress Relaxation," Materials & Design, **47**, pp. 295–299. https://doi.org/10.1016/j.matdes.2012.12.020.

[178] Pingale, A. D., Owhal, A., Katarkar, A. S., Belgamwar, S. U., and Rathore, J. S., 2021, "Recent Researches on Cu-Ni Alloy Matrix Composites through Electrodeposition and Powder Metallurgy Methods: A Review," Materials Today: Proceedings, **47**, pp. 3301–3308. https://doi.org/10.1016/j.matpr.2021.07.145.

[179] Czerwinski, F., 2024, "Aluminum Alloys for Electrical Engineering: A Review," J Mater Sci, **59**(32), pp. 14847–14892. https://doi.org/10.1007/s10853-024-09890-0.

[180] Zhou, M., Geng, Y., Zhang, Y., Ban, Y., Li, X., Jia, Y., Liang, S., Tian, B., Liu, Y., and Volinsky, A. A., 2023, "Enhanced Mechanical Properties and High Electrical

Conductivity of Copper Alloy via Dual-Nanoprecipitation," Materials Characterization, **195**, p. 112494. https://doi.org/10.1016/j.matchar.2022.112494.

[181] Jiang, Q., Zhang, P., Yu, Z., Shi, H., Wu, D., Yan, H., Ye, X., Lu, Q., and Tian, Y., 2021, "A Review on Additive Manufacturing of Pure Copper," Coatings, **11**(6), p. 740. https://doi.org/10.3390/coatings11060740.

[182] Stepanov, N. D., Kuznetsov, A. V., Salishchev, G. A., Raab, G. I., and Valiev, R. Z., 2012, "Effect of Cold Rolling on Microstructure and Mechanical Properties of Copper Subjected to ECAP with Various Numbers of Passes," Materials Science and Engineering: A, **554**, pp. 105–115. https://doi.org/10.1016/j.msea.2012.06.022.

[183] Singh Sivam, S. P. S., Rajendran, R., and Harshavardhana, N., 2023, "An Investigation of Stored Energy in Uniaxial and Biaxial Directional Rolling on Mechanical Properties and Microstructure of Pure Copper," Mechanics Based Design of Structures and Machines, **51**(5), pp. 2831–2843. https://doi.org/10.1080/15397734.2021.1909484.

[184] Pan, Q., Jing, L., and Lu, L., 2023, "Enhanced Fatigue Endurance Limit of Cu through Low-Angle Dislocation Boundary," Acta Materialia, **244**, p. 118542. https://doi.org/10.1016/j.actamat.2022.118542.

[185] Liu, C., Yang, X., Ding, Y., Li, H., Wan, S., Guo, Y., and Li, Y., 2023, "The Yielding Behavior of TU00 Pure Copper under Impact Loading," International Journal of Mechanical Sciences, **245**, p. 108110. https://doi.org/10.1016/j.ijmecsci.2023.108110.

[186] Jadhav, S. D., Goossens, L. R., Kinds, Y., Hooreweder, B. V., and Vanmeensel, K., 2021, "Laser-Based Powder Bed Fusion Additive Manufacturing of Pure Copper," Additive Manufacturing, **42**, p. 101990. https://doi.org/10.1016/j.addma.2021.101990.

[187] Davis, J. R., 2001, "Copper and Copper Alloys," ASM international, **446**. https://doi.org/10.31399/asm.tb.aub.t61170457.

[188] Chen, Y., Zuo, X., Zhang, W., Hao, Z., Li, Y., Luo, Z., and Ao, S., 2022, "Enhanced Strength-Ductility Synergy of Bimetallic Laminated Steel Structure of 304 Stainless Steel and Low-Carbon Steel Fabricated by Wire and Arc Additive Manufacturing," Materials Science and Engineering: A, **856**, p. 143984. https://doi.org/10.1016/j.msea.2022.143984.

[189] Gao, X., Jiang, Z., Wei, D., Jiao, S., Chen, D., Xu, J., Zhang, X., and Gong, D., 2014, "Effects of Temperature and Strain Rate on Microstructure and Mechanical Properties of High Chromium Cast Iron/Low Carbon Steel Bimetal Prepared by Hot Diffusion-Compression Bonding," Materials & Design, **63**, pp. 650–657. https://doi.org/10.1016/j.matdes.2014.06.067.

[190] Sahasrabudhe, H., Harrison, R., Carpenter, C., and Bandyopadhyay, A., 2015, "Stainless Steel to Titanium Bimetallic Structure Using LENS™," Additive Manufacturing, **5**, pp. 1–8. https://doi.org/10.1016/j.addma.2014.10.002.

[191] Tan, C., Zhou, K., Ma, W., and Min, L., 2018, "Interfacial Characteristic and Mechanical Performance of Maraging Steel-Copper Functional Bimetal Produced by Selective Laser Melting Based Hybrid Manufacture," Materials & Design, **155**, pp. 77–85. https://doi.org/10.1016/j.matdes.2018.05.064.

[192] Ghosh, M., and Chatterjee, S., 2005, "Effect of Interface Microstructure on the Bond Strength of the Diffusion Welded Joints between Titanium and Stainless Steel," Materials Characterization, **54**(4), pp. 327–337. https://doi.org/10.1016/j.matchar.2004.12.007.

[193] Beygi, R., Mehrizi, M. Z., Verdera, D., and Loureiro, A., 2018, "Influence of Tool Geometry on Material Flow and Mechanical Properties of Friction Stir Welded Al-Cu Bimetals," Journal of Materials Processing Technology, **255**, pp. 739–748. https://doi.org/10.1016/j.jmatprotec.2018.01.033.

[194] Findik, F., 2011, "Recent Developments in Explosive Welding," Materials & Design, **32**(3), pp. 1081–1093. https://doi.org/10.1016/j.matdes.2010.10.017.

[195] Yilmaz, O., and Çelik, H., 2003, "Electrical and Thermal Properties of the Interface at Diffusion-Bonded and Soldered 304 Stainless Steel and Copper Bimetal," Journal of Materials Processing Technology, **141**(1), pp. 67–76. https://doi.org/10.1016/S0924-0136(03)00029-3.

[196] Ahsan, M. R. U., Tanvir, A. N. M., Seo, G. J., Bates, B., Hawkins, W., Lee, C., Liaw, P. K., Noakes, M., Nycz, A., and Kim, D. B., 2020, "Heat-Treatment Effects on a Bimetallic Additively-Manufactured Structure (BAMS) of the Low-Carbon Steel and Austenitic-Stainless Steel," Additive Manufacturing, **32**, p. 101036. https://doi.org/10.1016/j.addma.2020.101036.

[197] Arivazhagan, N., Singh, S., Prakash, S., and Reddy, G. M., 2011, "Investigation on AISI 304 Austenitic Stainless Steel to AISI 4140 Low Alloy Steel Dissimilar Joints by Gas Tungsten Arc, Electron Beam and Friction Welding," Materials & Design, **32**(5), pp. 3036–3050. https://doi.org/10.1016/j.matdes.2011.01.037.

[198] Chuaiphan, W., Somrerk, C. A., Niltawach, S., and Sornil, B., 2013, "Dissimilar Welding between AISI 304 Stainless Steel and AISI 1020 Carbon Steel Plates," Applied Mechanics and Materials, **268–270**, pp. 283–290. https://doi.org/10.4028/www.scientific.net/AMM.268-270.283.

[199] Jafarzadegan, M., Abdollah-Zadeh, A., Feng, A. H., Saeid, T., Shen, J., and Assadi, H., 2013, "Microstructure and Mechanical Properties of a Dissimilar Friction Stir Weld between Austenitic Stainless Steel and Low Carbon Steel," Journal of Materials Science & Technology, **29**(4), pp. 367–372. https://doi.org/10.1016/j.jmst.2013.02.008.

[200] Chen, X., Li, J., Cheng, X., Wang, H., and Huang, Z., 2018, "Effect of Heat Treatment on Microstructure, Mechanical and Corrosion Properties of Austenitic Stainless Steel 316L Using Arc Additive Manufacturing," Materials Science and Engineering: A, **715**, pp. 307–314. https://doi.org/10.1016/j.msea.2017.10.002.

[201] Ahsan, M. R. U., Fan, X., Seo, G. J., Ji, C., Noakes, M., Nycz, A., Liaw, P. K., and Kim, D. B., 2021, "Microstructures and Mechanical Behavior of the Bimetallic Additively-Manufactured Structure (BAMS) of Austenitic Stainless Steel and Inconel 625," Journal of Materials Science & Technology, **74**, pp. 176–188. https://doi.org/10.1016/j.jmst.2020.10.001.

[202] Wu, B., Qiu, Z., Pan, Z., Carpenter, K., Wang, T., Ding, D., Duin, S. V., and Li, H., 2020, "Enhanced Interface Strength in Steel-Nickel Bimetallic Component Fabricated Using Wire Arc Additive Manufacturing with Interweaving Deposition Strategy," Journal of Materials Science & Technology, **52**, pp. 226–234. https://doi.org/10.1016/j.jmst.2020.04.019.

[203] Telasang, G., Narayanaswamy, S., Santhoshsarang, D. M., and Bathe, R., 2022, "Selective Laser Melting of Stainless Steel on the Copper Alloy: An Investigation of the Interfacial Microstructure and Mechanical Properties," Journal of Manufacturing Processes, **80**, pp. 920–929. https://doi.org/10.1016/j.jmapro.2022.06.055.

[204] Onuike, B., and Bandyopadhyay, A., 2019, "Bond Strength Measurement for Additively Manufactured Inconel 718- GRCop84 Copper Alloy Bimetallic Joints," Additive Manufacturing, **27**, pp. 576–585. https://doi.org/10.1016/j.addma.2019.04.003.

[205] Gotawala, N., and Shrivastava, A., 2021, "Investigation of Interface Microstructure and Mechanical Properties of Rotary Friction Welded Dissimilar Aluminum-Steel Joints," Materials Science and Engineering: A, **825**, p. 141900. https://doi.org/10.1016/j.msea.2021.141900.

[206] Vyas, H. D., Mehta, K. P., Badheka, V., and Doshi, B., 2021, "Processing and Evaluation of Dissimilar Al-SS Friction Welding of Pipe Configuration: Nondestructive Inspection, Properties, and Microstructure," Measurement, **167**, p. 108305. https://doi.org/10.1016/j.measurement.2020.108305.

[207] Kimura, M., Iijima, T., Kusaka, M., Kaizu, K., and Fuji, A., 2016, "Joining Phenomena and Tensile Strength of Friction Welded Joint between Ti–6Al–4V Titanium Alloy and Low Carbon Steel," Journal of Manufacturing Processes, **24**, pp. 203–211. https://doi.org/10.1016/j.jmapro.2016.09.004.

[208] Lee, W., Chung, K. H., Kim, D., Kim, J., Kim, C., Okamoto, K., Wagoner, R. H., and Chung, K., 2009, "Experimental and Numerical Study on Formability of Friction Stir Welded TWB Sheets Based on Hemispherical Dome Stretch Tests," International Journal of Plasticity, **25**(9), pp. 1626–1654. https://doi.org/10.1016/j.ijplas.2008.08.005.

[209] Cao, Z. H., Cai, Y. P., Sun, C., Ma, Y. J., Wei, M. Z., Li, Q., Lu, H. M., Wang, H., Zhang, X., and Meng, X. K., 2019, "Tailoring Strength and Plasticity of Ag/Nb Nanolaminates via Intrinsic Microstructure and Extrinsic Dimension," International Journal of Plasticity, **113**, pp. 145–157. https://doi.org/10.1016/j.ijplas.2018.09.012.

[210] Zhang, Y. F., Xue, S., Li, Q., Li, J., Ding, J., Niu, T. J., Su, R., Wang, H., and Zhang, X., 2019, "Size Dependent Strengthening in High Strength Nanotwinned Al/Ti Multilayers," Acta Materialia, **175**, pp. 466–476. https://doi.org/10.1016/j.actamat.2019.06.028.

[211] Chen, T., Yuan, R., Beyerlein, I. J., and Zhou, C., 2020, "Predicting the Size Scaling in Strength of Nanolayered Materials by a Discrete Slip Crystal Plasticity Model," International Journal of Plasticity, **124**, pp. 247–260. https://doi.org/10.1016/j.ijplas.2019.08.016.

[212] Ham, B., and Zhang, X., 2011, "High Strength Mg/Nb Nanolayer Composites," Materials Science and Engineering: A, **528**(4), pp. 2028–2033. https://doi.org/10.1016/j.msea.2010.10.101.

[213] Zbib, H. M., Overman, C. T., Akasheh, F., and Bahr, D., 2011, "Analysis of Plastic Deformation in Nanoscale Metallic Multilayers with Coherent and Incoherent Interfaces," International Journal of Plasticity, **27**(10), pp. 1618–1639. https://doi.org/10.1016/j.ijplas.2011.03.006.

[214] Li, J., Chen, Y., Xue, S., Wang, H., and Zhang, X., 2016, "Comparison of Size Dependent Strengthening Mechanisms in Ag/Fe and Ag/Ni Multilayers," Acta Materialia, **114**, pp. 154–163. https://doi.org/10.1016/j.actamat.2016.05.030.

[215] Abdolrahim, N., Zbib, H. M., and Bahr, D. F., 2014, "Multiscale Modeling and Simulation of Deformation in Nanoscale Metallic Multilayer Systems," International Journal of Plasticity, **52**, pp. 33–50. https://doi.org/10.1016/j.ijplas.2013.04.002.

[216] Misra, A., Hirth, J. P., and Hoagland, R. G., 2005, "Length-Scale-Dependent Deformation Mechanisms in Incoherent Metallic Multilayered Composites," Acta Materialia, **53**(18), pp. 4817–4824. https://doi.org/10.1016/j.actamat.2005.06.025.

[217] Cao, Z. H., Wei, M. Z., Ma, Y. J., Sun, C., Lu, H. M., Fan, Z., and Meng, X. K., 2017, "Cyclic Deformation Induced Strengthening and Unusual Rate Sensitivity in Cu/Ru Nanolayered Films," International Journal of Plasticity, **99**, pp. 43–57. https://doi.org/10.1016/j.ijplas.2017.08.005.

[218] Volokitina, I., Sapargaliyeva, B., Agabekova, A., Syrlybekkyzy, S., Volokitin, A., Nurshakhanova, L., Nurbaeva, F., Kolesnikov, A., Sabyrbayeva, G., Izbassar, A., Kolesnikova, O., Liseitsev, Y., and Vavrenyuk, S., 2023, "Increasing Strength and Performance Properties of Bimetallic Rods during Severe Plastic Deformation," Case Studies in Construction Materials, **19**, p. e02256. https://doi.org/10.1016/j.cscm.2023.e02256.

[219] Volokitina, I., Naizabekov, A. B., and Volokitin, A. V., 2023, "Effect of Deformation by Ecap-Drawing Method on Change in Steel-Aluminum Wire Properties," Metallurgist, **66**(9), pp. 1235–1240. https://doi.org/10.1007/s11015-023-01436-0.

[220] Lu, D., Zhang, K., Hu, G., Lan, Y., and Chang, Y., 2020, "Investigation of Yield Surfaces Evolution for Polycrystalline Aluminum after Pre-Cyclic Loading by Experiment and Crystal Plasticity Simulation," Materials, **13**(14), p. 3069. https://doi.org/10.3390/ma13143069.

[221] Hong, H. K., Liu, L. W., Shiao, Y. P., and Yan, S. F., 2022, "Yield Surface Evolution and Elastoplastic Model with Cubic Distortional Yield Surface," Journal of Engineering Mechanics, **148**(6), p. 04022027. https://doi.org/10.1061/(ASCE)EM.1943-7889.0002108.

[222] Shiratori, E., Ikegami, K., Yoshida, F., Kaneko, K., and Koike, S., 1976, "The Subsequent Yield Surfaces after Preloading under Combined Axial Load and Torsion," Bulletin of JSME, **19**(134), pp. 877–883. https://doi.org/10.1299/jsme1958.19.877.

[223] Kowalewski, Z. L., and Turski, K., 2003, "Multiaxial Proportional and Non-Proportional Cyclic Behaviour of 40H Steel and PA6 Aluminium Alloy," Key Engineering Materials, **233–236**, pp. 269–274. https://doi.org/10.4028/www.scientific.net/KEM.233-236.269.

[224] Sung, S. J., Liu, L. W., Hong, H. K., and Wu, H. C., 2011, "Evolution of Yield Surface in the 2D and 3D Stress Spaces," International Journal of Solids and Structures, **48**(6), pp. 1054–1069. https://doi.org/10.1016/j.ijsolstr.2010.12.011.

[225] Du, K., Huang, S., Hou, Y., Wang, H., Wang, Y., Zheng, W., and Yuan, X., 2023, "Characterization of the Asymmetric Evolving Yield and Flow of 6016-T4 Aluminum Alloy and DP490 Steel," Journal of Materials Science & Technology, **133**, pp. 209–229. https://doi.org/10.1016/j.jmst.2022.05.040.

[226] Kabirian, F., and Khan, A. S., 2015, "Anisotropic Yield Criteria in σ–τ Stress Space for Materials with Yield Asymmetry," International Journal of Solids and Structures, **67–68**, pp. 116–126. https://doi.org/10.1016/j.ijsolstr.2015.04.006.

[227] Naka, T., Uemori, T., Hino, R., Kohzu, M., Higashi, K., and Yoshida, F., 2008, "Effects of Strain Rate, Temperature and Sheet Thickness on Yield Locus of AZ31 Magnesium Alloy Sheet," Journal of Materials Processing Technology, **201**(1), pp. 395–400. https://doi.org/10.1016/j.jmatprotec.2007.11.189.

[228] Yang, C., Shi, B., Peng, Y., and Pan, F., 2019, "Loading Path Dependent Distortional Hardening of Mg Alloys: Experimental Investigation and Constitutive Modeling on Cruciform Specimens," International Journal of Mechanical Sciences, **160**, pp. 282–297. https://doi.org/10.1016/j.ijmecsci.2019.06.046.

[229] Liu, G. L., Huang, S. H., Shi, C. S., Zeng, B., Zhang, K. S., and Zhong, X. C., 2018, "Experimental Investigations on Subsequent Yield Surface of Pure Copper by Single-Sample and Multi-Sample Methods under Various Pre-Deformation," Materials, **11**(2), p. 277. https://doi.org/10.3390/ma11020277.

[230] Shiratori, E., Ikegami, K., and Kaneko, K., 1973, "The Influence of the Bauschinger Effect on the Subsequent Yield Condition," Bulletin of JSME, **16**(100), pp. 1482–1493. https://doi.org/10.1299/jsme1958.16.1482.

[231] Hu, G., Zhang, K., Huang, S., and Ju, J. W. W., 2012, "Yield Surfaces and Plastic Flow of 45 Steel under Tension-Torsion Loading Paths," Acta Mechanica Solida Sinica, **25**(4), pp. 348–360. https://doi.org/10.1016/S0894-9166(12)60032-9.

[232] Hou, Y., Min, J., Guo, N., Lin, J., Carsley, J. E., Stoughton, T. B., Traphöner, H., Clausmeyer, T., and Tekkaya, A. E., 2021, "Investigation of Evolving Yield Surfaces of Dual-Phase Steels," Journal of Materials Processing Technology, **287**, p. 116314. https://doi.org/10.1016/j.jmatprotec.2019.116314.

[233] Uscinowicz, R., 2013, "Experimental Identification of Yield Surface of Al–Cu Bimetallic Sheet," Composites Part B: Engineering, **55**, pp. 96–108. https://doi.org/10.1016/j.compositesb.2013.06.002.

[234] Wroński, M., Kumar, M. A., McCabe, R. J., Wierzbanowski, K., and Tomé, C. N., 2022, "Deformation Behavior of CP-Titanium under Strain Path Changes: Experiment and Crystal Plasticity Modeling," International Journal of Plasticity, **148**, p. 103129. https://doi.org/10.1016/j.ijplas.2021.103129.

[235] Gupta, A., Yoo, T. H., Kaushik, L., Lee, J. W., Kim, Y. K., and Choi, S. H., 2022, "Unveiling the Room-Temperature Softening Phenomenon and Texture Evolution in Room-Temperature- and Cryogenic-Rolled ETP Copper," International Journal of Plasticity, **156**, p. 103340. https://doi.org/10.1016/j.ijplas.2022.103340.

[236] Lee, J. S., Son, H. T., Oh, I. H., Kang, C. S., Yun, C. H., Lim, S. C., and Kwon, H. C., 2007, "Fabrication and Characterization of Ti–Cu Clad Materials by Indirect Extrusion," Journal of Materials Processing Technology, **187–188**, pp. 653–656. https://doi.org/10.1016/j.jmatprotec.2006.11.144.

[237] Matsushita, T., Noguchi, M., and Arimura, K., 1988, "Hot Hydrostatic Extrusion of Ti/Cu-Alloy Composite Materials," J. Soc. Mater. Sci., Jpn., **37**(413), pp. 107–113. https://doi.org/10.2472/jsms.37.107.

[238] Uścinowicz, R., 2022, "Effect of Elevated Temperature and Annealing Time on Mechanical Properties of Ti/Cu Bimetal," Materials, **15**(23), p. 8707. https://doi.org/10.3390/ma15238707.

[239] Avanzini, A., 2022, "Fatigue Behavior of Additively Manufactured Stainless Steel 316L," Materials, **16**(1), p. 65. https://doi.org/10.3390/ma16010065.

[240] Gor, M., Soni, H., Wankhede, V., Sahlot, P., Grzelak, K., Szachgluchowicz, I., and Kluczyński, J., 2021, "A Critical Review on Effect of Process Parameters on Mechanical and Microstructural Properties of Powder-Bed Fusion Additive

Manufacturing of SS316L," Materials, **14**(21), p. 6527. https://doi.org/10.3390/ma14216527.

[241] Bedmar, J., Riquelme, A., Rodrigo, P., Torres, B., and Rams, J., 2021, "Comparison of Different Additive Manufacturing Methods for 316L Stainless Steel," Materials, **14**(21), p. 6504. https://doi.org/10.3390/ma14216504.

[242] D'Andrea, D., 2023, "Additive Manufacturing of AISI 316L Stainless Steel: A Review," Metals, **13**(8), p. 1370. https://doi.org/10.3390/met13081370.

[243] Khalid, M., and Peng, Q., 2021, "Investigation of Printing Parameters of Additive Manufacturing Process for Sustainability Using Design of Experiments," Journal of Mechanical Design, **143**(3), p. 032001. https://doi.org/10.1115/1.4049521.

[244] Santonocito, D., Fintová, S., Di Cocco, V., Iacoviello, F., Risitano, G., and D'Andrea, D., 2023, "Comparison on Mechanical Behavior and Microstructural Features between Traditional and AM AISI 316L," Fatigue Fract Eng Mat Struct, **46**(2), pp. 379–395. https://doi.org/10.1111/ffe.13872.

[245] Elambasseril, J., Rogers, J., Wallbrink, C., Munk, D., Leary, M., and Qian, M., 2023, "Laser Powder Bed Fusion Additive Manufacturing (LPBF-AM): The Influence of Design Features and LPBF Variables on Surface Topography and Effect on Fatigue Properties," Critical Reviews in Solid State and Materials Sciences, **48**(1), pp. 132–168. https://doi.org/10.1080/10408436.2022.2041396.

[246] Alsalla, H. H., Smith, C., and Hao, L., 2018, "Effect of Build Orientation on the Surface Quality, Microstructure and Mechanical Properties of Selective Laser Melting 316L Stainless Steel," RPJ, **24**(1), pp. 9–17. https://doi.org/10.1108/RPJ-04-2016-0068.

[247] Smith, T. R., Sugar, J. D., San Marchi, C., and Schoenung, J. M., 2017, "Orientation Effects on Fatigue Behavior of Additively Manufactured Stainless Steel," Volume 6A: Materials and Fabrication, American Society of Mechanical Engineers, Waikoloa, Hawaii, USA, p. V06AT06A020. https://doi.org/10.1115/PVP2017-65948.

[248] Yang, N., Yee, J., Zheng, B., Gaiser, K., Reynolds, T., Clemon, L., Lu, W. Y., Schoenung, J. M., and Lavernia, E. J., 2017, "Process-Structure-Property Relationships for 316L Stainless Steel Fabricated by Additive Manufacturing and Its Implication for Component Engineering," J Therm Spray Tech, **26**(4), pp. 610–626. https://doi.org/10.1007/s11666-016-0480-y.

[249] Guo, P., Zou, B., Huang, C., and Gao, H., 2017, "Study on Microstructure, Mechanical Properties and Machinability of Efficiently Additive Manufactured AISI 316L Stainless Steel by High-Power Direct Laser Deposition," Journal of Materials Processing Technology, **240**, pp. 12–22. https://doi.org/10.1016/j.jmatprotec.2016.09.005.

[250] Lavery, N. P., Cherry, J., Mehmood, S., Davies, H., Girling, B., Sackett, E., Brown, S. G. R., and Sienz, J., 2017, "Effects of Hot Isostatic Pressing on the Elastic Modulus and Tensile Properties of 316L Parts Made by Powder Bed Laser Fusion," Materials Science and Engineering: A, **693**, pp. 186–213. https://doi.org/10.1016/j.msea.2017.03.100.

[251] Kumar, P., Jayaraj, R., Suryawanshi, J., Satwik, U. R., McKinnell, J., and Ramamurty, U., 2020, "Fatigue Strength of Additively Manufactured 316L Austenitic Stainless Steel," Acta Materialia, **199**, pp. 225–239. https://doi.org/10.1016/j.actamat.2020.08.033.

[252] Somlo, K., Frodal, B. H., Funch, C. V., Poulios, K., Winther, G., Hopperstad, O. S., Børvik, T., and Niordson, C. F., 2022, "Anisotropic Yield Surfaces of Additively

Manufactured Metals Simulated with Crystal Plasticity," European Journal of Mechanics - A/Solids, **94**, p. 104506. https://doi.org/10.1016/j.euromechsol.2022.104506.

[253] Wang, H., Shu, X., Zhao, J., and Alexandrov, I. V., 2023, "Biaxial Tensile Behavior of Stainless Steel 316L Manufactured by Selective Laser Melting," Sci Rep, **13**(1), p. 21925. https://doi.org/10.1038/s41598-023-49482-7.

[254] Kořínek, M., Halama, R., Fojtík, F., Pagáč, M., Krček, J., Krzikalla, D., Kocich, R., and Kunčická, L., 2020, "Monotonic Tension-Torsion Experiments and FE Modeling on Notched Specimens Produced by SLM Technology from SS316L," Materials, **14**(1), p. 33. https://doi.org/10.3390/ma14010033.

[255] Wood, P., Libura, T., Kowalewski, Z. L., Williams, G., and Serjouei, A., 2019, "Influences of Horizontal and Vertical Build Orientations and Post-Fabrication Processes on the Fatigue Behavior of Stainless Steel 316L Produced by Selective Laser Melting," Materials, **12**(24), p. 4203. https://doi.org/10.3390/ma12244203.

[256] Sasikumar, R., Kannan, A. R., Kumar, S. M., Pramod, R., Kumar, N. P., Shanmugam, N. S., Palguna, Y., and Sivankalai, S., 2022, "Wire Arc Additive Manufacturing of Functionally Graded Material with SS 316L and IN625: Microstructural and Mechanical Perspectives," CIRP Journal of Manufacturing Science and Technology, **38**, pp. 230–242. https://doi.org/10.1016/j.cirpj.2022.05.005.

[257] Wang, C., Tan, X., Liu, E., and Tor, S. B., 2018, "Process Parameter Optimization and Mechanical Properties for Additively Manufactured Stainless Steel 316L Parts by Selective Electron Beam Melting," Materials & Design, **147**, pp. 157–166. https://doi.org/10.1016/j.matdes.2018.03.035.

[258] Aversa, A., Saboori, A., Librera, E., de Chirico, M., Biamino, S., Lombardi, M., and Fino, P., 2020, "The Role of Directed Energy Deposition Atmosphere Mode on the Microstructure and Mechanical Properties of 316L Samples," Additive Manufacturing, **34**, p. 101274. https://doi.org/10.1016/j.addma.2020.101274.

[259] Benjamin, D., and Kirkpatrick, C. W., 1980, ASM Metals Handbook, Properties and Selection: Stainless Steels, Tool Materials and Special-Purpose Metals, Met. Handbook, Vol. 3, 9th Edn, American Society of Metals.

[260] Thijs, L., Kempen, K., Kruth, J. P., and Van Humbeeck, J., 2013, "Fine-Structured Aluminium Products with Controllable Texture by Selective Laser Melting of Pre-Alloyed AlSi10Mg Powder," Acta Materialia, **61**(5), pp. 1809–1819. https://doi.org/10.1016/j.actamat.2012.11.052.

[261] Thijs, L., Montero Sistiaga, M. L., Wauthle, R., Xie, Q., Kruth, J. P., and Van Humbeeck, J., 2013, "Strong Morphological and Crystallographic Texture and Resulting Yield Strength Anisotropy in Selective Laser Melted Tantalum," Acta Materialia, **61**(12), pp. 4657–4668. https://doi.org/10.1016/j.actamat.2013.04.036.

[262] Salman, O. O., Brenne, F., Niendorf, T., Eckert, J., Prashanth, K. G., He, T., and Scudino, S., 2019, "Impact of the Scanning Strategy on the Mechanical Behavior of 316L Steel Synthesized by Selective Laser Melting," Journal of Manufacturing Processes, **45**, pp. 255–261. https://doi.org/10.1016/j.jmapro.2019.07.010.

[263] Casati, R., Lemke, J., and Vedani, M., 2016, "Microstructure and Fracture Behavior of 316L Austenitic Stainless Steel Produced by Selective Laser Melting," Journal of

Materials Science & Technology, **32**(8), pp. 738–744. https://doi.org/10.1016/j.jmst.2016.06.016.

[264] Mertens, A., Reginster, S., Paydas, H., Contrepois, Q., Dormal, T., Lemaire, O., and Lecomte-Beckers, J., 2014, "Mechanical Properties of Alloy Ti–6Al–4V and of Stainless Steel 316L Processed by Selective Laser Melting: Influence of out-of-Equilibrium Microstructures," Powder Metallurgy, **57**(3), pp. 184–189. https://doi.org/10.1179/1743290114Y.0000000092.

[265] Charmi, A., Falkenberg, R., Ávila, L., Mohr, G., Sommer, K., Ulbricht, A., Sprengel, M., Saliwan Neumann, R., Skrotzki, B., and Evans, A., 2021, "Mechanical Anisotropy of Additively Manufactured Stainless Steel 316L: An Experimental and Numerical Study," Materials Science and Engineering: A, **799**, p. 140154. https://doi.org/10.1016/j.msea.2020.140154.

[266] Kumar, D., Shankar, G., Prashanth, K. G., and Suwas, S., 2024, "Control of Texture and Microstructure in Additive Manufacturing of Stainless Steel 316 L," Journal of Alloys and Compounds, **976**, p. 173040. https://doi.org/10.1016/j.jallcom.2023.173040.

[267] Liu, Z., Yang, Y., Xiao, Y., Lei, H., Yang, C., Liu, Z., Zhao, Q., and Song, C., 2024, "Investigation of 316L Microstructure Evolution Mechanism and Mechanical Properties in Dual-Laser Powder Bed Fusion with Controllable Remelting Time Interval," Materials & Design, **239**, p. 112761. https://doi.org/10.1016/j.matdes.2024.112761.

[268] Wang, J., Zhu, R., Liu, Y., and Zhang, L., 2023, "Understanding Melt Pool Characteristics in Laser Powder Bed Fusion: An Overview of Single- and Multi-Track Melt Pools for Process Optimization," Advanced Powder Materials, **2**(4), p. 100137. https://doi.org/10.1016/j.apmate.2023.100137.

[269] Iqbal, N., Jimenez-Melero, E., Ankalkhope, U., and Lawrence, J., 2019, "Microstructure and Mechanical Properties of 316L Stainless Steel Fabricated Using Selective Laser Melting," MRS Advances, **4**(44–45), pp. 2431–2439. https://doi.org/10.1557/adv.2019.251.

[270] Motaman, S. A. H., Roters, F., and Haase, C., 2020, "Anisotropic Polycrystal Plasticity Due to Microstructural Heterogeneity: A Multi-Scale Experimental and Numerical Study on Additively Manufactured Metallic Materials," Acta Materialia, **185**, pp. 340–369. https://doi.org/10.1016/j.actamat.2019.12.003.

[271] Agius, D., Wallbrink, C., and Kourousis, K. I., 2021, "Efficient Modelling of the Elastoplastic Anisotropy of Additively Manufactured Ti-6Al-4V," Additive Manufacturing, **38**, p. 101826. https://doi.org/10.1016/j.addma.2020.101826.

[272] Wilson-Heid, A. E., Qin, S., and Beese, A. M., 2018, "Anisotropic Multiaxial Plasticity Model for Laser Powder Bed Fusion Additively Manufactured Ti-6Al-4V," Materials Science and Engineering: A, **738**, pp. 90–97. https://doi.org/10.1016/j.msea.2018.09.077.